Engineering Optoelectronics and Smart Sensors Leveraging Metal-Organic Framework Materials

Annika Felicia Möslein
University College
University of Oxford

A thesis submitted for the degree of
Doctor of Philosophy
Trinity 2022

Preface

This dissertation is submitted for the degree of Doctor of Philosophy in the University of Oxford, United Kingdom. The research presented in this work was carried out by the author between January 2019 and July 2022 in the Department of Engineering Science, under the supervision of Professor Jin-Chong Tan.

To the best of my knowledge, the work described in this dissertation is original, except where due reference has been made, acknowledging the work of others. Nothing has been included that is the outcome of work done in collaboration with others, except where explicitly noted. No part of this dissertation, or any similar to it, has been, or is currently being submitted for any degree at this, or any other university. This integrated thesis is less than 250 pages in length.

The work presented herein has been partially published in the following journal papers:

- **A.F. Möslein**, M. Gutiérrez, B. Cohen, and J.C.Tan, "Near-field infrared nanospectroscopy reveals guest confinement in metal-organic framework single crystals", *Nano Letters*, 20, 7446-7454 (2020).
- **A.F. Möslein**, L. Donà, B. Civalleri and J.C. Tan, "Defect Engineering in Metal-Organic Framework Nanocrystals: Implications for Mechanical Properties and Performance", *ACS Applied Nano Materials,* 5, 6398-6409 (2022).
- **A.F. Möslein** and J.C. Tan, "Vibrational Modes and Terahertz Phenomena of the Large-Cage Zeolitic Imidazolate Framework-71", *The Journal of Physical Chemistry Letters*, 13, 2838-2844 (2022).
- **A.F. Möslein**, M. Gutiérrez, K. Titov, L. Donà, B. Civalleri, M.D. Frogley, C. Cinque, S. Rudić, and J.C. Tan, "A Multimodal Study on the Unique Sensing Behavior of a Guest@Metal-Organic Framework Material for the Detection of Volatile Acetone", *Advanced Materials Interfaces*, 10, 2201401 (2023).

Other manuscripts related to the work presented in this thesis:

- M. Gutiérrez, **A.F. Möslein**, and J.C. Tan, "Facile and Fast Transformation of Non-Luminescent to Highly Luminescent MOFs: Acetone Sensing for Diabetes Diagnosis and Lead Capture from Polluted Water", *ACS Applied Materials & Interfaces*, 13, 7801-7811 (2021).

- A.S. Babal, B.E. Souza, **A.F. Möslein**, M. Gutiérrez, M.D. Frogley, and J.C. Tan, "Broadband dielectric behavior of MIL-100 metal-organic framework as a function of structural amorphization", *ACS Applied Electronic Materials*, 3, 1191-1198 (2021).

- T. Xiong, Y. Zhang, L. Donà, M. Gutiérrez, **A.F. Möslein**, N. Amin, B. Civalleri and J.C. Tan, "Tunable Fluorescein-Encapsulated Zeolitic Imidazolate Framework-8 Nanoparticles for Solid-State Lighting", *ACS Applied Nano Materials*, 4, 10321-10333 (2021).

- Y. Zhang, T. Xiong, **A.F. Möslein**, S. Mollick, V. Kachwal, A.S. Babal, N. Amin, and J.C. Tan, "Nanoconfinement of Tetraphenylethylene in Zeolitic Metal-Organic Framework for Turn-on Mechanofluorochromic Stress Sensing", *Applied Materials Today*, 27, 101434 (2022).

- S. Mollick, Y. Zhang, W. Kamal, M. Tricarico, **A.F. Möslein**, V. Kachwal, N. Amin, A.A. Castrejón-Pita, S.M. Morris, and J.C. Tan, "Surface Modulation of Metal-Organic Frameworks for On-demand Photochromism in the Solid State', Submitted (2022).

Other manuscripts published during my DPhil but not directly related to the work developed in this thesis:

- B.E. Souza, L. Donà, K. Titov, P. Bruzzese, Z.X. Zeng, Y. Zhang, A.S. Babal, **A. Möslein**, M.D. Frogley, M. Wolna, G. Cinque, B. Civalleri, and J.C. Tan, "Elucidating the Drug Release from Metal-Organic Framework Nanocomposites via in situ Synchrotron Microspectroscopy and Theoretical Modelling", *ACS Applied Materials & Interfaces*, 12, 5147-5156 (2020).

- B.E. Souza, **A.F. Möslein**, K. Titov, J.D. Taylor, S. Rudic, and J.C. Tan, "Green Reconstruction of MIL-100 (Fe) in Water for High Crystallinity and Enhanced Guest Encapsulation", *ACS Sustainable Chemistry & Engineering*, 8, 8247-8255 (2020).

- B.E. Souza, **A.F. Möslein**, K. Titov, J.D. Taylor, S. Rudić, and J.C. Tan, "Drug guest molecules as modulators during one-step mechanochemical encapsulation in MIL-100 (Fe) framework", Submitted (2022).

This thesis is dedicated to
Heike Görner.

Acknowledgements

The experiences, learnings, and memories from the last few years are only just sinking in. We know that navigating our dreams is not only about pushing ourselves and work harder, but without doubt, it is about seeking out those truly inspiring people who surpass us, not in mere intelligence or allure, but in the depth of their kindness and boundless generosity. We can draw from their well of wisdom, though placing our trust in them may seem like dancing on the edge of vulnerability. Yet, it is precisely in embracing this delicate dance that we unveil life's best rewards.

First and foremost, I would like to thank my supervisor Professor Jin-Chong Tan whose support, enthusiasm, and insight into the subject matter steered me through my doctoral studies. I am especially grateful to Jin-Chong Tan for opening the door to academia by trusting my potential and giving me the chance to discover the fascinating nanoworld. Without him, I would have neither started nor be standing at the end of my DPhil journey.

I am also grateful to all the great scientists who went beyond their role as collaborators and continued to inspire me with their motivation and dedication to science: Dr Sevmir Rudić, Prof. Bartolomeo (Mimmo) Civalleri, Lorenzo Dona, Dr Gianfelice Cinque, and Mark Frogley.

I gratefully acknowledge the financial funding provided by the Oxford Ashton Memorial Scholarship for Engineering, the ERC Consolidator Grant (771575 (PRO-MOFS)), and the Vincent's Avery W. Broadbent Award. Thank you for the support of the Blues Performance Scheme, especially to Duncan, Tiahan and Mark.

Furthermore, I would like to recognise all the past and present members of the Multifunctional Materials & Composites (MMC) Laboratory, especially Bárbara, Mario, Yang, Arun, Michele, Dylan, and Samraj. Thank you for the stimulating scientific conversations, as well as the numerous happy moments we have shared in the lab, during nightshifts in the accelerator, and beyond.

During my time in Oxford, I have been fortunate to meet incredible people whose friendship warmed me like the sun. To Lulu, Bryn, Josh, Sean, Rory, Méli, Becca, JJ, Skiddy, Sam, Fraser, Meirian, and Sandy, thank you for all the countless adventures shared on and off the water. To Amelia, Jirka, Samuel, and Emily, thank you for becoming my little family in our house and motivating me with all our workouts, bike rides, yoga, and climbing sessions. And to Darlan, Mick, Bárbara (again), I cannot thank you enough for the connection, laughs, advise, and friendship.

I am also grateful to my friends from home whose remote support and visits have carried me along the way: to Max, Maja, Izzy, Stefania, Cecilia, Sebi, Miri, and Benedikt, thank you for being there even when I was far away.

Most importantly, I would like to thank my family, especially my parents Stefanie and Christoph, my heroes and role models. Thank you for always trusting and helping me; this achievement is as much yours as it is mine. And thank you to my brothers Dominik and Victor who are my greatest inspiration. I do not have the words to tell you how truly fortunate I feel to have you by my side.

Abstract

Metal-organic frameworks (MOFs) have emerged as promising nanomaterials for the development of advanced sensing technologies. Indeed, their unparalleled features comprising structural diversity, tailorability, high porosity, large surface area, and adsorption affinities can offer superior sensing performance unattainable by the array of conventional materials for selective, fast, and sensitive detection of gases. However, for the integration of MOFs into sensor devices, a thorough understanding of the material's underpinning properties and mechanisms is vital. In this integrated thesis, the key principles, which are used for functionalising MOFs with desired properties, are studied from the single-crystal level (Chapter 1). Herein, Chapter 2 introduces near-field infrared spectroscopy techniques for the chemical characterisation of individual MOF-type crystals at the nanoscale.

Based on this technique, Chapter 3 presents a new strategy to reveal the encapsulation of luminescent 'guest' molecules in the pores of the 'host' MOF framework. This so-called guest@MOF principle is a smart way to engineer novel material for sensors and optoelectronics, however, unambiguously proving the successful encapsulation in lieu of surface adsorption has been challenging thus far.

Turning to defect tuning - another strategy to tune MOF materials for sensing applications - Chapter 4 demonstrates how the combination of nanoscale analytics and density functional theory calculations can probe point defects in individual MOF crystals, further scrutinising their impact on mechanical properties.

Chapter 5 offers insights into the sensing mechanism itself by studying the exceptional response of a guest@MOF material towards volatile acetone. Herein, several spectroscopy techniques ranging from nanoscale analytics to *in situ* and *operando* techniques based on inelastic neutron scattering and synchrotron radiation, all corroborated by theoretical simulations, are used to explore the underlying principles of the unique sensing performance.

Building upon the findings of Chapter 3-5, Chapter 6 presents a detailed characterisation of a promising MOF material for sensing applications. Specifically, theoretical calculations and spectroscopy techniques can explain the interplay between the physical, chemical, and mechanical properties to provide a fundamental understanding of the material's behaviour and structure-function relations.

Finally, Chapter 7 serves as a critical review of the presented findings, further highlighting their contribution to the future development of tailored MOF materials as next-generation sensors.

Contents

Appendices

List of Figures

List of Tables

List of Abbreviations

1-D, 2-D, 3-D	One-, two-, or three-dimensional, referring in this thesis to spatial dimensions.
4-, 6-, or 8MR	4-, 6- or, 8-membered-ring
8HQ	8-hydroxyquinoline
AFM	Atomic force microscopy
ARC	Advanced Research Computing
ATR	Attenuated total reflectance
Au	Gold
B22	Beamline 22 at Diamond Light Source, UK
B3LYP	Becke, 3-parameter, Lee–Yang–Parr (functional)
BET	Brunauer–Emmett–Teller
BDC	1,4-benzenedicarboxylic acid
BS	Basis set
BTC	Benzene-1,3,5-tricarboxylic acid
C	Carbon
Ca	Calcium
CIF	Crystallographic information file
Cl	Chlorine
CO	Carbon monoxide
CO_2	Carbon dioxide
CSD	Cambridge structural database
Cu	Copper
dcIm	4,5-dichloroimidazole
DFG	Difference-frequency generator
DFT	Density functional theory

DMC	Dimethyl carbonate
DMF	Dimethylformamide or N,N-Dimethylformamide
EDS	Energy dispersive (X-ray) spectroscopy
far-IR	far-infrared
FLIM	Fluorescence lifetime imaging
FTIR	Fourier transform infrared (spectroscopy)
FWHM	Full width at half maximum
GaSe	Gallium selenide
guest@MOF	Encapsulation of a ’guest’ molecule into the pores of a ’host’ framework
H	Hydrogen
He	Helium
HDPE	High-density polyethylene
HKUST-1	Hong Kong University of Science and Technology-1
HCR	High-concentration reaction
HRTEM	High-resolution transmission electron microscopy
HPC	High-performance cluster
HeNe	Helium-neon
INS	Inelastic neutron scattering
IR	Infrared
KBr	Potassium bromide
MCT	Mercury cadmium telluride
mid-IR	mid-infrared
mIm	Methylimidazole
MIR	Mid-infrared
MIRIAM	Multimode InfraRed Imaging and Microspectroscopy
MMM	Mixed-matrix membrane
MOF	Metal-organic framework
N	Nitrogen
$\mathbf{N_2}$	Nitrogen gas

nanoFTIR	FTIR nanospectroscopy / near-field Fourier transform infrared spectroscopy
near-IR	Near-infrared
NMR	Nuclear magnetic resonance (spectroscopy)
OX-1	Oxford University-1 (material)
PBE	Perdew–Burke-Ernzerhof (exchange energy)
PBE-D	Perdew–Burke-Ernzerhof exchange energy with a damped dispersion term
PBEsol0-3c	Revised exchange-correlation functionals developed for solids with triple-zeta quality
PDMS	Polydimethylsiloxane
ppb	parts per billion
ppm	parts per million
PXRD	Powder X-ray diffraction
RhB	Rhodamine B
RMS	Root mean square
SEM	Scanning electron microscopy
Si	Silicon
SOD	Sodalite
SPM	Scanning probe microscopy
SR-FTIR	Synchrotron radiation Fourier transform infrared spectroscopy
s-SNOM	scattering-type scanning near-field optical microscopy
TEA	Triethylamine
TEM	Transmission electron microscopy
TFM	Tip-force microscopy
TGA	Thermogravimetric analysis
THz	Terahertz
TPE	Tetraphenylethylene
UiO-66	Universitetet i Oslo-66
UV	Ultraviolet
VOC	Volatile organic compound

XRD	X-ray diffraction
ZIF	Zeolitic imidazolate framework
ZIF-7	Zeolitic imidazolate framework-7
ZIF-71	Zeolitic imidazolate framework-71
ZIF-72	Zeolitic imidazolate framework-72
ZIF-8	Zeolitic imidazolate framework-8
Zn	Zinc
ZnO	Zinc oxide
ZnQ	Zinc(II)-bis(8-hydroxyquinoline)
ZnSe	Zinc selenide
Zr	Zirconium

List of Symbols

Φ	Phase
Δx	Spatial resolution
Γ	Gamma point
Ω	Oscillation frequency
$\hbar$	Planck's constant, $\hbar = 6.62607015 \times 10^{-34}\mathrm{m}^2\mathrm{kg/s}$
α	Amplitude
α	Polarizability
α_{eff}	Effective polarizability
α_n	Local absorption, nanoFTIR absorption spectrum
β	Surface response function
$\beta(\mathbf{u})$	Linear compressibility
δ	Retardation
ϵ	Permittivity
$\epsilon(\omega)$	Dielectric function
η_n	Near-field spectrum
θ	Angle
κ	Absorption coefficient
λ	Wavelength
λ_i	Eigenvalue
ν	Poisson's ratio
σ	Complex scattering coefficient
σ_{in}	Inelastic cross section
υ	Frequency
ϕ	Phase
ω	Angular frequency

A	Complex amplitude
$A(\delta)$	Apodization function
A_{ff}	Far-field absorption
C	Elastic constant
C_{ijkl}	Elasticity tensor
D	Constant
$\mathbf{E}$	Electromagnetic wave
E	Energy; Young's modulus
E_{bf}	Electromagnetic field of background scattering
E_{in}	Incident electromagnetic field
E_{nf}	Electromagnetic field of near-field scattering
E_{scat}	Scattered electromagnetic field
ET	Energy transfer
F	Instrumental factor
G	Shear modulus
H	Height; hardness
I	Intensity
I_{det}	Intensity at the detector
I_{scat}	Scattered intensity
M	Phase modulation frequency
N	Natural number
NA	Numerical aperture
Q	Momentum transfer
R_0	Instrumental correction factor
$R(\omega)$	Response function of the instrument
R	Radius
S	Transition energy
S_{ijkl}	Compliance matrix
U	Amplitude
V_{tot}	Total volume
c	Speed of light, $c \approx 2.99 \times 10^8$ m/s

d	Distance
f	Function
i	imaginary number
k	Wavenumber
n	Refractive index
p	Dipole moment
r	Radius
r_s	Far-field reflection coefficient
s	Optical amplitude
t	Time
$\mathbf{u}$	Unit vector
$\mathbf{v}$	Unit vector
m	Metres
cm	Centimetres
μ**m**	Micrometres
nm	Nanometres
Å	Angstroms
min	Minutes
s	Seconds
ms	Milliseconds
ps	Picoseconds
fs	Femtoseconds
g	Grams
mg	Milligrams
L	Litres
μ**L**	Microlitres
K	Kelvin
°**C**	Degrees Celsius
THz	Terahertz
kHz	Kilohertz
GPa	Gigapascal

MPa	Megapascal
N	Newton
V	Volt

Und es passierte wirklich, und es geschah, und es war gemeint, und es war möglich, [...].
And it really happened, and it materialised, and it was meant, and it was possible, [...].

— Thomas Glavinic *Das grössere Wunder*

1

Introduction

Contents

1.1 Motivations

The repertoire of senses is perhaps the most remarkable and astonishing source of data collection through which living systems perceive, understand, and interact with the outside world. From the detection of external stimuli including touch, pressure, vibrations, temperature, light, and sound to the conscious sensation and response, sensing organs convert chemical and physical information into neuronal signals levering thermodynamics, Nernstian potentials, photochemical processes, and molecular recognition. Inspired by natural sensing systems, scientists and engineers strive to develop new technologies that can probe physical and chemical changes to enhance the perception of the surrounding environment.[1–3] Amongst them are chemical sensing devices that convert a chemical or physical property of a specific analyte into a quantifiable signal, and offer solutions for detection, measurement, smart automation, and monitoring across a wide range of industries.

These include medical diagnostics[4], industrial and manufacturing detection[5], civil security[6], food safety[7], and environmental monitoring[8, 9]. For instance, in the medical sector, chemical sensors are utilized to detect the concentration of glucose or electrolytes in human blood.[10] Piloted by the rising demand of consumers to track data of their personal health, the use of wearable sensing devices has weaved itself into society and can be coupled with new ways for screening and monitoring of critical conditions.[11–13] However, there is no portable sensor to detect low concentrations of volatile organic compounds (VOCs) in exhaled human breath, even though they serve as important biomarkers for disease early detection, response to treatment, exposure to hazardous substances, or precision monitoring.[14–16] Sensing devices that analyse VOCs in breath samples can thus present a non-invasive solution for diagnostics and monitoring.

Similarly, low levels of toxic or explosive VOCs in the industrial and manufacturing sector, or civil security, are difficult to detect, and yet are most hazardous to human health and the environment.[17, 18] Thus, their rapid detection is paramount for controlling the air quality especially in enclosed spaces to ensure workplace and public safety.[19] Although existing portable sensing devices target toxic VOCs such as benzene, dichloromethane, or formaldehyde; all of them inherently have limitations associated with sensitivity, selectivity, operating temperature, or cost that prevent general use.[20–22]

The two exemplary problems described above are in fact intertwined. They can be solved through the engineering of revolutionary sensing technologies that incorporate metal-organic frameworks (MOFs), a new class of nanomaterials offering unique properties beyond the array of conventional materials. Constructed *via* self-assembly of metal clusters and organic linkers, naturally, MOFs are hybrid materials, which crystallise in extended coordination networks.[23–25] Significantly, their characteristic features include structural diversity, tailorability, high porosity, large surface area, and adsorption affinities [26]; and while all of these are hugely beneficial for applications in gas storage and separation [27], catalysis [28], drug delivery [29], and electronics [30, 31], their unparalleled advantages for sensing application can be easily understood.[32–34] Firstly, their high surface areas allow for concentration of the analyte into the pores, which enhances the detective sensitivity. Secondly, the tuneable pore size and functional binding sites enhance the selectivity through size exclusion and specific host-guest interactions; and thirdly, the high porosity of MOFs renders them a promising candidate for reversible uptake and release of guest molecules, which ensures the regeneration and recycling of detection.

While the deployment of novel MOF-based sensor technologies will bring major benefits to the economy, public services, and to the wider society, their realisation depends upon rational design and control of the material functions.[35] Hence, prior to designing high-performance and high-precision sensors for targeted applications, a thorough understanding of the underpinning physical and chemical phenomena in MOFs as well as their structure-function relationships is indubitably necessary.

1.2 Contributions

This DPhil thesis aims to address these challenges by unravelling the principal characteristics of MOFs that are crucial for sensing technologies, including host-guest interactions, defect engineering, sensing mechanisms, and terahertz (THz) phenomena. Specifically, the results comprised in the following chapters shed new light on the ongoing advancements from a new perspective – the single crystal level – by leveraging near-field techniques.

This integrated thesis is composed of 7 chapters: a brief introduction sets off with an exploration of the primary goals and accomplishments presented by each chapter. Chapter 2 demonstrates the use of near-field spectroscopy techniques for advancing the field of MOF characterisation. After a detailed introduction to the technique itself, the chapter then presents several use cases for MOF single-crystal characterisation, highlighting how nanoscale analytics provide a significant tool for distinguishing between different MOF materials and studying the material's behaviour and phenomena at such local scales.

Each of the following chapters begins with a literature review, and then expands on a summary of the corresponding published paper, further providing additional insights based on the Supplementary Information of each manuscript.[36–38] Finally, a scientific discussion and contextualisation of the results herein achieved will be included.

More specifically, Chapter 3 seeks to unravel host-guest interactions of MOFs. While a guest@MOF composite material, where ‘guest’ molecules with desired properties are confined into the nanoscale pores of the ‘host’ framework, depicts a facile strategy to engineer the functions of MOFs even further, as will be outlined in the literature review, it remains challenging in this field of research to distinguish whether the guest molecules are effectively encapsulated within the MOF or adsorbed onto their external surface.[39] This difference however is central not only for designing specific adsorption sites for targeted analytes, and controlling their interactions, but also to achieve high guest loading in the MOF by leveraging its porosity. Chapter 3, therefore, addresses this open question by providing a strategy to confirm guest encapsulation in MOF-type single crystals.

Chapter 4, in turn, explores the tuning of defects in MOF crystals to enhance their reactivity. For instance, open metal-sites introduce additional adsorption affinities, which can be crucial for gas capture and targeted chemical sensing. Following a detailed literature review on defect engineering in MOFs, and accordingly, techniques to characterise structural defects, Chapter 4 then delves into defect transformation during the crystallisation of a prototypical MOF: the zeolitic imidazolate framework ZIF-8. Again, near-field nanoscale analytical techniques, substantiated by *ab initio* density functional theory (DFT) calculations, reveal new insights into defects in MOFs, and their implications for materials performance and stability – key for potential sensing applications.

In Chapter 5, the sensing mechanism itself is unravelled for a guest@MOF composite material with exceptional gas sensing abilities. Firstly, potential use cases for VOC sensing are outlined, and even though advances of MOFs for gas sensing are discussed in literature, the underlying sensing mechanisms is yet to be understood. This is precisely why this chapter demonstrates the efficacy of synchrotron-radiation spectroscopy and inelastic neutron scattering (INS), as well as fluorescence and near-field infrared spectroscopy to afford *in situ* gas dosing experiments. Corroborated by DFT calculations, this synergistic approach discovers the chemical and physical dynamics of the guest@MOF system upon exposure to volatile gases. Knowledge of the underpinning mechanisms that can explain the sensing behaviour in response to physical and chemical stimuli is central to harnessing the unique sensing ability, and further tune it towards potential applications.

Building upon the results of Chapters 3-5, Chapter 6 suggests a MOF system with enhanced sensing performance, namely the zeolitic imidazolate framework ZIF-71. Whereas its structure, synthesis, and basic characterisation have been reported in literature[40], and the material has been proven beneficial for applications in gas adsorption and separation, a detailed understanding of the interplay between physical, mechanical, and chemical properties has been lacking thus far. Herein, Chapter 6 summarises studies on the molecular vibrations and single-crystal properties derived from frequency calculations and nanoscale analytics. This is followed by a detailed analysis of the key vibrational modes in the low-energy region, where phenomena like gate-opening, phase transitions and shearing can be linked with the core physical and mechanical behaviour of ZIF materials.[41] Leveraging the concepts of guest encapsulation and defect engineering (the latter to introduce open metal site as additional reaction sites), and knowledge of the underpinning mechanisms of vapour sensing allow for tailored design of a guest@ZIF-71 system with enhanced sensing abilities.

These ideas are discussed in the last and concluding chapter, which provides an overview of the results and discoveries made, and presents perspective for future areas for exploration in the field. Together, the results compiled in this thesis provide a detailed investigation of the key phenomena of MOFs that offer a versatile platform to inspire further tuning, and development of MOF-based sensing technologies.

It is sometimes of great use in natural philosophy to
doubt of things that are commonly taken for granted;
especially as the means of resolving any doubt, when
once it is entertained, are often within our reach.

— Sir William Herschel

2

Background

Contents

2.1 Introduction

The design of cutting-edge sensing technologies based on MOF materials relies on a thorough understanding of the material's intrinsic properties and response behaviour when exposed to external stimuli. In particular, due to their nanoscopic nature, the features of MOF crystals determine not only the mechanical, optical, physical and chemical properties, but also the overall performance. The power of engineering MOF systems for application is, therefore, solely ascribed to knowledge and meticulous control of the size, shape, and structure of the nanocrystals. Although most common characterisation techniques in the field of MOF research, including powder X-ray diffraction (PXRD), nitrogen adsorption/ desorption isotherms, thermogravimetric analysis (TGA), or nuclear magnetic resonance (NMR) spectroscopy, are used respectively to confirm crystallinity, porosity, thermal stability, or purity of the sample, they all determine (averaged) bulk properties from a powder sample.[42] If, however, the morphologies of single crystals are investigated, additional imaging techniques may include atomic force microscopy (AFM) or scanning electron microscopy (SEM). While these are powerful tools to image MOF-type crystals with nanoscale resolution, they do not offer fully qualitative analysis about local structure, or chemical composition. One way to achieve this is to couple SEM with energy dispersive X-ray spectroscopy (EDS), however, based on an electron beam, this technique is better suited for probing heavier elements such as metal incorporation in MOFs; and it is a technique deemed destructive, since a conductive coating is required to alleviate image artifacts given the insulating nature of most MOFs.[42] A common approach to obtain chemical information is based on Fourier transform infrared (FTIR) spectroscopy. In the infrared region of the electromagnetic spectrum, corresponding to wavenumbers of approximately 300 to 3000 cm^{-1}, the photon energies match the vibrational frequencies in a material. If a material is illuminated at a frequency that corresponds to a fundamental vibration, the molecular vibration v is excited as the energy ΔE is absorbed, following the relation $\Delta E = \hbar v$, where $\hbar$ is the Planck's constant.

2.2 Vibrational modes

The discovery of absorption bands in the infrared (IR) region, as a pioneering proof for a region of the electromagnetic spectrum beyond the visible light, led to the first studied vibrational spectrum by Sir William Herschel in 1800.[43] However, it

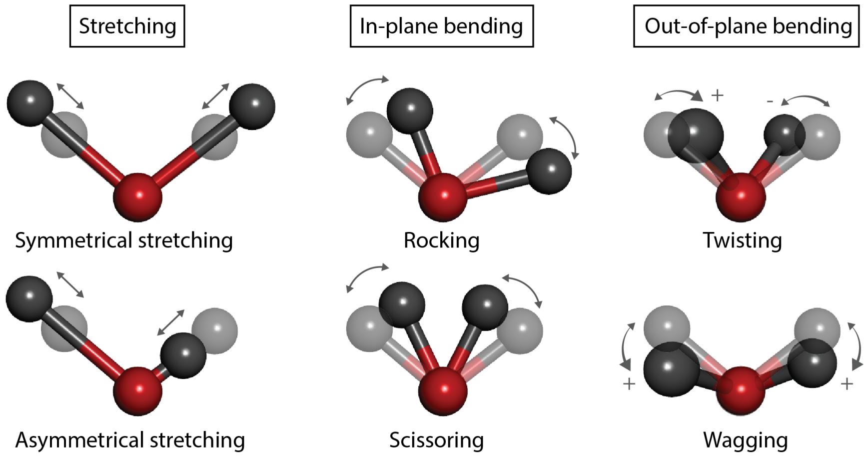

Figure 2.1: The normal vibrational modes of polyatomic molecules.

was not until quantum theory advanced at the beginning of the twentieth century that an understanding of the molecular vibrations in the entire spectrum could be achieved.[23] Employing the Schrödinger wave equation successfully correlated the observable IR frequencies with transitions between quantised vibrational energy levels. In general, a molecular vibration describes the coherent oscillations of atoms relative to each other at a characteristic frequency. As the modes only involve (approximately) harmonic displacements of the atoms from their equilibrium positions, the centre of gravity is preserved. Therefore, the three translational motions of the entire molecule along the x-, y- and z-axes, as well as the three rotational motions about these mutually perpendicular directions are excluded when considering vibrational modes. A molecule with N atoms has thus $3N-6$ degrees of freedom, which correlate with the number of normal molecular vibrations.[44] However, for molecules with certain elements of symmetry, some vibrations may be deteriorated, while in linear molecules, the rotation around the axis of the bond is lost as a degree of freedom since there is no displacement of any of the atoms involved. As a result, a linear molecule has an additional vibration, and the total number of molecular vibrations is $3N-5$. Each normal mode is associated with a combination of displacements of the atoms. Only if these collectively evoke a change in dipole moment, a transition to another quantum state is observed. This leads to the so-called optical selection rule, where a molecule is only promoted to the excited state in IR-active modes, while in IR-inactive modes, its dipole moment does not change.[45]

Each molecular vibration is described by a combination of coupled motions of atoms, including displacements with a change in the length of a bond, either symmetrical or asymmetrical stretching, and modes with a change in angle. The latter are described by in-plane bending modes (scissoring and rocking) and out-of-plane vibrations (wagging and twisting), as illustrated in Figure 2.1. For many vibrational modes, only a few atoms are subject to a large displacement, and thus the frequency of such modes is characteristic of the specific functional group. Because their frequency and intensity also depend on the atomic environment in the molecule, these absorption bands are unique for a particular molecule, and can thus be used to distinguish one molecule from another containing similar functional groups.[46] Beyond this so-call fingerprint region, the low-energy vibrations are prevalent in the far-IR or Terahertz (THz) region ranging from 0 to 300 cm^{-1}, as indicated in Figure 2.2. As opposed to the mid-IR region, where vibrational bands are used to identify the presence or absence of specific functional groups, simultaneous vibrations of all atoms, or in other words collective modes, are excited in the low-energy region. Therefore, these THz modes provide structural information and can hold the key to the intrinsic mechanical and physical properties of a material.[47] However, their investigation demands for advanced techniques employing synchrotron radiation (SR), coupled with theoretical methods such as density functional theory (DFT) to aid in, since the absorbed long wavelength radiation is often below the cut-off of conventional mid-IR detectors.

2.3 Density functional theory

Ab initio density functional theory (DFT) calculations, in principle, evaluate the force fields acting on the electrons. As the second derivative of the energy, the force constant considers the interactions emerging from electrons and nuclei within the molecule. In the DFT approach, the terms involving the Coulomb interactions between the electrons (exchange correlation energy) are modelled by functionals

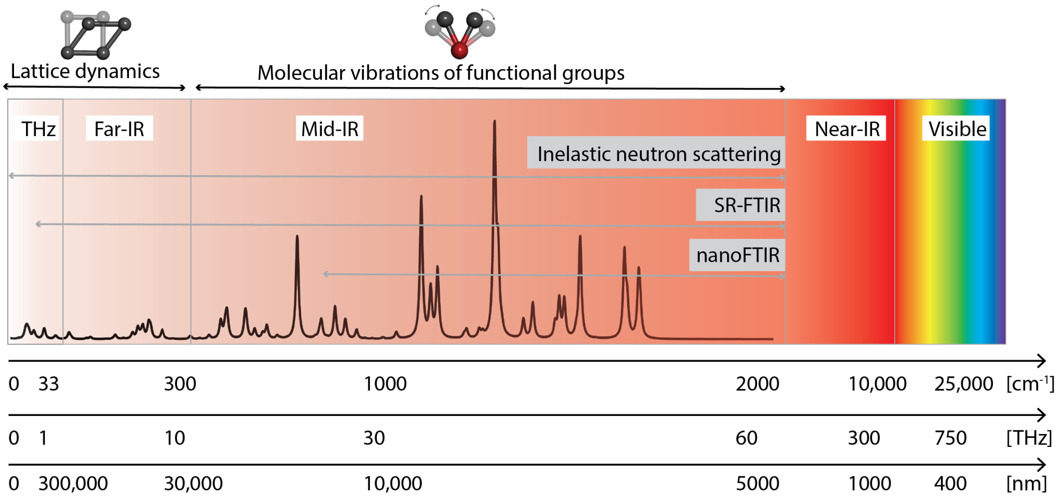

Figure 2.2: The infrared (IR) region of the electromagnetic spectrum. Different types of IR radiation are characterised by their frequency and wavelength, and the characteristic vibrational dynamics, as well as suitable techniques to probe them, are illustrated.

employing different levels of theory. Here the crystal orbital is approximated by a linear combination of Bloch functions, built from localized functions ("atomic orbitals"). These atomic orbitals are respectively represented as linear combinations of Gaussian-type functions whose constant coefficients are defined by the input data.[48] Commonly used, for instance, is the B3LYP functional, a hybrid model proposed by Becke (B3)[49] to advance the gradient-corrected correlation of Lee et al.(LYP)[50]. Combined with the Grimme's dispersion correction (B3LYP-D3)[51], the DFT calculations yield theoretical IR spectra demonstrating the closest resemblance with experimental frequencies.[52]

2.4 Fourier transform infrared (FTIR) spectroscopy

To measure the infrared absorption spectrum of a sample, the core of a FTIR spectrometer is an interferometer whose purpose is to modulate the IR radiation intensity or optical signal. Even though there exists a range of interferometers, modern FTIR spectroscopy still relies on the theoretical concept and design that was originally developed by Michelson in 1891.[53] In a Michelson interferometer, modulation is achieved by separating the incident radiation into two beams at a beamsplitter, as illustrated in Figure 2.3. One beam is transmitted to a fixed mirror,

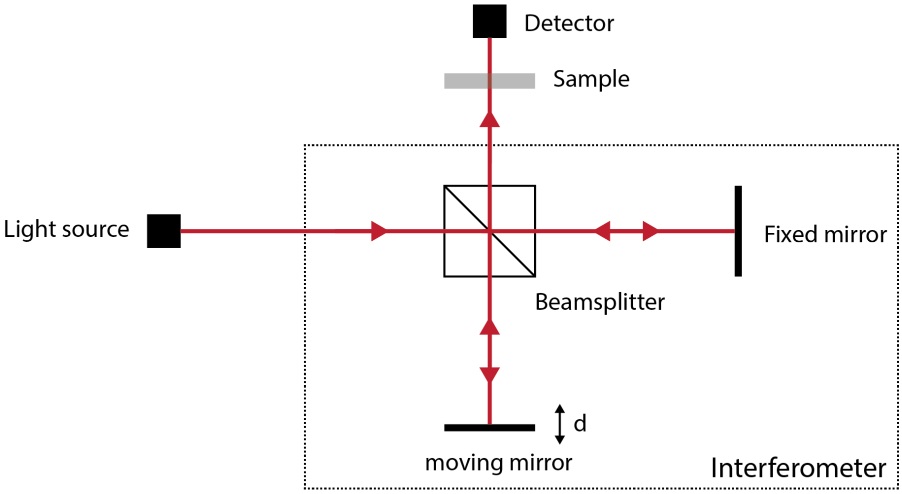

Figure 2.3: Setup of a Michelson interferometer. A collimated beam from an IR light source is split by a beamsplitter. Both beams are back-reflected by different mirrors, superpositioned at the beamsplitter and focussed onto a detector.

while the other beam passes to a moving mirror translated along the optical path. Both mirrors reflect the beams back to the beamsplitter, where they are recombined and focussed onto a detector. Because of the translational motion of the mirror, the back-reflected beam has been Doppler shifted, and after superposition, the new beam exhibits a time-dependent interference. As a result, the intensity of each wavelength measured at the detector varies with the optical path difference. The corresponding interferogram can be demodulated and Fourier transformed to yield the IR absorption spectrum. In the following sections, the working principle and theory of FTIR spectroscopy will be introduced, following the detailed descriptions provided in the *Handbook of Vibrational Spectroscopy* by Chalmers and Griffiths, and *Fourier Transform Infrared Spectroscopy* by Griffiths and Haseth.[23, 54, 55]

2.4.1 Principles of an interferometer

Before considering the broadband IR light source that is used for FTIR spectroscopy, it is useful to assume a monochromatic, perfectly collimated IR beam. If the wavelength of such a source is λ_0 [cm], the corresponding wavenumber ω_0 [cm^{-1}], or spatial frequency, is

$$\omega_0 = \frac{1}{\lambda_0}. \tag{2.1}$$

For a monochromatic light source, the electromagnetic wave $\mathbf{E}$ propagating as a function of time t along the z-axis can be represented in terms of a cosine function

$$\mathbf{E}(z,t) = a\cos[2\pi(\upsilon t - \frac{z}{\lambda})], \tag{2.2}$$

with the amplitude of the light wave a, its frequency υ, and wavelength λ. The wavefront travels along the z direction with a speed

$$c = \lambda\upsilon. \tag{2.3}$$

In vacuum, the speed of light is approximately $2.99 \times 10^8 \frac{m}{s}$, while in a medium with refractive index n, the speed of a light wave is described by

$$v = \frac{c}{n}. \tag{2.4}$$

With a constant frequency, the wavelength is

$$\lambda_n = \frac{\lambda}{n}. \tag{2.5}$$

Now, using the angular frequency ω, with

$$\omega = 2\pi\upsilon, \tag{2.6}$$

and the propagation constant k given by

$$k = \frac{\omega}{c}n = \frac{2\pi\upsilon}{\lambda\upsilon}n = \frac{2\pi}{\lambda_n}, \tag{2.7}$$

leads to a compact form of equation 2.2 describing a plane wave propagating through space:

$$\mathbf{E}(z,t) = a\cos(\omega t - kz). \tag{2.8}$$

Considering an ideal point source, a spherical wave can be assumed leading to

$$\mathbf{E}(r,t) = \frac{a}{r}\cos(\omega t - kr). \tag{2.9}$$

However, a complex exponential representation is often preferred such that equation 2.8 can be written in the form

$$\mathbf{E}(z,t) = \Re\Big\{ae^{i(\omega t - kz)}\Big\}. \tag{2.10}$$

This expression can be divided into factors with spatial and time dependence:

$$\begin{aligned}\mathbf{E}(z,t) &= \Re\Big\{ae^{-ikz}e^{i\omega t}\Big\} \\ &= \Re\Big\{ae^{-i\phi}e^{i\omega t}\Big\} \\ &= \Re\Big\{Ae^{i\omega t}\Big\},\end{aligned} \tag{2.11}$$

where $\phi = 2\pi\frac{z}{\lambda}$, and $A = ae^{-i\phi}$ is the complex amplitude.

At a particular value of z, the intensity is given by

$$I \propto EE^{*}. \tag{2.12}$$

If two waves are superimposed (or in other words, they interfere) and they are propagating in the same direction with the same polarisation and frequency, the complex amplitude at any point is the sum of the two respective amplitudes:

$$A = A_1 + A_2. \tag{2.13}$$

Again, $A_1 = ae^{-i\phi_1}$ and $A_2 = ae^{-i\phi_2}$ represent the complex amplitudes of each wave, and the resulting intensity can be written as

$$\begin{aligned}I &= |A|^2 \\ &= (A_1 + A_2)(A_1^{*} + A_2^{*}) \\ &= |A_1|^2 + |A_2|^2 + A_1A_2^{*} + A_1^{*}A_2 \\ &= I_1 + I_2 + 2\sqrt{I_1I_2}\cos(\Delta\phi),\end{aligned} \tag{2.14}$$

where I_1 and I_2 are the intensities of the two waves with the phase difference $\Delta\phi = \phi_1 - \phi_2$ between them.

Since the two waves originate from the same source ($\Delta\phi = 0$ at the origin), the phase difference is introduced by the translational motion of the moving mirror described by the optical path difference or retardation δ:

$$\Delta\phi = \frac{2\pi}{\lambda}\delta. \tag{2.15}$$

Considering an ideal beamsplitter, where $I_1 = I_2 = 0.5I_0$, the intensity at the detector is

$$I_{det} = 0.5I_0(1 + \cos\phi) = 0.5I_0\Big(1 + \cos(\frac{2\pi}{\lambda}\delta)\Big). \tag{2.16}$$

If the retardation δ is a multiple of λ, the two beams interfere constructively and $I_{det} = I_0$, while the opposite is true if, for instance, the retardation is $\delta = \frac{\lambda}{2}$. In this case, destructive interference occurs, and the resulting intensity is $I_{det} = 0$. Moving the mirror with a constant speed thus results in a sinusoidal variation of the intensity measured at the detector.

In practice, however, the signal at the detector is affected by experimental factors, including beamsplitter efficiency and responsivity of the detector. Given the same system set-up, these factors are constant and can be described by a correction factor R_0:

$$I_{det} = 0.5R_0I_0(1 + \cos\phi) = 0.5R_0I_0\Big(1 + \cos(\frac{2\pi}{\lambda}\delta)\Big). \tag{2.17}$$

Since the first term describes the intensity of one beam without interference, and is therefore independent of the optical path length, it is the second term that is of interest in FTIR spectroscopy. This modulated component is called an interferogram, and is recorded at the detector:

$$I(\delta) = F_0\cos(\frac{2\pi}{\lambda}\delta), \tag{2.18}$$

where F_0 is defined as $F_0 = 0.5R_0I_0$. Thus, in the case of a monochromatic light source, the wavelength λ can be measured directly from the interferogram, and the amplitude of the interferogram is direclty related to the intensity of the source I_0, only altered by the instrumental characteristics R_0.

2.4.2 Theory of FTIR spectroscopy

Turning now from the monochromatic beam to a broadband light source, the incoming wave will consist of a distribution of wavelengths such that

$$I(\delta) = \int_{-\infty}^{+\infty} F(\lambda) \cos(\frac{2\pi}{\lambda}\delta)\, d\lambda, \tag{2.19}$$

or for an ideal interferometer:

$$I(\delta) = \int_{-\infty}^{+\infty} 0.5 I_0(\lambda) \Big(1 + \cos(\frac{2\pi}{\lambda}\delta)\Big)\, d\lambda. \tag{2.20}$$

Using the wavenumber $k = \frac{2\pi}{\lambda}$, this can be written as

$$\begin{aligned} I(\delta) &= \int_{-\infty}^{+\infty} 0.5 I_0(k) \Big(1 + \cos(k\delta)\Big)\, dk \\ &= \int_{-\infty}^{+\infty} 0.5 I_0(k)\, dk + \int_{-\infty}^{+\infty} 0.5 I_0(k) \cos(k\delta)\, dk. \end{aligned} \tag{2.21}$$

Again, only the second term is modulated, while the first term that describes the time-averaged intensity, or direct current component, for one beam is filtered out. The resulting modulated signal with alternating current (and therefore varying intensity about the constant term) is written as

$$I(\delta) = \int_{-\infty}^{+\infty} I(k) \cos(k\delta)\, dk. \tag{2.22}$$

This interferogram is a Fourier transform, the solution of which yields the spectrum of the incident light:

$$I(k) = \frac{2}{\pi} \int_{-\infty}^{+\infty} I(\delta) \cos(k\delta)\, d\delta. \tag{2.23}$$

Thus, by measuring the interferogram at the detector for varying optical path differences, the spectral intensity distribution of the beam is obtained as a function of wavenumber. If, in the case of spectroscopic measurements, the beam has passed

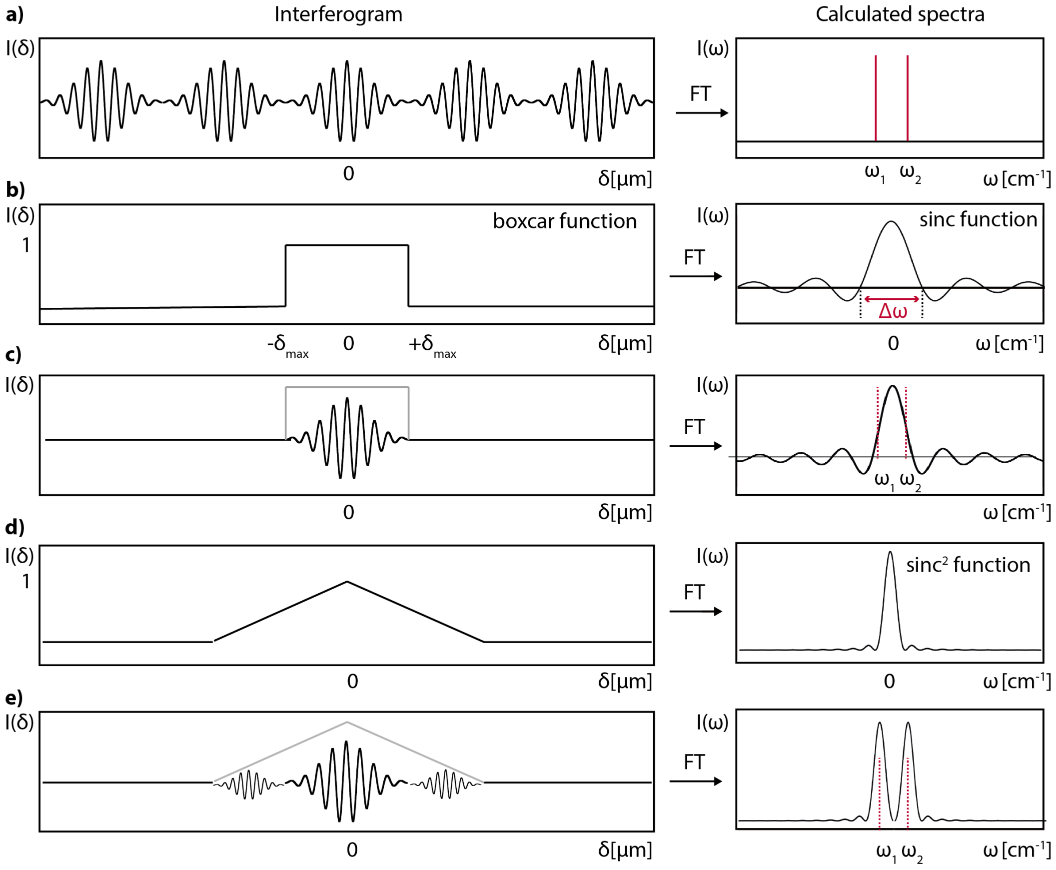

Figure 2.4: Apodization in FTIR spectroscopy. a) A section of an infinitely long interferogram composed of two cosine waves with equal amplitude, and the resulting Fourier-transformed (FT) spectrum. b) Boxcar apodization function and its corresponding spectrum in Fourier-space with indicated spectral resolution. c) Interferogram of a) convoluted with boxcar function of b) and the resulting spectrum. d) Triangular apodization function and corresponding spectrum. e) Convolution of interferogram of a) with apodization function of d), and resulting spectrum.

through a sample, and accordingly, energy at specific frequencies gets absorbed *via* excitation of molecular vibrations, characteristic absorption bands are observed in the spectrum. This yields the unique IR absorption spectrum for a material.

In practice, however, the measured spectrum inherently contains instrumental effects and background contributions, which are omitted through normalisation with a reference spectrum recorded under the same conditions. Similarly, an ideal interferometer that can measure an intensity spectrum with infinitely high spectral resolution and bandwidth, has been assumed thus far.[56] Yet, in reality, the optical path difference can only be varied by a finite distance, limiting the integration, and thus the resolution of the recorded spectrum. These truncations lead to a sinc ($\frac{\sin(x)}{x}$) line shape that is affected by large side lobes, as shown in Figure 2.4 (b,c).

To suppress these effects, and account for the sampling over a finite optical path difference, the interferogram is multiplied by an apodization function $A(\delta)$ that is unity at the centre burst and decreases monotonically with increasing retardation δ (i.e. zero at $\pm\delta_{max}$).

$$I(k) = \frac{2}{\pi} \int_{-\infty}^{+\infty} I(\delta) A(\delta) \cos(k\delta)\, d\delta. \tag{2.24}$$

If the apodization function is a linear ramp, convolution with the interferogram results in a line shape given by a sinc^2 function

$$A(\delta) = \frac{\sin^2(\pi k \delta_{max})}{(\pi k \delta_{max})^2}, \tag{2.25}$$

which is the Fourier transform of the apodization function (see Figure 2.4 d,e).

Accordingly, for a sinc^2 function, the spectral resolution $\Delta\omega$ is given by

$$\Delta\omega = \frac{1}{\delta_t}. \tag{2.26}$$

It therefore depends on the total retardation δ_t that describes the limited translation of the moving mirror. For instance, if the mirror changes position between $+480\,\mu$m and $-480\,\mu$m (retardation 960 μm), the spectral resolution is limited to $\Delta\omega = \frac{1}{0.096\text{ cm}} = 10.4\text{ cm}^{-1}$.

Similarly, the true spectrum is digitised and sampled at finite intervals $\Delta\delta$, which limits the maximum frequency ω_{max}, known as the spectral bandwidth:

$$\omega_{max} = \frac{1}{\Delta\delta}. \tag{2.27}$$

Even if the spectrum derived from the interferogram ranges from 0 to ω_{max}, information is only obtained about the first half, since the second half is simply its conjugate, as described by Nyquist theorem. In addition, discrete sampling limits the number of data points in the resulting spectrum. Only spectral features that are separated by $\frac{1}{\delta_t}$, are fully resolved. One way to improve and smoothen the spectrum is given by adding zeros to both ends of the interferogram, thereby

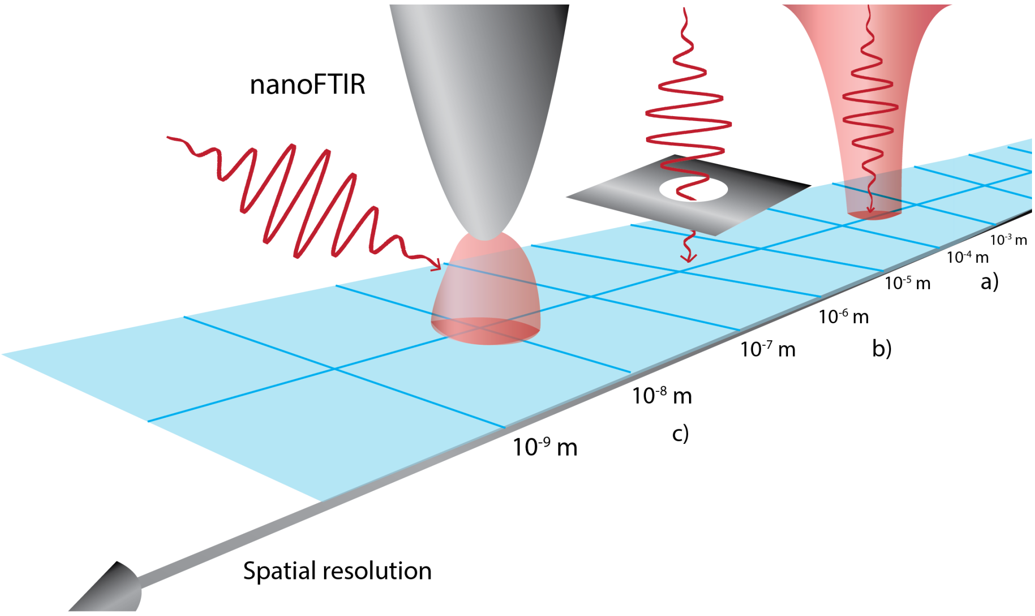

Figure 2.5: Spatial resolution of different FTIR techniques. Typically, macroscopic ('bulk') samples are probed with conventional FTIR spectroscopy (a), as free-space focussing of an IR beam is limited by diffraction. In micro-FITR (b), the spatial resolution of about 10 μm is achieved by imaging the sample in transmission mode through small apertures. The spatial resolution can be improved yet further, to the 10 nm scale, by performing s-SNOM and nanoFTIR leveraging a sharp metal tip (c). Adapted from ref. [57] with permission from Springer Nature Copyright (2021).

artificially increasing the total retardation. This technique called zero-filling does not change the original data points, but instead, new points are added in between, and higher sampling of the spectrum is achieved.

2.4.3 FTIR spectroscopy techniques

Building upon the fundamental principles of a Michelson interferometer and Fourier transformation of the recorded signal, various spectroscopy techniques have been developed, where a broadband infrared beam either passes through a sample (transmission FTIR spectroscopy), or gets reflected by it, as in the case of attenuated total reflectance (ATR-) FTIR. In these most commonly used techniques, FTIR spectra are measured of a macroscopic (bulk) sample (see Figure 2.5). To push the level of detection towards smaller scales, and gain chemical and structural information that is spatially resolved, micro-FTIR spectroscopy was introduced.

Here, a spatial resolution of about 10 μm is achieved by imaging the sample in transmission mode through small apertures.[47, 58, 59] A better resolution is however unattainable using classical optical measurement techniques due the wave nature of light that imposes a physical constraint on the spatial resolution. As was shown by Abbe at the end of the 19th century, the diffraction limit of light depends on the wavelength λ of the light source.[60] If two features are closer than the minimum distance Δx_{min}, they cannot be unambiguously resolved:

$$\Delta x_{min} = \frac{0.61\lambda}{NA}. \tag{2.28}$$

Here, n is the refractive index of the surrounding medium through which the beam passes (usually air), and $NA = n\sin(2\theta_{max})$ is the numerical aperture derived from the maximum collection angle $2\theta_{max}$ of the instrument. Given that the largest values of the NA achievable with state-of-the-art measurement techniques are in the range of $0.9 - 1.4$, the maximum spatial resolution of conventional optical techniques is approximated by $\Delta x_{min} = \frac{\lambda}{2}$. Therefore, for infrared light, the spatial resolution is limited to a few micrometers.

One way to circumvent the diffraction limit, and still obtain chemical and structural information of a sample at the nanoscale, is offered by scattering-type scanning near-field optical microscopy (s-SNOM) coupled with FTIR nanospectroscopy (nanoFTIR).[61–63] These techniques enable simultaneous imaging and FTIR spectroscopy with nanoscale spatial resolution, and their principles will be described in Section 2.5, following the concepts presented in publications [64–71].

2.5 Principles of s-SNOM

Scattering-type scanning near-field optical microscopy (s-SNOM) is based on a monochromatic infrared laser beam that, instead of illuminating the sample directly, is focussed onto a metal-coated probing tip by a parabolic mirror. Akin to scanning probe microscopy (SPM), where the sample is scanned by virtue of a sharp tip measuring certain properties, this probing tip is in proximity to the sample.

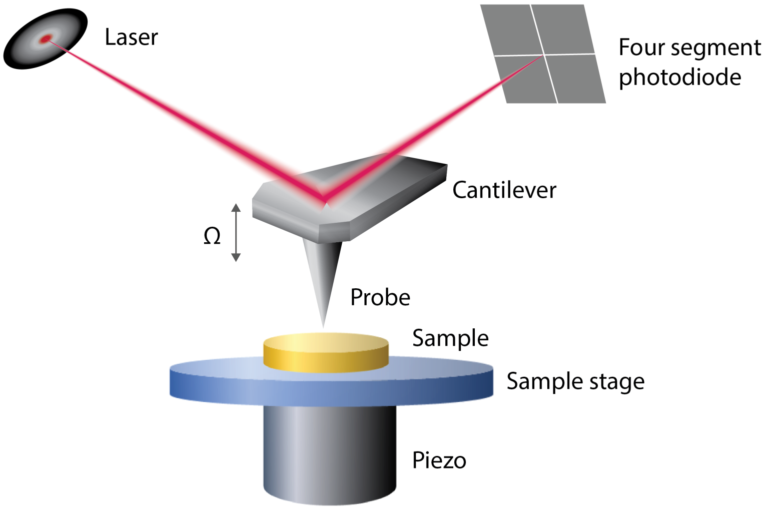

Figure 2.6: Schematic representation of an atomic force microscopy (AFM) setup. The AFM cantilever reflects a laser to a position-sensitive detector to record the cantilever deflection, which depends on the sample height. In tapping-mode, the tip oscillates with a frequency Ω.

However, in this case, it is illuminated and serves as an optical antenna, since the electromagnetic field gets confined towards the tip apex creating an evanescent near-field in its close surrounding. Due to the near-field interaction between the tip and the sample, the optical properties of the sample modify the radiation that is backscattered from the tip to a parabolic mirror. Therefore, the backscattered light contains information about the sample, and if interferometric detection is employed, the characteristic optical phase and amplitude (or absorption and reflection) of the sample at the illumination frequency can be measured. Significantly, these are measured from near-field interactions which only extend to the scale of the tip radius (20 nm), thus scanning the sample surface provides images of the optical phase and amplitude with nanoscale resolution.

2.5.1 Atomic force microscopy

Typically, s-SNOM is based on atomic force microscopy (AFM), which provides spatially localised information about the topography of a sample.[72] This is achieved by scanning a sharp probe (AFM tip) across the surface of the sample under investigation, while monitoring the deflection of the long, flexible probe cantilever.

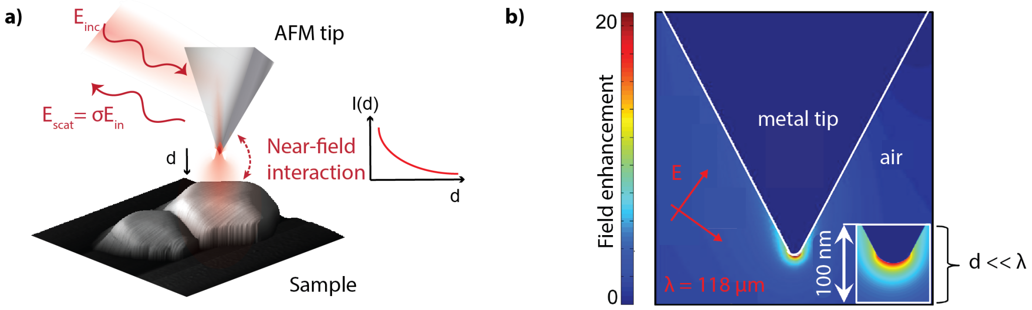

Figure 2.7: Working principle of s-SNOM. a) A focussed infrared laser beam illuminates a metallic AFM tip, which creates an evanescent near-field in close proximity. The back-scattered light from the tip contains information about the sample's optical properties due to this near-field interaction. b) Numerical simulation of field distribution of a metal tip illuminated with far-infrared light with $\lambda = 118\ \mu$m, adapted from ref. [73] with permission from American Chemical Society, Copyright 2008.

Since the sample and tip are in close proximity, mechanical interactions such as attractive and repulsive forces affect the cantilever due to its low spring constant. The corresponding bending of the cantilever is detected by focussing a laser beam on the backside, and measuring its reflection with a position-sensitive photodiode (see Figure 2.6). If the tip is operated in contact mode, a feedback system adjusts the height of the cantilever such that the deflection is constant, from which the height of a sample at each pixel can be derived. s-SNOM, however, is based on a tapping-mode AFM, where the tip oscillates with a resonance frequency Ω without establishing contact with the sample. Instead, when the tip approaches the sample, the oscillation amplitude is damped due to bespoke interaction forces. Akin to contact mode, a feedback system is employed to keep the amplitude constant by changing the vertical position of either the sample or the tip using a piezoelectric driver. Therefore, by recording the vertical position, the topography of the scanned sample can be measured with the resolution only being limited by the radius of the tip apex.

2.5.2 Field enhancement

For the purpose of s-SNOM imaging, an infrared laser beam is focussed by a parabolic mirror onto a metallic AFM tip. Upon illumination, the tip acts as an optical antenna, with surface plasmon polaritons being excited, and charge accumulation being induced towards the apex of the tip. The distribution of the electric field is visualised in Figure 2.7, where a plane wave with linear polarisation parallel to the tip axis (p-polarisation) is numerically simulated with a wavelength $\lambda = 118$ nm, as indicated by the red arrows.[73] In this figure, the colour scheme describes the ratio between the local and incident electric fields, or in other words, the field enhancement. At the apex of the metallic tip, a very high local field (near-field) is induced that decays exponentially with the distance. If a sample is placed in close proximity (e.g. closer than the spatial decay of the evanescent near-field), the optical properties of the sample, due to near-field interactions, alter the light that is backscattered from the tip. This is best described by the complex scattering coefficient σ linking the incident field E_{in} with the scattered field E_{scat} following the relation:

$$E_{scat} = \sigma E_{in}. \tag{2.29}$$

Importantly, the complex coefficient $\sigma = se^{i\varphi}$ includes the optical amplitude s and phase φ of the sample, and thus, collecting the backscattered light with the same parabolic mirror and employing an interferometric detection scheme yields information about optical properties the sample. Further, since the near-field interactions are localised around the apex of the tip, these are in fact local sample properties.

2.5.3 Detection of the backscattered light

However, the back-propagating light collected by the parabolic mirror contains more than just the near-field interactions. This is due to reflection from other optical elements and direct scattering from the tip without any near-field contributions. Therefore, assuming the simplest case, the intensity of the backscattered light I_{det} directly measured by the detector depends on the electric fields of near-field scattering E_{nf} and background scattering E_{bg}:

$$I_{det} = I_{scat} \propto |E_{scat}|^2 = |E_{nf} + E_{bg}|^2 = (E_{nf} + E_{bg})(E_{nf} + E_{bg})^*. \tag{2.30}$$

Because s-SNOM is based on a tapping-mode AFM, the tip is subjected to vertical oscillations with a frequency Ω and an amplitude set to values significantly smaller than the wavelength of the incident light. Thus, both scattering contributions are in fact modulated by the oscillation frequency:

$$E_{scat} = E_{nf} + E_{bg} = \sum_{n=0}^{\infty} E_{nf,n} \cos(n\Omega t) + \sum_{n=0}^{\infty} E_{bg,n} \cos(n\Omega t), \tag{2.31}$$

where

$$E_{nf,n} = \sigma_{nf,n} E_{in} = s_{nf,n} e^{i\varphi_{nf,n}} E_{in}, \tag{2.32}$$

and

$$E_{bg,n} = \sigma_{bg,n} E_{in} = s_{bg,n} e^{i\varphi_{bg,n}} E_{in} \tag{2.33}$$

are the n^{th}-order complex-valued Fourier coefficients of the two electric fields.

Significantly, the tip oscillation differently affects the two contributions: since the near-field scattering is associated with an exponential decay of the evanescent waves from the tip apex, it exhibits a non-linear decrease as the distance from the tip increases. The background contributions, in contrast, only depend on the spatial variations of the incident field that are of the order of its wavelength. Therefore, and since the tapping amplitude is significantly smaller than the wavelength ($\Omega << \lambda$), the background scattering is deemed to change linearly with the tip position. Considering higher harmonics of the tip frequency thus reduces contributions of the background scattering, and, at sufficiently high harmonics (i.e. integer multiples of the tip frequency $n\Omega$), the corresponding Fourier coefficients are negligible in comparison with the ones of the near-field scattering due to the non-linearity of the latter.[74]

Therefore, demodulation at higher harmonics ($n \geq 2$ for infrared light) will suppress the background contributions if the electric field E_{scat} was measured. Instead, however, the signal measured at the detector is proportional to the intensity I_{scat}, with $I_{det} \propto I_{scat} \propto |E_{scat}|^2$, and thus, it is quadratic with background and near-field terms being mixed. Given that higher harmonics of the background

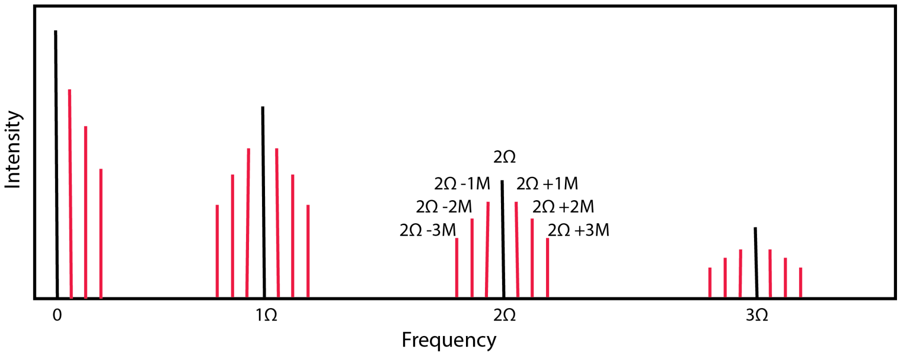

Figure 2.8: Signal splitting in pseudo-heterodyne detection in s-SNOM.The tip frequency is denoted by Ω, while M is the phase modulation frequency. Adapted from ref. [75] with the permission of AIP Publishing (2006).

scattering are negligible (i.e. $E_{bg,n} \approx 0$ for $n > 1$), any harmonic component of the detected intensity is denoted as

$$I_{det,n} = E_{bg,0}E^*_{nf,n} + E_{nf,n}E^*_{bg,0}. \tag{2.34}$$

This indicates that all harmonic components of the detected signal $I_{det,n}$ are affected by the background $E_{bg,0}$, which cannot be fully suppressed by simple demodulation at higher harmonics. To effectively obtain a near-field signal without background contributions, this demodulation scheme is coupled with a pseudo-heterodyne interferometric detection scheme explained below.

2.5.4 Pseudo-heterodyne detection

Building upon the principles of an asymmetrical Michelson interferometer, where the sample stage represents one of the interferometer arms illuminated by the transmitted beam, Oelic *et al.* suggested a pseudo-hetereodyne detection.[75] Here, the second beam that is reflected by the beamsplitter is seen as the reference beam and is modulated by a planar reference mirror moving sinusoidally in direction of the beam propagation. After recombination of both beams at the beamsplitter, the resulting interference is measured at the detector:

$$I_{det} = [E_{scat} + E_{ref}]^2 = (E_{bg,0} + E_{nf,n} + E_{ref})(E_{bg,0} + E_{nf,n} + E_{ref})^*. \tag{2.35}$$

Importantly, as the probing tip oscillates with a frequency Ω, the scattering field (near-field and background contributions) is modulated at the same frequency and its higher harmonics, while the reference beam is phase-modulated with the frequency M of the moving mirror. Since the phase modulation frequency M ($\sim$300 Hz) is chosen to be significantly lower than the tip frequency Ω ($\sim$250 kHz), the interfered signal measured at the detector exhibits a spectrum, where sidebands appear at multiples of the phase modulation frequency M around the tip oscillation frequency Ω and its higher harmonics (i.e. at positions $n\Omega + mM$), as indicated in Figure 2.8. Therefore, assuming background contributions at sufficiently high harmonics are negligible, the background-free near-field signals can be reconstructed by measuring the Fourier coefficients at the first and second sidebands ($n\Omega + 1M$ and $n\Omega + 2M$, $n > 1$). Another important implication of the pseudo-heterodyne detection is that both optical amplitude and phase can be derived simultaneously and independently from the modulus and argument of the n^{th} harmonic of the near-field scattering:

$$s_{nf,n} \sim |E_{nf,n}| \tag{2.36}$$

and

$$\varphi_{nf,n} \sim Arg(E_{nf,n}). \tag{2.37}$$

2.5.5 Theory of s-SNOM

One might however ask how exactly the amplitude and phase of the scattering coefficient are linked with the optical properties of the sample. Yet, even if a completely accurate description using analytical methods is preferred, the probe-sample coupling depends on too many variables (including precise tip geometry, beam profile and wavelength of the incident light, sample topography, the material of the probe and the sample, or probe height) to allow for numerically solving these interactions. Instead, several analytical models have been established to describe the complex interactions between light, s-SNOM probe and the sample. One of the commonly used concepts to approach the relations between the complex-valued scattering coefficient and the dielectric properties of the sample is the point-dipole

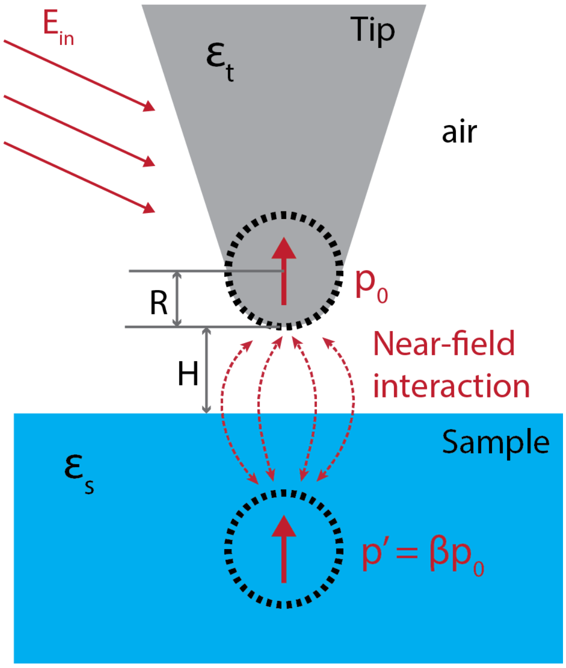

Figure 2.9: Illustration of the point-dipole model for s-SNOM. The incident electric field creates a point dipole p_0 in the metallic tip. Due to near-field interactions, a mirror dipole p' emerges in the sample.

model, as visualised in Figure 2.9, based on two assumptions.[76] Firstly, the probe is approximated as a small sphere (with radius R), assuming that only the very tip creates a near-field that is interacting with the sample. Secondly, the dipole induced by polarisation at the tip due the incoming light (E_{in}) is considered to be infinitely small with a dipole moment along the tip axis:

$$p_0 = \alpha E_{in}. \tag{2.38}$$

Here, α denotes the polarizability of a sphere in air:

$$\alpha = 4\pi R^3 \frac{\epsilon_t - 1}{\epsilon_t + 2}, \tag{2.39}$$

with ϵ_t describing the permittivity (or dielectric function) of the tip.

Since the dipole at the tip is in close proximity, it effectively polarises the sample by inducing a mirror dipole:

$$p' = \beta p_0. \tag{2.40}$$

It is the surface response function β that introduces the local dielectric properties ϵ_s of the sample into the model through the relation

$$\beta = \frac{\epsilon_s - 1}{\epsilon_s + 2}. \tag{2.41}$$

Now, the additional dipole moment acts back on the probe, thereby enhancing the original dipole moment in the tip, which in turn leads to stronger polarisation of the sample. It is precisely this reciprocal polarisation that describes the near-field interaction between the tip and the sample. Assuming that the incident field E_{in} creates the dipole moment in the tip according to $p = \alpha E$, the final solution of the dipole moment in the tip is given by

$$p = E_{in} \frac{\alpha}{1 - \frac{\alpha\beta}{16\pi(R+H)^3)}}, \tag{2.42}$$

where H is the height of the sample and R the radius of the probe. This leads to the effective polarizability $\alpha_{eff} = \frac{p}{E_{in}}$ as follows:

$$\alpha_{eff} = \frac{\alpha}{1 - \frac{\alpha\beta}{16\pi(R+H)^3)}}. \tag{2.43}$$

Previously, the near-field scattering coefficient σ_{nf} was introduced in Equation 2.29 relating the incoming and back-scattered light as $\sigma_{nf} = \frac{E_{scat}}{E_{in}}$. Relating E_{in} and E_{scat} with α_{eff}, yields, as the scattering coefficient is proportional to the dipole moment p of the tip-sample coupling, and thus to the effective polarizability, the following relation:

$$\alpha_{eff} \propto \sigma_{nf} = s_{nf} e^{i\varphi_{nf}}. \tag{2.44}$$

Considering the oscillation of the tip and demodulation at its higher harmonics, α_{eff} is given by

$$\alpha_{eff} = \alpha_{eff}[h(t)], \tag{2.45}$$

with

$$h(t) = A(1 + \cos(\Omega(t)), \tag{2.46}$$

Fourier transformation leads to $\alpha_{eff,n}$, the n^{th} Fourier coefficient corresponding to the n^{th} demodulation (w.r.t. Ω). Accordingly, the corresponding amplitude s and phase φ are denoted as

$$s_{nf,n} = |\alpha_{eff,n}|, \tag{2.47}$$

and

$$\varphi_{nf,n} = Arg(\alpha_{eff,n}). \tag{2.48}$$

It is worth mentioning that the point-dipole model is the simplest approximation, and more advanced theoretical models, such as the finite-dipole model [77], have been developed recently to provide a better match with experimental data.

2.5.6 Fourier transform infrared nanospectroscopy (nanoFTIR)

Merging s-SNOM microscopy and FTIR spectroscopy enables FTIR spectroscopy with nanoscale resolution; this technique is termed nanoFTIR. As opposed to conventional FTIR spectroscopy, the tip and the sample are located on one of the interferometric arms, and thus both amplitude and phase spectra are simultaneously obtained from the backscattered signal.[66] Pseudo-heterodyne detection, demodulation of the detector signal at higher harmonics of the tip frequency, and Fourier transformation of the interferogram lead to the complex-valued near-field spectrum $E_n(\omega)$. However, and despite background contributions have been omitted, this spectrum is still influenced by instrumental features including beamsplitter and detector characteristics, as well as atmospheric absorption. The near-field spectrum is thus given by

$$E_n(\omega) = \sigma_n(\omega)R(\omega)E_{inc}(\omega), \tag{2.49}$$

where $R(\omega)$ is the response function of the instrument. To eliminate any absorption features associated with the set-up and medium (air), the spectrum is, akin to conventional FTIR techniques, normalised to a reference spectrum. However, normalisation to a reference spectrum without any sample is not suitable, since the near-field signal emerges from tip-sample interactions. Thus, this is best done with a spectrally flat substrate without any spectral absorption peaks or other resonances (that is $\sigma_{n,Si}(\omega) = D = const$) such as silicon or gold, where

$$E_{n,Si}(\omega) = DR(\omega)E_{inc}(\omega). \tag{2.50}$$

The near-field contrast, is thus obtained as:

$$\eta_n(\omega) = \frac{E_{n,sam}(\omega)}{E_{n,Si}(\omega)} = \frac{\sigma_{n,sam}(\omega)R(\omega)E_{inc}(\omega)}{DR(\omega)E_{inc}(\omega)} \propto \sigma_{n,sam}(\omega), \tag{2.51}$$

where the subscripts *sam* and *Si* correspond to the sample and silicon calibrant, respectively.

Derived from this normalised near-field spectrum (or so-called nanoFTIR spectrum), the nanoFTIR amplitude spectrum is given by

$$s_n = \frac{s_{n,sam}}{s_{n,Si}}, \tag{2.52}$$

while the phase spectrum is

$$\varphi_n = \varphi_{n,sam} - \varphi_{n,Si}. \tag{2.53}$$

Direct correlation between the nanoFTIR spectrum and conventional FTIR spectra (e.g. absorption and reflection) – which, at first glance, might be surprising given that nanoFTIR measures scattered light from near-field interactions between tip and sample – is possible when considering that the nanoFTIR spectrum is proportional to the scattering coefficient.[67] As derived from the point-dipole model, or the more advanced finite-dipole model [77], the scattering coefficient can also be written as

$$\sigma(\omega, H) \propto \alpha_{eff}(f\beta)(1 + r_s)^2. \tag{2.54}$$

with

- α_{eff} the effective polarizablity of the tip,
- r_s the far-field reflection coefficient of the sample surface,

- $\beta = \beta(\omega) = \frac{\epsilon_s - 1}{\epsilon_s + 1}$, the surface reflection function that depends only on the sample permittivity ϵ_s, and

- $f = f(H)$, a function that is independent of frequency and is described by the tip-sample distance H.

Apart from regions close to plasma or phonon resonance, the product $(f\beta)$ is smaller than 1, since the height-dependent function f is less than unity in s-SNOM measurements, and β is around 1 (smaller than 1 for weak oscillators such as organic materials, slightly larger for metals and doped semiconductors). Therefore, $\sigma(\omega, H)$ can be expanded to a Taylor series as:

$$\sigma(\omega, H) = (1 + r_s)^2 \sum_{j=1}^{J} F_n[a^{(j)} f^j] \beta^j. \tag{2.55}$$

This leads to a polynomial equation, where the factors that are independent of β can be directly computed. In the simplest case, $(j = 1)$, this leads to

$$\sigma(\omega, H) \approx [a_0 + a_1 f(H) \beta(\omega)](1 + r_s)^2, \tag{2.56}$$

where the coefficients a_0 and a_1 only depend on the material and size of the tip and are thus constants that are independent of frequency or height. For samples that are thinner than the wavelength of the incident light ($t << \lambda = 10\,\mu$m for IR light), the far-field reflection r_s only depends on the substrate, leading to:

$$\eta_n = \sum_{j=1}^{J} \frac{F_n[\alpha^{(j)} f^j]}{F_n[\alpha_{eff,ref}]} \beta^j. \tag{2.57}$$

Thus, if normalised to a reference spectrum, this equation leads to

$$\eta_n = \frac{\sigma_n(\omega)}{\sigma_{n,ref}} \approx \frac{\beta(\omega)}{\beta_{ref}}, \tag{2.58}$$

which can be solved for $\beta(\omega)$ if σ is measured. Importantly, the local permittivity of the sample can be determined through

$$\epsilon(\omega) = \frac{1 + \beta(\omega)}{1 - \beta(\omega)}. \tag{2.59}$$

The real and imaginary parts of the dielectric function $\epsilon(\omega)$ can accordingly be derived, where the absorption coefficient is

$$\kappa(\omega) = Im(\sqrt{\epsilon(\omega)}) \sim Im(\beta(\omega)). \tag{2.60}$$

Since $Im(\eta_n(\omega)) \sim Im(\sigma_n(\omega)) \sim Im(\beta(\omega))$, the so-called nanoFTIR spectrum can be defined as the local absorption of the sample according to

$$\alpha_n(\omega) = Im(\eta_n(\omega)) = \frac{s_n(\omega)}{s_{n,ref}(\omega)} \sin(\varphi_n(\omega) - \varphi_{n,ref}(\omega)). \tag{2.61}$$

It is this nanoFTIR absorption spectrum that can be directly compared with conventional FTIR spectroscopy, where the far-field absorption A_{ff} follows the relation: $A_{ff} \propto \kappa(\omega)$, and therefore

$$\alpha_n(\omega) \sim Im(\beta(\omega)) \sim \kappa(\omega) \sim A_{ff}. \tag{2.62}$$

This link - $\alpha_n(\omega) \sim A_{ff}$ - allows for direct chemical recognition of a material with nanoscale resolution.[67]

2.5.7 Experimental setup

In this work, the nanoFTIR measurements were performed with a neaSNOM instrument (neaspec GmbH) encompassing a tapping-mode AFM, mid-IR illumination optics, and electronics for data recording. Its setup is illustrated in Figure 2.10. The broadband coherent mid-IR beam was generated based on a nonlinear difference-frequency generator (DFG), where two near-IR beams emerging from 100-fs pulsed fibre lasers (TOPTICA Photonics Inc.) were synchronously superimposed in a GaSe crystal. To obtain the broadband spectrum from 700 – 2200 cm^{-1}, at least two spectra measured with illumination sources tuned to cover different ranges were merged. The coherent mid-IR light passed through a ZnSe beamsplitter, the core of the asymmetric Michelson interferometer dividing the incident beam into reference and sample arms. In the reference arm, the beam is reflected by a moving reference mirror that is translated along the position d by a piezo-driven linear stage in direction of the beam at a constant velocity for 1600 μm to perform FTIR

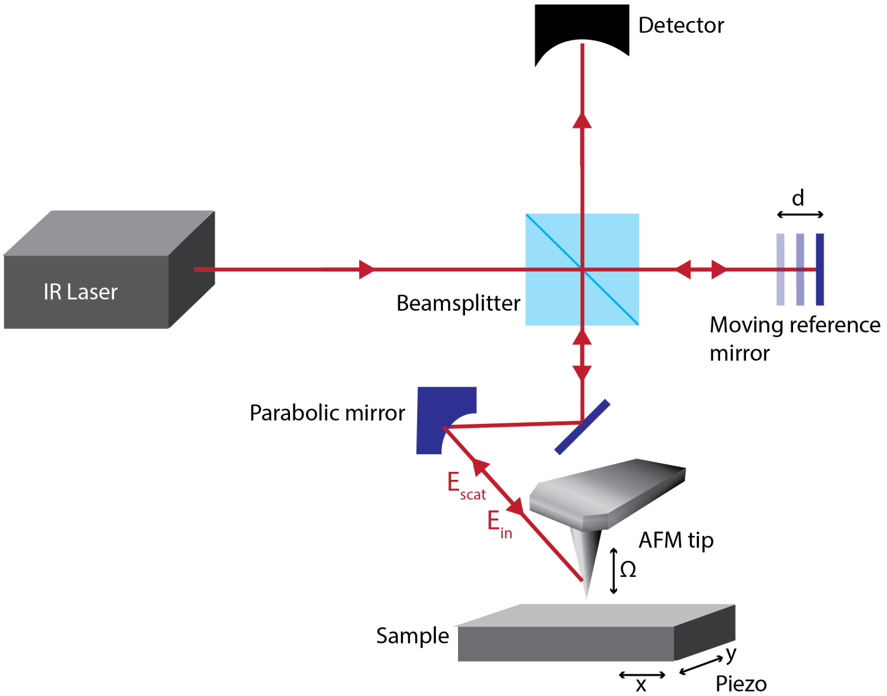

Figure 2.10: Experimental setup of the s-SNOM instrument.

spectroscopy. The second beam illuminates the platinum-coated AFM tip with a cantilever resonance frequency $\Omega = 250$ kHz, and nominal tip radius 20 nm (NanoAndMore GmbH). To maintain constant and well-aligned tip illumination, the tip position is fixed, and the sample stage is moved by piezoelectrics for scanning. Furthermore, for alignment purposes, a visible red beam generated by a HeNe laser was used to focus the incident beam onto the AFM tip. The back-scattered light from the tip is collected by the same parabolic mirror, superimposed with the modulated reference light in the beamsplitter, and focussed onto the detector with a second parabolic mirror. The mercury cadmium telluride (MCT) detector (FTIR-160-0.10, Infrared Associates, Inc.) is cooled with liquid nitrogen, and the signal is recorded with a fast data acquisition card as a function of the mirror position d. Demodulation at higher harmonics $n\Omega$ ($n = 2$ for nanoFTIR, $n = 3$ for s-SNOM imaging) of the tip oscillation frequency Ω generates the interferogram $I_n(\delta)$, with $\delta = 2\Delta d$, and subsequent Fourier transformation leads to the spectrum of the back-scattered light. Normalisation to a reference spectrum measured on silicon, and data processing with the neaSNOM software yields the amplitude and phase of the near-field signal, and thus, the local absorption spectrum of the sample with a resolution akin to AFM.

2.6 Nanospectroscopy of metal-organic frameworks

Because nanoFTIR can provide high-quality broadband IR absorption spectra with unprecedented spatial resolution, it has naturally emerged as an excellent tool for nanoscale analysis of 2-D materials[78], polymers[65], biological samples[79, 80], and inorganic materials[81] in diverse areas of research. In the field of metal-organic frameworks, however, the use of this powerful technique is still in its infancy. Indeed, the first application of nanoFTIR and s-SNOM imaging for MOFs was only reported in 2018, when the combination of these techniques was employed to characterise mixed matrix membranes (MMM) comprising the zeolitic imidazolate framework ZIF-94 as a filler material.[82] Specifically, s-SNOM images, recorded with an illumination wavelength characteristic for ZIF-94, revealed a strong optical absorption of individual particles on the surface, thereby differentiating between MOF crystals and the polymeric membrane. However, it was not until the first systematic study in 2020 that the strengths of nanoFTIR were introduced into the field of MOF research.[37] Through a detailed comparison with conventional far-IR techniques and DFT simulations, we demonstrated that the nanoFTIR spectra can be directly compared to standard databases, allowing for straightforward chemical identification of MOF materials. In addition, these techniques were used for establishing the host-guest interactions of prototypical MOF systems loaded with emissive molecules to pinpoint the precise location of the latter, as outlined in Chapter 3. The concepts and strategies gained from this study revealed a new dimension in the characterisation of MOFs at the single crystal level by encouraging not only conventional imaging, but also chemical characterisation. Indeed, several studies have adopted the ideas: for instance, nanoFTIR was used to confirm thorough washing and guest encapsulation in two MOF systems (ZIF-8 and ZIF-71) with luminescent guests to afford solid-state lighting, and stress sensing, respectively.[83, 84] While these two examples focussed on the emerging host-guest interactions rather than the MOF itself, another study leveraged nanoFTIR to investigate the amorphisation of the nano-porous MIL-100 (MIL: Materials of Institut Lavoisier) material under increasing pressure.[85] As the pelleting pressure increased, most vibrational bands were unaffected; however; one additional peak that can be associated with under-coordinated carboxylates appeared in the nanoFTIR spectrum. Significantly, these salient spectral changes indicate that specific bond breakages are responsible for the structural transition of crystalline to amorphous MIL-100. Similarly, bond breakages and structural changes were exposed by nanoFTIR in the surrounding of nanoindents in ZIF monoliths.[86]

Even though phase transitions and structural transformations may negatively affect the stability of MOFs in applications, there exists another smart strategy that takes advantage of transformations to enhance the overall performance of MOF materials. It is the MOF-to-MOF transformation, where the substitution of metal cations leads to a new MOF material with striking properties unattainable through conventional synthesis routes. Recently, Gutierrez *et al.* described the post-synthetic MOF-to-MOF transformation of a non-luminescent framework into a highly luminescent counterpart with sensitivity to acetone.[87] This has been achieved by simply immersing the original MOF in a solution containing the metal clusters of the desired MOF; however, there was some doubt whether this conversion has been completed, or if it was in fact a partial transformation. Herein, nanoFTIR unambiguously proved the co-existence of both MOF materials in the same sample: crystals with two distinct morphologies were discovered with AFM imaging, and local probing with nanoFTIR could assign them to the MOFs before and after transformation, respectively, by revealing their characteristic chemical compositions. Thus, nanoFTIR enabled chemical recognition between different MOF phases in the same sample.

Pushing these capabilities to the single crystal level, another study chemically mapped the spatial organisation of two different enzymes encapsulated in a single multi-shelled MOF crystal.[88] Herein, nanoFTIR and s-SNOM imaging with characteristic wavelengths of the amide stretches of the immobilised enzymes revealed chemical heterogeneity between the inner and outer shells. Accordingly, the confinement of two enzymes in the multi-shelled MOF, which serves as scaffolding to compartmentalise them, was confirmed.

To date, these studies, as well as the four manuscripts presented in this thesis, are the only examples of the use of nanoFTIR in the field of MOF research. There exist, however, other techniques merging the spatial resolution of AFM with the chemical recognition of FTIR to overcome the diffraction-based limitations of classical IR spectroscopy. These include photo-thermal (or photoexpansion) microscopy, and photo-induced force microscopy (PiFM). While both techniques are based on an AFM tip and rely on the IR-illumination of the sample, their approaches are fundamentally different. Specifically, photothermal AFM is operated in contact-mode, using the high sensitivity of AFM to vertical height changes to measure the expansion of a sample due to absorption of mid-IR light. Even if this technique has been used to probe the intrinsic thermal conductivity of MOF-type microcrystals, for example, or detect individual MOF particles with far-IR illumination, its resolution is typically limited to the order of 100 nm.[89, 90] More promisingly, PiFM can achieve chemical specificity and spatial resolution down to the level of the AFM tip apex (∼a few tens of nanometres).[91, 92] Leveraging the dipole-dipole interactions that create the near-field scattering in s-SNOM, PiFM measures the resulting attractive force between the laser-induced molecular dipole in the sample and its mirrored dipole in the metal-coated AFM tip. Significantly, not only the excitation is based on near-field interactions, but also the detection of the optical response. Therefore, and as opposed to s-SNOM imaging, which involves far-field contributions, PiFM allows background-free detection of molecular vibrations. Indeed, since its first use in 2016 [91], PiFM, too, has emerged as a promising tool for investigating MOFs at the nanoscale.

For instance, the growth process of surface-mounted HKUST-1 (HKUST: Hong Kong University of Science and Technology) was investigated [93], followed by a study in 2021 on nano-patterned domains of HKUST-1 and ZIF-8.[94] Grown side-by-side on a gold substrate, the hydrophilic HKUST-1 and hydrophobic ZIF-8 yield a bifunctional surface, with its chemical heterogeneity being revealed by PiFM. In addition, their distinct water adsorption was detected, as well as the corresponding defect formation in the hydrophilic HKUST-1.[94]

To conclude, AFM-based nanospectroscopy has clearly proven to be an exciting tool not only for identifying MOF single crystals, but also for exploring their multi-faceted virtues and basic phenomena at the nanoscale. In this thesis, several examples based on nanoscale analytics unveil how nanoscopic mechanisms govern the structural, chemical, physical, and mechanical properties of MOFs in the quest of tuning them for targeted sensing applications.[40, 85, 95]

Happiness [is] only real when shared.

— Jon Krakauer, *Into the Wild*

3

A strategy to reveal guest encapsulation in metal-organic frameworks

Contents

3.1 Guest@MOF principle

Since their early discovery in the 1990s, metal-organic frameworks (MOFs) have emerged as a new class of nanoporous materials considered among the most fascinating and compelling advancements in nanoscience and nanotechnology.[24, 25] They are porous coordination materials, where metal clusters are bridged by organic ligands, thus offering hybrid properties unattainable from purely organic or inorganic systems alone. Constructed from these basic building blocks in self-assembly, MOFs crystallise in highly ordered 2-D or 3-D network architectures that form a porous framework with well-defined cavities (see Figure 3.1). One of their merits is ascribed to the possibility of tuning the properties of MOFs by rationally selecting the inorganic clusters and organic ligands from a plethora of potential combinations.[26, 96] Similarly, because of the strong coordination bonds between the building blocks instead of $\pi - \pi$ stacking or hydrogen bonding that are prevalent in purely organic compounds, they can be accurately predicted to afford the design and meticulous control of the material's properties.[97] This is further facilitated by the crystalline nature of MOF materials, since their structure can be characterised with great accuracy as opposed to amorphous, disordered counterparts whose precise description is deemed challenging.[98] Yet, even if MOFs are highly crystalline materials, there is one feature that differentiates them from conventional porous structures: structural flexibility. Because flexible MOFs combine crystalline order and structural transformability, these soft porous crystals can exhibit intriguing physical functions and anomalous mechanical characteristics that can be tuned by rational design.[99, 100] For instance, their unique responses to physical, mechanical and chemical stimuli may include negative Poisson's ratio, negative thermal expansion, or phase transitions triggered by adsorption, which are rare in other conventional solid-state materials.[101]

But while all these features – organic-inorganic building blocks, strong coordination between them, as well as crystallinity and flexibility – allow for precise tailoring of unique properties, it is the void in the MOF that is even more striking than the framework itself: MOFs can exhibit nanopores whose internal surface areas exceed those found in any other commercial porous material including zeolites, activated carbons or silica gels.[24] Inherently, the first applications leveraging this remarkable porosity focussed on gas storage and separation[27], CO_2 capture[102] or catalysis [28]. Recently, however, the opportunity to encapsulate a variety of guest molecules

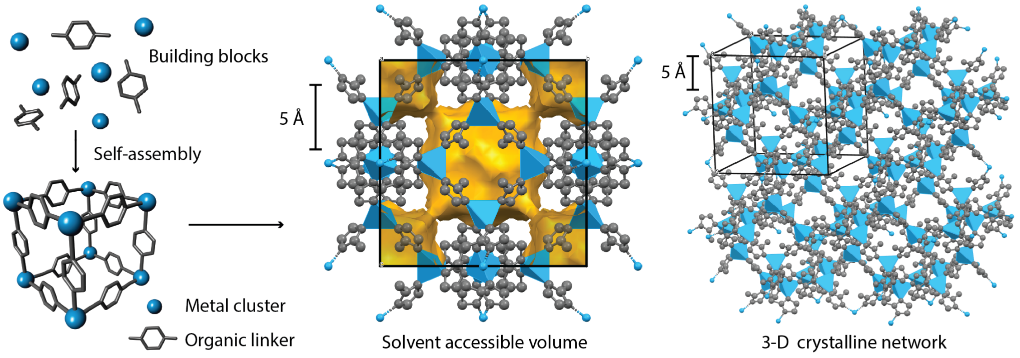

Figure 3.1: Schematic representation of a metal-organic framework (MOF). Self-assembly of the metal and organic building blocks leads to a porous, crystalline framework. The unit cell is shown for the prototypical zeolitic imidazolate framework ZIF-8. Solvent accessible volume is illustrated in yellow, calculated with a probe radius of 1.2 Å.

in MOF systems has sparked innovative applications in photonics, optoelectronics, drug delivery and sensing beyond the array of conventional use cases for nanoporous materials.[29, 32, 35, 103] Because MOF materials afford the infiltration of their pores with guest molecules to create novel properties uncharacteristic for either component, guest@MOF composite systems have emerged as a promising concept.[39] This is defined by the encapsulation of guest molecules in the pores of the 'host' framework, where the host-guest interactions lead to a new material, while the advantages of MOF materials are still preserved: firstly, the emergent properties of the guest@MOF system are not intrinsic to either guest or host; they are therefore of interest due to guest-induced properties distinct from the MOF itself. Indeed, to name one example, MOFs are usually electrical insulators, but if suitable guest molecules are introduced, the corresponding host-guest interactions can enable electrical conductivity.[104–106] Secondly, the interactions between guest and MOF are characterised by coordination bonds that are relatively stronger when compared to weak physisorption. Because these interactions in fact alter the inherent properties of both materials, the confinement of luminescent guests, for instance, can lead to exciting emergent optical phenomena including mechanochromic, solvatochromic, or thermochromic behaviour.[39, 107] Thirdly, the guest@MOF material shall be stable in a stand-alone state; and yet, the effects of guest encapsulation can be reversed if the guest is removed from the host framework.

One way to harness these adsorptive properties is to design promising guest@MOF systems with luminescent guest molecules, thereby offering exciting new properties for optoelectronics, photonics, and sensing devices.[107] Applications include solid-state lighting, temperature and pressure measuring, and chemical sensing, where the tailored host-guest interactions are altered due to external stimuli, or when a targeted analyte infiltrates the porous framework.[33, 108] Typically, luminescent sensing is achieved by encapsulating fluorophores or luminescent dyes in the MOF host, but other possible guests involve metal ions or clusters, quantum dots or perovskites.[107] There exist two ways to encapsulate guests in the host framework yielding guest@MOF composite systems: the first strategy is based on the synthesis of the MOF itself, followed by a 'post-synthesis' insertion of the guest, while, in the second approach, the guest@MOF system is formed *in situ* during the same synthesis, as illustrated in Figure 3.2.

3.1.1 Post-synthetic encapsulation

The post-synthesis confinement method entails separate processes for assembling the MOF framework and the encapsulation of guest molecules. Firstly, a standard synthesis yields the pristine MOF structure, which is subsequently exposed to the guest material intended for absorption. One way to achieve this is *via* liquid impregnation, where the MOF crystals are immersed in a concentrated solution containing the guest molecules.[109] Because ion exchange and diffusion lead to an infiltration of the framework by the guest molecules, they will be adsorbed to yield the guest@MOF system. Extensive washing and drying are performed as additional steps, akin to conventional synthesis protocols, to obtain the guest@MOF crystals without residual precursors. However, in liquid impregnation, the presence of a diluter can lead to an undesired competition between the absorption of guest and solvent molecules; a challenge that can be circumvented by gas-phase infiltration.[110] In practice, a specially designed vessel, high temperature, and a

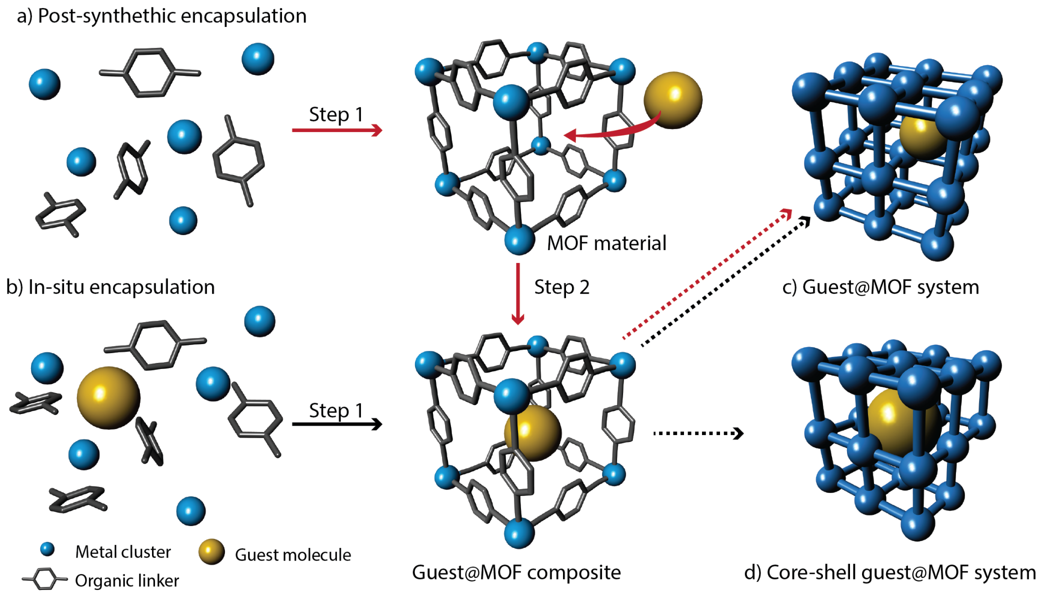

Figure 3.2: Different strategies for synthesising guest@MOf systems. a) Post-synthetic encapsulation and b) *in situ* encapsulation can lead to a c) guest@MOF composite material. d) A core-shell guest@MOF structure is illustrated.

high-pressure environment are required to vaporise the guest that will be captured in the pores of the MOF. While both post-synthetic methods help preserve the guest species from degradation, because they may not be stable if exposed to the harsh conditions during the MOF synthesis including high temperature, or acidic/ basic media, they are time-consuming and involve several synthesis steps.[111] In addition, they may lead to an uneven distribution of the guest in the MOF due to different diffusion rates favouring accumulation of the guest on or close to the external surface of the crystals.[112] Importantly, the size of the guest molecules must be smaller than the window aperture of the MOF pore to allow for guest infiltration.

3.1.2 *In situ* encapsulation

As opposed to the post-synthetic confinement methods, an *in situ* approach could yield guest@MOF systems with bulky guest molecules that can be encapsulated in the pore but would not fit through the window aperture otherwise.[113] This is because the guest molecules are directly immersed in the solution containing the metal and organic building blocks to form the MOF structure simultaneously with the confinement of guest in the pores. Even larger molecules can be encapsulated if a core-shell type structure is leveraged, where the periodic framework is formed around the guest molecules to immobilise them. In general, the *in situ* encapsulation approach is relatively faster when compared with post-synthetic methods due to fewer reaction steps, and it could lead to a more homogenous distribution of guest molecules throughout the entire crystal; however, the feasibility of this approach is determined by the stability of the guest species upon exposure to the synthesis conditions of the MOF.[107] Most commonly, the *in situ* encapsulation is achieved through a one-pot synthesis. After directly combining the guest material, metal salt and organic linkers in the same solution, the mechanisms of self-assembly and host-guest interactions lead to the desired guest@MOF system. Another strategy, which has been developed recently to grant faster reaction times (minutes or less), higher sample yield, and smaller crystal sizes (10-100 nm), is the so-called 'high-concentration reaction' (HCR) method.[114] In this case, the metal salt, organic linkers, and guest materials are dispersed in suitable solvents, respectively. Initially, the two solutions containing the guest and linker are combined before adding the third solution with the metal centres of the intended MOF system, and immediately, a gel-like material which surrounds the guest@MOF crystals will be formed. Through extensive washing with an organic solvent, the crystals can be isolated from the supramolecular gel. Importantly, since a deprotonation agent, such as triethylamine (TEA), is typically added to the linker solution, the deprotonation and therefore the reaction rate is accelerated. As a result, the crystals obtained from the HCR approach are relatively smaller when compared to conventional one-pot reactions, yielding nanocrystals in the range of 10 to 100 nm, or even 2-D morphologies such as nanoplates and nanosheets.[114] For instance, the confinement of fluorescein in the zeolitic imidazolate framework ZIF-8 (Zn(mIm), mIm = 2-methylimidazole) *via* HCR reaction happens instantly and leads to nanocrystals with a size ranging from 50 – 100 nm, whereas the conventional one-pot synthesis of fluorescein@ZIF-8 would take 24 hours yielding microcrystals exhibiting a size of 1-5 μm.[83] Similarly, if rhodamine B (RhB) is encapsulated in ZIF-71 (ZIF-71

= Zn(dcIm)2, dcIm = 4,5-dichloroimidazole) employing the HCR method, the crystal size is reduced from 800 nm to 50-150 nm, and instead of a reaction time of 24 hours, they are formed immediately.[115]

3.2 Characterisation methods for guest@MOF systems

While all these synthetic methodologies produce guest@MOF materials, it remains very challenging to unambiguously pinpoint whether the guest molecules are truly encapsulated in the MOF pore or adsorbed only on the crystal surface.[107] Establishing a precise knowledge of this is crucial to the engineering of designer guest@MOF systems. An array of techniques exists to characterise either guest loading, the presence of the properties of the guest, or the structure of the MOF; and yet, none of these methods alone can prove the encapsulation of guest materials in the MOFs. Therefore, a synergistic use of complimentary techniques is recommended to attain information about structure, chemical composition, and physical properties.

3.2.1 X-ray diffraction

Powder X-ray diffraction (PXRD) is a common tool to determine the crystalline structure of MOFs, especially for guest@MOF systems. In general, it can be used either to confirm that the structure of MOFs remains unaltered upon encapsulation, or to study how the inclusion of guest molecules may distort the long-range order of the framework. The latter phenomenon can be noticeable in core-shell type guest@MOF systems or flexible MOFs, where an expansion of the unit cell parameters may indicate the presence of guest molecules confined in the pores. For instance, when CO_2 was adsorbed in the framework, an increase in cell volume was observed for the flexible [Zn(ndc)(o-phen)]DMF_n MOF (o-phen = 1,10-phenanthroline, ndc =2,6-napthalenedicarboxylate), revealing structural changes due to guest encapsulation.[116] Such structural reorganisation is however distinctive for particular flexible MOFs, because, generally, the crystalline structure of MOFs is unaffected by the inclusion of guest compounds: since the weight percentage of guest molecules is usually low, and they are randomly distributed in the framework, there is a lack of long-range periodicity that could be detectable with PXRD techniques.[117–119] Therefore, this technique is normally not sensitive enough to confirm the presence of low-concentration guest species.

3.2.2 Steady-state UV-visible and fluorescence spectroscopy

One method to reveal the guest compounds in MOF composite systems is steady-state UV-visible or fluorescence spectroscopy, especially for luminescent guest compounds.[107] By measuring the characteristics of the ground and electronically excited states, these techniques can detect the distinct absorption, excitation, and emission spectra of the fluorescent guest. In addition to these qualitative measurements, it is further possible to quantify the amount of guest loading in the host material by assessing the optical density at the maximum absorption intensity of the guest solution prior and post interaction with the MOF.[120] But while these techniques provide information about the presence or absence of the guest species in the material[114, 119], little is known about their precise location: are they truly encapsulated in the pores or solely attached to the surface? If host-guest interactions or the confinement in pores instead of aggregation lead to changes in energy-, charge- or proton-transfer mechanisms, fluorescence spectroscopy, especially in combination with time-resolved techniques, may offer some answers about the fate of the guest compounds. Yet, the recorded signal is usually independent of whether the guest is encapsulated in the pore, entrapped between crystals, or attached on the surface.

3.2.3 Nuclear magnetic resonance (NMR) spectroscopy

Akin to UV-visible spectroscopy, the amount of guest loading can be derived from ^1H nuclear magnetic resonance (NMR) spectra based on the integral areas of peaks, as shown in recent guest@ZIF-8 examples.[84] Thus, this approach can precisely determine the molar ratio between the organic linker and the guest, thereby revealing the guest occupancy of the pores but importantly, only if successful encapsulation is assumed.[118] While complimentary techniques, such as N_2 adsorption and thermogravimetric analyses (TGA), could substantiate this assumption, elucidating the complex host-guest interaction and the precise location of the guest in the framework is deemed challenging even with a synergistic use of these techniques.[107]

3.2.4 FTIR spectroscopy

To unravel the chemical interactions between the guest and the host framework, FTIR spectroscopy is a powerful tool, not only because the characteristic absorption bands of both - guest species and host - can simultaneously be identified, but also because specific vibrational modes may change upon guest encapsulation.[121–123] If, for instance, the atomic environment of functional groups is altered as the guest interacts with the ligands, the modes associated with open metal clusters are changed due to guest absorption, or if the free-space vibrations of the guests are inhibited due to confinement in the pore, these phenomena may affect the vibrational characteristics and can thus be discovered in the FTIR spectrum. Especially in combination with *ab initio* calculations by density functional theory (DFT), it is possible to assign such salient changes in the spectrum to distinct host-guest interactions. For instance, a recent study merging simulated and empirically measured IR spectra established that fluorescein is effectively encapsulated in the cages of ZIF-8, since the observed shifts in the IR peaks could be directly assigned to confinement and interactions between the luminescent guest and the framework.[84] Albeit indubitably a powerful technique for chemical characterisation, FTIR spectroscopy can only provide information that may suggest the location of the guest in very specific cases. In general, the chemical changes underpinning host-guest interactions are revealed, but neither the exact position of the guest in the MOF nor the amount of guest can be determined from this technique.

3.3 A strategy to elucidate guest encapsulation using nanoscale analytics

While several characterisation techniques have been proposed to pinpoint the complex nature of guest@MOF materials, it became evident that there exist only a few examples where the location of the guest could be accurately determined. Significantly, all these methods probe bulk, polycrystalline materials, and therefore, even if host-guest interactions are observed, it remains challenging to confirm whether the guest species are effectively encapsulated in the pores, embedded between crystals, or attached only on the outer surface of the MOF crystals. Knowledge of this is however paramount for accurately predicting the properties and performance of tailored guest@MOF materials for real-world applications.[107]

We herein address this challenge by employing s-SNOM and nanoFTIR combined with conventional techniques described in Section 3.2. Crucially, this work provides the first systematic study elucidating the guest@MOF concept on a single crystal level. Before turning to host-guest systems, we confirm the efficacy of nanoFTIR on MOF crystals, since this is among the first applications of near-field spectroscopy techniques in the field of MOF research.

3.3.1 NanoFTIR on MOF single crystals

Being a proof-of-concept study, the zeolitic imidazolate framework ZIF-8 was chosen as a prototypical MOF system due to its ease of synthesis, stability and well-researched characteristics that render it a promising candidate for an array of applications.[124, 125] The ZIF-8 nanocrystals were obtained with a standard synthesis protocol before dropcasting onto gold substrates and drying at 80 °C for 4 hours in vacuum to remove any residual solvent as preparation for nanoscale characterisation akin to AFM. NanoFTIR spectra were attained with the experimental setup described in Chapter 2 with two lasers employed to cover the broadband mid-IR region from 700 to 2100 cm^{-1}. Each interferogram was measured with a 10 cm^{-1} spectral resolution, 2048 points per interferogram, and with an integration time of 18 ms. Figure 3.3 depicts exemplary positions, where the local nanoFTIR spectra were collected: a reference spectrum was measured on the gold substrate (region A), and a local spectrum was obtained from 3 measurements at the same position, each averaged from 20 individual point spectra, respectively (Region B). To gather chemical information about the sample, multiple nanocrystals at different

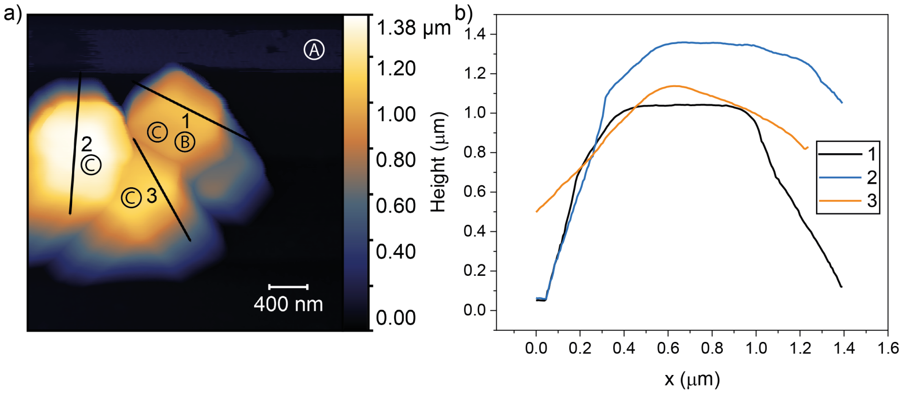

Figure 3.3: The exemplary positions of the local nanoFTIR measurements performed on micron-sized crystals. a) AFM image indicating the precise locations for local probing. Region A: reference spectrum measured on a gold substrate. Region B: Three measurements with 20 individual point spectra each were performed to obtain the local properties of an individual crystal. Regions C: Several crystals were measured (at various positions on the sample, not shown here) and further compared to probe the sample-specific properties. b) Height profiles of the crystals along the designated lines (1-3) in the AFM image.

locations were probed and averaged. As shown in Chapter 2, the amplitude and phase of the scattering coefficient are measured, however, the imaginary part of the near-field contrast is directly related to the far-field FTIR absorption spectra and thus provides a better match.[67] While only the imaginary part, defined as the nanoFTIR absorption, is shown in the manuscript (see Section 3.4), for completeness, Figure 3.4 summarises the raw data of the amplitude, phase, as well as the real and imaginary parts measured on an individual ZIF-8 crystal, and normalised to the gold substrate. The far-field FTIR spectrum was measured on the (bulk) polycrystalline powder sample using a Nicolet iS10 attenuated total reflection (ATR) - FTIR spectrometer. Indeed, the local spectra obtained from near-field measurements are in good agreement with the far-field measurements and are further consistent with *ab initio* theoretical predictions (see Figure 1 in the manuscript). These were computed with the CRYSTAL14 code using DFT at the PBE level of theory with a damped empirical dispersion term (PBE-D), carried out on HPC facilities.[126–128]

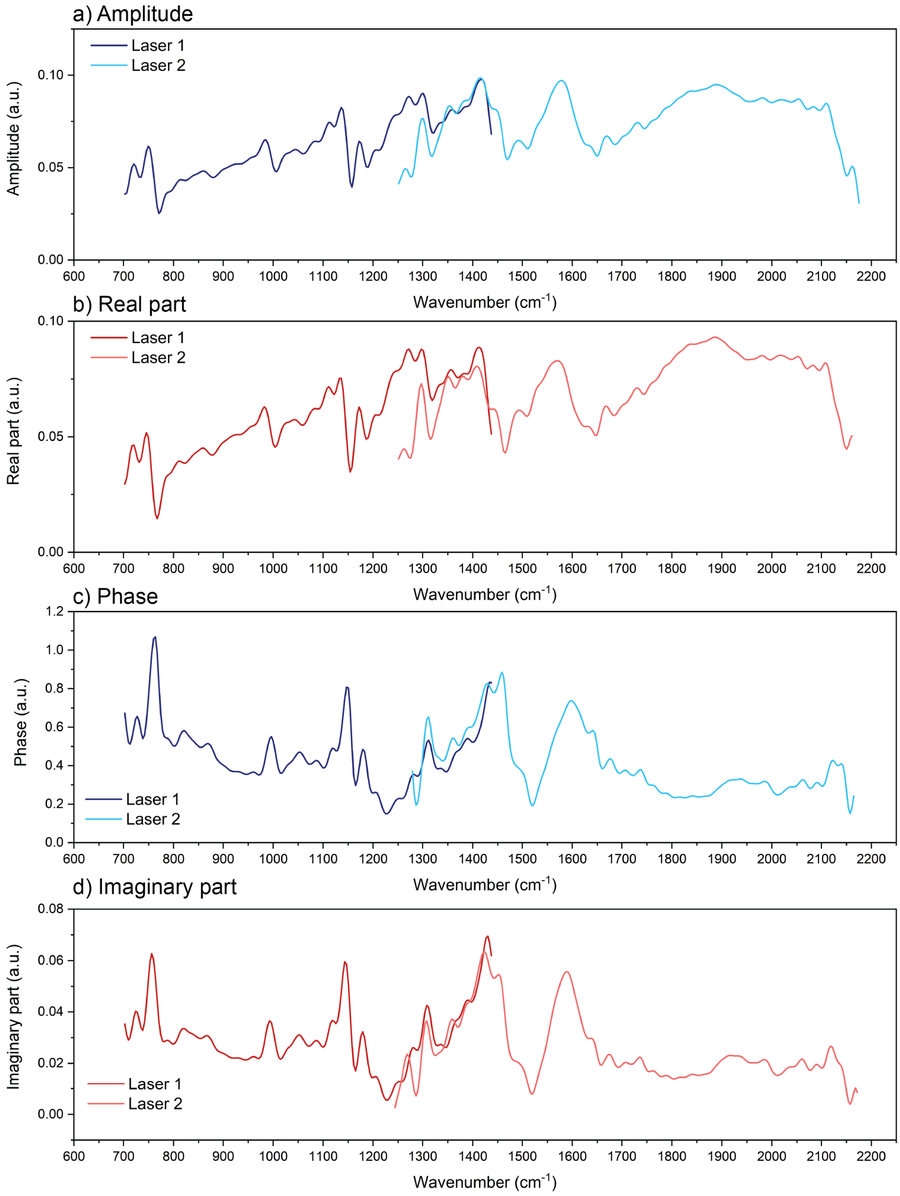

Figure 3.4: Comparison of near-field spectra. a) Amplitude, b) real part, c) phase, and d) imaginary part of the near-field spectra obtained through nanoFTIR measurements on a single crystal of ZIF-8 with two different lasers. All spectra are normalised to a gold substrate.

3.3.2 How to confirm guest encapsulation

With the efficacy of nanoFTIR on MOF crystals confirmed, we present in Figure 2 in the manuscript in Section 3.4 the effects of host-guest interactions on the RhB@ZIF-8 crystals, revealing the nanoscale vibrational dynamics detectable at a 20 nm spot. To establish the influence of surface contributions, we employ s-SNOM imaging (see Figure 3) for chemically mapping and discrimination between the host and guest materials. Finally, we demonstrate the robustness of the above methodologies by considering two case studies using novel systems of RhB@UiO-66 and Fluorescein@UiO-66 (Figures 4 and 5).

After synthesis of the exemplary guest@MOF systems, PXRD patterns were measured using the Rigaku MiniFlex diffractometer equipped with a Cu Kα source (step size of 0.02 ° and 0.01 °/min). These measurements were validated against the simulated pattern derived from crystallographic information files (CIF) from the Cambridge Structural Database (CSD) to confirm the intact crystalline structure despite guest encapsulation (see Figures 3.5 and 3.6). To locally characterise the luminescent guest@MOF systems, nanoFTIR and s-SNOM imaging were employed. Importantly, because nanoFTIR and s-SNOM imaging are surface techniques, guest encapsulation can only be deduced indirectly by revealing the presence or absence of the guest species adhered on the surface of MOF crystals. Indeed, vibrational modes associated with the guest molecules are detected in the nanoFTIR spectrum indicating their adsorption on the surface prior to the washing step. If, however, the samples have been thoroughly washed, no traces of the guest materials were observable with these surface techniques.

This demonstrates the importance of the washing process as the first step to elucidate guest encapsulation. To confirm thorough washing, the absorption spectra of the supernatant of the last washing step – DMF in the case of Guest@UiO-66 and acetone for RhB@ZIF-8 - were measured, and because neither of them show any signal of the guest, one can conclude that the previous washing steps were sufficient to remove any residual guest material. Similarly, emission spectra, with their higher sensitivity to the luminescent dyes, were collected and compared with the obtained

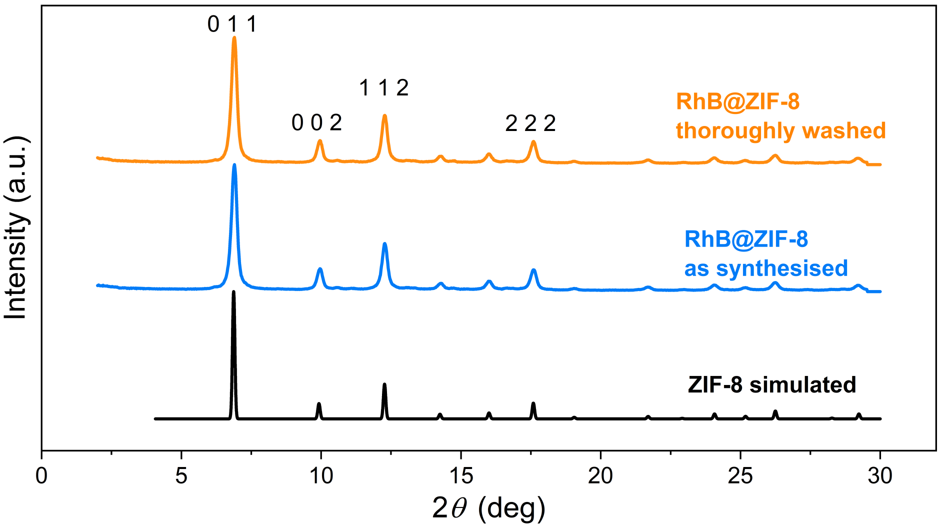

Figure 3.5: XRD patterns of the RhB@ZIF-8 composite systems.

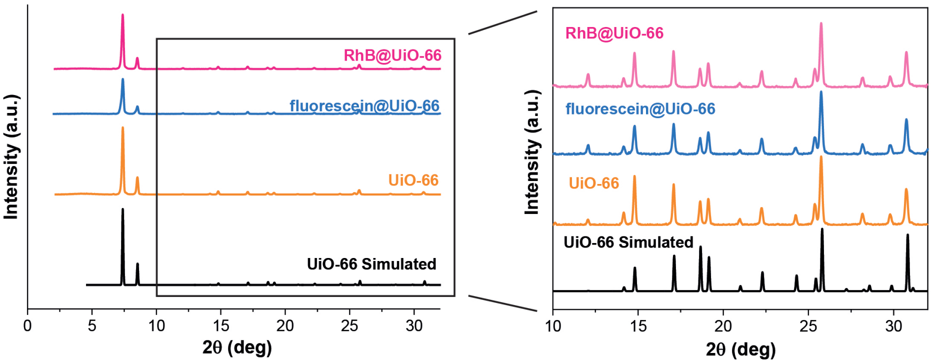

Figure 3.6: XRD patterns of the guest@UiO-66 composite systems.

guest@MOF materials. Because no traces of any guest materials in the supernatant is detectable, the washing process is considered complete (see Figure 3.7).

The second step to prove successful guest encapsulation involves SEM imaging. Backscattered electron and secondary electron SEM images were obtained at 10 keV under high vacuum, and were not only performed to image the MOF-type crystals, but, more importantly, to confirm the absence of any residual guest material in the sample. Figures 3.8 and 3.9, as snapshots of thorough studies of the entire sample, indicate that there are no areas of aggregated guest material.

Thirdly, the absence of any guest material on the surface of individual crystals has to be established. This is best done with nanoFTIR and s-SNOM with their

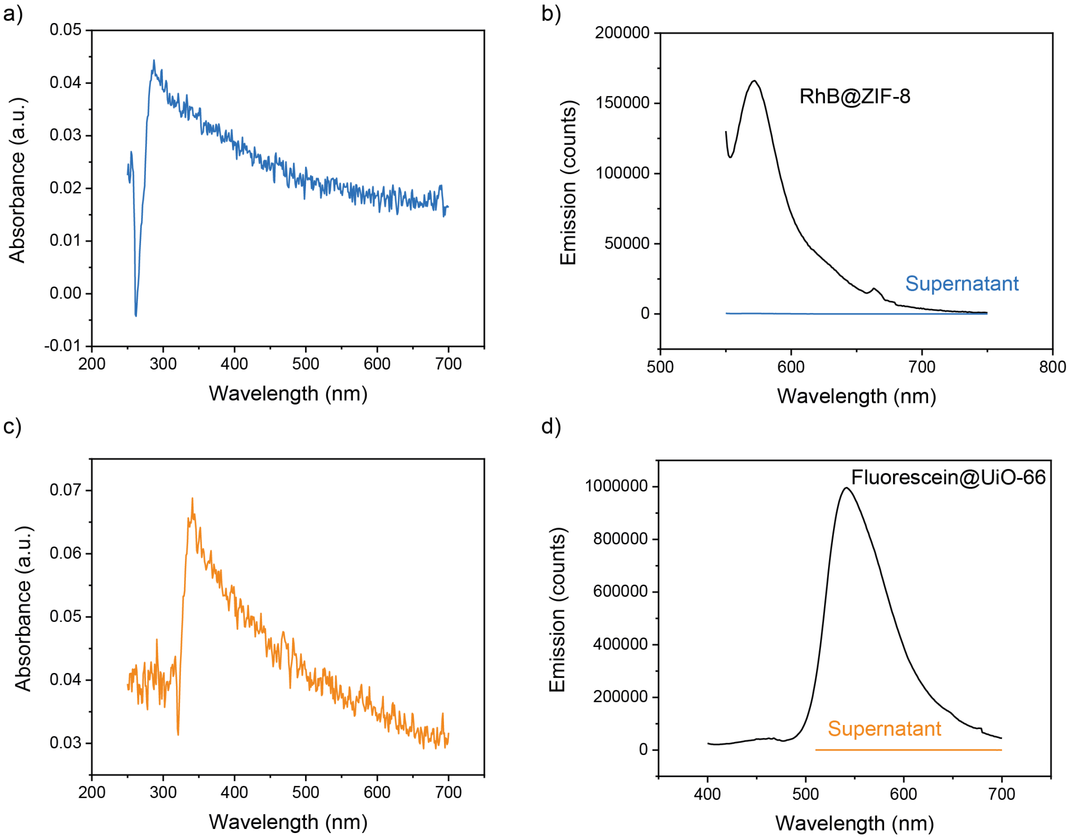

Figure 3.7: Absence of the dyes in the supernatant of the last washing step confirms thorough washing. a) Absorbance spectrum of acetone supernatant after removal of RhB@ZIF-8 showing no signal of RhB. b) Emission spectrum of acetone supernatant compared with the RhB@ZIF-8 (excitation wavelength 540 nm). c) Absorbance spectrum of DMF supernatant after removal of fluorescein@UiO-66 showing no signal of the fluorescein dye. d) Emission spectrum of DMF supernatant (excitation wavelength 500 nm) compared with the fluorescein@UiO-66 (excitation wavelength 380 nm).

probing depth of only a few nanometres, or several unit cells: if guest species are adsorbed and accumulated on the surface, their characteristic absorbance bands will be detectable in the local nanoFTIR spectrum, but if the opposite is the case, and they are truly encapsulated in the pores, the contribution of their vibrations will be undermined by the relatively stronger vibrations of the periodic framework. After thorough washing, the lack of vibrational features that are associated with the guest species in the nanoFTIR spectrum, indicates their absence on the crystalline surface.

One can thus conclude that, after steps one to three, no guest materials are directly detectable on the sample or the surface of individual nanocrystals. Therefore, if the luminescent properties of the guests are still traceable, this

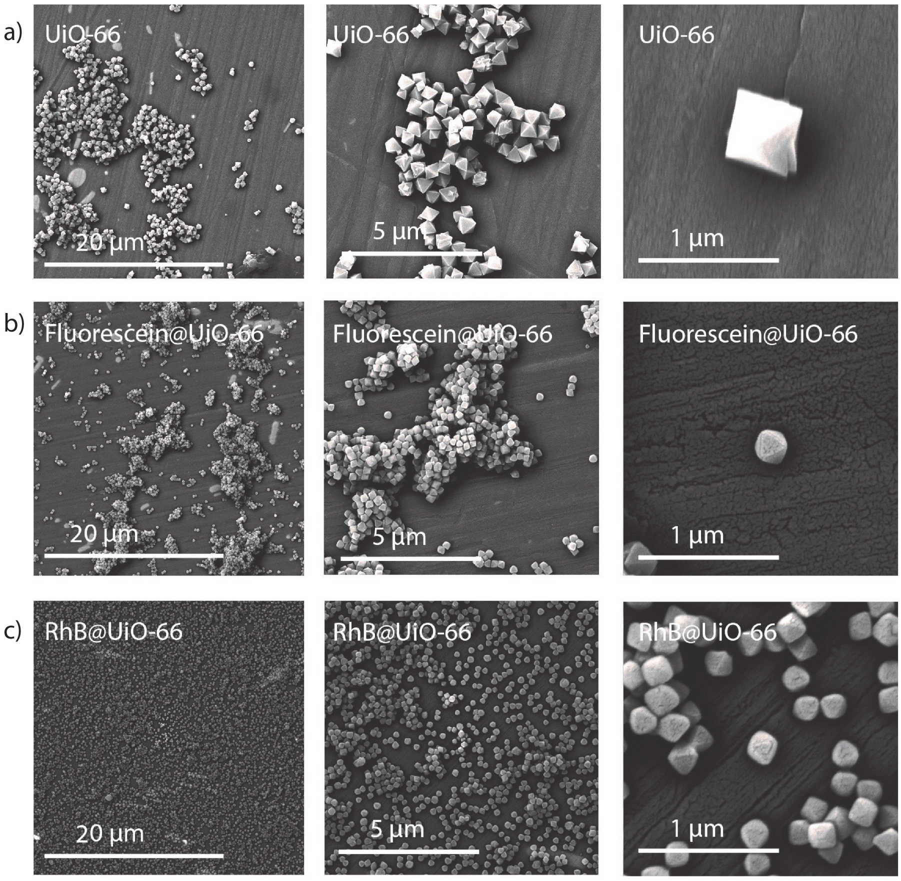

Figure 3.8: Backscattered electron SEM micrographs of the single crystals of a) UiO-66, b) fluorescein@UiO-66, and c) RhB@UiO-66.

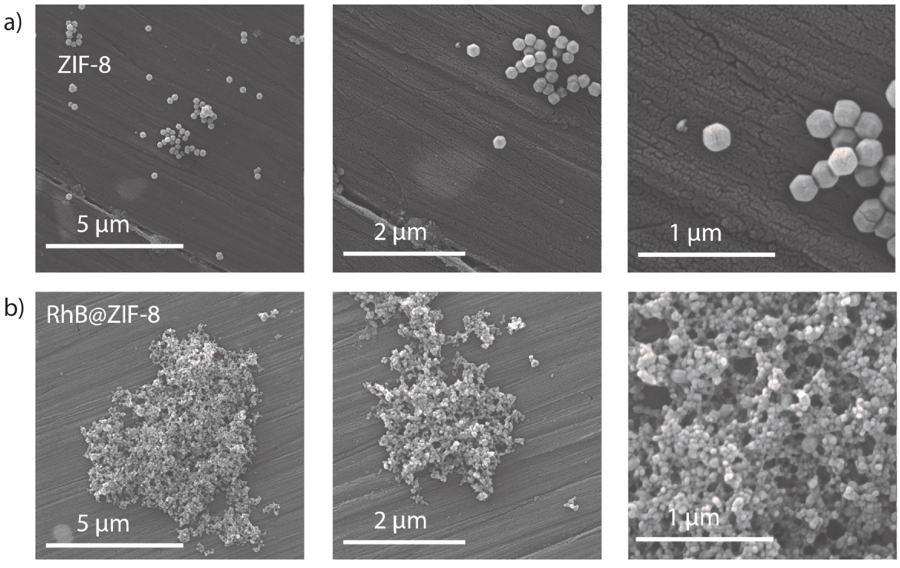

Figure 3.9: SEM micrographs of pristine a) ZIF-8 and b) RhB@ZIF-8 crystals.

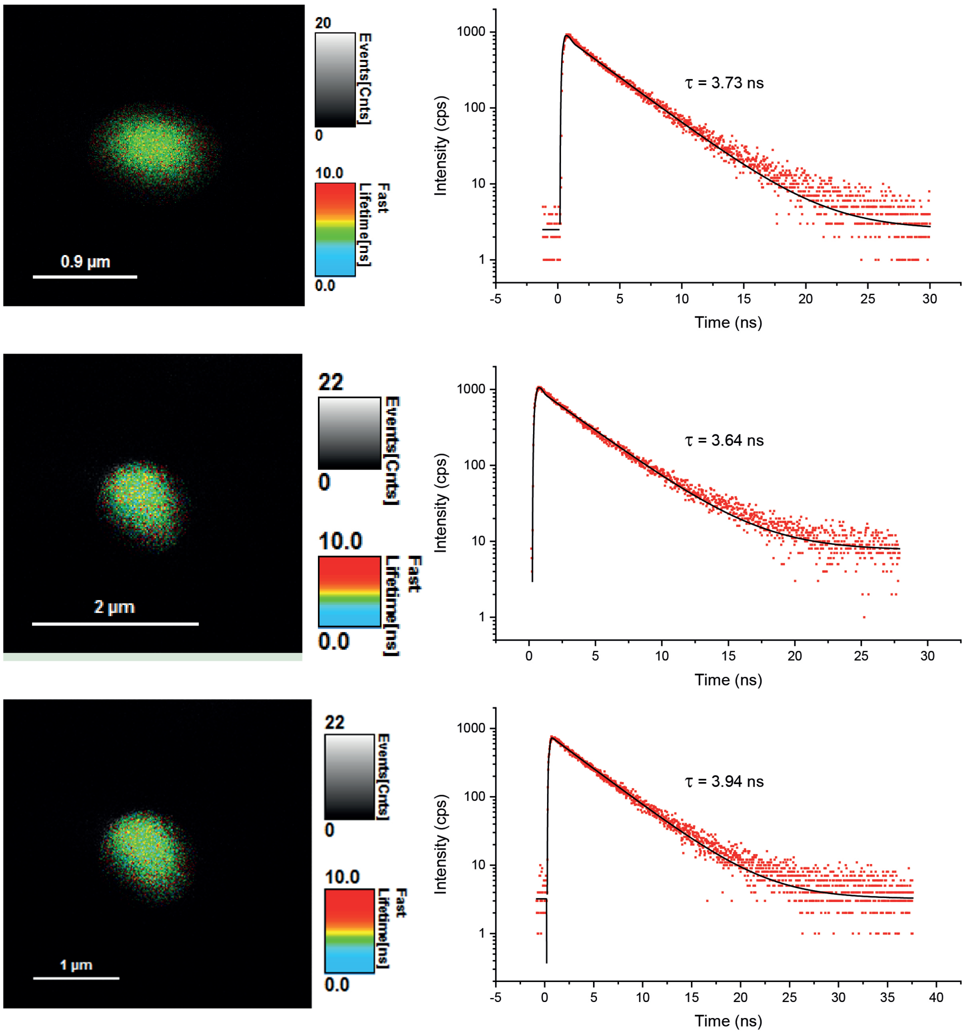

Figure 3.10: Fluorescence lifetime images and decay curves of fluorescein@UiO-66 single crystals (false colour scale). Here, τ designates the monoexponential lifetime derived from fitting of the decay curves.

suggests the successful encapsulation in the pores of the framework. Steady-state fluorescence spectra, measured with a dwell time of 0.2 nm and a step size of 1 nm using the FS-5 spectrofluorometer (Edinburgh Instruments), indeed confirmed the characteristic excitation and emission properties of the luminescent dyes. To rule out that these signals stem from aggregated guest material confined between crystals, a homogeneous distribution is revealed with fluorescence lifetime images (FLIMs) recorded with an inverted-type scanning confocal laser scanning microscope (MicroTime-200, Picoquant, Berlin). Herein, an image was created based on the time a fluorophore remains in an excited state before emitting a detectable photon. A pulsed diode laser (pulse width circa 40 ps) with a wavelength of 470 nm was employed as the excitation source, therefore, only fluorescein@UiO-66 crystals were probed, because RhB would require an excitation source of at least 520 nm, which is unattainable in the available setup. As shown in Figure 3.10, the fluorescein molecules are homogenously distributed over an area that matches the size of the MOF crystals. While this technique can neither achieve the same resolution of nanoFTIR and s-SNOM, nor can it determine the location of the guest inside or outside the framework, the exponential decay rate of the photon emission can in fact carry information about the fate of the guest: for instance, the observed monoexponential decay, which is consistent with the mean lifetime of fluorescein in different solvents, is a strong indication that the fluorophores are isolated in the pores, as the formation of aggregates will lead to multiexponential decays.[129–131] This homogeneous distribution of isolated monomers combined with the finding that no guest materials is attached on the surface of the UiO-66 crystals, as derived from nanoFTIR and s-SNOM, unambiguously prove that the guests are effectively encapsulated into the pores of the framework.

3.4 Near-field infrared nanospectroscopy reveals guest confinement in metal-organic framework single crystals

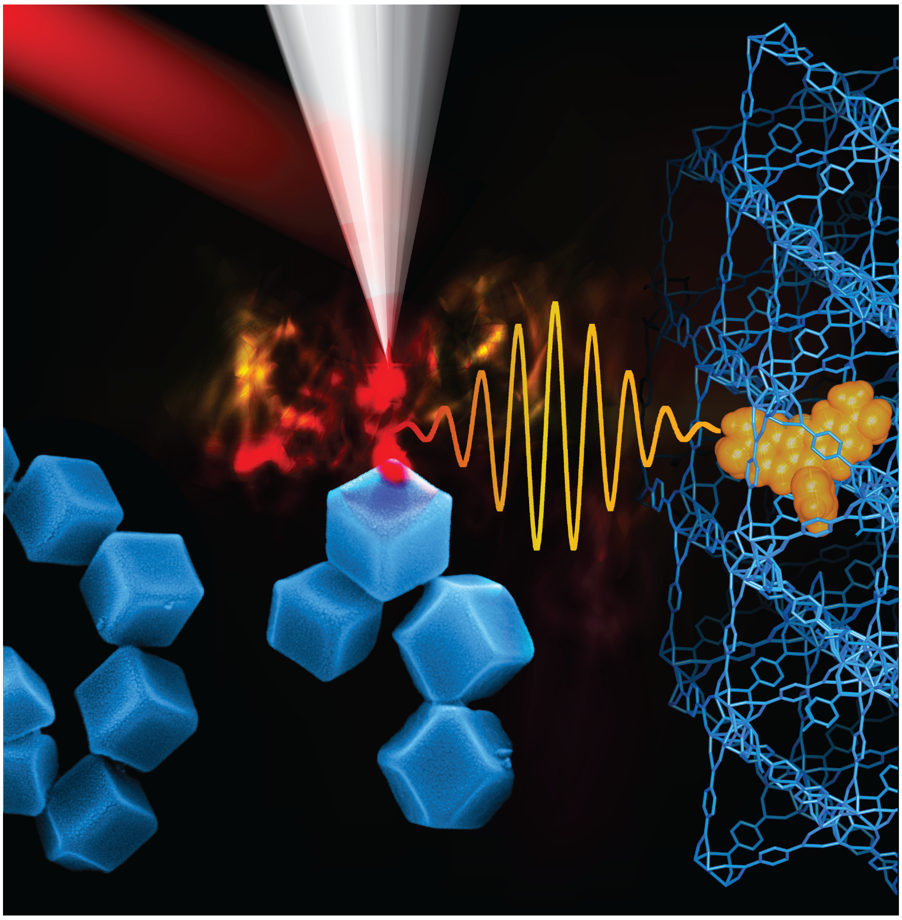

Figure 3.11: Nanospectroscopy reveals guest confinement in MOF single crystals.

The supporting information for this manuscript can be found here:

https://pubs.acs.org/doi/suppl/10.1021/acs.nanolett.0c02839/suppl_file/nl0c02839_si_001.pdf.

NANO LETTERS

pubs.acs.org/NanoLett Letter

Near-Field Infrared Nanospectroscopy Reveals Guest Confinement in Metal–Organic Framework Single Crystals

Annika F. Möslein, Mario Gutiérrez, Boiko Cohen, and Jin-Chong Tan*

Cite This: *Nano Lett.* 2020, 20, 7446–7454 Read Online

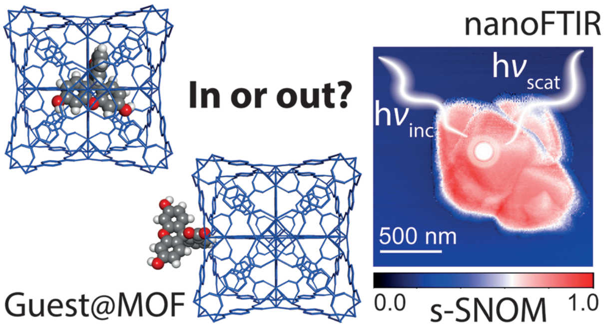

ABSTRACT: Metal–organic frameworks (MOFs) can provide exceptional porosity for molecular guest encapsulation useful for emergent applications in sensing, gas storage, drug delivery, and optoelectronics. Central to the realization of such applications, however, is the successful incorporation of a functional guest confined within the host framework. Here, we demonstrate, for the first time, the feasibility of scattering-type scanning near-field optical microscopy (s-SNOM) and nano-Fourier transform infrared (nanoFTIR) spectroscopy, in concert with density functional theory (DFT) calculations to reveal the vibrational characteristics of the Guest@MOF systems. Probing individual MOF crystals, we pinpoint the local molecular vibrations and, thus, shed new light on the host–guest interactions at the nanoscale. Our strategy not only confirms the successful encapsulation of luminescent guest molecules in the porous host framework in single crystals but also further provides a new methodology for nanoscale-resolved physical and chemical identification of wide-ranging framework materials and designer porous systems for advanced applications.

KEYWORDS: *Metal–organic frameworks, infrared nanospectroscopy, host–guest interaction, optical near-field microscopy, single crystal, nanoconfinement*

INTRODUCTION

Metal–organic frameworks (MOFs), characterized by their crystalline hybrid structure, are constructed from metal clusters and organic linkers via self-assembly at the molecular level. MOFs exhibit remarkably large internal surface areas, far exceeding those found in conventional porous materials such as zeolites and carbon black.[1] Merging the hybrid nature of MOFs with the ability to precisely tailor the characteristics of the pore yields multifunctional properties, boosting their deployment in emerging technologies ranging from gas storage and catalysis to luminescence, dielectrics, drug delivery, and sensors.[2−6] Due to their potential in prospective optoelectronic and sensing technologies, the research interest in luminescent MOFs has intensified toward accomplishing MOF-based devices for real-world applications.[7−9] In this context, the encapsulation of "guest" functional molecules into the "host" MOF pores is a versatile strategy to engineer the Guest@MOF composite materials with tunable physicochemical properties arising from host–guest interactions.[10,11]

There are, however, outstanding challenges to be addressed to achieve the full potential of Guest@MOF systems. Particularly, it is very plausible that during the *in situ* synthesis or *ex situ* infiltration process the guest molecules are adsorbed onto the external surfaces of MOFs instead of truly being encapsulated inside the pores. Unambiguously proving the latter is not a trivial task. Herein, we confirm—on single crystals—the fundamental encapsulation of luminescent guest molecules (fluorophores) into the framework structures of the MOF host material. Our nanoscale multimodal approach combines fluorescence lifetime imaging microscopy (FLIM) with precise determination of the vibrational dynamics of individual crystals, employing the scattering-type scanning near-field optical microscopy (s-SNOM) integrated with nano-Fourier transform infrared (nanoFTIR) spectroscopy, circumventing the diffraction limit of light.[12] The combination of the latter local-scale techniques enables us to perform single-crystal imaging and nanoscale chemical characterization by simultaneously measuring topography and infrared-active vibrational modes, which yields spectral information spatially resolved down to 20 nm.[13] While interference microscopy and scanning transmission electron microscopy have been used to study crystal diversity with time-resolution[14] and heterodomains of MOFs,[15] respectively, s-SNOM measurements could surpass

Received: July 10, 2020
Revised: August 29, 2020
Published: September 1, 2020

https://dx.doi.org/10.1021/acs.nanolett.0c02839

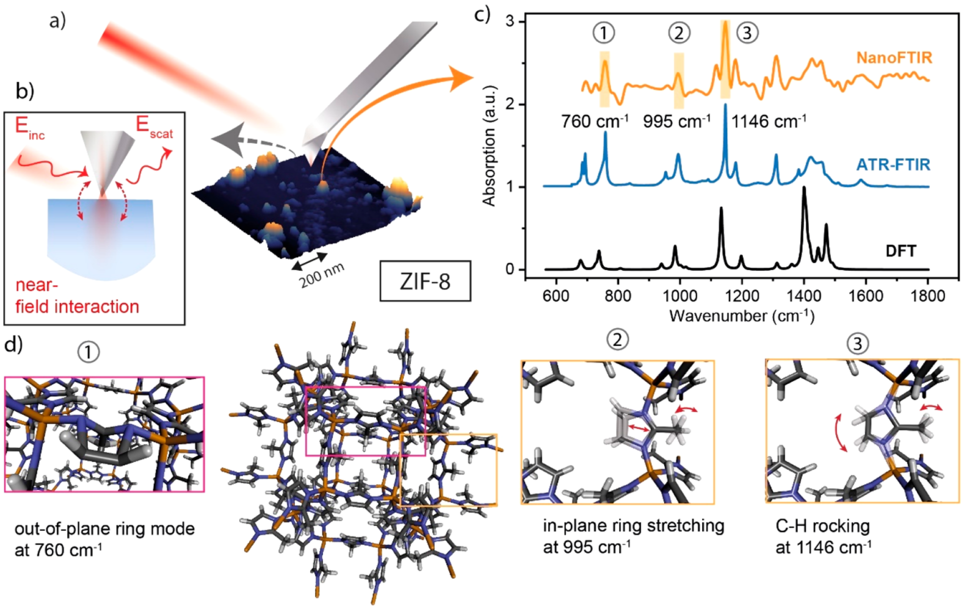

Figure 1. Near-field optical spectroscopy of individual ZIF-8 nanocrystals. (a) Representation of the setup of the s-SNOM measurement stage; the illuminated AFM tip generates a nanofocus on the sample. (b) The near-field interaction between the tip and the sample changes the scattered light from which the local optical properties of the sample are derived. (c) Mid-IR spectra of ZIF-8 crystals obtained via nanoFTIR and ATR-FTIR measurements, compared with the DFT calculations. The DFT spectrum was shifted by a factor of 0.97 to better match the experimental measurements.[21] (d) Characteristic vibrational modes of the ZIF-8 crystal structure: (1) out-of-plane deformation of the mIM ring at 760 cm^{-1}, (2) in-plane stretching of the mIM ring at 995 cm^{-1}, and (3) C−H rocking of the mIM linker at 1146 cm^{-1}.

the spatial resolution of these techniques. The s-SNOM setup employed in this work is based on an atomic force microscope (AFM), where a platinum-coated cantilever tip serves as a topographical and near-field optical probe simultaneously (Figure 1a). Upon illumination, the probe induces an evanescent near-field by acting as a nanoscale light confiner, enhancer, and scatterer, which is key to obtain wavelength-independent resolution (Figure 1b).[16] As the tip polarizes the sample, the optical near-field interaction between the metallic tip and the sample modifies the elastically scattered light. Interferometric detection provides sensitivity to measure the sample's permittivity at a resolution comparable to the dimension of the tip apex.[16] When this signal is Fourier transformed, sample-specific FTIR spectra with a spatial resolution of down to 20 nm are obtained (hereafter we refer to these length scales as "local").[13,17]

For the nanoFTIR method, the tip is operating in tapping mode at its mechanical resonance frequency (Ω = 250 kHz) under illumination from a tunable broadband IR laser. Demodulating the detector signal at higher harmonics of the tip oscillation frequency ($n\Omega$) extracts the near-field interaction from background contributions.[18] Once normalized to a reference signal, this gives the complex-valued near-field contrast, whose imaginary part defines the local nanoFTIR absorption (further details in SI sections 1−2). s-SNOM imaging is achieved via a monochromatic irradiation source instead of a broadband laser. In this case, the illumination wavelength is tuned close to an absorption band of interest to map the material surface on a 2D areal scan. Analogous to nanoFTIR, the scattered light is detected and deconvoluted at higher harmonics of the tip frequency to record the local optical properties through near-field contributions. Optical amplitude and phase now indicate regions of the sample's reflection and absorption at the specific wavelength to derive contrast images with nanoscale resolution.

In this work, we first demonstrate the efficacy of the near-field optical techniques for the physical and chemical characterization of MOF single crystals (ca. 100s nm to 1 μm). As a proof of concept, we measure nanoFTIR absorption spectra from individual crystals of zeolitic imidazolate framework ZIF-8 [$Zn(mIM)_2$; mIM = 2-methylimidazolate],[19] which represents a prototypical imidazole-based MOF with sodalite cage topology. We compare the near-field spectra with far-field FTIR measurements of a bulk sample and with the theoretical spectra of ZIF-8. Subsequently, we demonstrate how to confirm the nanoscale confinement of luminescent dye guest molecules, such as rhodamine B (RhB) or fluorescein, encapsulated in ZIF-8 and UiO-66, where the latter is a prototype of a highly stable zirconium-based framework [$Zr_6O_4(OH)_4(BDC)_6$; BDC = benzene-1,4-dicarboxylate].[20] Specifically, we study the RhB@ZIF-8, RhB@UiO-66, and fluorescein@UiO-66 composite systems, finally validating the Guest@MOF concept.

■ RESULTS AND DISCUSSION

IR Spectroscopy of MOF Single Crystals. We first demonstrate that the described nanoFTIR method can be employed to probe individual MOF-type crystals. Herein, we compare the vibrational spectra of near-field nanoFTIR experimental measurements of ZIF-8 crystals with far-field attenuated total reflection (ATR-FTIR) measurements and these experiments against *ab initio* quantum mechanical calculations from density functional theory (DFT). The results are shown in Figure 1c. In the mid-IR region, the characteristic peaks at 760, 995, and 1146 cm^{-1} are all fully resolved in the nanoscale measurements. Guided by DFT calculations of ZIF-8,[22] we assign these vibrational bands to the out-of-plane and

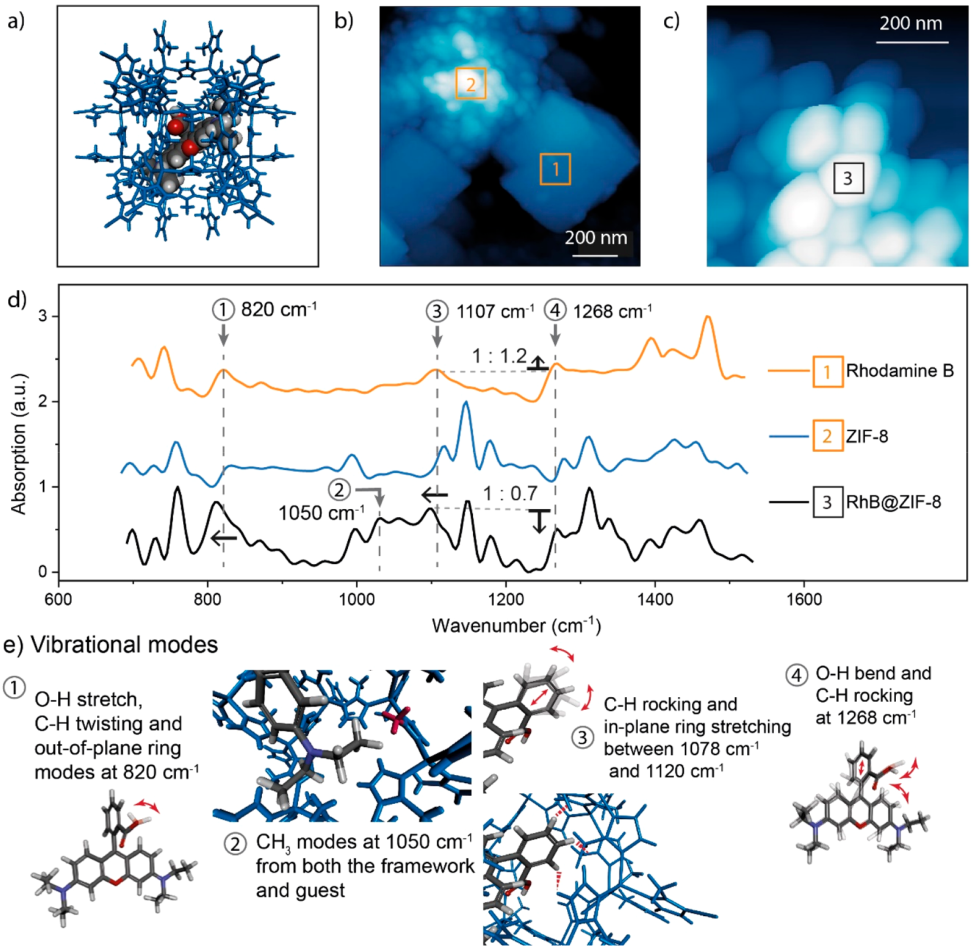

Figure 2. Vibrational analysis of rhodamine B (RhB) and ZIF-8 via nanoFTIR and DFT calculations. (a) Schematic representation of the RhB@ZIF-8 composite, depicting a RhB guest molecule being encapsulated in the pore of the ZIF-8 host framework (in blue). (b) AFM image of the as-synthesized sample containing two distinctive phases, i.e., (1) RhB and (2) ZIF-8, showing the positions where IR spectra were recorded. (c) AFM image of a single-phase sample of ZIF-8 nanocrystals adsorbing RhB. (d) nanoFTIR spectra determined at the designated locations on the AFM image. (e) Vibrational modes of the RhB@ZIF-8 composite illustrating the interactions between the ZIF-8 host framework and the RhB guest.

the in-plane ring stretching modes of the mIM linker, as well as the rocking mode of its C−H bonds, respectively, as illustrated in Figure 1d. Similarly, the in-plane ring bending modes of C−N bonds at 1116 and 1311 cm^{-1}, as well as the symmetric C−N stretching mode at 1445 cm^{-1}, are present in the nanoFTIR spectra.

Indeed, the matching IR spectra demonstrate the capability of nanoFTIR spectroscopy to characterize a MOF-type single crystal; nonetheless, this near-field technique yields minor changes in the IR spectrum. It is worth mentioning that our DFT calculation assumes a defect-free periodic crystal and neglects anharmonicity, while the far-field ATR-FTIR method measures the averaged response of a bulk (polycrystalline) powder material. In contrast, a local scale characterization of individual single crystals is achieved by leveraging nanoFTIR. Here, with a probing depth of ∼20 nm, surface effects might influence the IR spectrum. Close to the crystal boundary, where the framework symmetry is lost, some functional groups are surrounded by voids and air instead of their atomic neighbors assumed in a periodic crystalline structure. Such changes in the atomic environment will affect the strength of the bonds, altering their vibrational frequencies, and as a result, additional peaks and broader peak shapes are observed (Figure 1c). Although subtle alterations in the IR spectrum are observable, they are explained by the nature of experimental surface measurements. In fact, nanoFTIR spectroscopy yields good agreement with established FTIR and DFT methods, thus allowing direct chemical recognition of MOFs through standard FTIR databases; furthermore, it has the unique advantage to directly measure a local IR spectrum reflecting the complex nature of a single MOF crystal whose size is of the order of ∼100 nm.

Host−Guest Interactions at the Nanoscale. Local probing enables a deeper examination of the host−guest interactions in Guest@MOF systems. Crucially, one might ask whether the guest molecule is actually incorporated in the pores of the framework or adsorbed only to its external surface, which, to date, has been a major challenge. Utilizing nanoFTIR and s-SNOM imaging, for the first time, give us the unique opportunity to chemically pinpoint the interaction of the guest molecule at the nanoscale with the MOF host.

Here, we consider an example Guest@MOF system, termed RhB@ZIF-8 (Figure 2a), comprising the luminescent RhB guest in ZIF-8 host, resulting in a fluorescent material potentially useful for optoelectronics and photonic sensors.[23,24] However, the adsorption of RhB in preassembled ZIF-8

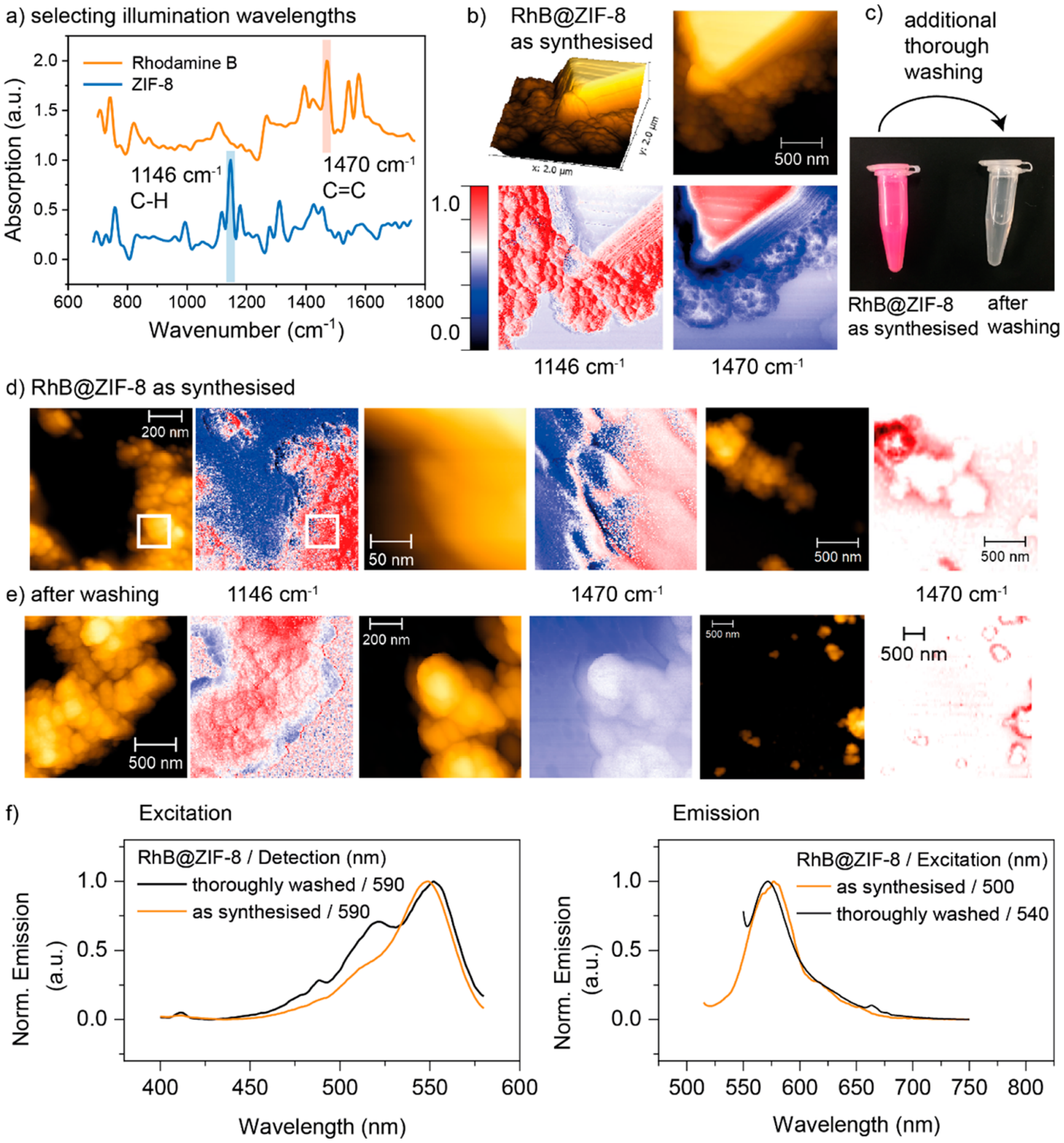

Figure 3. s-SNOM imaging of RhB@ZIF-8. (a) The illumination source was tuned to the characteristic peaks of RhB and ZIF-8. (b) Validation of the contrast images with known, distinguishable material distribution. (c) Samples before and after thorough washing, viewed under daylight. (d) AFM and near-field optical phase imaging of as-synthesized RhB@ZIF-8 with illumination at 1146 cm^{-1}, confirming the presence of ZIF-8, and illumination at 1470 cm^{-1} still revealing RhB on the surface. (e) Near-field optical phase imaging of RhB@ZIF-8 after thorough washing, verifying the complete removal of residual RhB from the sample surface. (f) Normalized excitation and emission spectra of the as-synthesized and thoroughly washed RhB@ZIF-8 (dispersed in acetone) confirming the presence of RhB in both samples. Excitation and detection wavelengths are indicated in the figure.

crystals only leads to surface interactions, since the size of the RhB molecule (13.5 Å) exceeds the window aperture of the ZIF-8 pore (3.4 Å), thus hindering guest infiltration.[25] Therefore, we applied an *in situ* encapsulation of RhB molecules during ZIF-8 formation to synthesize the RhB@ZIF-8 composite (see Methods and Figure S3). Albeit, to isolate the as-synthesized RhB@ZIF-8, several washing steps were performed. AFM imaging revealed different phases with round nanocrystals and micrometer-sized blocks as their distinct morphologies (Figure 2b). Equally, local probing of the features with nanoFTIR spectroscopy yields two significantly different IR spectra. First, the cuboidal block is identified as pure RhB crystals through comparison with the DFT-simulated IR peaks (at 820, 1107, 1268, 1470, and 1576 cm^{-1}, calculated by Gaussian). Second, the frequencies measured at the individual round nanocrystals are matching the IR spectrum of pristine ZIF-8. Consequently, disparate regions of RhB and ZIF-8 are clearly distinguishable by nanoFTIR, where the topography and chemical fingerprint for each constituent material are identifiable without any indication of molecular interaction.

In the third region (Figure 2c), the block crystals of RhB are absent, and the topography resembles the ZIF-8 nanocrystals. Interestingly, probing the individual crystals in this region yields an IR spectrum with characteristic features of both constituent materials (Figure 2d). Although far-field FTIR

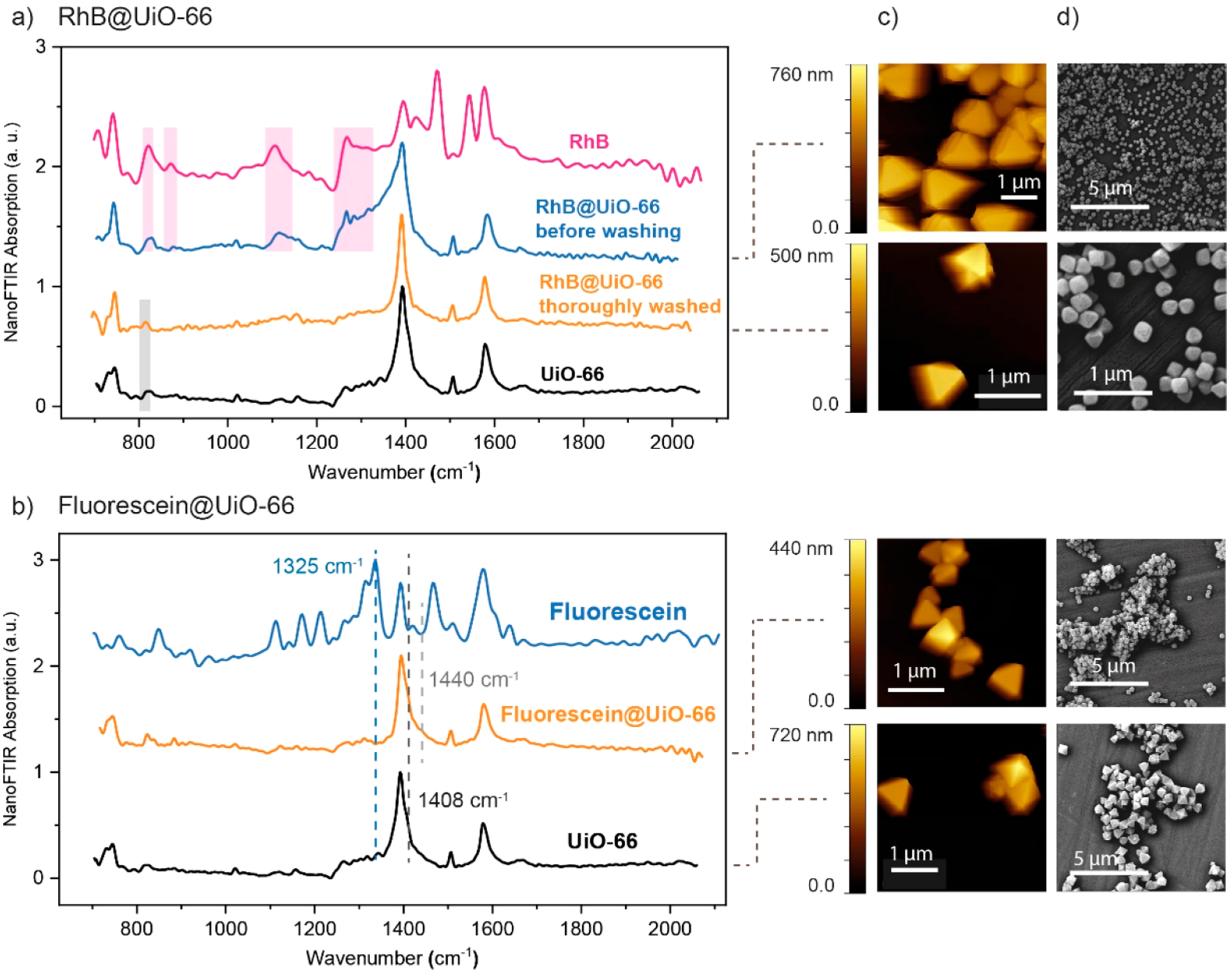

Figure 4. Near-field nanospectroscopy of UiO-66 single crystals with the encapsulated guest RhB and fluorescein, respectively. (a) Near-field IR absorption spectra of RhB, UiO-66, and as-synthesized RhB@UiO-66 composite (without washing the sample) and after thorough washing. (b) The nanoFTIR spectrum of fluorescein@UiO-66 measured on thoroughly washed nanocrystals revealing the absence of fluorescein on the sample surface. Distinguishable wavelengths are selected for subsequent s-SNOM imaging. (c) AFM and (d) SEM images of UiO-66, RhB@UiO-66, and fluorescein@UiO-66 crystals.

measurements may equally lead to a combined IR spectrum, it is worth emphasizing that this is due to the averaged probing over the bulk polycrystalline material without discriminating between the constituent materials present at the local scale. At the measured spot size of 20 nm, in contrast, the superposition of the spectra reveals the concurrent presence of RhB and ZIF-8, leading to the conclusion that the RhB interacts with the ZIF-8 framework due to two reasons. First, all characteristic modes associated with the host framework were identified in the IR spectrum. Second, the vibrational bands assigned to RhB have been modified, revealing host−guest interactions. Considering the O−H group, for instance, with its stretch mode at 820 cm^{-1} experiencing a small shift to lower energies, an interaction between the O−H group of the guest molecule and the host framework is indicated, possibly with the Zn-atoms at defect sites.[25,26] Similarly, the bending mode of the O−H group at 1268 cm^{-1} reveals a change in relative intensity with respect to the peak at 1107 cm^{-1}. We found that the CH_3 vibrations in the region ~1050 cm^{-1} are reinforced due to superposition. The presence of both materials at a nanoscale spot demonstrates the interaction of RhB with the framework; however, this might be influenced by surface adsorption effects. We also observed reduced energy of the phenyl ring stretching modes in RhB at 1107 and 1118 cm^{-1}, which may indicate guest encapsulation. As the dimensions of the RhB molecule almost completely fill the pore of ZIF-8, upon confinement, the free-space vibrations of the trapped molecules are suppressed.

Confirming the Confinement of RhB in the ZIF-8 Framework. One reason for the observed simultaneous presence of guest and framework material at a spot size of 20 nm may be attributed to surface adhesion. To eliminate any residual RhB from adhering on the surface of ZIF-8 nanocrystals, the synthesized RhB@ZIF-8 material was subjected to a second, more thorough washing process (see Methods). If, despite any dye material being removed from the surface, the luminescent properties of RhB are still observable, then the luminescent guests shall be incorporated. On this basis, the material was thoroughly washed until the sample resembled the white color of pristine ZIF-8 rather than the characteristic pink of RhB (Figure 3c). As verification, the

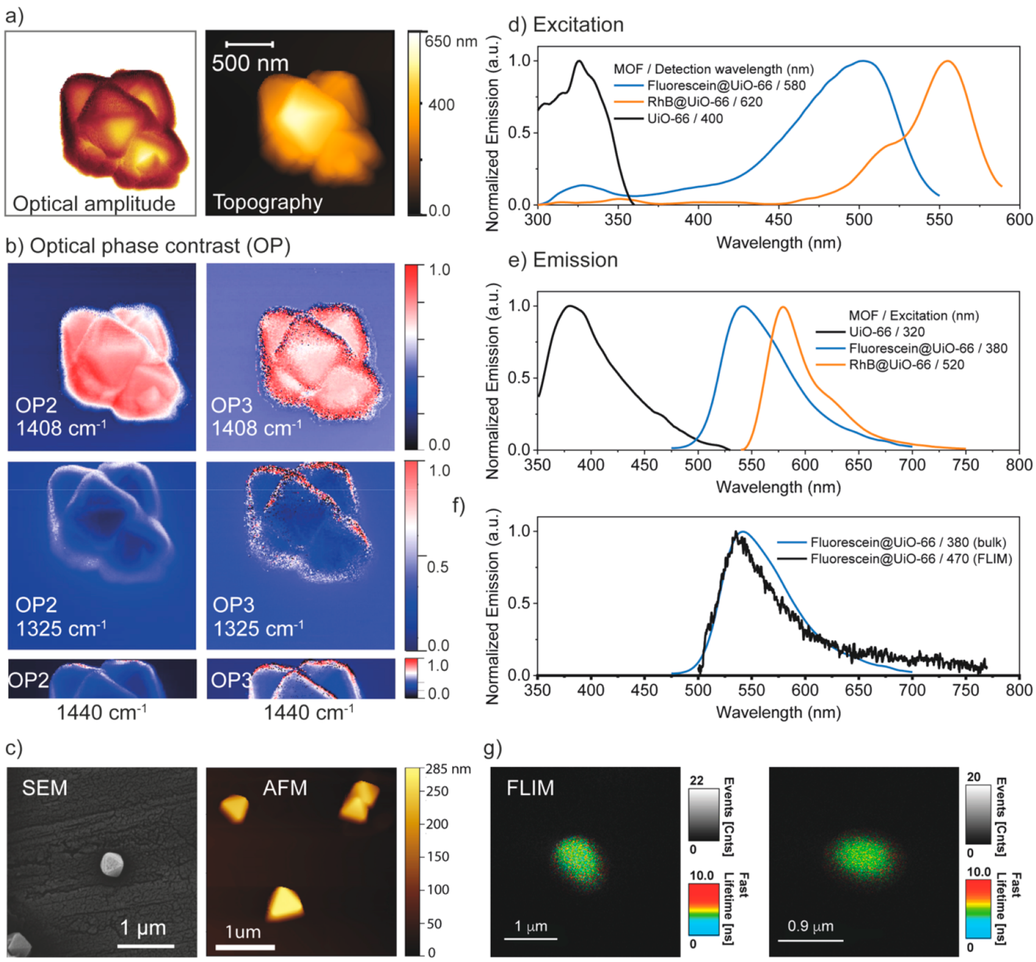

Figure 5. Nanoscale imaging confirming guest encapsulation in UiO-66. (a) Topography and optical amplitude imaging demonstrating the typical size and morphology of the crystals. (b) s-SNOM imaging technique proves that there are no traces of fluorescein on the surface of the UiO-66 crystals. The optical phase images were obtained via illumination at the major absorption peaks of UiO-66 (1408 cm^{-1}) and fluorescein (1325 cm^{-1}) and at a reference position (1440 cm^{-1}), as shown in Figure 4b. (c) SEM and AFM imaging of the individual UiO-66 crystals. (d, e) Excitation and emission spectra of UiO-66 and thoroughly washed Guest@UiO-66 powder samples. Excitation and detection wavelengths are indicated in the figures. (f) Emission spectrum of a single crystal of fluorescein@UiO-66 obtained with a confocal fluorescence microscope compared with the spectrum of powder sample revealing the presence of fluorescein. (g) Fluorescence lifetime imaging microscopy (FLIM) confirming the encapsulation of fluorescein in UiO-66 single crystals, measured under an excitation wavelength of 470 nm.

supernatant of the final washing step was characterized by UV absorption and fluorescence spectroscopy, and since no signal of the dye was obtained, the thorough washing is confirmed (Figure S12). Both the as-synthesized RhB@ZIF-8 (Figure 3d) and the material obtained after thorough washing (Figure 3e) were initially probed using s-SNOM imaging at the illumination wavelength of 1146 cm^{-1}, a characteristic peak of ZIF-8 (Figure 3a), to confirm the presence of ZIF-8 nanocrystals. Upon illumination, only the ZIF-8 crystals absorb IR radiation, represented by the red color in the optical contrast image (Figure 3b), while the RhB block appears transparent like the gold substrate (blue color). Conversely, excitation at 1470 cm^{-1} leads to the inverted contrast due to the strong absorbance of the excited C=C modes of RhB (Figure 3b). Since the surface of the nanocrystals isolated prior to exhaustive washing exhibits regions where the distinctive wavelength for RhB is absorbed, we can unambiguously conclude that RhB is still attached to the surface. After thorough washing, however, no trace of RhB can be found on the surface of the ZIF-8 nanocrystals. The same phenomenon was observed at larger scan areas, where, for clarity, the optical phase contrast is normalized to demonstrate the excess RhB on the RhB@ZIF-8 material before washing. Note that the red contrast in the thoroughly washed material can be assigned to a shadowing effect at the crystal edges (not originating from intrinsic optical properties of the material), because only the areas surrounding the nanocrystals absorb light.

s-SNOM imaging thus indicates the absence of RhB adhered onto the surface of the ZIF-8 nanocrystals (after thorough washing), with the removal of any excess guest material from the sample further confirmed by SEM imaging (Figure S8). Remarkably, the excitation and emission spectra of the thoroughly washed RhB@ZIF-8 composite show the characteristic bands of RhB (Figure 3f). Fluorescence spectroscopic data reveal the presence of the luminescent dye within ZIF-8, which leads to the conclusion that the guest molecule is successfully encapsulated within the framework. This is strong evidence verifying the formation of the RhB@ZIF-8 composite.

Revealing the Guest Encapsulation in UiO-66. To demonstrate the efficacy of the developed methodologies for determining the confinement of guest molecules in MOFs, we have employed two novel Guest@MOF systems as case studies, i.e., RhB@UiO-66 and fluorescein@UiO-66 (Figure 4 and Figure S4). We found that the as-synthesized RhB@UiO-66 still exhibits traces of excess guest material on the surface of the nanocrystals probed via nanoFTIR (Figure 4a). Here, the peaks correlating to the characteristic modes of RhB (in the region between 820 and 1268 cm^{-1}) are visible in the nanoFTIR spectrum in addition to the peaks of the pristine UiO-66 crystals (Figure 4a). An exhaustive washing process—again, confirmed by probing the supernatant with UV absorption and fluorescence spectroscopy (Figure S12)—eliminates any unconfined RhB, and thus, the IR spectrum probed at nanoscale resolution on the surface of the crystals only reveals the representative peaks of UiO-66 (Figure 4a). Turning to the fluorescein@UiO-66 system, likewise, after thoroughly removing any excess guest material, the nanocrystals were identified via nanoFTIR as UiO-66 without any sign of fluorescein on the surface (Figure 4b).

AFM and SEM imaging of the thoroughly washed samples demonstrate the homogeneous crystals without any excess guest material on the sample (Figure 4c,d and Figure S9). To further confirm the absence of the guest adhering on the surface (Figure 5a), not only local point spectra but also the surface of the fluorescein@UiO-66 crystals were examined using s-SNOM imaging (Figure 5b). Hereby, tuning the monochromatic irradiation source to the pronounced peak of UiO-66 at 1408 cm^{-1} illustrates the strong absorbance and reflectance of the crystals in comparison with the substrate. Little contrast, on the other hand, was obtained from illumination at 1325 cm^{-1}, a characteristic peak of fluorescein. Although some absorbance can be observed on the edges of the crystals, again, this can be attributed to noise and shadowing because the same phenomenon emerges at a reference wavelength (1440 cm^{-1}), where neither fluorescein nor the UiO-66 material absorbs. Hence, the absence of any guest material adsorbed on the crystal surface is confirmed. As opposed to the surface techniques, where no signal of the guest molecules is detected, the characteristic emission and excitation bands of RhB and fluorescein are clearly identified for RhB@UiO-66 and fluorescein@UiO-66 composites when measuring their photophysical properties via fluorescence spectroscopy (Figure 5d,e).

Finally, to further corroborate the encapsulation of the fluorophores at a single crystal level, the fluorescence lifetime image (FLIM) of fluorescein@UiO-66 was recorded using a confocal fluorescence microscope (see Methods). Figure 5g shows two single-crystal FLIMs, where clearly, the fluorescein molecules are homogeneously distributed within the UiO-66 crystal. Moreover, the emission spectrum (Figure 5f) of these crystals correlates well with the emission of bulk fluorescein@UiO-66, proving that the emission signal is generated by the fluorescein guest molecules. The mean lifetime of the single crystals is a monoexponential decay of $\tau = 3.77 \pm 0.15$ ns (Figure S10), consistent with the lifetime of fluorescein in different solvents.[27−29] This result suggests that fluorescein molecules are isolated in the form of monomers when partitioned by the pores, as the formation of aggregates will give multiexponential decays.[30] The homogeneous distribution of fluorescein molecules in the form of isolated monomers, alongside with the non-observation of fluorescein on the surface of UiO-66 crystals derived from the nanoFTIR experiments, unequivocally proves the encapsulation of the fluorophores into the MOF pores.

■ CONCLUSIONS

In summary, this first study of individual ZIF-8 and UiO-66 nanocrystals using near-field optical nanospectroscopy yields new understanding about MOFs and their host−guest interactions. We show the capability of the nanoFTIR methodology to characterize individual MOF-type crystals by comparison with established far-field techniques and *ab initio* theoretical calculations. Taking a step further toward precisely unravelling the physical and chemical properties of MOFs, we present the first near-field spectroscopic evidence of host−guest interactions by locally characterizing both constituent materials at a 20 nm irradiation spot. A detailed analysis of the nanocrystals leveraging s-SNOM imaging confirms the absence of any guest material adsorbed on the surface (after thorough washing), while the photophysical properties of the luminescent molecules are still observable. We conclude that the guest molecule is confined in the framework, thus evidencing the Guest@MOF concept. Our findings provide the groundwork to gain a fundamental understanding of the host−guest interactions underpinning hybrid framework materials, further inviting the examination of other porous materials, e.g., covalent organic frameworks, 2D nanosheets,[11] mixed-matrix membranes,[31] and polycrystalline films for sensing devices.[32,33] Confirming the guest encapsulation paves the way to controlling properties at the nanoscale—the key to engineer a multifunctional platform for nanotechnological applications.

■ ASSOCIATED CONTENT

Supporting Information

The Supporting Information is available free of charge at https://pubs.acs.org/doi/10.1021/acs.nanolett.0c02839.

> Synthetic procedures in detail, methods used for materials characterization (PXRD, nanoFTIR spectroscopy, s-SNOM imaging, fluorescence spectroscopy, FLIM, DFT calculations), further details on measuring the local infrared absorption, and additional figures of material characterization (XRD, AFM, SEM, FLIM) (PDF)

■ AUTHOR INFORMATION

Corresponding Author

Jin-Chong Tan − *Multifunctional Materials & Composites (MMC) Laboratory, Department of Engineering Science, University of Oxford, Oxford OX1 3PJ, United Kingdom;* orcid.org/0000-0002-5770-408X; Email: jin-chong.tan@eng.ox.ac.uk

Authors

Annika F. Möslein − *Multifunctional Materials & Composites (MMC) Laboratory, Department of Engineering Science, University of Oxford, Oxford OX1 3PJ, United Kingdom;* orcid.org/0000-0002-2056-6437

Mario Gutiérrez − *Multifunctional Materials & Composites (MMC) Laboratory, Department of Engineering Science, University of Oxford, Oxford OX1 3PJ, United Kingdom;* orcid.org/0000-0001-9222-3647

Boiko Cohen − *Departamento de Química Física, Facultad de Ciencias Ambientales y Bioquímica, and INAMOL, Universidad* *de Castilla-La Mancha, 45071 Toledo, Spain;* orcid.org/0000-0002-5400-4678

Complete contact information is available at:
https://pubs.acs.org/10.1021/acs.nanolett.0c02839

Notes

The authors declare no competing financial interest.

■ ACKNOWLEDGMENTS

A.F.M. thanks the Oxford Ashton Memorial scholarship for a DPhil studentship award. J.C.T. and A.F.M. are thankful to the ERC Consolidator Grant (771575 (PROMOFS)) for funding. B.C. acknowledges support from JCCM, Spain, grant no. SBPLY/19/180501/000212. We would like to acknowledge the use of the University of Oxford Advanced Research Computing (ARC) facility in carrying out this work (10.5281/zenodo.22558). We are grateful to the Research Complex at Harwell (RCaH) for the provision of advanced materials characterization facilities. A.F.M. would like to thank Dr. Cyril Besnard and Prof. Alexander Korsunsky for their help with SEM imaging and neaspec GmbH for the opportunity to perform s-SNOM imaging in Haar, Germany. We also thank Dr. Abhijeet Chaudhari for the provision of the RhB@ZIF-8 samples.

■ REFERENCES

(1) Furukawa, H.; Cordova, K. E.; O'Keeffe, M.; Yaghi, O. M. The chemistry and applications of metal-organic frameworks. *Science* **2013**, *341* (6149), 1230444.

(2) Zhu, L.; Liu, X. Q.; Jiang, H. L.; Sun, L. B. Metal-Organic Frameworks for Heterogeneous Basic Catalysis. *Chem. Rev.* **2017**, *117* (12), 8129−8176.

(3) Horcajada, P.; Gref, R.; Baati, T.; Allan, P. K.; Maurin, G.; Couvreur, P.; Ferey, G.; Morris, R. E.; Serre, C. Metal-organic frameworks in biomedicine. *Chem. Rev.* **2012**, *112* (2), 1232−1268.

(4) Li, B.; Wen, H. M.; Zhou, W.; Chen, B. Porous Metal-Organic Frameworks for Gas Storage and Separation: What, How, and Why? *J. Phys. Chem. Lett.* **2014**, *5* (20), 3468−3479.

(5) Lustig, W. P.; Mukherjee, S.; Rudd, N. D.; Desai, A. V.; Li, J.; Ghosh, S. K. Metal-organic frameworks: functional luminescent and photonic materials for sensing applications. *Chem. Soc. Rev.* **2017**, *46* (11), 3242−3285.

(6) Ryder, M. R.; Zeng, Z.; Titov, K.; Sun, Y.; Mahdi, E. M.; Flyagina, I.; Bennett, T. D.; Civalleri, B.; Kelley, C. S.; Frogley, M. D.; Cinque, G.; Tan, J.-C. Dielectric Properties of Zeolitic Imidazolate Frameworks in the Broad-Band Infrared Regime. *J. Phys. Chem. Lett.* **2018**, *9* (10), 2678−2684.

(7) Kaur, H.; Sundriyal, S.; Pachauri, V.; Ingebrandt, S.; Kim, K.-H.; Sharma, A. L.; Deep, A. Luminescent metal-organic frameworks and their composites: Potential future materials for organic light emitting displays. *Coord. Chem. Rev.* **2019**, *401*, 213077.

(8) Stassen, I.; Burtch, N.; Talin, A.; Falcaro, P.; Allendorf, M.; Ameloot, R. An updated roadmap for the integration of metal-organic frameworks with electronic devices and chemical sensors. *Chem. Soc. Rev.* **2017**, *46* (11), 3185−3241.

(9) Gutiérrez, M.; Martín, C.; Van der Auweraer, M.; Hofkens, J.; Tan, J. C. Electroluminescent Guest@MOF Nanoparticles for Thin Film Optoelectronics and Solid-State Lighting. *Adv. Opt. Mater.* **2020**, *8*, 2000670.

(10) Allendorf, M. D.; Foster, M. E.; Leonard, F.; Stavila, V.; Feng, P. L.; Doty, F. P.; Leong, K.; Ma, E. Y.; Johnston, S. R.; Talin, A. A. Guest-Induced Emergent Properties in Metal-Organic Frameworks. *J. Phys. Chem. Lett.* **2015**, *6* (7), 1182−1195.

(11) Chaudhari, A. K.; Kim, H. J.; Han, I.; Tan, J. C. Optochemically Responsive 2D Nanosheets of a 3D Metal-Organic Framework Material. *Adv. Mater.* **2017**, *29* (27), 1701463.

(12) Knoll, B.; Keilmann, F. Near-field probing of vibrational absorption for chemical microscopy. *Nature* **1999**, *399*, 134−137.

(13) Huth, F.; Govyadinov, A.; Amarie, S.; Nuansing, W.; Keilmann, F.; Hillenbrand, R. Nano-FTIR absorption spectroscopy of molecular fingerprints at 20 nm spatial resolution. *Nano Lett.* **2012**, *12* (8), 3973−3978.

(14) Remi, J. C. S.; Lauerer, A.; Chmelik, C.; Vandendael, I.; Terryn, H.; Baron, G. V.; Denayer, J. F.; Kärger, J. The role of crystal diversity in understanding mass transfer in nanoporous materials. *Nat. Mater.* **2016**, *15* (4), 401−406.

(15) Collins, S. M.; Kepaptsoglou, D. M.; Butler, K. T.; Longley, L.; Bennett, T. D.; Ramasse, Q. M.; Midgley, P. A. Subwavelength Spatially Resolved Coordination Chemistry of Metal-Organic Framework Glass Blends. *J. Am. Chem. Soc.* **2018**, *140* (51), 17862−17866.

(16) Keilmann, F.; Hillenbrand, R. Near-field microscopy by elastic light scattering from a tip. *Philos. Trans. R. Soc., A* **2004**, *362* (1817), 787−805.

(17) Zenhausern, F.; Martin, Y.; Wickramasinghe, H. K. Scanning interferometric apertureless microscopy: Optical imaging at 10 angstrom resolution. *Science* **1995**, *269*, 1083−1085.

(18) Govyadinov, A. A.; Amenabar, I.; Huth, F.; Carney, P. S.; Hillenbrand, R. Quantitative Measurement of Local Infrared Absorption and Dielectric Function with Tip-Enhanced Near-Field Microscopy. *J. Phys. Chem. Lett.* **2013**, *4* (9), 1526−1531.

(19) Tan, J.-C.; Civalleri, B.; Lin, C.-C.; Valenzano, L.; Galvelis, R.; Chen, P.-F.; Bennett, T. D.; Mellot-Draznieks, C.; Zicovich-Wilson, C. M.; Cheetham, A. K. Exceptionally Low Shear Modulus in a Prototypical Imidazole-Based Metal-Organic Framework. *Phys. Rev. Lett.* **2012**, *108* (9), 095502.

(20) Cavka, J. H.; Jakobsen, S.; Olsbye, U.; Guillou, N.; Lamberti, C.; Bordiga, S.; Lillerud, K. P. A New Zirconium Inorganic Building Brick Forming Metal Organic Frameworks with Exceptional Stability. *J. Am. Chem. Soc.* **2008**, *130* (42), 13850−13851.

(21) Rauhut, G.; Pulay, P. Transferable Scaling Factors for Density Functional Derived Vibrational Force Fields. *J. Phys. Chem.* **1995**, *99* (10), 3093−3100.

(22) Ryder, M. R.; Civalleri, B.; Bennett, T. D.; Henke, S.; Rudic, S.; Cinque, G.; Fernandez-Alonso, F.; Tan, J. C. Identifying the role of terahertz vibrations in metal-organic frameworks: from gate-opening phenomenon to shear-driven structural destabilization. *Phys. Rev. Lett.* **2014**, *113* (21), 215502.

(23) Zhang, Y. Q.; Wu, X. H.; Mao, S.; Tao, W. Q.; Li, Z. Highly luminescent sensing for nitrofurans and tetracyclines in water based on zeolitic imidazolate framework-8 incorporated with dyes. *Talanta* **2019**, *204*, 344−352.

(24) Chaudhari, A. K.; Tan, J. C. Dual-Guest Functionalized Zeolitic Imidazolate Framework-8 for 3D Printing White Light-Emitting Composites. *Adv. Opt. Mater.* **2020**, *8* (8), 1901912.

(25) Chin, M.; Cisneros, C.; Araiza, S. M.; Vargas, K. M.; Ishihara, K. M.; Tian, F. Rhodamine B degradation by nanosized zeolitic imidazolate framework-8 (ZIF-8). *RSC Adv.* **2018**, *8* (47), 26987−26997.

(26) Zhang, C.; Han, C.; Sholl, D. S.; Schmidt, J. R. Computational Characterization of Defects in Metal-Organic Frameworks: Spontaneous and Water-Induced Point Defects in ZIF-8. *J. Phys. Chem. Lett.* **2016**, *7* (3), 459.

(27) Zhang, X. F.; Zhang, J.; Liu, L. Fluorescence properties of twenty fluorescein derivatives: lifetime, quantum yield, absorption and emission spectra. *J. Fluoresc.* **2014**, *24* (3), 819−26.

(28) Magde, D.; Rojas, G. E.; Seybold, P. G. Solvent Dependence of the Fluorescence Lifetimes of Xanthene Dyes. *Photochem. Photobiol.* **1999**, *70* (5), 737−744.

(29) Martin, M. M.; Lindqvist, L. The pH dependence of fluorescein fluorescence. *J. Lumin.* **1975**, *10* (6), 381−390.

(30) Hungerford, G.; Benesch, J.; Mano, J. F.; Reis, R. L. Effect of the labelling ratio on the photophysics of fluorescein isothiocyanate (FITC) conjugated to bovine serum albumin. *Photochem. Photobiol. Sci.* **2007**, *6* (2), 152−158.

(31) Dechnik, J.; Sumby, C. J.; Janiak, C. Enhancing Mixed-Matrix Membrane Performance with Metal-Organic Framework Additives. *Cryst. Growth Des.* **2017**, *17* (8), 4467−4488.

(32) Yuan, H.; Li, N.; Linghu, J.; Dong, J.; Wang, Y.; Karmakar, A.; Yuan, J.; Li, M.; Buenconsejo, P. J. S.; Liu, G.; Cai, H.; Pennycook, S. J.; Singh, N.; Zhao, D. Chip-Level Integration of Covalent Organic Frameworks for Trace Benzene Sensing. *ACS Sens.* **2020**, *5* (5), 1474−1481.

(33) Stassen, I.; Styles, M.; Van Assche, T.; Campagnol, N.; Fransaer, J.; Denayer, J.; Tan, J.-C.; Falcaro, P.; De Vos, D.; Ameloot, R. Electrochemical Film Deposition of the Zirconium Metal-Organic Framework UiO-66 and Application in a Miniaturized Sorbent Trap. *Chem. Mater.* **2015**, *27* (5), 1801−1807.

Statement of Authorship for joint/multi-authored papers for PGR thesis

To appear at the end of each thesis chapter submitted as an article/paper

The statement shall describe the candidate's and co-authors' independent research contributions in the thesis publications. For each publication there should exist a complete statement that is to be filled out and signed by the candidate and supervisor **(only required where there isn't already a statement of contribution within the paper itself).**

Title of Paper	Near-Field Infrared Nanospectroscopy Reveals Guest Confinement in Metal−Organic Framework Single Crystals
Publication Status	☒Published ☐ Accepted for Publication ☐Submitted for Publication ☐Unpublished and unsubmitted work written in a manuscript style
Publication Details	A. F. Möslein, M. Gutiérrez, B. Cohen, and J.C.Tan, "Near-field infrared nanospectroscopy reveals guest confinement in metal-organic framework single crystals", Nano Letters, 20, 7446-7454 (2020).

Student Confirmation

Student Name:	Annika F. Möslein		
Contribution to the Paper	Experimental design, experimental execution, and data analysis: A.F.M. FLIM measurements: M.G and B.C. Preparation of guest@UiO-66 samples: M.G. Numerical simulations A.F.M. Writing of the original draft: A.F.M. Writing, editing, and reviewing: all authors. Supervision: J.-C.T.		
Signature		Date	27/07/2022

Supervisor Confirmation

By signing the Statement of Authorship, you are certifying that the candidate made a substantial contribution to the publication, and that the description described above is accurate.

Supervisor name and title:	Prof. Jin-Chong Tan		
Supervisor comments	I support this application and confirm the information entered is correct.		
Signature		Date	29 July 2022

This completed form should be included in the thesis, at the end of the relevant chapter.

Things get broken, and sometimes they get repaired, and in most cases, you realize that no matter what gets damaged, life rearranges itself to compensate for your loss, sometimes wonderfully.

— Hanya Yanagihara, *A Little Life*

4

Defects in single MOF-type crystals

Contents

4.1 Defect tuning in MOFs

While the guest@MOF principle is a smart strategy towards engineering novel materials with desired properties, there exists another way to tune MOFs for tailored applications. It is the artificial control of defects and imperfections, or the so-called defect engineering, that allows for precise tuning of distinct properties by introducing defects into the framework.[132] Of course, the most common example of defect engineering is the development of doped semiconductors, which are now considered essential components in many electronic devices. Akin to semiconductors, where the conducting properties are altered, MOF materials can be optimized by introducing defects into the crystal to improve catalytic and adsorptive behaviour, or electronic conductivity, among several other physical properties.[133] Despite these opportunities, defects, with their ubiquitous nature in crystalline materials, could diminish the performance of otherwise highly ordered MOFs, too. Firstly, the stability of the framework may be affected by structural defects possibly leading to a faster degradation. Secondly, MOF systems are typically modelled as ideal, defect-free crystals to predict the material's properties, and the results of such calculations are used for material discovery or screening for targeted applications. Little however is known about how defects may influence the properties that form the basis of such predictions. A systematic understanding of the role of defects in MOFs is therefore crucial to either control or enhance the material properties. Yet, establishing the function-property correlation in defective MOFs challenges the set of conventional techniques.[132]

4.1.1 X-ray diffraction for structural defects

Because structural characterisation techniques, such as X-ray diffraction, rely on the periodic long-range order of the crystalline lattice, probing point defects – which only introduce local disorder - lies beyond their resolution. One exemption however exists, where the complimentary use of powder XRD and DFT could expose metal vacancies in UiO-66 crystals.[134] This is because these structural defects propagate linker vacancies in adjacent areas forming nanoregions of a different crystalline phase (reo topology) in the parent UiO-66 crystallising in a fcu topology, as shown in Figure 4.1. These domains of correlated missing linkers and nodes effectively lead to diffuse scattering profiles, additionally to the sharp Bragg peaks, in the PXRD pattern. Inspired by these finding, several experimental and computational investigations have focussed on UiO-66, which has thus emerged as the model system amid defective MOFs.[133] For instance, correlations between specific modulators and the formation of defective nanodomains have been established via PXRD merged with NMR spectroscopy, BET (N_2 physisorption) measurements, and computational modelling.[135–137] Similarly, synchrotron-based XRD performed on sufficiently

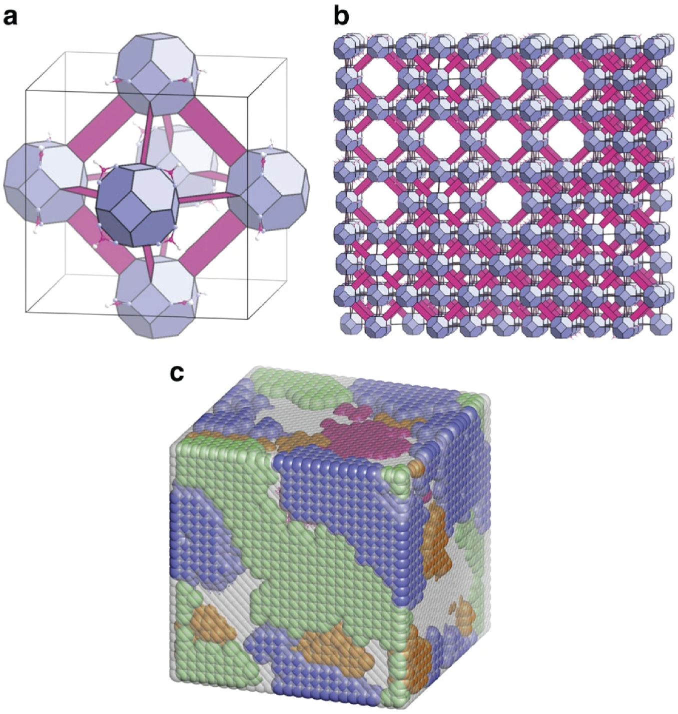

Figure 4.1: Correlated defect nanoregions in UiO-66. a)A polyhedral representation of a single-unit cell of the (ordered) reo defect structure. b) A representative section of the atomistic model, where defect-rich nanoregions are dispersed throughout a matrix of defect-free fcu framework. c) The defect concentration and domain size parameters determined experimentally are used to generate atomistic representations of defect nanoregions in UiO-66. Reprinted from ref. [134] with permission from Springer Nature, Copyright 2014.

large crystals (5 – 100 μm) revealed structural defects in UiO-66 caused by missing linkers.[138] In elucidating defect concentration and distribution with PXRD, it is important to highlight that this method only applies to UiO-66 and its derivatives, since nanoregions of correlated structural defects have hitherto not been observed in other MOF systems; and point defects alone would not noticeably impact the long-range order. Instead, an array of indirect characterisation techniques can be employed to study the effects of a defect on certain properties.

4.1.2 Indirect characterisation of defects

One useful technique to assess the presence and chemistry of defects is thermogravimetric analysis (TGA). Derived from TGA data, it was shown that defective UiO-66 systems exhibit lower thermal stability when compared to their intact counterpart.[136] To further study the stoichiometry and quantity of defects in UiO-66, TGA coupled with mass spectroscopy was employed revealing, on average, the intrinsic absence of one of the 12 linkers coordinated to each metal node.[139] Only insights about the overall composition are however attained *via* TGA, and complimentary techniques are required to account for the lack of structural information.

If, for instance, a combination of different or fragmented linkers is used to introduce defects into the MOF, conventional spectroscopic techniques can qualitatively evaluate their incorporation, as their vibrational behaviour might differ. Considering UiO-66 again, IR and UV-vis spectroscopy in conjunction with DFT calculations could disclose the characteristics of structural derivatives.[139] In other MOF systems, the presence of defects was indirectly probed *via* FTIR techniques by leveraging the adsorption and desorption of probe molecules such as CO.[140, 141] Because the adsorption sites of defective and regular building units differ, their distinct atomic environments may alter the vibrations of the adsorbed CO molecules. Indeed, such salient changes can be detected in the vibrational spectrum measured on HKUST-1, where two signals associated to CO are observable indicating coordination to either Cu^{2+}, or in the case of defective ligands, Cu^{+} nodes.[142]

4.1.3 Ordered disorder

Even if aforementioned techniques suggest the presence of defective sites in MOFs, they do not differentiate between isolated and correlated defects. In fact, defect clustering may have implications for the porosity of MOF crystals, as it has been demonstrated with N_2 adsorption (type-IV isotherms) for HKUST-1 and UiO-66, among others.[142, 143] Equally, correlations between defect concentration and porosity could be drawn from BET surface area calculations.[136, 139, 143, 144] Moving from defect clustering to the extreme case of long-range ordering, such extended defects can either be measured with XRD, as shown for UiO-66, or directly imaged using AFM, SEM and TEM techniques. Examples include screw dislocations in HKUST-1, which lead to the formation of spiralling steps on the surface, or oriented fractures occurring during solvent removal.[145] Inspired

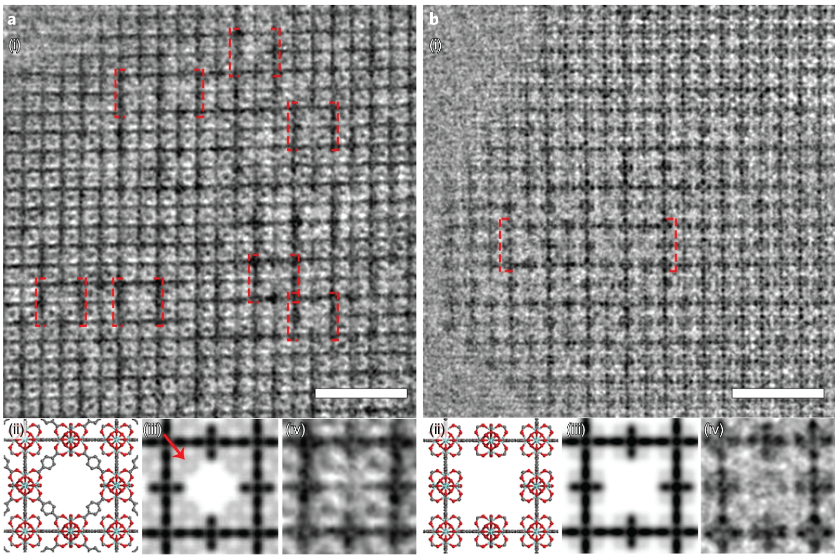

Figure 4.2: Imaging defects in UiO-66. HRTEM images of the [001] direction of UiO-66, showing different types of missing-cluster defects, adopting a) the reo structure and b) the scu structure. Reprinted from ref. [146] with permission from Springer Nature, Copyright 2019.

by these findings, additional studies using confocal microscopy established that these fractures associated with extended defects are catalytically active due to the presence of acid sites. This is a significant observation, because it directly links the presence of defects with the impact on the material's performance. Similarly, regions of missing-linker and missing-cluster defects in UiO-66 were directly imaged using high-resolution TEM (HRTEM), as visualised in Figure 4.2.[146] Not only a break-through resolution at the atomic scale was achieved, but it was further discovered that defects distinctively transform during crystallisation. Interestingly, the two types of structural defects revealed different catalytic activity, paving the way to advanced defect engineering in UiO-66.

4.1.4 Defects in ZIF materials

Generally, the developed principles relating the nature of defects with their implications on the performance of MOF materials are derived from studies on UiO-66 crystals and derivatives. Among the most promising MOF materials for application are however zeolitic imidazolate frameworks (ZIFs) owing to their excellent chemical and thermal stability.[147] Although analogies for lattice defects such as linker or metal vacancies can be drawn between the parent MOF materials and ZIFs, it is important to note that point defects, albeit expected, have not been directly detected in ZIFs. Most likely, they will emerge as missing metal atoms resulting in two protonated linkers (‘dangling linkers’), or missing imidazolate ligands, which yield open metal sites for adsorption of radicals or modulators. Despite the lack of direct measurements, there exists evidence suggesting the presence of structural defects in ZIFs. One of the strongest indications originated from water adsorption experiments: ZIF-8, being intrinsically hydrophobic, should not support strong adsorption of water molecules, especially at low loadings, according to computational modelling.[148] In practice, however, the opposite phenomenon was determined by experimental findings from which the existence of hydrophilic defects was deduced.[149] Nevertheless, the question of which structural defects were responsible for such abnormal behaviour could not be answered based on these experiments. Herein, computational studies have provided potential explanations, as they predicted the presence of local point defects, namely missing linkers, and missing nodes, in ZIF-8.[150, 151] But while the feasibility of structural defects has been demonstrated through theoretical calculations, and it is plausible that imperfections may occur in the crystalline lattice, they have not been directly probed in ZIF materials. Indirect measurements, from which structural defects could be deduced, included the removal of solvent molecules after crystallisation.[152] Because this led to structural changes in ZIF-7, the degradation of unit cells close to the crystal surface was suggested; however, the wide-ranging implications of such surficial collapse were not further investigated. Given the significance of surface properties on the catalytic or adsorptive behaviour of nanocrystals, this demanded further studies. Accordingly, detailed characterisation of surface-terminating defects has been performed on ZIF-8 thin films [153], while other scarce experimental studies examined the effects of defects in ZIF-8 on gas separation and storage.[154, 155] Yet, most questions about the occurrence and nature of defects in ZIF materials, and a detailed understanding of the function-structure correlations, which is key for the stability and performance demanded by many applications, remain thus far unresolved. Only if a detailed knowledge is attained, then a controlled insertion of defects into the MOF system can be achieved to endow the materials with tailored properties; or contrarily, if the origin of defects is fully understood, then defect-free crystals can be synthesised for certain applications. Until now, this remains a challenge owing to the lack of appropriate techniques merging high sensitivity to structural defects (unattainable in diffraction-based methods) with non-destructive approaches unlike local-scale measurements based on electron beams.

4.2 A strategy to reveal defects in MOF single crystals

This is precisely where the development of nanoscale analytical methods offers exciting prospects to tackle the outstanding challenges described in Section 4.1. Indeed, proposing a novel, multimodal approach of nanoscale techniques combined with computational modelling, we report the first direct observation of structural defects in ZIF-8. In particular, we shed light on the evolution of structural defects in the ZIF structure during crystal growth, and further investigate their implications on the material's performance. Through the first use of s-SNOM, in combination with nanoFTIR, to probe imperfections, these non-destructive techniques let us expose and chemically characterise structural defects in fine-scale crystalline materials. More precisely, we image the evolution of individual ZIF-8 nano- and micro-sized crystals at different stages of crystallisation, and locally probe their chemical structure by pinpointing the infrared vibrational dynamics with a resolution akin to AFM. While the crystals obtained after a short growth time ($\sim$minutes) resemble those from a prolonged crystallisation, in the sense that their size and structural characteristics, as shown in Figure 4.3 and confirmed with PXRD, are similar, the average of their local nanoFTIR spectra reveal significant discrepancies (see Figure 4.4). Through comparison with the spectra of pristine building materials (zinc salt and 2-methylimidazole linker), we discovered that defects such as zinc cations that are bound to nitrate molecules of the reactant rather than linker units gradually disappear with the ripening of the crystals, while dangling and missing linker defects prevail (see Figures 1 and 2 in the manuscript of Section 4.3). This is an unexpected result in the domain of ZIF materials, subsequently motivating us to study how it affects the crystal functions.

To understand the impact of structural defects on the material's properties, we investigate the mechanical properties both computationally and experimentally, hereby proposing a novel nanoscale technique for the field of metal-organic frameworks: tip-force microscopy (TFM). Based on the same experimental setup as nanoFTIR, albeit operated in contact mode, this becomes a powerful tool for quantitative characterisation of nanomaterials and their local mechanical behaviour, especially in conjunction with computational modelling. For instance, we image the variation in the Young's moduli of individual crystals with a resolution of 20 nm, which offers a new fundamental understanding of defects and their implications on function. For defective ZIF-8 crystals, we observed a higher anisotropy in the elastic properties, whilst the crystals obtained after prolonged crystallization, and thus with fewer defects, reveal a greater, and more isotropic, Young's modulus (shown in Figures 4.5 and 4.6).

These TFM findings are explained through computational modelling based on density functional theory (DFT). To model the mechanical behaviour, we calculated the elastic response of ZIF-8, which has been simulated as an orthorhombic system. As the cubic system led to negative frequencies in the frequency calculations, some symmetry restrictions had to be removed to yield a stable, orthorhombic system. After this geometry optimisation, the single-crystal elastic constants were calculated. Importantly, the elastic constants completely describe the elastic behaviour, because they link stress and strain following Hooke's law:

$$\sigma_{ij} = \sum_{kl} C_{ijkl} \epsilon_{kl} \tag{4.1}$$

where C_{ijkl} represents a fourth-rank elasticity tensor with the elastic constants obtained as follows:

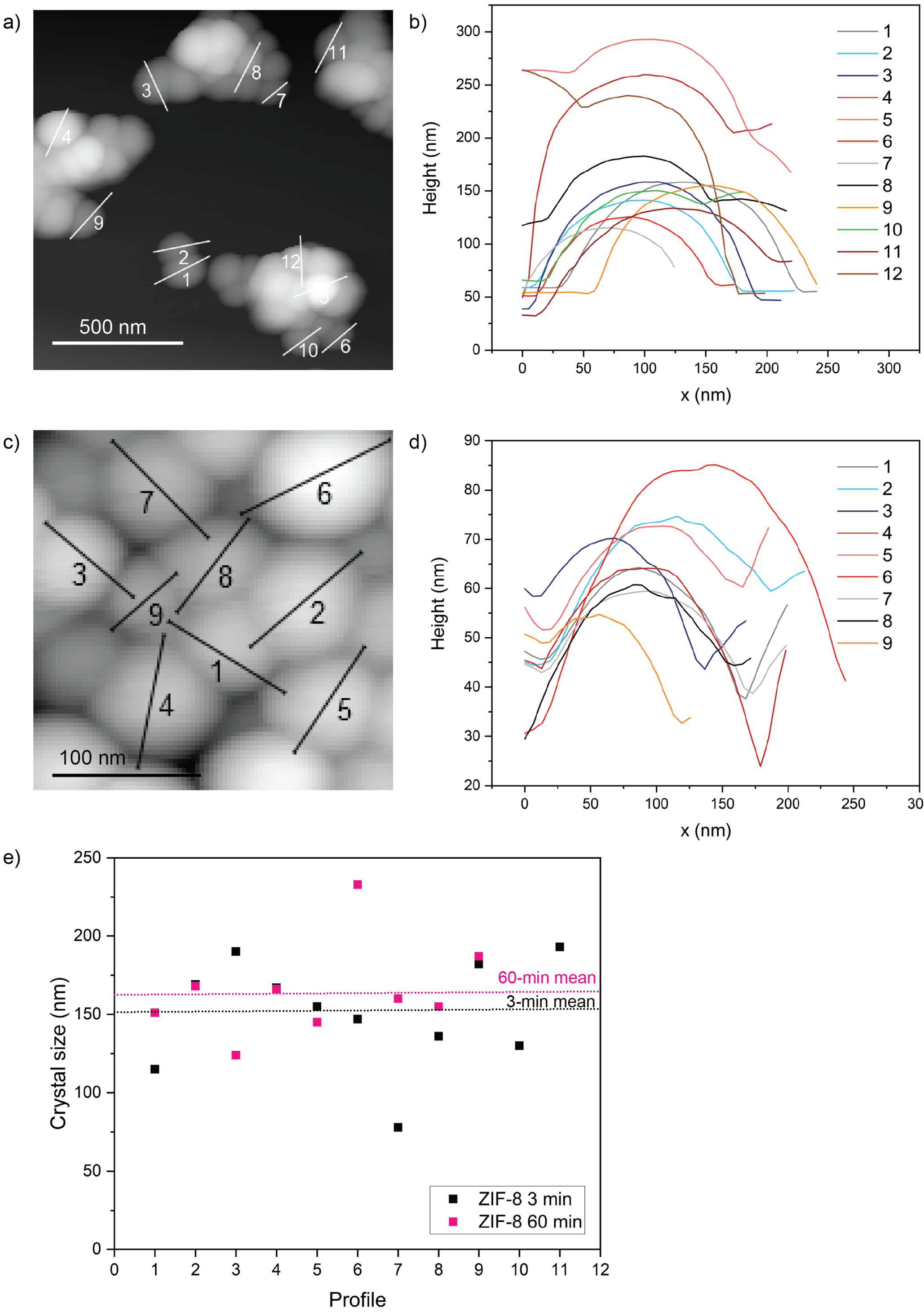

Figure 4.3: Size of ZIF-8 crystals with different growth time: a) AFM image of ZIF-8 nanocrystals with a 3-minute growth time. b) Corresponding height profiles. c) AFM image of ZIF-8 nanocrystals with 60-minute growth time. d) Corresponding height profiles. e) Crystal size (width) calculated from the x-values of each profile in b) and d).

a) 5 min

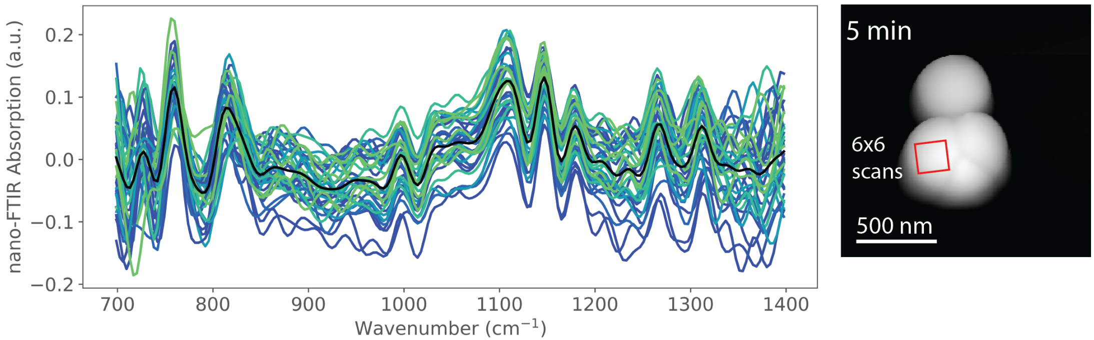

b) 60 min

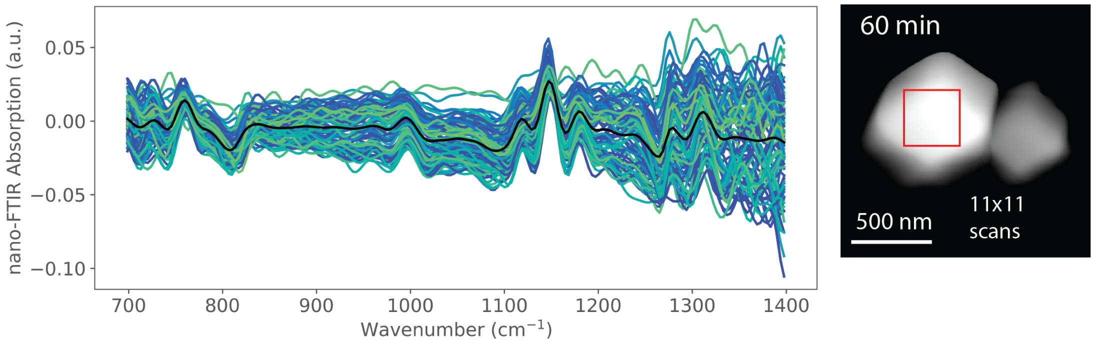

Figure 4.4: Spectral scanning of the ZIF-8 microcrystals with different growth times. a) AFM image of ZIF-8 crystals obtained after a growth time of 5 minutes, indicating the region, where nanoFTIR spectra were measured. 36 nanoFTIR spectra measured from each pixel of the scanned area. The black spectrum represents their average. b) AFM image of ZIF-8 crystals obtained after a growth time of 60 minutes, indicating the region, where nanoFTIR spectra were measured. 121 nanoFTIR spectra measured from each pixel of the scanned area. The black spectrum represents their average.

$$C_{ijkl} = \begin{pmatrix} 11.578 & 9.372 & 9.835 & 0 & 0 & 0 \\ 9.732 & 12.008 & 9.806 & 0 & 0 & 0 \\ 9.835 & 9.806 & 12.405 & 0 & 0 & 0 \\ 0 & 0 & 0 & 1.251 & 0 & 0 \\ 0 & 0 & 0 & 0 & 1.192 & 0 \\ 0 & 0 & 0 & 0 & 0 & 1.115 \end{pmatrix} GPa. \tag{4.2}$$

Here, the framework stiffness along each of the principal crystal axes under uniaxial strain is described by the diagonal coefficients C_{11} to C_{33}. The shear stiffness, or in other words the angular distortion against shear deformation, is represented by the other three diagonal coefficients C_{44}, C_{55} and C_{66}. The off-diagonal coefficients define the tensile-tensile coupling between any two orthonormal axes. In a cubic system, as all principal crystal axes are equal, only three coefficients describe the elastic stiffness because $C_{11} = C_{22} = C_{33}$, $C_{44} = C_{55} = C_{66}$, and all

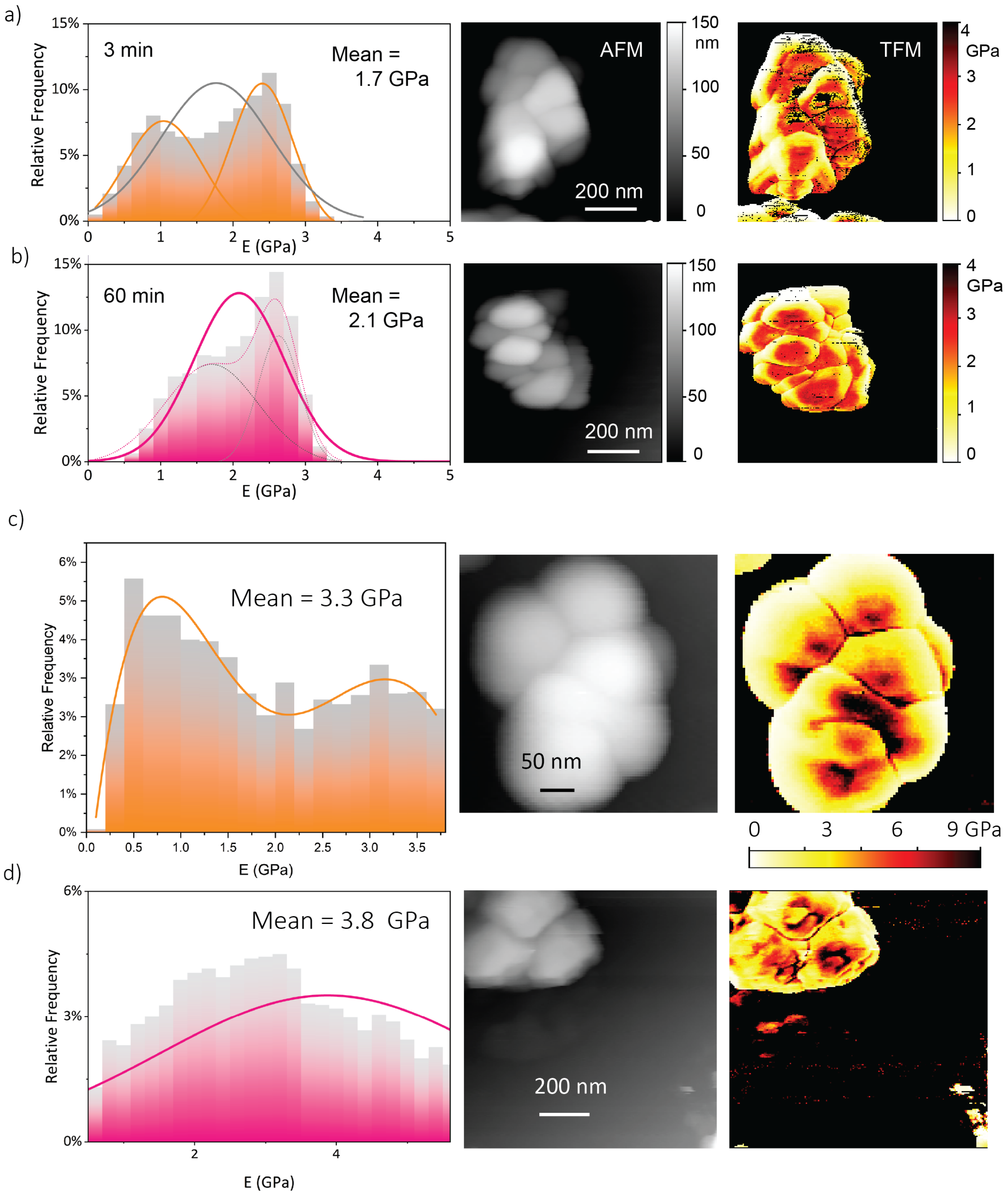

Figure 4.5: Tip Force Microscopy (TFM) on ZIF-8 nanocrystals with different growth times. a,c) Histogram and normal distribution of Young's modulus corresponding to data collected on the ZIF-8 nanocrystals with a 3-minute growth time, along with AFM images, and mapping of the Young's modulus, measured with TFM. b,d) Histogram and normal distribution of Young's modulus corresponding to data collected on the ZIF-8 nanocrystals with a 60-minute growth time, along with AFM images, and mapping of the Young's modulus, measured with TFM.

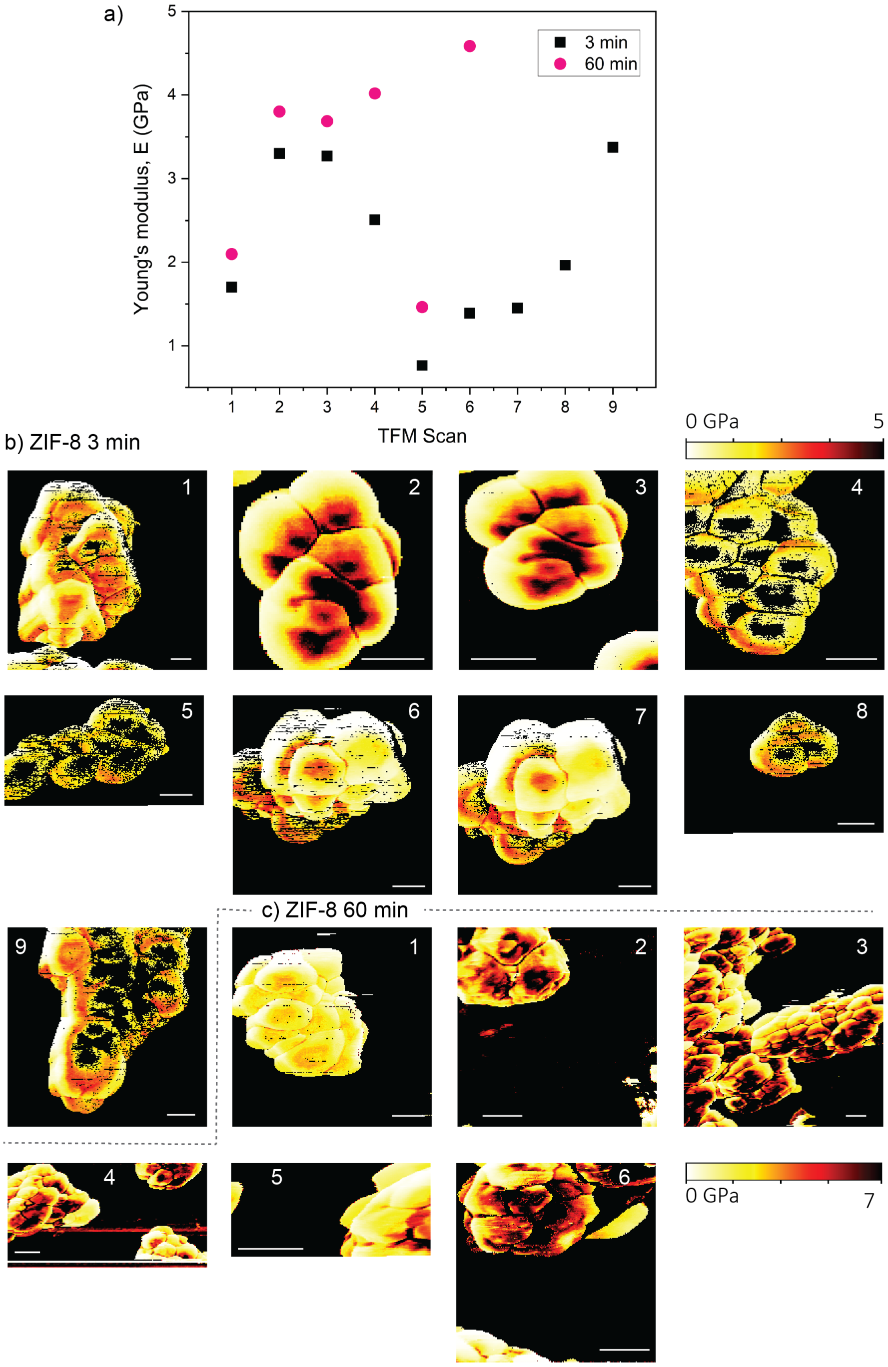

Figure 4.6: TFM on ZIF-8 nanocrystals. a) Mean Young's modulus *E* plotted for each TFM image. b) Young's modulus measured by TFM on ZIF-8 nanocrystals with a growth time of 3 minutes. c) Young's modulus measured by TFM on ZIF-8 nanocrystals with a growth time of 60 minutes.

non-zero off-diagonal coefficients are equal to C_{12}. Therefore, the pseudo-cubic values are averaged from equation 4.2 as follows:

$$C_{11} = 11.997,\ C_{44} = 1.186,\ C_{12} = 9.791. \tag{4.3}$$

Before discussing the mechanical properties, it is necessary to confirm stability of the modelled system by confirming the elastic stability conditions.

Elastic stability conditions:

$$\begin{cases} 1.\ C_{11} > 0 & C_{11} = 11.578, \text{ satisfied} \\ 2.\ C_{11}C_{22} > C_{12}^2 & 139.029 > 94.712, \text{ satisfied} \\ 3.\ C_{11}C_{22}C_{33} + 2C_{12}C_{13}C_{23} - & \\ -C_{11}C_{23}^2 - C_{22}C_{13}^2 - C_{33}C_{12}^2 > 0 & 152.084.0, \text{ satisfied} \\ 4.\ C_{44} > 0 & C_{44} = 1.251, \text{ satisfied} \\ 5.\ C_{55} > 0 & C_{55} = 1.192, \text{ satisfied} \\ 6.\ C_{66} > 0 & C_{66} = 1.115 \text{ satisfied} \\ 7.\ \text{All eigenvalues } \lambda_i \text{ are positive.} & \lambda_i = \{1.115, 1.192, 1.251, \\ & 2.0013, 2.4061, 31.584\}, \text{ satisfied.} \end{cases} \tag{4.4}$$

According to the analysis above, and because all eigenvalues are positive, the ZIF-8 structure satisfies the elastic stability criteria; it is thus mechanically stable from a theoretical standpoint.

We further simulated defective ZIF-8 by introducing point defects into the unit cell. Firstly, to consider missing zinc defects, one of the six metal atoms in the unit cell was removed and N-H bonds replaced two Zn-N bonds to create dangling linkers. Secondly, a system with a missing linker defect was created by replacing a ligand with an associating water and a hydroxide anion to fill the resulting unsaturated metal sites. As a result, the defective ZIF-8 system comprises 11 instead of 12 linker units in the unit cell. However, as DFT simulations are based on periodic boundary conditions, a regular repetition of the point defect in each unit cell is assumed, while in reality, their appearance is, most likely, random, and not expected in every unit cell.

For the defective systems, as they cannot be modelled as orthorhombic crystals anymore, simple stability conditions are difficult to determine. Because the obtained systems belong to the triclinic Laue's class, the positivity of all eigenvalues can be considered a sufficient condition for stability.

For the missing linker defect:

$$\lambda_i = \{0.891, 1.126, 1.395, 1.870, 2.730, 26.536\} > 0. \tag{4.5}$$

For the missing zinc defect:

$$\lambda_i = \{0.760, 0.829, 1.106, 1.871, 1.952, 20.433\} > 0. \tag{4.6}$$

According to the positive eigenvalues of the stiffness matrix, the two defective ZIF-8 structures are mechanically stable.

To attain a complete picture of the mechanical properties, tensorial analysis using the ELATE[156], EIAM[157], and Mathematica[158] software tools derived them based on the inversion of the elasticity tensor known as the compliance matrix S:

$$S_{ijkl} = {C_{ijkl}}^{-1}. \tag{4.7}$$

For instance, the Young's modulus E, e.g. the ratio of uniaxial stress over strain, can be obtained through

$$E(\mathbf{u}) = \frac{1}{u_i u_j u_k u_l S_{ijkl}}, \tag{4.8}$$

depending on the unit vector $\mathbf{u}$.

While an isotropic behaviour of the Young's modulus is observed for the defect-free crystal, modelled as an pseudo-cubic system, the defective structures lead to a stiffness that is directionally dependant. Interestingly, the higher anisotropy can be linked with the specific orientation of the defects (see Figure 4 c-e in the manuscript in 4.3): the material's stiffness is reduced where the periodic framework

Elastic properties	ZIF-8	defect-free	missing Zn	missing linker
Young's modulus, E (GPa)	E_{max}	3.49	3.48	3.97
	E_{min}	2.88	1.74	1.94
	$A_E = E_{max}/E_{min}$	1.21	2.00	2.04
Shear modulus, G (GPa)	G_{min}	1.03	0.75	0.84
	G_{max}	1.25	1.11	1.54
	$A_G = G_{max}/G_{min}$	1.22	1.48	1.83
Poisson's ratio, ν (-)	ν_{min}	0.37	0.25	0.19
	ν_{max}	0.53	0.61	0.80

Table 4.1: DFT-predicted mechanical properties of ZIF-8 and defective structures.

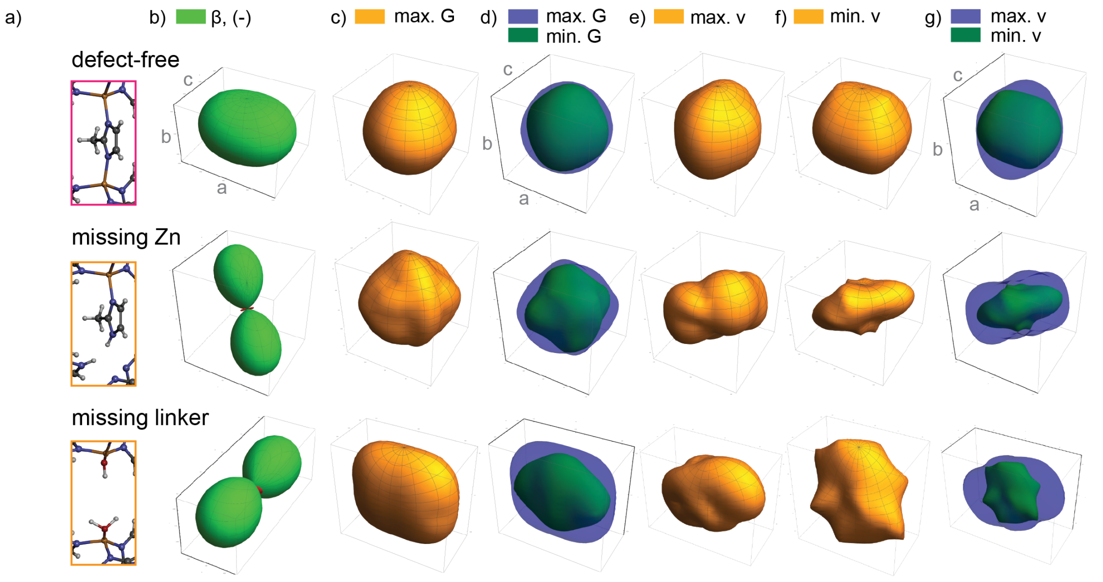

Figure 4.7: Graphical representation of the simulated mechanical properties of ZIF-8. a) Schematic of ZIF-8 and defective structures. b) Surface representation of the linear compressibility (β). c, d) Surface representation of the maximum and minimum shear moduli (G). e-g) Surface representation of the maximum and minimum Poisson's ratios (ν).

is disrupted by missing zinc atoms, as the resulting dangling linkers now twist under pressure. Missing linkers, in turn, create open metal sites, allowing the adsorption of water molecules with corresponding weak hydrogen bonds. These imperfections significantly affect the pore structure, thereby increasing the anisotropy in mechanical properties.

Similarly, the shear modulus G, which represents the framework rigidity against angular distortion imposed by external forces, and is derived as

Property	K_{VRH}	G_{VRH}	E_{VRH}	ν_{VRH}
defect-free	10.52	1.15	3.33	0.45
missing Zn	5.60	0.95	2.70	0.42
missing linker	7.01	1.18	3.36	0.42

Table 4.2: Isotropic Voigt–Reuss–Hill (VRH) averaged elastic properties, corresponding to the polycrystalline state. The bulk (K), Young's (E), and shear (G) moduli are in GPa and the Poisson's ratio (ν) is dimensionless.

$$G(\mathbf{u}, \mathbf{v}) = \frac{1}{u_i v_j u_k v_l S_{ijkl}}, \tag{4.9}$$

indicates strong directional relationships upon insertion of defects. Because the shear modulus depends on two unit vectors ($\mathbf{u}, \mathbf{v}$), the 3-D surface representation is limited to the maxima and minima in each direction (see Figure 4.7). The exceptionally low shear modulus that has been attributed to the intrinsic flexibility of ZIF-8, is reduced even further in the defective ZIF-8 structures.[159] Here, the vacancies introduce either dangling linkers or change the conformation of the pore as a whole, and thus allow for strong rotations and deformations upon external forces.

The same applies for the Poisson's ratio ν that relates the transversal strain to the axial strain under uniaxial deformation:

$$\nu(\mathbf{u}, \mathbf{v}) = \frac{u_i v_j u_k v_l S_{ijkl}}{u_i u_j u_k u_l S_{ijkl}}. \tag{4.10}$$

The Poisson's ratio remains positive and, in the case of missing zinc defects, exhibits a maximum when the framework is axially stretched along the direction of the intact bonds, because the metal vacancy disrupts the lattice dynamics and offers additional flexibility in transverse directions. If however the framework is stretched along the axis of the missing bond, the axial deformation is reduced while the rigidity is maintained in vertical directions, and thus, the Poisson's ratio is at a minimum. Similarly, the missing linker defects result in a minimum contraction when stretched along the diagonal direction of the deformed pore, since the intact bonds and newly formed hydrogen bonds lead to rigidity in the transverse direction.

Now, since the defects introduce changes at the atomic level that affect the conformation of the pore and the lattice itself, the Poisson's ratio is strongly directionally dependant. The complex 3-D behaviour is linked to the orientation of the defects, however, as the introduced vacancy is periodically repeated per unit cell, the model assumes a repeating pattern, whereas, in practice, a random distribution of defects is more likely. Therefore, the calculated mechanical responses reveal the structure-property relationships that depend on the atomistic arrangement of the defective structure but they are still based on an idealised long-range order of defects.

Even if the material's response to uniaxial deformation reveals extreme anisotropy, the Poisson's ratio remains between 0.2 and 0.8, and no auxetic behaviour is observed. Yet, when calculating the linear compressibility β following the equation

$$\beta(\mathbf{u}) = u_i u_j S_{ijkl}, \tag{4.11}$$

the defective systems expand in one direction upon hydrostatic pressure. This phenomenon can be attributed to the vacancies introducing additional flexibility in the otherwise relatively rigid framework, following a trend that has been observed in other defect-free materials with highly anisotropic mechanical properties.

We also calculate the theoretical infrared absorption spectra of ZIF-8 and the defective derivatives, which unambiguously confirm our experimental findings from near-field nanospectroscopy: the co-existence of missing linker and missing zinc defects at early stages of the growth process. In addition, missing linker defects seem to remain even after the ripening of the crystals (see Figure 4 in the manuscript). These linker vacancies create open metal sites, which are possible reaction sites for water adsorption, thus decreasing the hydrophobicity, and the long-term stability of the material. On the other hand, the same phenomenon could be leveraged for advanced reactivity in applications such as catalysis, gas adsorption, or chemical sensing, where tailored reaction sites are crucial for boosting the material's performance.

In summary, the multimodal near-field approach we presented here, encompassing novel nanoscale analytics in the field of MOF research, combined with DFT calculations, allows us to directly probe structural defects and their impact on the framework stability of an extended crystalline framework. This non-destructive approach that synergistically provides physical, chemical, and mechanical information at the nanoscale offers a deeper understanding of the fundamental mechanisms of crystal growth and defects. With its significant insights crucial for defect-tuning, this work could further pave the way to downstream applications involving the design of framework materials with enhanced abilities in targeted applications such as catalysis, sensing, or adsorption.

4.3 Defect engineering in metal-organic framework nanocrystals: implications for mechanical properties and performance

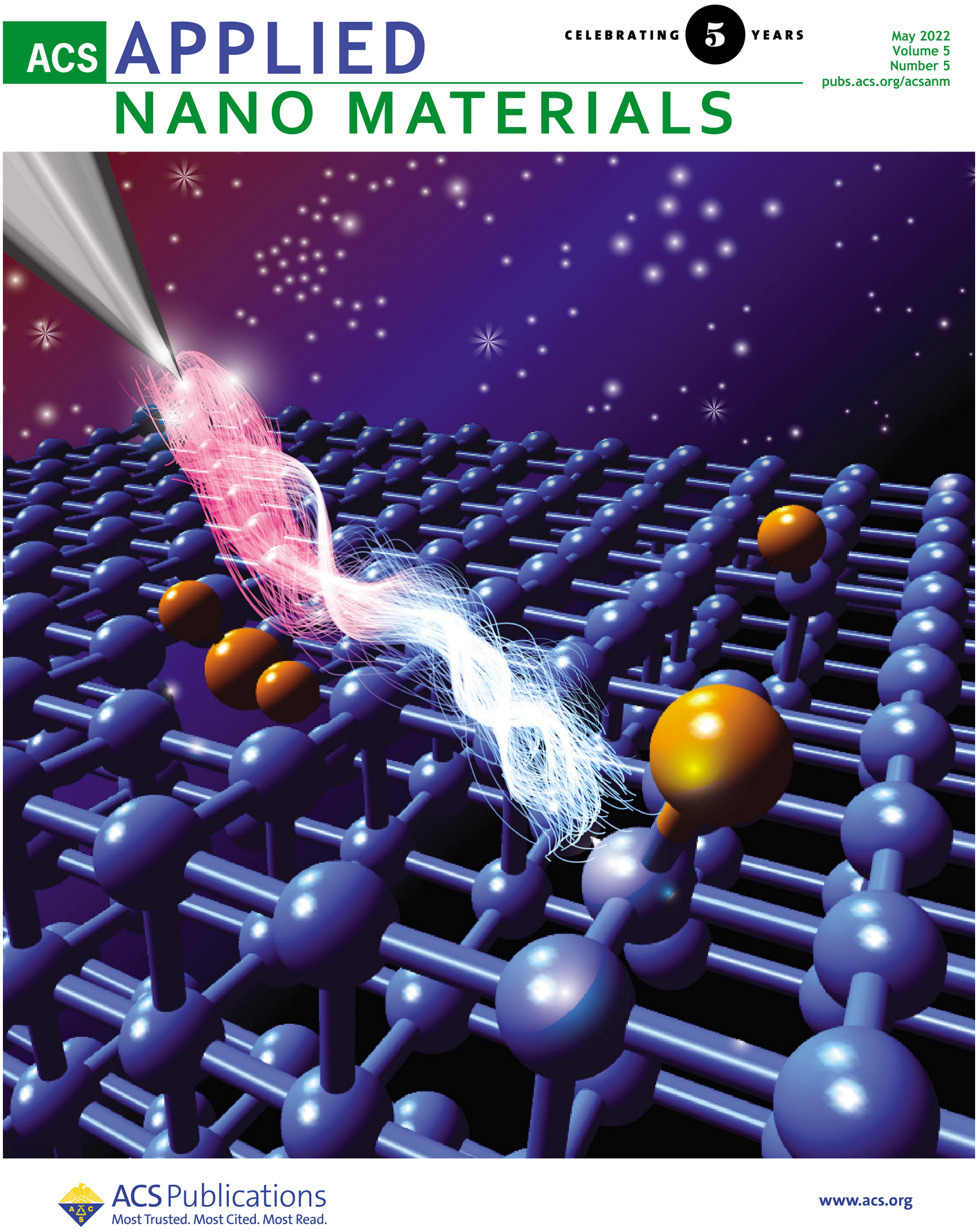

The supporting information for this manuscript can be found here: https://pubs.acs.org/doi/suppl/10.1021/acsanm.2c00493/suppl_file/an2c00493_si_001.pdf.

ACS APPLIED NANO MATERIALS

www.acsanm.org

Article

Defect Engineering in Metal–Organic Framework Nanocrystals: Implications for Mechanical Properties and Performance

Annika F. Möslein, Lorenzo Donà, Bartolomeo Civalleri, and Jin-Chong Tan*

Cite This: *ACS Appl. Nano Mater.* 2022, 5, 6398–6409

Read Online

ACCESS | Metrics & More | Article Recommendations | Supporting Information

ABSTRACT: The growth process of metal–organic framework (MOF) nanocrystals defines their properties and functions. However, defects may be prevalent during the crystallization of even seemingly perfect MOFs, such as zeolitic imidazolate framework-8 (ZIF-8), and yet direct probing of such structural defects has been challenging because of the lack of nanoscale techniques to locally examine individual nanocrystals. Here, we directly study local defects, such as missing linkers or metal vacancies, in ZIF-8 nano- and microcrystals with near-field IR nanospectroscopy combined with density functional theory calculations. We track the chemical changes during crystallization and show that structural defects like zinc cations that are bound to molecules of the reactant gradually disappear with ripening of the crystals, while dangling and missing linker defects prevail. The resulting defect-terminating groups or open-metal sites produce mechanical anisotropy and reduce the Young's modulus, as measured via tip force microscopy with nanoscale resolution and supported by theoretical modeling. However, these structural defects also open the door for defect engineering to tune the performance of ZIF-8 by offering additional adsorption sites for targeted catalytic reactions, chemical sensing, or gas capture.

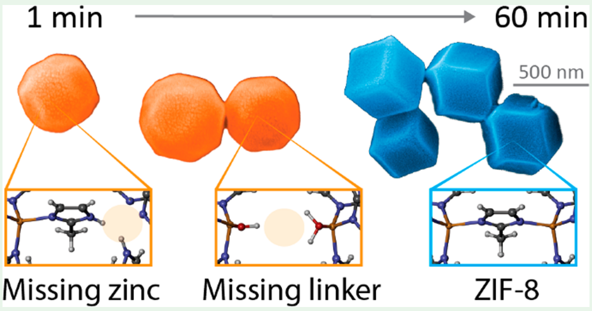

KEYWORDS: *metal–organic frameworks, crystal growth, defects, near-field IR spectroscopy, density functional theory, mechanical properties*

INTRODUCTION

At the nanoscale, metal–organic framework (MOF) crystals feature miscellaneous shapes and sizes. Their diversity gives rise to their vast physical and chemical properties, paving the way for applications in sensing technologies, drug delivery, gas capture, or catalysis, among others.[1−5] This multifunctionality emerges not simply because MOFs are *per se* hybrid materials, built from metal clusters and organic linkers with a boundless number of possible combinations, but mostly because of their exceptional porosity and chemical tunability, which affords the adsorption, encapsulation, or release of versatile guest molecules.[6,7] The power of engineering MOF nanocrystals for application is, therefore, ascribed solely to meticulous control of the framework properties and its interactions, which essentially originates in the material synthesis.[7] For instance, the zeolitic imidazole framework ZIF-8, one of the most well-studied frameworks because of its stability and ease of synthesis, is obtained by combining zinc nitrate hexahydrate [$Zn(NO_3)_2 \cdot 6H_2O$] and 2-methylimidazole (mIm) ligands.[8] The material with a sodalite cage topology is then formed by molecular self-assembly, a process where the basic building blocks—metal and linker—aggregate spontaneously to form a highly ordered extended 3D structure: the crystalline framework. While the ZIF-8 crystals may materialize as nano- or microcrystals exhibiting rounded or faceted shapes, the development of size- and shape-controlling syntheses, in turn, benefits considerably from a detailed understanding of the crystallization process.

In particular, the formation of ZIF-8 crystals, or MOF crystals in general, can be divided into nucleation and growth (Figure 1).[9] Because the nucleation is driven by random fluctuations in the bulk solution without dedicated nucleation sites, little can be done to tailor this mechanism. The crystal growth, on the contrary, can be manipulated by changing the molar ratio of reactants, amount of solvent, and other stimuli to yield crystals with the desired sizes and shapes. Indeed, several studies have scrutinized the impact of the growth time, temperature, or use of different modulators on the formation of ZIF-8 nanocrystals by employing techniques such as atomic force microscopy (AFM) or scanning electron microscopy (SEM) combined with diffraction or adsorption–desorption analysis to capture the size distribution, shape, and crystallinity of the crystals.[10−15]

Received: February 2, 2022
Accepted: February 27, 2022
Published: March 8, 2022

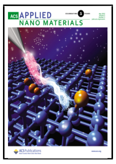

https://doi.org/10.1021/acsanm.2c00493
ACS Appl. Nano Mater. 2022, 5, 6398–6409

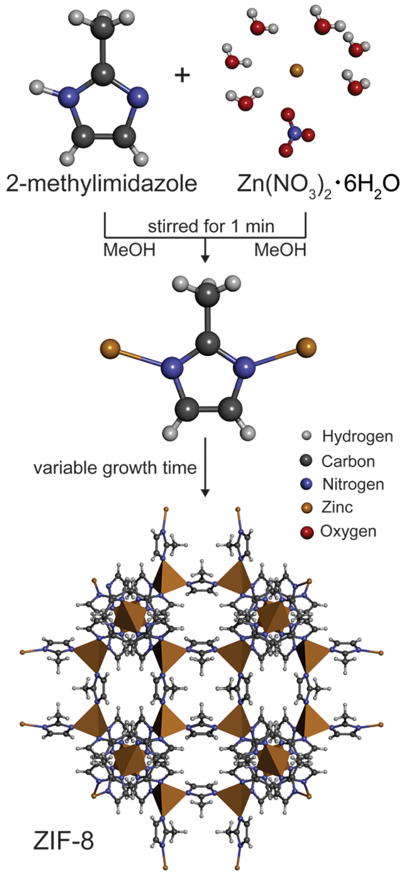

Figure 1. Schematic of the synthesis route of ZIF-8.

Yet, if seen in the context of controlling the material properties, another factor plays a crucial role in crystalline nanomaterials: the presence of defects.[16] Defect engineering opens pathways to locally tune the intrinsic porosity, create open metal sites, and modulate the surface properties of MOFs, which has significant implications for separation, gas capture, catalysis, and mechanical responses.[17−25] Perhaps the model system for defective MOFs is UiO-66 (Universitetet i Oslo); here, nanoregions of ordered defects had been reported, which inspired detailed studies on the defects and their effects on the material.[19,26−29] For instance, structural defects in UiO-66 were observed using a combination of low-dose transmission electron microscopy (TEM) and electron crystallography, further confirming the increased catalytic activity for defective structures.[30]

Little is known, in contrast, about defects in ZIF-8; this may be partly because this material is considered to be among the most stable frameworks, but while this is true, it is, in fact, very plausible that defects or other irregularities may occur during the crystal growth process, possibly with a significant impact on the performance of the materials, and its subsequent long-term stability.[31] Hitherto, only the feasibility of local defects in ZIF-8, such as linker and metal vacancies or dangling linkers, has been predicted by computational modeling.[32,33] However, despite that fact that a few other studies have focused on the implications of defects in gas separation[34] and storage[35] or found surface-terminating defects,[36] many open questions remain. One might ask, do defects occur and transform during crystallization of ZIF-8? Also, to what extent do the defects affect the properties and, as such, the performance of the material for potential applications including gas capture, chemical sensing, and catalysis?

To answer these questions, we employ scattering-type scanning near-field optical microscopy (s-SNOM), merging AFM with IR spectroscopy to enable near-field IR nanospectroscopy. It is this combination that can unravel the fine-scale features, mechanisms, and chemical interactions of MOFs at the nanoscale by yielding a Fourier transform infrared (FTIR) spectrum of a local 20 nm spot.[37−41] Previously, we demonstrated the capability of this technique to probe individual MOF-type nanocrystals, such as ZIF-8, opening the door for discovering their previously unreported characteristics from a new perspective: at the single-crystal level.[39] Compared with conventional techniques, this nondestructive approach allows not only direct imaging but also simultaneous measurement of the sample's properties including chemical information or physical properties at a resolution akin to AFM.[40] For instance, the mechanical properties can be obtained with the same setup, albeit operated in contact mode instead of tapping mode. In these tip force microscopy (TFM) measurements, a force−distance curve is attained from every pixel of the AFM scan by retracting the AFM tip, measuring the required force to do so. The local stiffness is then determined from the force difference between the maximum force and the reference trigger point on the curve.[42] From the measured stiffness data of a sample surface, an image of the Young's modulus map can be derived. By simultaneous measurement of the shape, size, chemical composition, and mechanical properties at the nanoscale, using a suite of multimodal near-field techniques—s-SNOM, nanoFTIR, AFM, and TFM—allows us to shine new light on the growth process of the ZIF-8 nanocrystals.

In this study, we explore how defects transform during crystallization of ZIF-8, further elucidating their impact on the mechanical properties of the material. First, we study ZIF-8 nanocrystals before turning to microcrystals, obtained through two different synthesis routes. To examine the intermediate steps of the crystallization, the crystal growth was stopped after 1, 3, and 60 min by removing some material from the same batch and performing three washing steps. The experimental evidence was corroborated by *ab initio* density functional theory (DFT) calculations through a comparison between ZIF-8 ideal and defective model structures.

■ RESULTS AND DISCUSSION

Inhomogeneity after a Short Growth Time. After 1 min of growth time, the sample is dominated by inhomogeneous regions, although small, rounded shapes are already observable at the nanoscale (Figure 2). Local probing of these nanoscopic morphologies reveals their spectral resemblance with the metal source, as confirmed by the presence of the characteristic vibrational peaks of $Zn(NO_3)_2 \cdot 6H_2O$ at 824, 1042, 1128, and 1315 cm^{-1} in the nanoFTIR spectrum (Figure 2a,b). In contrast, the planate areas of the sample exhibit spectral features of the mIm linkers, such as the distinctive vibrational band at 745 cm^{-1} (Figure 2a,c). Of course, it is the brief crystallization period and the lack of successfully formed nuclei and subsequent Ostwald ripening[43] that explain these distinct regions, where either the uncoordinated linker or the metal reactant dominates without evolved interactions between them. Only a closer examination reveals local variations, as illustrated in the optical amplitude and phase images, which qualitatively contrast materials with different optical properties

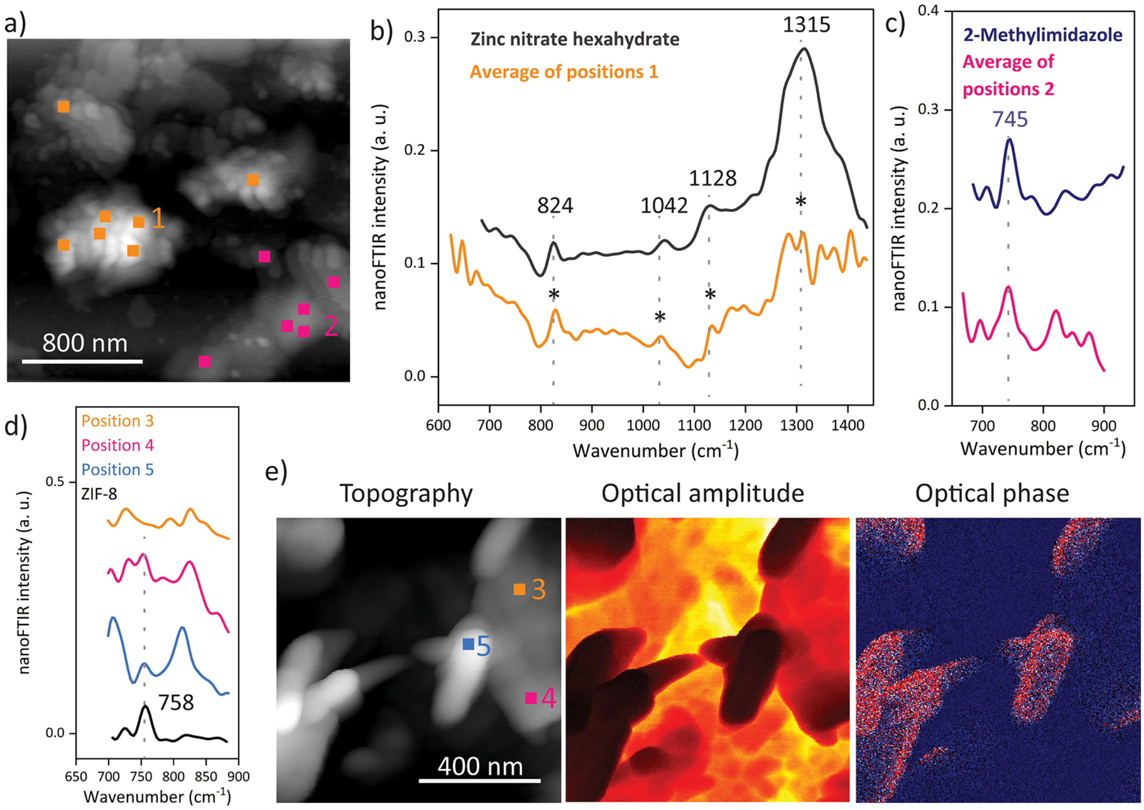

Figure 2. Near-field IR spectroscopy of ZIF-8 with 1 min growth time. (a) The AFM image indicates the positions where the local nanoFTIR spectra (b and c) are measured, which resemble the spectra of the reactants. The curves are shifted in the *y* direction for a better comparison, and the spectra measured on the nanocrystals show a higher noise level than that of the nanocrystals obtained from larger quantities of reactants. The emergence of a characteristic ZIF-8 peak (d) is already observable by local probing at the positions shown in the AFM image (e), and local variations are further revealed in the optical amplitude and optical phase images (e).

(Figure 2d,e). Interestingly, the nanoFTIR spectra measured at different local spots with 20 nm resolution show contributions from both materials, even displaying the emergence of the characteristic peak of ZIF-8 at 758 cm^{-1}, assigned to an out-of-plane ring mode of the framework (Figure 2d). This finding confirms not merely the growing chemical interactions and bond formations but provides a snapshot of the assembly stage of the framework itself, which, at least partially, is beginning to crystallize within the first minute. Nonetheless, the large amount of uncoordinated linker and metal salt may indicate which defects could materialize during further crystallization.

Defects Gradually Disappearing with Prolonged Crystallization. After a growth time of only 3 min, the ZIF-8 nanocrystals have already formed, as confirmed by comparing their X-ray diffraction (XRD) pattern and attenuated-total-reflectance (ATR)-FTIR spectra with those measured on crystals after a growth time of 60 min (Figure 3a,b). In particular, the Bragg peaks from XRD are fully resolved, matching the reported characteristic peaks at 2θ values of 7.3, 10.3, 12.6, 16.4, and 17° and thus clearly revealing the crystallinity for the nanocrystals attained after 3 min (Figure S1).[8] Here, the high intensity of the (110) peak at 7.3° is attributed to the formation of ZIF-8 with a regular rhombic dodecahedron morphology, which resembles the final stage of the growth of ZIF-8 crystals.[14] Small variations, however, can be detected, such as the absence of the (125) peak at 28°, or a changing relative intensity of the (110):(211) planes, corresponding to the two most intense diffraction peaks. Albeit minimal, a rise in the intensity of the (110) plane, accompanied by a narrowing of the full width at half-maximum (fwhm) from 0.299 to 0.288, is observed upon prolonged crystallization (Figure S2). Either this can be attributed to the particle size effects via the Debye-Scherer equation or, given that the increase in the average size is minimal (Figure S3), this may indicate a stronger long-range ordering, thus implying a higher crystallinity.[44] At first glance, these findings are in good agreement with the previously reported result, where the crystallinity increased with the synthesis duration due to the Ostwald ripening process.[13−15] It has been suggested that 5 min was insufficient to grow ZIF-8 crystals,[13] but here, paradoxically, it is the marginal increase of the crystallinity, and the ATR-FTIR spectrum of the crystals with 3 min growth time, which matches that of the final growth stage, that indicate the completion of the self-assembly of ZIF-8 nanocrystals after only 3 min.[13−15]

Although these bulk measurements, in combination with the close topological resemblance of the shape and size, suggest the growth of ZIF-8 nanocrystals after a relatively short crystallization time, near-field IR spectroscopy reveals that, in fact, these crystals are far from being defect-free. For instance, the average of several local nanoFTIR spectra measured on individual crystals exposes the strong contribution of Zn(NO_3)$_2$·6H_2O, with its characteristic peaks around 824 and 1042 cm^{-1} associated with the stretching modes of the NO_3^- anions (Figure 3d,g).[45] As opposed to ATR-FTIR, where the spectra are obtained from an average of the bulk polycrystalline material, the nanoFTIR spectrum is measured locally with a probing depth of only a few nanometers, or tens of unit cells.

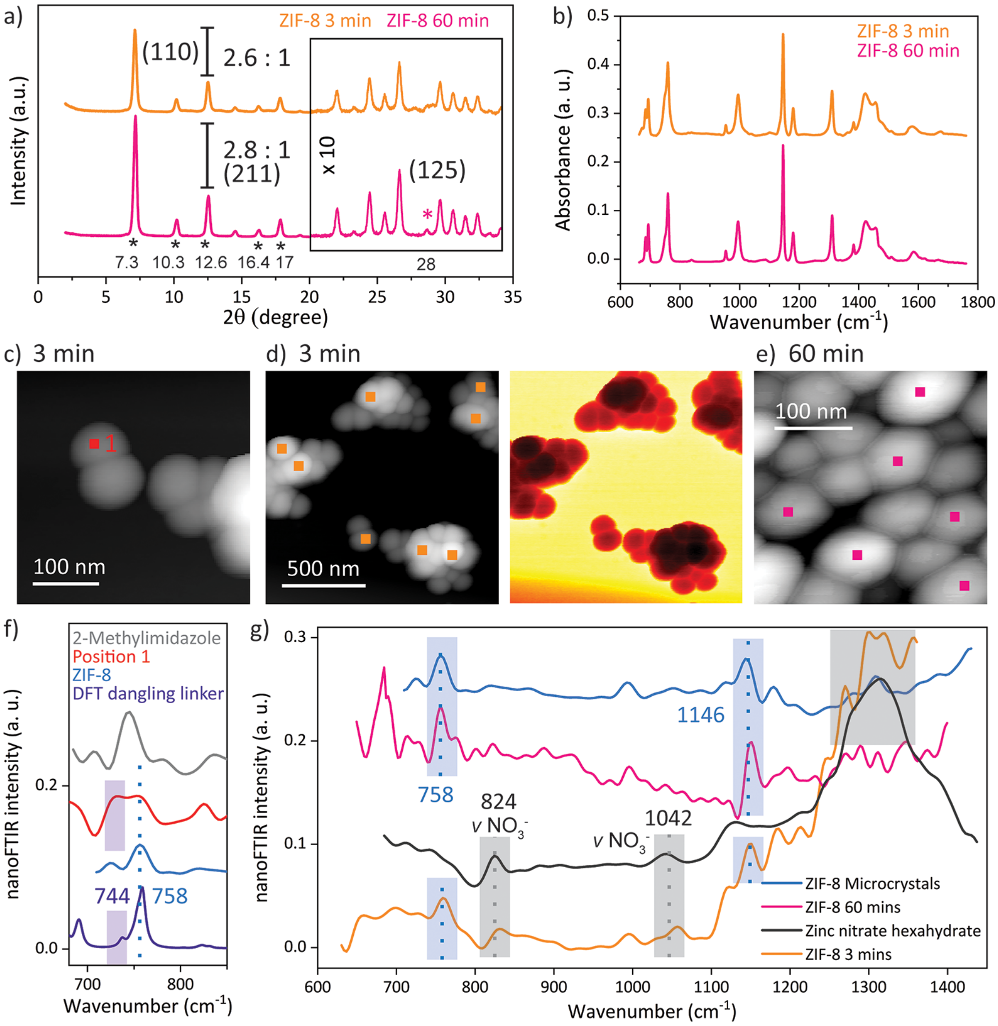

Figure 3. Comparison between the ZIF-8 nanocrystals obtained after 3 and 60 min: (a) The XRD pattern confirms the crystallinity of the sample obtained after 3 min. (b) The ATR-FTIR spectra reveal that ZIF-8 crystals are formed after 3 min. (c and d) The topography and optical amplitude of the nanocrystals were imaged after 3 min of growth time with s-SNOM. (e) The AFM image of the final growth stage of the ZIF-8 crystals is given. (f) The nanoFTIR spectra of a 20 nm spot, as indicated in the AFM image (c), compared with the spectrum of the linker, ZIF-8, and a simulated FTIR spectrum of ZIF-8 with a dangling linker defect are given. (g) The average of several local spectra (positions illustrated in parts d and e) reveal local variations, which vanish with prolonged crystallization.

Therefore, the presence of vibrational modes associated with the metal reactant indicates local variations close to the surface of the framework, such as different termination groups or undercoordinated metal clusters. One reason for the predominant appearance of these modes in the vibrational spectrum averaged over several positions could stem from the recurring defect of missing linkers, where nitrate molecules are instead coordinated to the zinc cations. The defect of missing linkers accordingly leads to a strong contribution of metal clusters or, in other words, zinc-rich regions that can emerge on the outermost surface of ZIF-8.[36,46] Creating open metal sites through defects can be leveraged as a strategy to enhance the reactivity of framework materials, whether it is in catalytic applications or gas adsorption. Here, the undercoordinated zinc ions close to the crystal surface present additional reaction sites. Zhang et al. hypothesized that such defects could be responsible for higher adsorption energy with water for ZIF-8, and our chemical characterization can finally provide the so-far-lacking experimental proof to explain these previous findings.[47] Precisely this feature, however, may alleviate the long-term stability of the material by deteriorating its hydrophobicity.[34]

Turning even more locally, individual point spectra show the superposition of peaks assigned to ZIF-8 (758 cm^{-1}) and the mIm linkers (745 cm^{-1}), further uncovering local defects associated with the linker, such as a partially coordinated linker or a dangling linker, as the termination units close to the crystal surface (Figure 3c,f). This is confirmed by DFT calculations using the *CRYSTAL* code.[48] A defective ZIF-8 crystal was modeled, where a metal vacancy introduced dangling linker groups. While both point defects and extended defects are likely to exist in zeolites, up to now, the latter has not been identified in the sodalite-type framework topology that is characteristic for ZIF-8.[33,49] Therefore, we concentrate solely on point defects, even though these local techniques might probe a combination of various types of defects. In the simulated FTIR spectrum, an additional peak appears at 744 cm^{-1}, which is assigned to the vibrational modes of the dangling linker. Of course, such irregularities close to the external surface of the crystallites are to be expected when

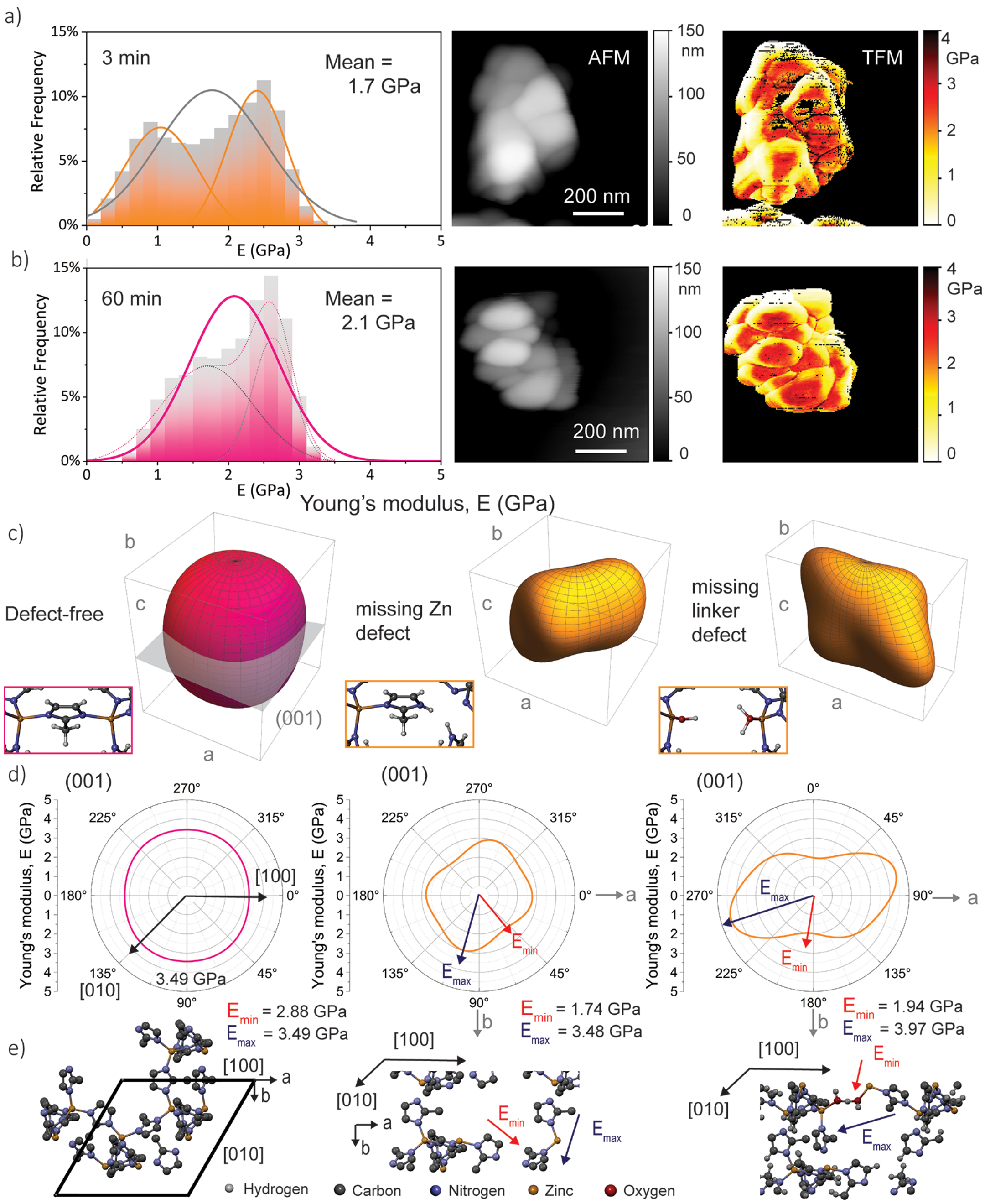

Figure 4. TFM on the ZIF-8 nanocrystals with different growth times (top, 3 min; bottom, 60 min). (a and b) Histogram and normal distribution of the Young's modulus corresponding to data collected on the nanocrystals on each pixel, along with AFM images, and mapping of the Young's modulus, measured with a tip force. (c) Young's modulus representation surface in 3D spherical coordinates, along with schematics of ZIF-8 and defective structures. (d) Polar plots projected onto the (001) planes. (e) Schematics of the structure−property relationships, indicating the orientations of the maximum and minimum Young's moduli.

materials on the nanoscale are examined. However, none of these structural defects are observed in the nanoFTIR spectrum of the nanocrystals with a growth time of 60 min. Instead, the local measurements resemble the average spectrum and reveal neither local variations nor individual contributions of the reactants (Figures 3g and S4). This leads to the conclusion that structural defects, such as the different crystal lattice terminations, are gradually disappearing with prolonged crystallization.

Mechanical Property Evolution with Vanishing Defects. Of course, the different termination units, the undercoordinated metal, and the dangling linker all invite the question of how and to what extent they might influence the properties of the nanocrystals, which are so intrinsically linked with the framework assemblage, arrangements of the functional groups, and characteristics of the pore. Even if only slightly, defects may affect the material's stability by disrupting the crystalline order of the framework material, but whether the relationship between the defects and their impact on the material performance can be precisely established remains to be studied. Because of the lack of other experimental techniques to probe the mechanical properties of individual nanocrystals, this is best done with TFM, where the Young's modulus E (i.e., ratio of the uniaxial stress over the strain in the elastic regime) is measured at every pixel of the scan, while simultaneously imaging the topography at nanoscale resolution. In that way, the local stiffness of the sample under investigation is acquired with a resolution akin to AFM imaging (Figure 4).[42] It is worth mentioning that the artifacts in the measurements (e.g., black lines) have been filtered out before the mean stiffness of the nanocrystals is derived (Figure 4a,b). The stiffness has a generally higher variance than that previously measured for ZIF-8 with conventional techniques, whether it is with indentation or AFM nanoindentation, an observation that can be attributed to the effect of edges. Here, establishing contact between the AFM tip and the sample is challenging, which leads to weaker interactions and thus lower stiffness, accordingly reducing the mean stiffness. Another drawback of such a local surface technique is that, in order to generate 3D Young's moduli from the experimental data, probing the sample from all angles would be required, which is unfeasible for individual nanocrystals like those prepared for AFM-based measurements. Yet, at such small scales—as measured with TFM—the obtained stiffness reflects the local mechanical response of individual nanocrystals.[50] Given the same calibration, these TFM measurements can thus be employed for a comparison between different materials. For ZIF-8 crystals with a growth time of 3 min, the Young's modulus is attained from one scan with a mean and standard deviation value of $E(3\text{ min}) = 1.7 \pm 0.7$ GPa (or between 0.8 and 3.4 GPa considering nine different scans), which is lower compared with the stiffness of the crystals at the final growth stage when it was determined that $E(60\text{ min}) = 2.1 \pm 0.5$ GPa (or 1.4−4.6 GPa for six scans; Figure S7). Likewise, the crystals with short crystallization unveil more variance in the local Young's moduli, even revealing a bimodal distribution (Figures 4a and S6). A simple way of putting this is to say that higher crystallinity, and thus stiffness, is achieved with prolonged crystallization, but there is more to it than that, especially because the increase in crystallinity is marginal, as discussed earlier. An alternative explanation might be to suggest that the observed structural defects, whether they are different termination units, uncoordinated metal clusters, or dangling linkers, introduce local disturbance to the otherwise periodic bulk structure and thus disrupt the stability of the framework as a whole; in other words, one might describe them as local disorder with a far-reaching impact. This applies particularly to the mechanical properties due to their dependencies upon the long-range order of the crystal. The observed phenomenon that the local structural stiffness of the framework, or the mechanical stability of crystal in general, is lowered with increasing defect level coincides with previously reported simulations, where the elastic constants were calculated for defective UiO-66 crystals; however, the assumption that defects in ZIF structures lead to different mechanical properties demands further proof.[51]

Hence, we performed DFT calculations with the *CRYSTAL17* code[48] to compute the elastic tensors C_{ij} for three different structures of ZIF-8: first, the ideal defect-free crystal was simulated using the PBEsol0-3c method.[52] Derived from this ideal unit cell, the missing zinc defect was introduced as a zinc vacancy and by the replacement of two N−Zn bonds with N−H bonds, thereby creating dangling or undercoordinated linkers. The third system, which, in turn, simulates the missing linker defect, was attained by removing a linker group, while an associating water and the conjugate base of the proton-donating group filled the two unsaturated metal sites. Visualizing the elastic representation surfaces (Figure 4c) and the associated mechanical properties derived from the C_{ij} tensors (Tables S2 and S3 and Figures S8−S11) reveals the differences in the mechanical properties due to defects, corroborating the trends derived from the experimental findings. As shown in Figure 4c,d, the Young's modulus of the defect-free crystal is highly isotropic, consistent with previous studies on the elastic constants of a ZIF-8 single crystal.[53,54] On the contrary, with the introduction of a missing zinc defect, an anisotropic behavior is revealed. The anisotropic mechanical response of ZIF-8 has previously been investigated, e.g., as a function of the pressure,[54] but in this work, we focus on the impact of point defects on the mechanical properties.

In the case of missing zinc defects, although the maximum stiffness in the direction of the stable, undisturbed zinc bonds is akin to that of the perfect crystal, the minimum Young's modulus is significantly smaller (Figure 4e). If forces are applied in the direction of the longest pore width, the dangling linker groups can now rotate or twist because of the missing zinc defect, which decreases the framework stiffness accordingly. Similarly, the effect of increased anisotropy due to defects can be noticed in the model of the missing linker; in fact, it is this system where it becomes most evident. Here, a bond between the associated water and conjugate base is formed to yield a mechanically stable system. This, however, changes the conformation of the pore significantly: in the direction of this additional bond, the framework stiffness is increased because of the shorter bond lengths and associated pore conformation. As a consequence, the maximum Young's modulus is even larger than that in the defect-free case. Yet, in the vertical direction, these weak hydrogen bonds are easily disrupted under compressive or tensile forces, leading to a much larger pore than that in the defect-free crystal, which describes the decrease in the minimum Young's modulus.

The theoretical results above can explain the observed characteristics of the local stiffness measured with TFM: the average stiffness and, as such, the material's stability are generally reduced in the defective structures. If inverted, the effect is that the structural flexibility, adsorption, or other anisotropic responses to external stimuli can be enhanced in an otherwise "rigid" MOF (greater stiffness) by introducing structural defects.[51] On the question of anisotropy, it is worth mentioning that anisotropy is linked to the distribution of defects along given directions. The calculations assume a periodic occurrence of the introduced defects, while, in reality, the number of defects and their orientation is, most likely, random. Yet, even if only one defective site is modeled per unit cell to preserve a mechanically stable system, the defect is replicated throughout the entire crystalline structure because of periodic boundary conditions. Therefore, the DFT models translate to the single-crystal level when the elastic constants are computed, enabling us to make the link to experiments. However, although the simulations predict the mechanical properties of the defective ZIF-8 systems under investigation and the local measurements confirm the corresponding decrease and anisotropy in stiffness, it remains challenging to distinguish between the type or location of defects from these nanoscale measurement techniques.

Defect Transformation in Microcrystals. Additional observations are made by tracking the changes in key

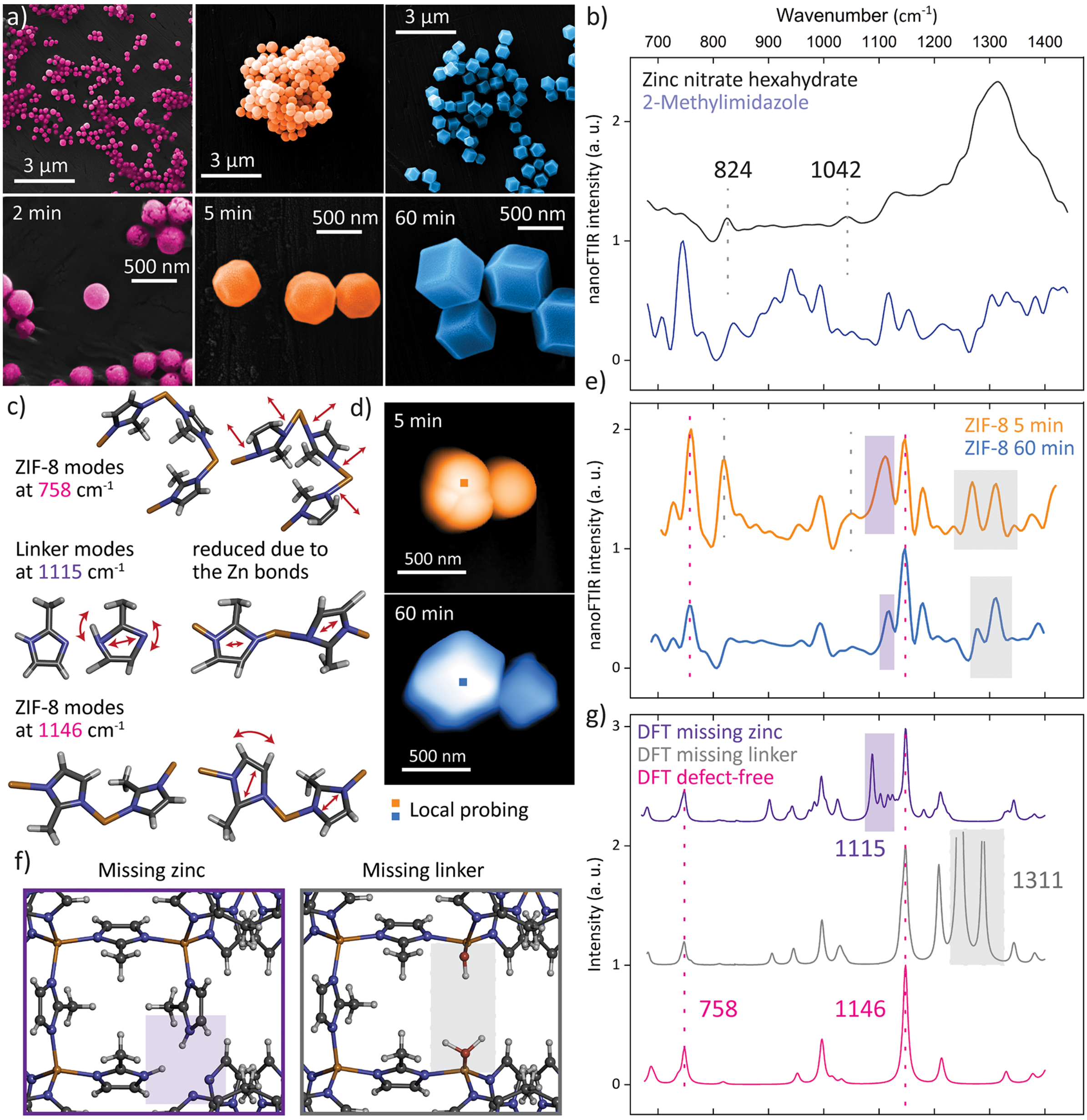

Figure 5. Transformation of ZIF-8 microcrystals. (a) SEM imaging of ZIF-8 crystals with different growth times. (b) nanoFTIR spectra of the reactants. (c) Schematic representations of key vibrational modes. (d) AFM images of ZIF-8 crystals obtained after 5 and 60 min, indicating crystals selected for local probing. (e) Corresponding local nanoFTIR spectra obtained from the averaging of 20 point spectra on the crystal. (f) Schematic representations of the simulated defects. (g) Corresponding simulated FTIR spectra compared with a perfect ZIF-8 crystal.

vibrational bands during the crystallization of ZIF-8 microcrystals, which further reveals how defects transform. As shown in the SEM images in Figure 5a, the crystal shape evidently changes from the round morphology obtained after 2 min of growth time to exhibition of the first facets after 5 min, eventually reaching the rhombic dodecahedron shape at the final growth stage after 60 min. This is accompanied by a gradual increase in the averaged crystal size from 200 to 500 nm. A comparison of the two nanoFTIR spectra, averaged for the 5 and 60 min growth times, with the DFT calculations depicts a close resemblance of the samples yet unravelling several salient changes in the peak positions and intensities (Figure 5d,e,g; see Figure S5 for a complete scan of the crystals). First, the nanoFTIR spectrum corresponding to the longer growth process shows a better match with the calculated spectrum of an idealized, periodic crystal because, with prolonged crystallization, the number of ideal bonds increases, and thus the positions and intensities resemble the calculated IR spectrum. Second, a detailed study of the individual vibrations, considering the DFT calculations as well as the nanoFTIR spectra of the reactants before synthesis, gives insights into both the structural and chemical changes happening during crystallization of the 3D framework. The pronounced peak at 758 cm^{-1}, for instance, correlates with the symmetric out-of-plane bending of the mIm ring and associated motions of the H−C═C−H bond present in the framework structure (Figure 5c). Conversely, the peak at 824 cm^{-1} is related to the vibrations of the metal salt [$Zn(NO_3)_2 \cdot 6H_2O$], which is not expected to appear after the construction of ZIF-8, where both reactants are used up entirely to form ZIF-8 crystals. However, because the vibrational mode associated with the NO_3^- stretching is still present in the nanoFTIR spectrum, the crystals formed after only 5 min still contain residuals of excess reactants, thus suggesting that some metal clusters are not fully coordinated with the mIm linkers.

Given that extensive washing steps have been performed for all samples, one can conclude that the metal cations are, albeit poorly coordinated, bound to the framework. There is some doubt where the metal clusters could precisely be located, but the strong appearance of the vibrational mode, in fact, indicates a repeating pattern of this defect close to the crystal surface; most likely, it is the defect-terminating zinc clusters with missing linkers that could further explain why the crystals, rather than resembling the stable rhombic dodecahedron shape, only slightly imply facets after a 5 min growth time. In comparison with the characteristic peak of ZIF-8 at 758 cm^{-1}, the vibrational mode associated with the metal reactant at 824 cm^{-1} depicts a reduced relative intensity from 0.74:1 to 0.48:1 with a longer crystallization time, a finding that already contains, in essence, everything that has been observed for the nanocrystals. With prolonged growth time, the defects of ill-terminating metal clusters that are bound to molecules of the reactant gradually disappear. The same phenomenon is revealed in the reduction of the less pronounced peak at 1042 cm^{-1}; likewise, this peak simultaneously vanishes as the complete framework is assembled (Figure 5b,e).

So far, the emphasis fell on the defects attributed to the undercoordinated metal clusters; however, it is further evident that the defect of the dangling linker (or missing zinc) can be detected at such local scales. In particular, the vibrational mode at 1115 cm^{-1}, a peak associated with asymmetric in-plane ring stretching of the uncoordinated linker C−N−H bonds, is strongly present in the early stage of the crystal growth process. Interestingly, these modes appear in the simulated spectrum of a defective ZIF-8 crystal, where dangling linkers have been introduced by virtue of a metal vacancy. Meanwhile, in the final stage of crystal growth, this mode has reduced in intensity because the N−H bonds in the linker are replaced by the stable N−Zn bonds suppressing this vibration (Figure 5c).

Thus, in the 5 min crystallization, the high relative intensity of this vibration with 0.85:1 compared with the ZIF-8 peak at 1146 cm^{-1}—the latter is attributed to the C−H rocking and ring stretching in the framework—reveals the defect of unsaturated, ill-terminating ligands, or so-called dangling linkers, which are only bound to one zinc atom. As a result, the free-space vibrations of the linker, particularly the mode associated with the unwieldy asymmetric ring stretching and the N−H bonds, are enhanced and thus detectable in the nanoFTIR spectrum. Once bound to two zinc atoms in a fully assembled framework, these motions are mostly constrained, as indicated by the disappearance of this mode, or the decrease in the relative intensity to 0.47:1, with prolonged crystallization. In fact, the DFT assessment shows that this asymmetric ring stretching mode is even more suppressed in a defect-free crystal, as implied by the low relative intensity between the two simulated peaks (0.05:1). This suggests that, to some extent, this type of defect is found to prevail even when the final stage of the microcrystal growth is reached after 60 min. One can thus conclude that ordered dangling linker defects can exist in ZIF-8 microcrystals, including those deemed seemingly perfect.

Thus, the potential of measuring defects in ZIF-8, which is not by any means confined to the initial stages of early crystallization, emerged. The significance of this finding for understanding the prototypical “stable” ZIF-8 crystal is so great that it is worth discussing a little further. Whereas the bulk ATR-FTIR measurements perfectly match the calculated FTIR spectrum (Figure S12), the local nanoFTIR spectra do not. Instead, it is possible to pinpoint local characteristics in the vibrational modes and, in combination with computational modeling, associate them with chemical and structural peculiarities at the nanoscale. A glance at the vibrations between 1250 and 1350 cm^{-1} will further illustrate this because these additional vibrations are observed in the local spectra of ZIF-8 crystals and can be assigned to missing linker defects, yet they appear neither in the ATR-FTIR measurement nor in the calculated crystal, which is defect-free (Figure 5e,g). However, this is precisely what the nanocrystals are not because they feature these modes, namely, the missing linker defects, at such local scales. Akin to the DFT calculations, where the resulting two unsaturated metal sites are filled with an associating water and the conjugate base of the proton-donating group, the associated vibrational modes appear in the nanoFTIR spectrum, indicating the presence of such an aqueous linker vacancy at the crystal surface. These results highlight that the defect sites may alleviate the hydrophobicity, and as such the long-term stability of ZIF-8, by exposing open metal sites to solvents, gases, or other reactants. On the other hand, the same phenomenon could also enhance the adsorption capabilities of the material—what had previously been regarded as structural defects or, at best, imperfections may come to be considered as merits. For applications of defect engineering in ZIF-8, we refer to the findings of Lee et al.,[34] Cheng and Hu,[35] and Tian et al.,[36] who have shown an increase in the performance of defective ZIF-8 in gas separation and storage.

■ CONCLUSIONS

In this work, we tracked the transformation of defects in ZIF-8 by locally probing nano- and microcrystals at different stages during crystal growth with s-SNOM. As opposed to established techniques, which measure a spatial average over the bulk material, the use of s-SNOM yields chemical information with a nanoscale resolution akin to AFM imaging. In that way, the coexistence of defects can be observed during crystallization by pinpointing the vibrational dynamics of a 20 nm spot, encompassing several unit cells. Whereas after a 1 min growth time large amounts of uncoordinated linker and metal reactants are still dominant, it is already possible to note the presence of round nanocrystals; here, local probing with nanoFTIR confirms the emergence of characteristic IR peaks of ZIF-8, thus suggesting that the framework is already forming after such a short crystallization time. Indeed, ZIF-8 nanocrystals that match the characteristics of the final growth stage are attained after only 3 min, as corroborated with conventional characterization techniques like XRD, ATR-FTIR, and AFM. However, there is one distinction, which can only be revealed with nanospectroscopy: that between ZIF-8 crystals with perfect periodicity and those with structural defects. For instance, the local nanoFTIR spectra show the dominance of zinc ions, or of ill-coordinated metal clusters, close to the surface of the nanocrystals with 3 min growth time, even revealing the coexistence of vibrational modes associated with

ZIF-8 and the uncoordinated linker at the same 20 nm spot, thereby indicating defect-terminating ligands. With prolonged crystallization, or the ripening of the nanocrystals, these defects gradually vanish, and the final growth stage is reached after 60 min. Perhaps the most significant implication of this defect evolution—it is even more striking than observing the defect itself—consists of a change of the mechanical properties. A glance at the local Young's modulus, as measured with nanoscale resolution using TFM, has illustrated this: not only is the structural stiffness significantly lower in the presence of defects, but it also exhibits a higher local anisotropy. These experimental findings are confirmed by DFT calculations, where the mechanical properties of ZIF-8 and its defective structures have been computed. These trends are attributed to the fact that defects introduce local disorder to the otherwise highly ordered 3D periodic framework, ultimately compromising the material stability, although their impact on the material properties might extend even further. Knowledge of how defects affect the nanoscale mechanical behavior of ZIF-8 is key to targeted applications in catalysis, sensing, and gas capture, where not only is mechanical stability required but also defect engineering could further improve the material's performance.

The same phenomenon of defect transformation during crystallization was observed in ZIF-8 microcrystals. While the individual crystals transform from a spherical morphology to the rhombic dodecahedron shape, the chemical changes that underpin these features were tracked on the single-crystal level for the first time. After a growth time of 5 min, the faceted shape begins to emerge, yet several local structural defects are determined with nanospectroscopy; those include under-coordinated metal clusters and dangling linkers. Again, the trend of defect evolution is epitomized in their gradual disappearance with prolonged crystal growth time, although the defect of dangling linkers, if only slightly, is deemed to prevail. Similarly, defect sites of missing linkers lead to unsaturated metal sites, which adsorb water molecules, as confirmed with nanospectroscopy and DFT calculations. This phenomenon of open metal sites is crucial for the application of ZIF-8 because such additional adsorption sites allow for enhanced catalytic behavior, targeted chemical sensing, or increased gas capture. Out of that understanding grows doubt as to whether the stable, faceted ZIF-8 crystals, which have typically been assumed to be essentially defect-free, are, in fact, perfect or whether the defects were just invisible to most of the characterization techniques employed to date.

Hence, this first use of s-SNOM to probe defects in individual crystals offers an alternative, nondestructive method to low-dose TEM and electron crystallography for studies on defects in MOFs, with the additional advantage of providing chemical information at such local scales (∼20 nm). This novel tool can thus spark the exploration of local defects, not only in MOFs but also in other crystalline nanomaterials. In particular, the combination of s-SNOM with theoretical modeling of the mechanical properties unveils the missing link between previous studies on ZIF-8 that either computationally showed the feasibility of defects or employed defect tuning for enhancement of the material's performance. In addition, the first application of TFM in the field of MOFs enables the link to be established between the physical, chemical, and mechanical properties to shed new light on the implications of defects or, in fact, any features at the nanoscale. We envisage that these findings and techniques invite future studies on defects in MOFs and cognate framework materials either to evaluate the stability of "stable" MOFs for targeted application or, on the contrary, to leverage local defect engineering to tailor the material performance.

EXPERIMENTAL SECTION

Synthesis of ZIF-8 Nanocrystals. ZIF-8 nanocrystals were synthesized by dissolving 4.5 mmol of zinc nitrate hexahydrate [$Zn(NO_3)_2 \cdot 6H_2O$; 98%, Sigma-Aldrich] and 13.5 mmol of 2-methylimidazole (mIm; 98%, Sigma-Aldrich) in 60 mL of methanol, respectively. After the two clear solutions were combined, the white colloidal solution was rigorously stirred for 1 min and then left to form the nanocrystals. Immediately, some material was removed, diluted in fresh methanol, and washed three times. Each washing step encompassed centrifugation at 8000 rpm for 5 min, followed by solvent exchange with fresh methanol, and sonication for 30 s. The same procedure was repeated after 3, 5, and 60 min: after these time intervals, some material was removed and thoroughly washed to stop the growth process.

Synthesis of ZIF-8 Microcrystals. Two precursor solutions were prepared by dissolving 4 mmol of $Zn(NO_3)_2 \cdot 6H_2O$ and 4 mmol of mIm in 40 mL of methanol, respectively. A mixture was obtained by combining the two precursor solutions, which was stirred for 1 min and then left to stand. After specific time intervals (2, 5, and 60 min), some material was removed from the batch and immediately washed three times with methanol and centrifugation.

Sample Preparation for Nanoscale Analytics. Each sample was diluted in methanol and drop-casted onto a silicon substrate. To eliminate any excess solvent, the sample was dried in a vacuum oven at 80 °C for at least 30 min. The spectra of the reactants were measured by dissolving $Zn(NO_3)_2 \cdot 6H_2O$ (98%, Sigma-Aldrich) or mIm (98%, Sigma-Aldrich) in methanol, respectively. Likewise, the solution was drop-casted onto a clean silicon substrate and dried at 80 °C for 30 min.

Powder X-ray Diffraction (PXRD). The PXRD patterns were measured at a step size of 0.02° and step speed of 0.01°/min using a Rigaku MiniFlex diffractometer equipped with a Cu Kα source and validated against the simulated XRD pattern (CSD database code: VELVOY).

ATR-FTIR. ATR-FTIR measurements on bulk material were performed using a ThermoFisher Scientific Nicolet iS10 FTIR spectrometer with a spectral resolution of 4 cm^{-1}.

SEM Imaging. SEM images of the samples were obtained with a TESCAN LYRA3 electron microscope. Backscattered-electron and secondary-electron SEM images were obtained at 10 keV under high vacuum. The false-color images were produced using Adobe Photoshop.

nanoFTIR. The near-field optical measurements were performed with a neaSNOM instrument (neaspec GmbH) based on tapping-mode AFM, where the platinum-coated tip (NanoAndMore GmbH; cantilever resonance frequency 250 kHz; nominal tip radius ∼20 nm) was illuminated by a broadband femtosecond laser. The coherent mid-IR light was generated through the nonlinear difference−frequency combination of two beams from fiber lasers (TOPTICA Photonics Inc.) in a GaSe crystal. Laser A was selected for measurements covering the range from 700 to 1400 cm^{-1}. Demodulation of the optical signal at higher harmonics of the tip resonance frequency eliminated background contributions to yield the near-field signal, comprising the amplitude and phase of the scattered wave from the tip. When a pseudoheterodyne interferometric detection module was employed, the complex optical response of the material was measured, where the real part refers to the nanoFTIR reflectance and the imaginary part depicts the nanoFTIR absorption spectrum. Each spectrum was acquired from an average of 14 Fourier-processed interferograms with 10 cm^{-1} spectral resolution, 2048 points per interferogram, and 14 ms integration time per pixel. The sample spectrum was normalized to a reference spectrum measured on the silicon substrate. All measurements were carried out under ambient conditions.

TFM. TFM was employed as an additional module to the neaSNOM instrument, but here AFM was operated in contact mode. The z-piezo driver was modulated at a sinusoidal motion with an amplitude of 40 mV and a modulation frequency of 610 Hz. A complete force−distance cycle was performed at this rate for each pixel with an integration time of 33 ms (200 × 200 pixels per image). The technique followed the description of a pulsed-force mode.[42] Each cycle comprised an approach of the AFM tip from free oscillation until the establishment of contact with the sample, followed by subsequent retraction. More specifically, contact was established because of the (negative) attractive force between the tip and sample surface. Once in contact, the piezo drove the tip even closer to the sample until the (positive) repulsive force reached a maximum. Upon retraction of the tip, the repulsive force decreased and was replaced by the attractive force because of the adhesion between the sample and tip until contact was lost and the tip freely oscillated. From this cycle, various properties could be derived.[42,55,56] For instance, the topography image was obtained from the maximum force, which was fed back to the control circuit to maintain a constant normal force. An adhesion image could be created based on the maximum adhesion force for each pixel. The local stiffness was attained from the force difference between the maximum force and a set point in the repulsive part of the force signal. Hard surfaces led to a larger force difference than that observed for soft surfaces. Calibration measurements were carried out on the silicon substrate, and a polystyrene/poly(methyl methacrylate) polymer blend sample with known Young's moduli was used to validate the calibration. The mean local stiffness was obtained from the stiffness images by filtering out outliers and the background region containing the substrate. The normal and bimodal distributions were then calculated with the integrated analysis tools in *OriginPro 2019*.

COMPUTATIONAL DETAILS

DFT Calculations. Theoretical vibrational spectra along with elastic constants of ZIF-8 and defective ZIF-8 models were calculated with the PBEsol-3c method, a cost-effective 'composite method' developed for solid-state calculations.[52,57] It is based on a hybrid Hartree−Fock/DFT Hamiltonian combined with a double-ζ basis set, augmented with a semiclassical dispersion term and a geometrical counterpoise correction, which provides a good trade-off between cost and accuracy.[58,59] The calculations were carried out with a development version of the periodic *ab initio CRYSTAL17* code running in MPP mode on ARCUS-B, part of the high-performance computing facility at the University of Oxford (Oxford, U.K.), and on the U.K. national HPC facility ARCHER2.[48] The missing metal (or so-called dangling linker) defect was created by removing a metal atom and replacing two N−Zn bonds with N−H bonds similar to the uncoordinated linker. Removing a linker group, in turn, led to the missing linker defect, where the two unsaturated metal sites were filled by an associating water and the conjugate base of the proton-donating group. After geometry optimization, vibrational frequencies at the Γ point were computed, and the Berry phase approach was employed to calculate the IR intensities.[60,61] Subsequently, a simulated spectrum was obtained by fitting the calculated IR intensities with Lorentzian peak shapes with a fwhm of 10 cm^{-1}. To improve the match with the experimental data, the calculated IR spectra were scaled using distinct scaling factors for different spectral ranges, unlike adopting an overall scaling constant.[62] For the range from 600 to 850 cm^{-1}, the IR spectrum was scaled with a factor of 0.936, while the region between 850 and 1050 cm^{-1} was scaled by 0.964. Higher wavenumbers were scaled by a factor of 0.958.

The single-crystal elastic constants of the elasticity matrix (tensor) were calculated using the numerical first derivative of the analytic cell gradients.[63] These values correspond to the independent elastic stiffness coefficients, C_{ij}.[53] The unique coefficients were obtained via deformation of the optimized structure, using a three-point formula, in the symmetrically required directions of both positive and negative amplitudes. These deformations correspond to tensile and compressive strains required to obtain the elastic response. The magnitude of each individual strain deformation is defined as 1%, ensuring that the response is in the purely elastic region. For visualization of the elastic tensors and calculation of the mechanical properties, the *Elate*,[64] *Elam*,[65] and *Mathematica*[66] softwares were used to generate the 3D representation surfaces of different elastic moduli. Descriptions of the individual mechanical properties are given by Tan et al.[67]

ASSOCIATED CONTENT

Supporting Information

The Supporting Information is available free of charge at https://pubs.acs.org/doi/10.1021/acsanm.2c00493.

> Additional details about material characterization, including XRD, AFM, nanoFTIR, TFM, ATR-FTIR, and SEM, as well as DFT computational details and results (PDF)

AUTHOR INFORMATION

Corresponding Author

Jin-Chong Tan − *Multifunctional Materials and Composites Laboratory, Department of Engineering Science, University of Oxford, Oxford OX1 3PJ, U.K.*; orcid.org/0000-0002-5770-408X; Email: jin-chong.tan@eng.ox.ac.uk

Authors

Annika F. Möslein − *Multifunctional Materials and Composites Laboratory, Department of Engineering Science, University of Oxford, Oxford OX1 3PJ, U.K.*; orcid.org/0000-0002-2056-6437

Lorenzo Donà − *Dipartimento di Chimica, Università di Torino, Torino 10125, Italy*; orcid.org/0000-0001-7735-3881

Bartolomeo Civalleri − *Dipartimento di Chimica, Università di Torino, Torino 10125, Italy*; orcid.org/0000-0003-3198-3161

Complete contact information is available at: https://pubs.acs.org/10.1021/acsanm.2c00493

Author Contributions

Experimental design, experimental execution, and data analysis: A.F.M. Numerical simulations: L.D. and A.F.M. Writing of the original draft: A.F.M. Writing, editing, and reviewing: all authors. Scientific input and supervision: B.C. and J.-C.T.

Notes

The authors declare no competing financial interest.

ACKNOWLEDGMENTS

A.F.M. thanks the Oxford Ashton Memorial scholarship for a DPhil studentship award. J.-C.T. and A.F.M. are grateful for funding through the ERC Consolidator Grant [771575 (PROMOFS)] and the EPSRC Impact Acceleration Account Award (EP/R511742/1). We acknowledge use of the University of Oxford Advanced Research Computing facility in carrying out this work (10.5281/zenodo.22558). Via our membership of the U.K.'s HEC Materials Chemistry Consortium, which is funded by EPSRC (EP/R029431), this work used the ARCHER2 UK National Supercomputing Service (http://www.archer2.ac.uk). A.F.M. thanks Dr. Cyril Besnard and Prof. Alexander Korsunsky for their help with SEM imaging.

REFERENCES

(1) Lustig, W. P.; Mukherjee, S.; Rudd, N. D.; Desai, A. V.; Li, J.; Ghosh, S. K. Metal-Organic Frameworks: Functional Luminescent and Photonic Materials for Sensing Applications. *Chem. Soc. Rev.* **2017**, *46*, 3242−3285.

(2) Stassen, I.; Burtch, N.; Talin, A.; Falcaro, P.; Allendorf, M.; Ameloot, R. An Updated Roadmap for the Integration of Metal-Organic Frameworks with Electronic Devices and Chemical Sensors. *Chem. Soc. Rev.* **2017**, *46*, 3185−3241.

(3) Horcajada, P.; Gref, R.; Baati, T.; Allan, P. K.; Maurin, G.; Couvreur, P.; Ferey, G.; Morris, R. E.; Serre, C. Metal-Organic Frameworks in Biomedicine. *Chem. Rev.* **2012**, *112*, 1232−1268.

(4) Li, B.; Wen, H. M.; Zhou, W.; Chen, B. Porous Metal-Organic Frameworks for Gas Storage and Separation: What, How, and Why? *J. Phys. Chem. Lett.* **2014**, *5*, 3468−3479.

(5) Zhu, L.; Liu, X. Q.; Jiang, H. L.; Sun, L. B. Metal-Organic Frameworks for Heterogeneous Basic Catalysis. *Chem. Rev.* **2017**, *117*, 8129−8176.

(6) Allendorf, M. D.; Foster, M. E.; Leonard, F.; Stavila, V.; Feng, P. L.; Doty, F. P.; Leong, K.; Ma, E. Y.; Johnston, S. R.; Talin, A. A. Guest-Induced Emergent Properties in Metal-Organic Frameworks. *J. Phys. Chem. Lett.* **2015**, *6*, 1182−1195.

(7) Furukawa, H.; Cordova, K. E.; O'Keeffe, M.; Yaghi, O. M. The Chemistry and Applications of Metal-Organic Frameworks. *Science* **2013**, *341*, 1230444.

(8) Park, K. S.; Ni, Z.; Cote, A. P.; Choi, J. Y.; Huang, R.; Uribe-Romo, F. J.; Chae, H. K.; O'Keeffe, M.; Yaghi, O. M. Exceptional Chemical and Thermal Stability of Zeolitic Imidazolate Frameworks. *Proc. Natl. Acad. Sci. U.S.A.* **2006**, *103*, 10186−10191.

(9) Woehl, T. J.; Evans, J. E.; Arslan, I.; Ristenpart, W. D.; Browning, N. D. Direct in Situ Determination of the Mechanisms Controlling Nanoparticle Nucleation and Growth. *ACS Nano* **2012**, *6*, 8599−8610.

(10) Ghorbani, H.; Ghahramaninezhad, M.; Niknam Shahrak, M. The Effect of Organic and Ionic Liquid Solvents on Structure Crystallinity and Crystallite Size of ZIF-8 for CO_2 Uptake. *J. Solid State Chem.* **2020**, *289*, 121512.

(11) Malekmohammadi, M.; Fatemi, S.; Razavian, M.; Nouralishahi, A. A Comparative Study on ZIF-8 Synthesis in Aqueous and Methanolic Solutions: Effect of Temperature and Ligand Content. *Solid State Sci.* **2019**, *91*, 108−112.

(12) Zhang, Y.; Jia, Y.; Li, M.; Hou, L. Influence of the 2-Methylimidazole/Zinc Nitrate Hexahydrate Molar Ratio on the Synthesis of Zeolitic Imidazolate Framework-8 Crystals at Room Temperature. *Sci. Rep.* **2018**, *8*, 9597.

(13) Lai, L. S.; Yeong, Y. F.; Ani, N. C.; Lau, K. K.; Shariff, A. M. Effect of Synthesis Parameters on the Formation of Zeolitic Imidazolate Framework 8 (ZIF-8) Nanoparticles for CO_2 Adsorption. *Part. Sci. Technol.* **2014**, *32*, 520−528.

(14) Cravillon, J.; Nayuk, R.; Springer, S.; Feldhoff, A.; Huber, K.; Wiebcke, M. Controlling Zeolitic Imidazolate Framework Nano- and Microcrystal Formation: Insight into Crystal Growth by Time-Resolved in Situ Static Light Scattering. *Chem. Mater.* **2011**, *23*, 2130−2141.

(15) Venna, S. R.; Jasinski, J. B.; Carreon, M. A. Structural Evolution of Zeolitic Imidazolate Framework-8. *J. Am. Chem. Soc.* **2010**, *132*, 18030−18033.

(16) Dissegna, S.; Epp, K.; Heinz, W. R.; Kieslich, G.; Fischer, R. A. Defective Metal-Organic Frameworks. *Adv. Mater.* **2018**, *30*, 1704501.

(17) Fang, Z.; Bueken, B.; De Vos, D. E.; Fischer, R. A. Defect-Engineered Metal-Organic Frameworks. *Angew. Chem., Int. Ed.* **2015**, *54*, 7234−54.

(18) Shearer, G. C.; Chavan, S.; Bordiga, S.; Svelle, S.; Olsbye, U.; Lillerud, K. P. Defect Engineering: Tuning the Porosity and Composition of the Metal−Organic Framework UiO-66 Via Modulated Synthesis. *Chem. Mater.* **2016**, *28*, 3749−3761.

(19) Wu, H.; Chua, Y. S.; Krungleviciute, V.; Tyagi, M.; Chen, P.; Yildirim, T.; Zhou, W. Unusual and Highly Tunable Missing-Linker Defects in Zirconium Metal-Organic Framework UiO-66 and Their Important Effects on Gas Adsorption. *J. Am. Chem. Soc.* **2013**, *135*, 10525−32.

(20) Liu, Y.; Klet, R. C.; Hupp, J. T.; Farha, O. Probing the Correlations between the Defects in Metal-Organic Frameworks and Their Catalytic Activity by an Epoxide Ring-Opening Reaction. *Chem. Commun.* **2016**, *52*, 7806−9.

(21) Park, J.; Wang, Z. U.; Sun, L. B.; Chen, Y. P.; Zhou, H. C. Introduction of Functionalized Mesopores to Metal-Organic Frameworks Via Metal-Ligand-Fragment Coassembly. *J. Am. Chem. Soc.* **2012**, *134*, 20110−6.

(22) Taylor, J. M.; Dekura, S.; Ikeda, R.; Kitagawa, H. Defect Control to Enhance Proton Conductivity in a Metal−Organic Framework. *Chem. Mater.* **2015**, *27*, 2286−2289.

(23) Bennett, T. D.; Cheetham, A. K.; Fuchs, A. H.; Coudert, F. X. Interplay between Defects, Disorder and Flexibility in Metal-Organic Frameworks. *Nat. Chem.* **2017**, *9*, 11−16.

(24) Shöâeè, M.; Agger, J. R.; Anderson, M. W.; Attfield, M. P. Crystal Form, Defects and Growth of the Metal Organic Framework HKUST-1 Revealed by Atomic Force Microscopy. *CrystEngComm* **2008**, *10*, 646−648.

(25) Zeng, Z.; Flyagina, I. S.; Tan, J.-C. Nanomechanical Behavior and Interfacial Deformation Beyond the Elastic Limit in 2d Metal−Organic Framework Nanosheets. *Nanoscale Adv.* **2020**, *2*, 5181−5191.

(26) Cliffe, M. J.; Wan, W.; Zou, X.; Chater, P. A.; Kleppe, A. K.; Tucker, M. G.; Wilhelm, H.; Funnell, N. P.; Coudert, F. X.; Goodwin, A. L. Correlated Defect Nanoregions in a Metal-Organic Framework. *Nat. Commun.* **2014**, *5*, 4176.

(27) Valenzano, L.; Civalleri, B.; Chavan, S.; Bordiga, S.; Nilsen, M. H.; Jakobsen, S.; Lillerud, K. P.; Lamberti, C. Disclosing the Complex Structure of UiO-66 Metal Organic Framework: A Synergic Combination of Experiment and Theory. *Chem. Mater.* **2011**, *23*, 1700−1718.

(28) Shearer, G. C.; Chavan, S.; Ethiraj, J.; Vitillo, J. G.; Svelle, S.; Olsbye, U.; Lamberti, C.; Bordiga, S.; Lillerud, K. P. Tuned to Perfection: Ironing out the Defects in Metal−Organic Framework UiO-66. *Chem. Mater.* **2014**, *26*, 4068−4071.

(29) Atzori, C.; Shearer, G. C.; Maschio, L.; Civalleri, B.; Bonino, F.; Lamberti, C.; Svelle, S.; Lillerud, K. P.; Bordiga, S. Effect of Benzoic Acid as a Modulator in the Structure of UiO-66: An Experimental and Computational Study. *J. Phys. Chem. C* **2017**, *121*, 9312−9324.

(30) Liu, L.; Chen, Z.; Wang, J.; Zhang, D.; Zhu, Y.; Ling, S.; Huang, K. W.; Belmabkhout, Y.; Adil, K.; Zhang, Y.; Slater, B.; Eddaoudi, M.; Han, Y. Imaging Defects and Their Evolution in a Metal-Organic Framework at Sub-Unit-Cell Resolution. *Nat. Chem.* **2019**, *11*, 622−628.

(31) Penn, R. L.; Banfield, J. F. Imperfect Oriented Attachment: Dislocation Generation in Defect-Free Nanocrystals. *Science* **1998**, *281*, 969−971.

(32) Zhang, C.; Han, C.; Sholl, D. S.; Schmidt, J. R. Computational Characterization of Defects in Metal-Organic Frameworks: Spontaneous and Water-Induced Point Defects in ZIF-8. *J. Phys. Chem. Lett.* **2016**, *7*, 459.

(33) Han, C.; Verploegh, R. J.; Sholl, D. S. Assessing the Impact of Point Defects on Molecular Diffusion in ZIF-8 Using Molecular Simulations. *J. Phys. Chem. Lett.* **2018**, *9*, 4037−4044.

(34) Lee, M. J.; Kwon, H. T.; Jeong, H.-K. Defect-Dependent Stability of Highly Propylene-Selective Zeolitic-Imidazolate Framework ZIF-8 Membranes. *J. Membr. Sci.* **2017**, *529*, 105−113.

(35) Cheng, P.; Hu, Y. H. H_2O-Functionalized Zeolitic Zn(2-Methylimidazole)$_2$ Framework (ZIF-8) for H_2 Storage. *J. Phys. Chem. C* **2014**, *118*, 21866−21872.

(36) Tian, F.; Cerro, A. M.; Mosier, A. M.; Wayment-Steele, H. K.; Shine, R. S.; Park, A.; Webster, E. R.; Johnson, L. E.; Johal, M. S.; Benz, L. Surface and Stability Characterization of a Nanoporous ZIF-8 Thin Film. *J. Phys. Chem. C* **2014**, *118*, 14449−14456.

(37) Knoll, B.; Keilmann, F. Near-Field Probing of Vibrational Absorption for Chemical Microscopy. *Nature* **1999**, *399*, 134−137.

(38) Keilmann, F.; Hillenbrand, R. Near-Field Microscopy by Elastic Light Scattering from a Tip. *Philos. Trans. R. Soc. A* **2004**, *362*, 787−805.

(39) Möslein, A. F.; Gutierrez, M.; Cohen, B.; Tan, J. C. Near-Field Infrared Nanospectroscopy Reveals Guest Confinement in Metal-Organic Framework Single Crystals. *Nano Lett.* **2020**, *20*, 7446−7454.

(40) Huth, F.; Govyadinov, A.; Amarie, S.; Nuansing, W.; Keilmann, F.; Hillenbrand, R. Nano-FTIR Absorption Spectroscopy of Molecular Fingerprints at 20 Nm Spatial Resolution. *Nano Lett.* **2012**, *12*, 3973−3978.

(41) Govyadinov, A. A.; Amenabar, I.; Huth, F.; Carney, P. S.; Hillenbrand, R. Quantitative Measurement of Local Infrared Absorption and Dielectric Function with Tip-Enhanced near-Field Microscopy. *J. Phys. Chem. Lett.* **2013**, *4*, 1526−1531.

(42) Krotil, H. U.; Stifter, T.; Waschipky, H.; Weishaupt, K.; Hild, S.; Marti, O. Pulsed Force Mode: A New Method for the Investigation of Surface Properties. *Surf. Interface Anal.* **1999**, *27*, 336−340.

(43) Ostwald, W. Studien über Die Bildung und Umwandlung Fester Körper. *Z. fur Phys. Chem.* **1897**, *22U*, 289−330.

(44) Young, R. A. *X-ray Diffraction Studies of Thermal Motions in Crystals*; Engineering Experiment Station, Georgia Institute of Technology: Atlanta, GA1961.

(45) Brooker, M. H.; Irish, D. E. Vibrational Spectral Studies of Hexaquozinc Nitrate and Hexaquozinc Nitrate-D_2. *Can. J. Chem.* **1971**, *49*, 1510−1514.

(46) Chizallet, C. L. S.; Lazare, S.; Bazer-Bachi, D.; Bonnier, F.; Lecocq, V.; Soyer, E.; Quoineaud, A.-A.; Bats, N. Catalysis of Transesterification by a Nonfunctionalized Metal-Organic Framework: Acido-Basicity at the External Surface of ZIF-8 Probed by FTIR and Ab Initio Calculations. *J. Am. Chem. Soc.* **2010**, *132*, 12365−12377.

(47) Zhang, K.; Lively, R. P.; Zhang, C.; Koros, W. J.; Chance, R. R. Investigating the Intrinsic Ethanol/Water Separation Capability of ZIF-8: An Adsorption and Diffusion Study. *J. Phys. Chem. C* **2013**, *117*, 7214−7225.

(48) Dovesi, R.; Saunders, V. R.; Roetti, C.; Orlando, R.; Zicovich-Wilson, C. M.; Pascale, F.; Civalleri, B.; Doll, K.; Harrison, N. M.; Bush, I. J.; D'Arco, P.; Llunell, M.; Causà, M.; Noël, Y.; Maschio, L.; Erba, A.; Rerat, M.; Casassa, S. *CRYSTAL17 User's Manual*; University of Torino, Torino, Italy, 2017.

(49) Han, R.; Sholl, D. S. Computational Model and Characterization of Stacking Faults in ZIF-8 Polymorphs. *J. Phys. Chem. C* **2016**, *120*, 27380−27388.

(50) Zeng, Z.; Tan, J.-C. AFM Nanoindentation to Quantify Mechanical Properties of Nano- and Micron-Sized Crystals of a Metal−Organic Framework Material. *ACS Appl. Mater. Interfaces* **2017**, *9*, 39839−39854.

(51) Thornton, A. W.; Babarao, R.; Jain, A.; Trousselet, F.; Coudert, F. X. Defects in Metal-Organic Frameworks: A Compromise between Adsorption and Stability? *Dalton Trans.* **2016**, *45*, 4352−9.

(52) Dona, L.; Brandenburg, J. G.; Civalleri, B. Extending and Assessing Composite Electronic Structure Methods to the Solid State. *J. Chem. Phys.* **2019**, *151*, 121101.

(53) Tan, J.-C.; Civalleri, B.; Lin, C.-C.; Valenzano, L.; Galvelis, R.; Chen, P.-F.; Bennett, T. D.; Mellot-Draznieks, C.; Zicovich-Wilson, C. M.; Cheetham, A. K. Exceptionally Low Shear Modulus in a Prototypical Imidazole-Based Metal-Organic Framework. *Phys. Rev. Lett.* **2012**, *108*, 095502.

(54) Maul, J.; Ryder, M. R.; Ruggiero, M. T.; Erba, A. Pressure-Driven Mechanical Anisotropy and Destabilization in Zeolitic Imidazolate Frameworks. *Phys. Rev. B* **2019**, *99*, 014102.

(55) Derjaguin, B. V.; Muller, V. M.; Toporov, Y. P. Effect of Contact Deformations on the Adhesion of Particles. *J. Colloid Interface Sci.* **1975**, *53*, 314−326.

(56) Muller, V. M.; Derjaguin, B. V.; Toporov, Yu. P. On Two Methods of Calculation of the Force of Sticking of an Elastic Sphere to a Rigid Plane. *Colloids Surf.* **1983**, *7*, 251−259.

(57) Caldeweyher, E.; Brandenburg, J. G. Simplified DFT Methods for Consistent Structures and Energies of Large Systems. *J. Phys.: Condens. Matter* **2018**, *30*, 213001.

(58) Souza, B. E.; Dona, L.; Titov, K.; Bruzzese, P.; Zeng; Zhang, Y.; Babal, A. S.; Möslein, A. F.; Frogley, M. D.; Wolna, G.; Cinque, G.; Civalleri, B.; Tan, J. C. Elucidating the Drug Release from Metal-Organic Framework Nanocomposites Via in Situ Synchrotron Microspectroscopy and Theoretical Modelling. *ACS Appl. Mater. Interfaces* **2020**, *12*, 5147−5156.

(59) Dona, L.; Brandenburg, J. G.; Bush, I. J.; Civalleri, B. Cost-Effective Composite Methods for Large-Scale Solid-State Calculations. *Faraday Discuss.* **2020**, *224*, 292−308.

(60) Pascale, F.; Zicovich-Wilson, C. M.; López Gejo, F.; Civalleri, B.; Orlando, R.; Dovesi, R. The Calculation of the Vibration Frequencies of Crystalline Compounds and Its Implementation in the CRYSTAL Code. *J. Comput. Chem.* **2004**, *25*, 888−897.

(61) Dovesi, R.; Kirtman, B.; Maschio, L.; Maul, J.; Pascale, F.; Rérat, M. Calculation of the Infrared Intensity of Crystalline Systems. A Comparison of Three Strategies Based on Berry Phase, Wannier Function, and Coupled-Perturbed Kohn−Sham Methods. *J. Phys. Chem. C* **2019**, *123*, 8336−8346.

(62) Rauhut, G.; Pulay, P. Transferable Scaling Factors for Density Functional Derived Vibrational Force Fields. *J. Phys. Chem.* **1995**, *99*, 3093−3100.

(63) Perger, W. F.; Criswell, J.; Civalleri, B.; Dovesi, R. Ab-Initio Calculation of Elastic Constants of Crystalline Systems with the CRYSTAL Code. *Comput. Phys. Commun.* **2009**, *180*, 1753−1759.

(64) Gaillac, R.; Pullumbi, P.; Coudert, F. X. Elate: An Open-Source Online Application for Analysis and Visualization of Elastic Tensors. *J. Phys.: Condens. Matter* **2016**, *28*, 275201.

(65) Marmier, A.; Lethbridge, Z. A. D.; Walton, R. I.; Smith, C. W.; Parker, S. C.; Evans, K. E. Elam: A Computer Program for the Analysis and Representation of Anisotropic Elastic Properties. *Comput. Phys. Commun.* **2010**, *181*, 2102−2115.

(66) *Mathematica*; Wolfram Research Inc., 2015.

(67) Tan, J. C.; Cheetham, A. K. Mechanical Properties of Hybrid Inorganic-Organic Framework Materials: Establishing Fundamental Structure-Property Relationships. *Chem. Soc. Rev.* **2011**, *40*, 1059−80.

By the smallest of one's actions one can restore some sense of order to the world.

— Amor Towles, *A Gentleman in Moscow*

5

Unravelling the sensing mechanism of a metal-organic framework

Contents

5.1 Gas sensing in MOFs

The ever-increasing concerns over air quality, industrial gas leakage, food freshness, and medical diagnosis require portable gas sensors with excellent sensitivity and selectivity towards toxic gases and volatile organic compounds (VOCs).[33, 160] The sensing performance, specifically sensitivity or limit of detection, selectivity, response time, reproducibility, and stability, strongly depends on the intrinsic properties of the sensing materials (e.g., porosity, chemical composition, size, defects, conductivity), as well as on the material-analyte interactions. Because MOFs feature unparalleled structural diversity, flexibility, tailorability, high porosity, large surface area, and adsorption affinities, they have emerged as suitable candidate materials for gas sensing.[34, 35, 161] For instance, their high surface area and permanent porosity allows for concentration of gases into the pores, thereby enhancing sensitivity. Selectivity towards a targeted analyte can be achieved through tunable pore sizes (leading to size exclusion), tailored host-guest interactions, and functional adsorption sites such as unsaturated metal sites or active binding sites either present in the framework or introduced through defect engineering. Having investigated two key phenomena – guest encapsulation and defect tuning – which are crucial for developing MOF-based sensing devices for targeted detection, this chapter provides a detailed study on the gas sensing mechanism itself.

5.1.1 Basic principles of MOF-based gas sensors

If MOFs interact with target analytes, fluctuations in the luminescent, mechanical, or electrochemical properties can be induced. These can then be transduced into detectable signals for chemical sensing.[33] Among the different ways for gas sensing, a visible colour change of a material might be the simplest way of signal transduction.[33] This so-called vapochromism or solvatochromsim is induced by a large shift in the optical absorption across the visible region when exposed to gases from different solvents, most caused by the electronic transition from the ground to the excited state of the chromophore of the MOF.[162]. However, even if vapochromism can be easily detected and incorporated into an optical sensor, this phenomenon is to date unattainable in most MOF materials.[161] Instead, luminescence-based sensing is a promising solution to design MOF-based devices.[161, 163] Because some MOF systems can emit characteristic luminescence when transitioning from an excited state to the ground state, the interaction with guest molecules may lead to either quenching or enhancement of the emission intensity, or a shift in the emission frequency. For gas detection, a characteristic shift in emission is more suitable than a change in intensity alone, as especially a decrease in intensity could also be induced by photodegradation or other mechanisms. Importantly, the strength of changes in luminescent properties depends on the nature of the host material and the corresponding guest interactions and can thus be tuned by meticulous material design.[107] The luminescence in MOFs can originate from several concepts, as summarised in Figure 5.1: the emission can either stem from the organic linkers or the metal centres, or arise from charge transfer.[106] Another way to achieve luminescence is by encapsulating fluorescent guest molecules, allowing for additional sensitivity in sensing applications because the target analyte might not only interact with the host framework but also with the guest.[107] Although guest encapsulation may slightly reduce the porosity of the framework, and possibly the crystallinity, too, the main features that render MOFs such promising candidate materials for sensing are still retained in guest@MOF systems.[164] Compared to other optical sensors that are based on refractive index[165], dielectric constants[166, 167], scattering[168], or diffraction[169], luminescence sensing in MOFs offers high sensitivity, selectivity, and technical simplicity.[163] Other sensing mechanics that hold vital promise for MOF-based gas monitoring include electrochemical and electromechanical sensing techniques.[170–172] Again, upon interaction with a target gas, the electrical properties of the MOF (i.e. impedance, resistance, or capacitance) may be altered, but because MOFs are usually non-conductive, these changes may be too insignificant to allow for distinct sensing and require further development.[161] Similarly, the high surface area of MOFs coupled with their tailorable nature offer a promising platform for mechanical sensing; nevertheless, this method relies on a mass change due to the absorbed analyte and thus, the limit of detection might be unsatisfactory for specific applications.[161]

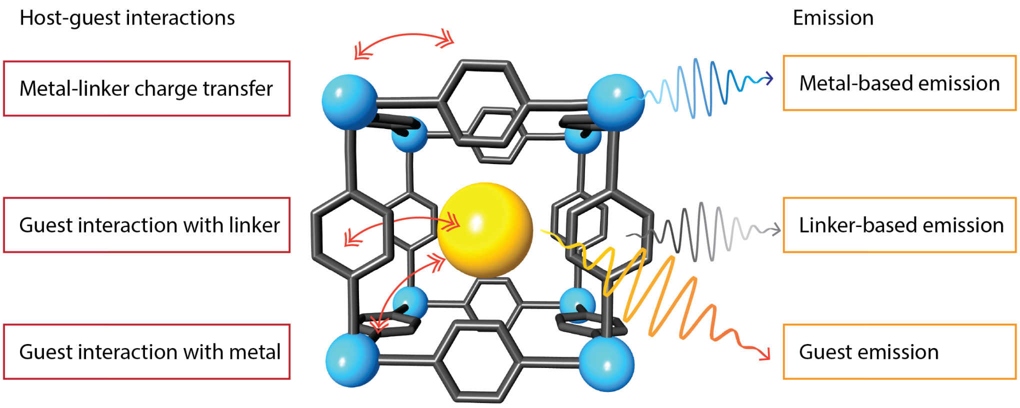

Figure 5.1: Schematic representation of a luminescent guest@MOF system. Metal nodes (in blue) are bridged by organic linkers (in gray) to form the crystalline framework with a fluorescent guest molecule (yellow) encapsulated in the pore. Different host-guest interactions and the possible emission pathways are indicated.

5.1.2 MOF-based gas sensing

MOFs have been explored in gas sensors for a variety of applications, ranging from humidity sensing for environmental monitoring[173–176], food inspections[177], and oxygen measuring techniques for chemical industrial processes[178–180] to the detection of harmful and toxic gases.[181] These include, at the most extreme, explosives[182–184] or chemical warfare agents[185, 186], whose detection, albeit challenging, is of unsurpassed importance for security and protection. Monitoring other inorganic gases, such as iodine or sulfur dioxide (SO_2), is equally essential for public safety since their presence may indicate nuclear leakages or cause acid rain, respectively, and their corrosive nature poses a threat for human health and environment.[187] Similarly, volatile organic compounds (VOCs), being widely present in indoor and outdoor air, are considered significant air pollutants due to their short- or long-term effects on human health.[17–19] In addition, VOCs in exhaled air serve as biological markers that can indicate conditions and diseases, or the response to a corresponding treatment.[14, 15] Since accurately detecting and identifying VOCs in human breath afford non-invasive diagnostics, breath analysers will facilitate monitoring and screening of critical conditions.

Inspired by the need for high-performance sensors, a vast range of MOF-based devices has been developed to address the aforementioned challenges.[161, 187]

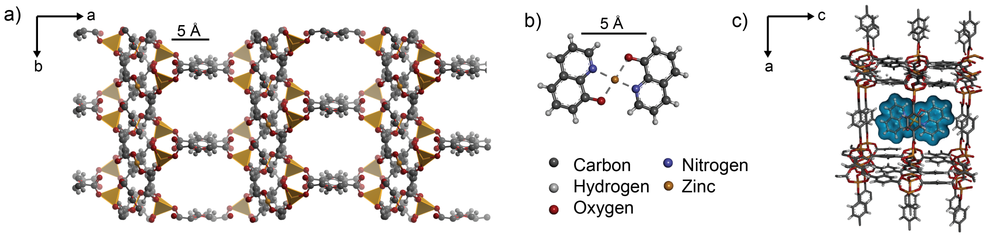

Figure 5.2: The ZnQ@OX-1 composite system. a) Structure of OX-1. b) Structure of ZnQ complex. c) Schematic of ZnQ guest encapsulated in the pores of OX-1 host.

However, even if numerous examples of the use of MOFs for gas detection exist, and their respective means of signal transduction are described in literature, the underlying sensing mechanisms are often poorly understood.

5.1.3 MOFs for acetone sensing

Let us, for instance, consider the detection of acetone in breath, which offers a non-invasive alternative for monitoring the blood glucose level. While state-of-the-art sensors for acetone sensing are mainly based on metal oxide films, as reported by Rydosz, they cannot meet the stringent requirements of selectivity and functionality at ambient conditions.[188] Additionally, even if wearable sensors for continuous blood glucose monitoring exist, they are still invasive, as they rely on measuring interstitial fluid. Focussing on non-invasive breath analysers, MOF-based sensing technologies may offer enhanced performance for the detection of volatile acetone owing to the unique features of the materials. Systems based on ZnO structures such as nanocages, or Au@ZnO could afford high sensitivity towards very low concentrations (<10 ppm) of acetone using resistance or electrical sensing methods, respectively.[189, 190] Reversible responses to acetone were achieved with copper-based MOF: HKUST-1 ($Cu_3(BTC)_2$, BTC = benzene-1,3,5,-tricarboxylic acid) was incorporated in a mechanical sensor for acetone and other solvents[191], while Cu-BTC exhibited sensitivity to acetone (100 ppm) in capacitance measurements.[192] Meanwhile, the luminescent octrahedron@ZIF-8 composite could remarkably display a visible colour change under UV irradiation when exposed to acetone for more than 15 minutes, while offering high selectivity and

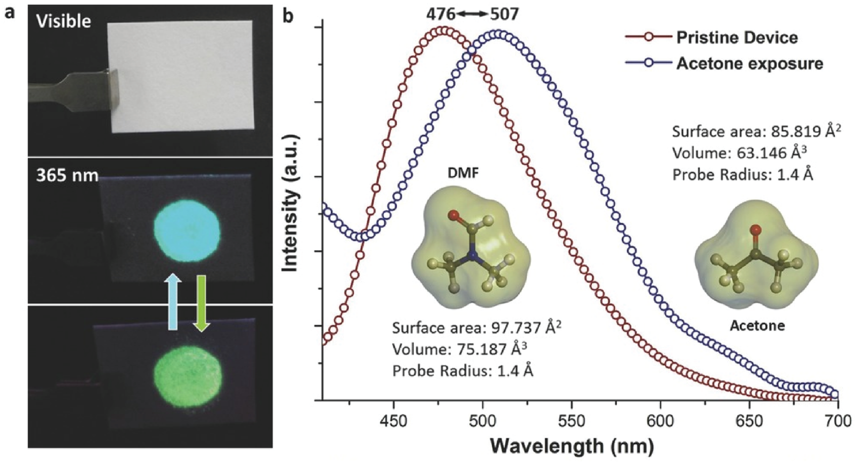

Figure 5.3: Vapochromism exhibited by the ZnQ@OX-1 material. a) Paper-based proof-of-concept sensor demonstrating reversible acetone sensing. b) Emission spectra of ZnQ@OX-1 measured before and during exposure to liquid acetone. Reprinted from ref. [114] with permission from WILEY-VCH, Copyright 2017.

sensitivity to acetone vapour.[95] An even faster response (∼seconds) was achieved with the 'OX-1' framework with zinc clusters bridged by 1,4-benzenedicarboxylic acid (BDC) linkers.[114] Importantly, the nanoconfinement of luminescent ZnQ (zinc(II)-bis(8-hydroxyquinoline)) complexes in the framework yields a photonic material – the ZnQ@OX-1 composite - with a vapochromic behaviour (see Figure 5.2). Under UV irradiation, the ZnQ@OX-1 system emits a blue light (480 nm), which immediately changes to a green emission when the material is exposed to acetone vapour, as shown in Figure 5.3. In fact, the vapochromism is based on both a spectral shift and a change in emission intensity, which significantly facilitates the detection. Because the colour change is visible with the naked eye, and the detection is fast and reversible in ambient conditions, this optochemically responsive ZnQ@OX-1 composite demonstrates excellent sensing performance towards acetone, unattainable in any other materials.[114] The efficacy of harnessing the visible shifts in wavelengths has been shown by a proof-of-concept paper device (see Figure 5.3). Yet, even if host-guest interactions have been postulated to cause the fluorescence attenuation, the underpinning sensing mechanism that is responsible for such unique sensing behaviour is still to be resolved and questions concerning the selectivity, limit of detection, and reversibility remain unanswered.

5.2 A strategy to investigate the sensing mechanism of a guest-MOF system

This is precisely why this study focusses on the sensing mechanism of the ZnQ@OX-1 system. To investigate the chemical and physical interactions that may be associated with the exceptional sensing, we employed a set of complementary spectroscopy techniques comprising inelastic neutron scattering (INS), synchrotron-radiation (SR) FTIR, fluorescence spectroscopy, and near-field spectroscopy; all these experimental findings were further substantiated by density functional theory (DFT) calculations.

5.2.1 Inelastic neutron scattering (INS) spectroscopy

We performed INS measurements using the TOSCA spectrometer at the ISIS Neutron and Muon Source, Rutherford Appleton Laboratory (Chilton, UK) to study the vibrational behaviour of the ZnQ@OX-1 composite system subjected to acetone vapour.[193–195] The high-resolution ($\Delta E/E \sim 1.25\%$) spectra, covering the broadband range from -20 to 4000 cm^{-1}, were collected from the bulk polycrystalline sample (~1 g) at 10 K. The conditions for each measurement are detailed in Table 5.1. At the TOSCA spectrometer, upon collision with the sample, the neutrons from a pulsed beam are scattered and Bragg reflected by a pyrolytic graphite analyser. Here, higher-order reflections beyond (002) were suppressed by a cooled ($T < 30$ K) Beryllium filter, acting as a long pass filter to analyse neutrons of a consistent final energy of $\sim 32\ \mathrm{cm}^{-1}$. The detector array comprises thirteen ^{3}He tubes, with five banks being in forward direction (scattering angle $\sim 45°$) and five in backwards direction ($\sim 135°$). Because a low final energy was used, a direct relationship between energy transfer (ET, cm^{-1}) and momentum transfer (Q, Å^{-1}) is obtained according to $ET \sim 16Q^2$. Energy transfer and spectral intensity, i.e. $S(Q, \omega)$, were then attained using the Mantid software.[196]

The pristine powder sample ZnQ was wrapped in a 4 cm × 4.8 cm aluminium sachet and placed into a 2.0 mm spaced flat aluminium cell, which was sealed with indium wire. For gas dosing experiments, OX-1 and ZnQ@OX-1 powder samples were loaded into a cylindrical vanadium gas handling cell (internal diameter of 11

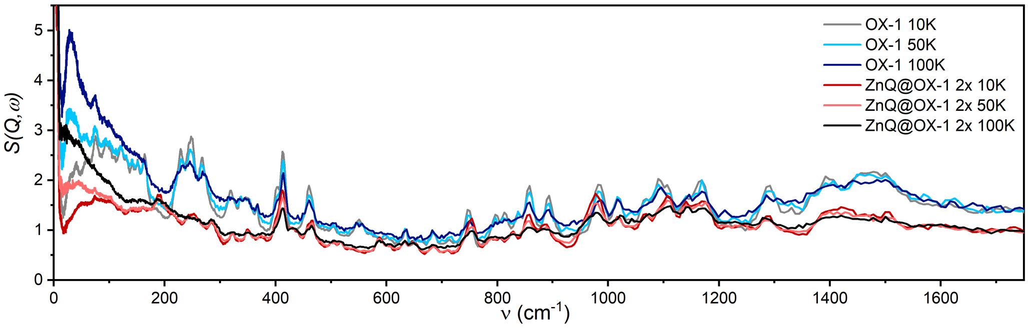

Figure 5.4: Broadband vibrational spectrum of the OX-1 host structure and ZnQ@OX-1 with double amount of guest loading (denoted by 2x), obtained *via* inelastic neutron scattering at TOSCA, recorded at temperatures of 10, 50, and 100 K.

mm) with an indium seal, and evaporated by pumping, such that the final pressure was below 6 x 10^{-4} bar, to remove any remaining air or traces of solvent and water. Liquid acetone was dosed at room temperature using a valve, preventing the air from entering the cell. After dosing, the closed cell was heated to 60 °C to yield a vapour phase of acetone for intrusion and adsorption that is spread more homogeneously in the solid ZnQ@OX-1 powder. Similar procedure was used for methanol dosing, while for methane, the sample cell was directly dosed with gas. Before the measurement, the sample cell was cooled to 10 K by a closed cycle refrigerator to reduce temperature-related effects. The INS spectrum was collected under vacuum over a duration of 4-6 hours. The spectra are normalised by the mass of the sample under investigation (see Table 5.1).

To pinpoint the specific vibrational dynamics of the guest@OX-1 system compared to the vacant framework, pristine OX-1 powder samples, as well as ZnQ material were probed first. Turning to the ZnQ@OX-1 composite, we found that, instead of a simple superposition of the peaks associated to the two pristine materials, actual host-guest interactions emerged upon guest encapsulation (see Figure 5.4). Subsequently, when the composite material is exposed to acetone, some vibrational modes are altered and interestingly, it is precisely the modes associated with host-guest interactions that are subjected to changes. Especially in the low-energy or THz region, particular modifications indicate structural changes following the adsorption of acetone in the composite, which are lacking in the pristine OX-1 material. If the latter is exposed to acetone, only a superposition of peaks associated with OX-1 and the analyte, respectively, is observed without any indication of chemical interactions. It is however worth mentioning that the well-defined peaks of acetone in the THz region exhibit overall broadening, while the peaks in higher energy regions above 200 cm^{-1} remain unaffected, an effect attributed to the vanishing long-range order, as the acetone molecules are more separated in the pores of the framework. Because distinctive changes in the vibrational dynamics are observed in the ZnQ@OX-1 system upon exposure to acetone, this leads to the conclusion that the host-guest interactions rather than solely the framework itself play a crucial role for the sensing mechanism. Careful examination of the INS spectra of ZnQ@OX-1 material before and after dosing with acetone reveals that the peaks that have emerged from host-guest interactions are now altered in the presence of acetone, indicating that the acetone molecules may rupture the weak chemical bonds between ZnQ and OX-1 (Figure 1 in the manuscript 5.4).

Sample	**OX-1**	**OX-1 & acetone**	**ZnQ**	**ZnQ@OX-1**	**ZnQ@OX-1 & acetone**
Mass of powder	1.446 g	1.446 g	1.073 g	1.249 g	1.249 g
Mass of acetone	-	0.425 g	-	-	0.436 g

Table 5.1: Sample details for INS measurements.

5.2.2 Computational modelling

To determine the precise chemical and structural changes, we performed density function theory (DFT) calculations, since the theoretical approach can assign specific vibrations, and thus physical meaning, to the observed peaks and their modifications. All calculations were performed with the PBEsol0-3c method, recently implemented in a development version of the CRYSTAL17 code in its massively parallel version (MPPcrystal) on the Advanced Research Computing (ARC) high-performance cluster facility.[197, 198] PBEsol0-3c is a composite *ab initio* method that is based on a double-zeta quality Gaussian basis set especially devised for inorganic systems and metal-organic materials.[199] Previously, this method has been successfully applied to study geometrical and vibrational properties of MOFs, providing results in good agreement with the experimental findings.[38, 83, 200, 201]

For the evaluation of the DFT exchange-correlation term an XLGRID (75,974) pruned grid was used. Default convergence criterion for both geometry optimisation and frequencies calculations were employed. The tolerances for one- and two-electron integrals calculation were set to 10^{-7} and 10^{-7} for the Coulomb and to 10^{-7}, 10^{-7}, and 10^{-25} for the exchange series, respectively. The shrinking factors for the diagonalisation of the Kohn-Sham matrix in the reciprocal space were set to 4 for the Monkhorst-Pack net and to 4 for the Gilat net.

The initial structure of OX-1 used for simulations was taken from Cambridge Crystallographic Data Center (CCDC 281855), and the molecules of *N*,*N*- diethylformamide solvents were removed from the pores of the MOF. A geometry optimisation was performed with the constraints imposed by the symmetry of the system. Subsequently, on the local minimum geometry, the harmonic frequencies were computed in the Γ-point using the three-point formula. The IR intensity were calculated with the Berry phase approach, and were fitted with a Lorentzian peak shape with a FWHM of 10 cm^{-1} (see Figure 5.5).[202] A complete assignment of all IR-active modes can be found in the Appendix A. The INS spectrum was calculated from the output of the frequency calculation using the AbINS v1 execution in the Mantid software.[196] Herein, the scattering of the neutrons by the nuclei is described by the observed intensity S of the transition at energy ω, given by the product of the inelastic cross section σ, the momentum transfer Q, and the amplitude U of vibration for the mode at energy ω, and the total amplitude of motion U_T damped by a Debye-Waller factor:

$$S(Q,\omega) = \sigma_{in} Q^2 U_\omega^2 \exp(-Q^2 U_T^2). \tag{5.1}$$

Because the inelastic cross section and the amplitude of vibration relates to the observed intensity, it will show dominant sensitivity to atoms with large cross-section and small masses, such as hydrogen.[203] It is also worth noting that, in principle, all modes are INS active, since no terms depend on symmetry, and

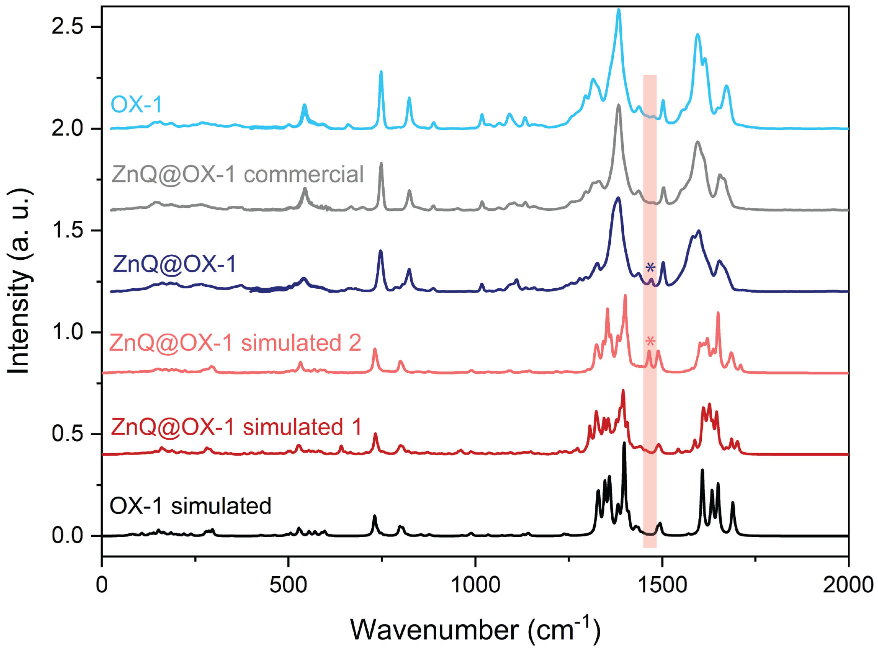

Figure 5.5: Comparison of measured and simulated IR spectra of OX-1 and ZnQ@OX-1. A shift of 0.95 was applied to the theoretical spectra simulated by DFT. Simulation 1 assumes that ZnQ is simply encapsulated into the pore, while simulation 2 maximises the π-π stacking interactions between the aromatic rings of ZnQ and OX-1 linkers.

therefore, this technique, as opposed to IR spectroscopy, is not limited by the optical selection rule. In addition, the expression reveals that ideally, the spectra should be obtained at low temperatures to reduce the impact of the Debye-Waller factor. With the transition energies and amplitudes of the vibrations being obtained from the frequency calculation, a reasonable match between the theoretical and experimental spectrum was obtained.

5.2.3 Synchrotron-based FTIR spectroscopy

While INS measurements provide excellent resolution in the low-energy regions, in practice, this technique is particularly sensitive to vibrations encompassing hydrogen due to the exceptionally large scattering cross-section of the hydrogen nuclei. Therefore, FTIR spectroscopy can yield additional information, albeit limited by the optical selection rule. We performed Fourier-transform infrared (FTIR) spectroscopy experiments based on two different techniques at the Multimode InfraRed Imaging and Microspectroscopy (MIRIAM) Beamline (B22) at the Diamond Light Source, UK. Firstly, FTIR absorption spectra were collected from powder samples before and after exposure to various solvents. Secondly, employing a flow cell, *in situ* gas dosing was achieved using transmission FTIR spectroscopy. All FTIR spectra were measured using a Bruker Vertex 80V Fourier Transform IR (FTIR) interferometer (Bruker Optics, Germany).

FTIR absorption spectroscopy

FTIR absorption spectra were measured to probe the THz modes and fingerprint region of ZnQ@OX-1 and its derivatives to unveil which vibrational modes are affected when the material is exposed to VOCs. From these findings, we can derive which functional groups and interactions are crucial for the sensing abilities. Interestingly, even if other MOF materials may exhibit solvatochromism, that is a visible colour change upon exposure to liquid solvents, their vibrational spectra do not change before or after exposure. In the case of ZnQ@OX-1, with its ability to change its emission colour in the presence of acetone vapour, actual changes in the vibrational spectrum are observed. Therefore, FTIR absorption spectroscopy is a powerful technique to investigate the sensing mechanisms. In these measurements, the samples are exposed to solvents, which are subsequently evaporated, such that the effect of the adsorbed molecules on the frameworks can be elucidated.

A liquid helium-cooled bolometer in combination with a 6-μm Mylar multilayer beamsplitter in the interferometer allowed for measurements in the far-IR spectral region between 0 and 650 cm^{-1}. Mid-IR measurements (550 – 4000 cm^{-1}), in addition, were carried out using a KBr beamsplitter and an in-built detector. IR spectra were collected with a resolution of 2 cm^{-1}, 256 scans per spectrum, and normalised to a background spectrum measured on an IR reflective mirror. All measurements were performed under vacuum (lower than 10^{-5} bar), and the samples were maintained at room temperature. Since these are relatively fast measurements ($\sim$ minutes), it was possible to probe various samples during the allocated beamtime, as summarised in Table 5.2. We focussed on two main questions: i) which chemical interactions are associated with the exceptional sensing? ii) how selective is the material? In our attempt to answer these questions, we prepared derivative systems of ZnQ@OX-1. For instance, the confinement of pristine 8HQ, one of the building blocks of ZnQ, led to the 8HQ@OX-1 system with a blue luminescence akin to ZnQ@OX-1; however, it does not possess any sensing abilities. Unlike ZnQ@OX-1, which is simultaneously formed by combining all individual components, that is BDC linker, metal salt, and 8HQ, in a one-pot synthesis, the encapsulation of commercially available ZnQ into the already self-assembled OX-1 framework yields a non-sensing material with a green emission. Considering the vibrational spectra, it becomes evident that, whereas the spectra of ZnQ@OX-1 material with commercial ZnQ matches the one of pristine OX-1, the ZnQ@OX-1 system exhibits in fact structural differences. This is a strong indicator for host-guest interactions that may even disrupt the framework structure, possibly leading to defects. In addition, instead of the expected ZnQ molecule, it is in fact a derivative complex evolving due to interactions with the framework that can further explain the blue emission of the composite system: if it was pristine ZnQ, a yellow emission would be expected in powder, or if encapsulated and isolated in the pores of the framework, then a green emission would be indicative akin to ZnQ in solvents. Only the distinct chemical interactions in the ZnQ@OX-1 complex lead to a blue emission, and a visible colour change when exposed to acetone.

Interestingly, if this material is exposed to other small molecule solvents such as methanol, the same vibrational changes can be observed, while the exposure to *N*,*N*-dimethylformamide (DMF), air, or water only leads to a general decrease of intensity. Derived from these observations, we can conclude that small solvent molecules can infiltrate the pores of the framework and disrupt the host-guest interactions, as described in the manuscript in Section 5.4.

In situ **gas dosing employing transmission SR-FTIR**

Since the amount of acetone in the system cannot be estimated in the FTIR absorption measurements, to address the question of sensitivity, *in situ* gas dosing experiments are required. Herein, a Harrick gas flow cell was used in a transmission

References	**Guest@MOF**	**Solvents**
OX-1	ZnQ@OX-1	Acetone
ZnQ	ZnQ@OX-1 c.	Methanol (MeOH)
8HQ	8HQ@OX-1	Dimethylformamide (DMF)
BDC		Isopropanol (IPA)
		Water
		Air
		MeOH & acetone

Table 5.2: Samples under investigation with *operando* SR-FTIR absorption measurements. The guest@MOF systems were exposed to the solvents. Abbreviation: c. = commercial.

FTIR setup based on the same interferometer at B22 MIRIAM.[204] Far-IR measurements were performed with synchrotron radiation, while a Globar IR source was employed for mid-IR measurements. Spectra were collected with a resolution of 2 cm^{-1}. The number of scans per spectrum was reduced from 128 to 64 for far-IR measurements, and from 64 to 32 for mid-IR spectra to improve time resolution. All measurements were performed at vacuum (lower than 10^{-5} bar), and the samples were maintained at room temperature. In the dosing experiments with a Harrick gas flow cell, the sample was dropcasted onto a high-density polyethylene (HDPE) window from a dispersion in hexane. An aluminium spacer was used between two windows to allow for gas flow through the cell with a chamber volume of 50 μL. The gas flow (5 cm^3/min) was achieved with a mass flow controller dosed with liquid acetone in dry carrier nitrogen gas using an SGE 50 μL gas chromatography syringe. Between measurements, the sample cell was flushed with N_2 gas at 100 cm^3/min to remove acetone from the system. Background spectra were collected by measuring the empty flow cell with dry carrier gas.

To estimate the amount of acetone in the cell at a given time, an empty cell was dosed with acetone at volumes from 1 - 50 μL. After two minutes, the first indication that acetone has reached the cell is shown, as the characteristic peaks associated with acetone emerge in the FTIR spectrum (see Figure 4 in the manuscript of Section 5.4). Their intensities increase sharply before reaching a plateau around 5 min after injection. Depending on the amount of acetone injected into the dry carrier gas, it will take between 5 and 10 minutes at the given flow rate to flush the cell and remove acetone from the cell (i.e. the characteristic peaks of acetone vanish in the measured spectrum). Knowing the volume of the cell, and the volume of acetone injected, the actual amount of acetone in the cell at a specific time can be calculated as follows:

1. The region of interest is defined as the time between the injection and the increase in flowrate to flush out all remaining acetone from the cell.
2. For each time step in the region of interest, the total area under the FTIR absorption spectrum is integrated. This is then integrated over time to obtain the total volume V_{tot} under all peaks.
3. The mass of acetone per unit volume under the peaks (arbitrary unit) is calculated by dividing the mass of injected acetone by the total volume V_{tot}.
4. The instantaneous acetone content in the cell is obtained by integrating the volume per time element (area under the spectrum at given time), and multiplying this by the mass of acetone per unit volume, divided by the volume of the cell.

As shown in Figure 4 in the manuscript 5.4, the instantaneous amount of acetone in the cell never exceeded 8 g/L based on the assumption that all injected acetone evaporated and subsequently reached the cell. In practice, however, some acetone might stick to the inner walls of the tubes such that the actual acetone content might be even lower.

Having established the upper limit for the acetone content in the cell at a given time step for each injected volume, the flow experiments were performed on powder samples of OX-1 and ZnQ@OX-1. The same spectral changes that could be observed in the *ex situ* FTIR experiments were revealed in the *in situ* gas dosing measurements, as shown in Figure 5.2.5 b: while the exposure of OX-1 to acetone only led to a superposition of the peaks associated with each material, actual changes in peak position and intensity emerged in the ZnQ@OX-1 composite system when dosed with acetone vapour. In addition, as little as 5 μL of acetone, or less than 0.2% of acetone in the cell, were sufficient to induce measurable spectral changes in the ZnQ@OX-1 sample. On the question of reversibility, it was shown that the repeated injection of 30 μL led to reproducible modifications in the spectrum that were reversed as soon as the acetone vapour was flushed out of the cell (Fig. 5c in the manuscript). However, the general peak intensity is decreased, and especially after exposure to relatively larger amount of acetone (100 μL), some irreversible transformations are revealed.

5.2.4 Fluorescence spectroscopy

To push the limit of detection even further, steady-state fluorescence spectroscopy was employed based on a FS-5 spectrofluorometer (Edinburgh Instruments). Fluorescence spectroscopy, measuring the emission of a sample, is recognised to afford higher sensitivity than other spectroscopy techniques. Compared with UV-Vis absorption, fluorescence spectra are measured over a dark background, which is inherently more sensitive than detecting small variations in intensities as in absorption spectroscopy. Or, considering vibrational spectroscopy, its sensitivity is reduced because this technique depends on the periodic vibrations of bulk material. If only a few unit cells are affected by acetone intrusion, then the strong contributions of the lattice may still dominate.

For gas dosing experiments, the instrument was equipped with a custom-built flow cell module. The inlet to the sample cell was connected with a pipe to a sealed 2 L round bottom flask, heated to 50 °C, while the outlet was connected to a syringe. Acetone was injected into the flask with a 5 μL syringe, and slow pumping of the syringe initiated the gas flow through the cell. The detection and excitation wavelengths for measuring the steady-state excitation and emission spectra, respectively, are indicated in the corresponding Figure 5 in the manuscript of Section 5.4. Each measurement is acquired from one scan with a dwell time of 0.2 s and a step size of 1 nm. To exclude the possibility that the observed decrease in intensity and shift in wavelength are caused by other effects, such as temperature of photodegradation, several stability experiments were performed prior to gas dosing. For instance, these included constant measurements in the

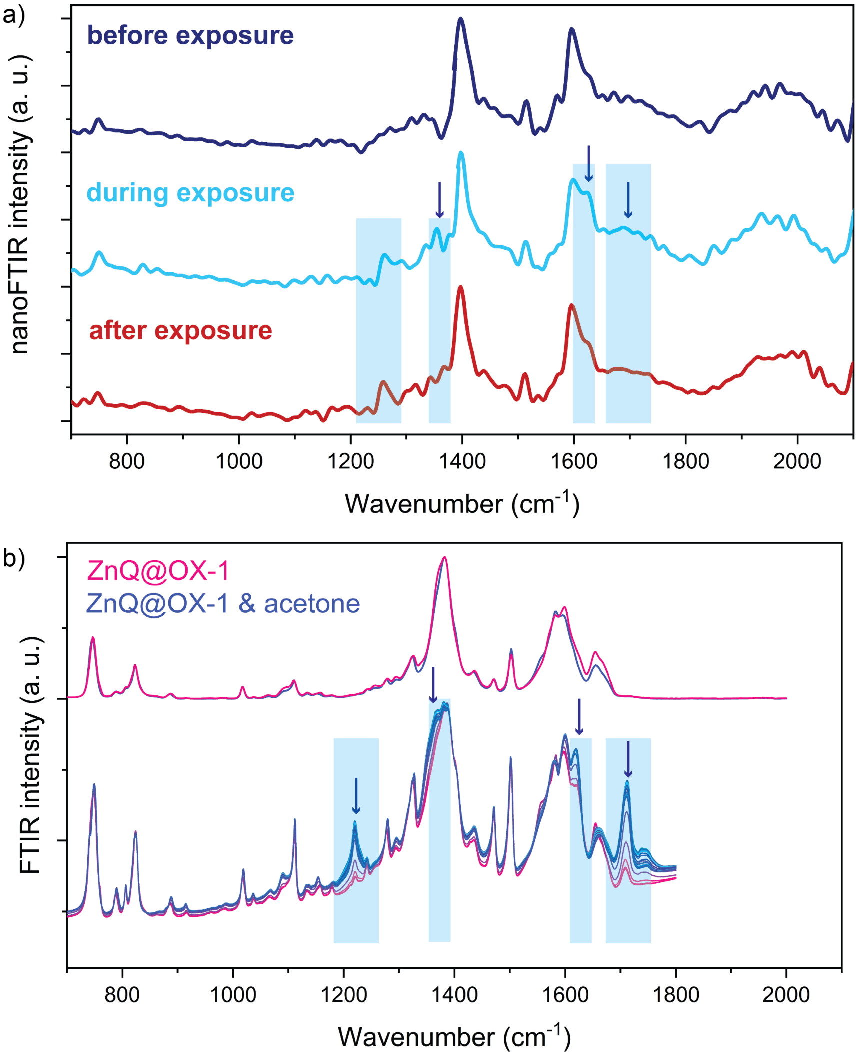

Figure 5.6: *In situ* gas dosing with nanoFTIR and SR-FTIR. a) nanoFTIR spectra of ZnQ@OX-1 before, during, and after exposure to volatile acetone. b) Comparison of *in situ* gas dosing (bottom) with *operando* SR-FTIR measurements (top).

closed system with and without heated air, or only one initial measurement followed by a second one after 80 minutes in air to avoid exposure to the xenon lamp of the instrument. In all cases, the initial intensity was decreased, but not shifted, before reaching a stable intensity that did not decrease any further. If acetone is then injected into the system, the characteristic shift in wavelength from 480 to 510 nm is observed, even for acetone amounts as low as 20 ppm.

5.2.5 *In situ* gas dosing with near-field IR nanospectroscopy

Although fluorescence spectroscopy unveiled an exceptionally high sensitivity of ZnQ@OX-1 towards acetone, this measurement technique still relies on probing bulk material (~10 mg). The amount of sample ultimately defines the limit of detection, because if only a few unit cells were occupied by acetone molecules, the response of the material would be undermined by the relatively stronger contribution of the unaffected lattice, and therefore beyond the detection limit of these spectroscopy techniques. Therefore, reducing the amount of sample under investigation is a way to push the sensitivity to even lower levels. Near-field infrared nanospectroscopy affords measuring the IR spectrum of individual MOF-type crystals. Hypothetically, fluorescence spectroscopy coupled with near-field techniques would provide the highest sensitivity to investigate the sensing behaviour of the luminescent ZnQ@OX-1 system, but to date, such technique has not yet been developed. However, even nanoFTIR enables us to measure *in situ* gas adsorption on the single crystal, which is a striking observation given that vibrational spectroscopy is deemed less sensitive than its fluorescence counterparts. Akin to the previous nanoFTIR measurements, near-field probing was achieved with the setup outlined in Chapter 2. Each spectrum was acquired from an average of 10 Fourier-processed interferograms with 9 cm^{-1} spectral resolution, 1024 points per interferogram, and 10-ms integration time per pixel. All measurements were carried out under ambient conditions. For *in situ* gas adsorption measurements, an open vial with liquid acetone was placed close to the sample stage (3 cm distance), and the evaporated acetone reached the material under investigation. Estimating the exact amount of volatile acetone reaching the sample is not possible using the current setup, but the emergence of the acetone peak in the spectrum only during exposure is a clear indication that acetone was present during the measurement. Furthermore, the same acetone-induced chemical changes that have been observed in the bulk FTIR measurements can be observed on the single-crystal level (see Figure 5.6). Remarkably, this is the first application of nanoFTIR for studying *in situ* gas adsorption, providing a new pathway for this technique. In addition, because the probing area of nanoFTIR are 20 nm, or several hundred unit cells, these findings shed light on the exceptional sensing sensitivity of ZnQ@OX-1 towards acetone.

5.3 Limitations and outlook

This multimodal study, encompassing a range of spectroscopy techniques in combination with DFT calculations, addressed the open questions on the sensing mechanisms, further governing sensitivity, selectivity, and reproducibility. However, during these experiments, we found that ZnQ@OX-1 is sensitive to humidity, and even if the shift in emission is characteristic for acetone sensing, this instability depicts a major challenge for applications, especially if targeting a breath analyser. Therefore, the design of an appropriate sensing device demands further development, either by enhancing the material to avoid humidity-induced degradation (e.g. introducing a hydrophobic matrix), or by tuning the material itself further to enhance its resistance to humidity. In both cases, the knowledge of the underlying sensing mechanism holds the key for developing a system with better stability while maintaining the exceptional sensing performance.

5.4 A multimodal study on the unique sensing behaviour of a guest@metal-organic framework material for the detection of volatile acetone

The supporting information for this manuscript can be found here:
https://onlinelibrary.wiley.com/doi/10.1002/admi.202201401.

ADVANCED MATERIALS INTERFACES
www.advmatinterfaces.de

A Multimodal Study on the Unique Sensing Behavior of a Guest@Metal-Organic Framework Material for the Detection of Volatile Acetone

*Annika F. Möslein, Mario Gutiérrez, Kirill Titov, Lorenzo Donà, Bartolomeo Civalleri, Mark D. Frogley, Gianfelice Cinque, Svemir Rudić, and Jin-Chong Tan**

Owing to their unique functionalities and tailorable properties that are unattainable in conventional materials, metal-organic frameworks (MOFs) have emerged as candidate materials for next-generation chemical sensors and optoelectronics. For instance, the ZnQ@OX-1 composite material, comprising a light-emitting guest encapsulated in the pores of the OX-1 framework, affords excellent sensing performance: a visible color change upon exposure to volatile acetone. In this work, a multimodal study on the exceptional vapochromism of this composite material using high-resolution spectroscopy techniques based on inelastic neutron scattering and synchrotron radiation is presented, supported by density functional theory calculations. While FTIR spectroscopy in the far-IR and mid-IR regions reveals the underlying interactions between ZnQ, OX-1, and acetone, the limit of detection at 50 ppm is determined through in situ gas dosing experiments using fluorescence spectroscopy. In addition, in situ gas dosing on the single crystal level is achieved with near-field infrared nanospectroscopy.

1. Introduction

The growing challenges of monitoring air pollution, industrial gas leakage, food safety, and personal health require chemical sensors with high sensitivity towards toxic gases and volatile organic compounds (VOCs).[1] In the medical sector, for instance, chemical sensors are used for the detection of glucose levels or electrolytes in human blood.[2] A noninvasive solution to detect low concentrations of VOCs in exhaled human breath does not yet exist, even if these biomarkers can be leveraged for early diagnosis and health monitoring.[3–5] In fact, this problem can be solved through the design of novel sensing technologies that harness the unique properties of metal-organic framework (MOF) materials.[6] Self-assembled from metal and organic building blocks and crystallizing in extended coordination networks, MOFs feature structural diversity, tailorability, high porosity, large surface area, and adsorption affinities, which offer unparalleled advantages for sensing applications.[1,7,8] First, selectivity can be achieved through size exclusion and specific host–guest interactions offered by their tunable pore size and functionalized binding sites. Secondly, the high porosity and large surface area of MOFs not only facilitate reversible uptake and release, but also accumulate the targeted analyte inside the pores for enhanced adsorption, and sensitivity, accordingly.

Inspired by the need for high-precision sensors, and the potential of MOF materials, several MOF-based devices have been developed to address the challenge of detecting small amounts of volatile acetone, summarized in Table S2 in the Supporting Information, as a non-invasive alternative for blood glucose measurements. In particular, metal-oxide systems that are prepared using MOFs as precursors can achieve sub-ppm limits of detection based on changes in resistance when acetone is adsorbed in the surface layer.[9–13] However, their high operating temperatures (>250 °C) seriously hinder their application in portable devices. Other MOF-based sensors, with sensitivity at room temperature, rely on changes in mechanical properties or capacitance upon exposure to acetone; these are however limited by the high concentration of the analyte required for detection, or slow response time, respectively.[14,15]

A. F. Möslein, M. Gutiérrez, K. Titov, G. Cinque, J.-C. Tan
Multifunctional Materials and Composites (MMC) Laboratory
Department of Engineering Science
University of Oxford
Parks Road, Oxford OX1 3PJ, UK
E-mail: jin-chong.tan@eng.ox.ac.uk
L. Donà, B. Civalleri
Dipartimento di Chimica
Università di Torino
Via P. Giuria 5, Torino 10125, Italy
M. D. Frogley, G. Cinque
Diamond Light Source
Harwell Campus
Chilton, Oxford OX11 0DE, UK
S. Rudić
STFC Rutherford Appleton Laboratory
ISIS Neutron and Muon Source
Chilton, Didcot OX11 0QX, UK

The ORCID identification number(s) for the author(s) of this article can be found under https://doi.org/10.1002/admi.202201401.

DOI: 10.1002/admi.202201401

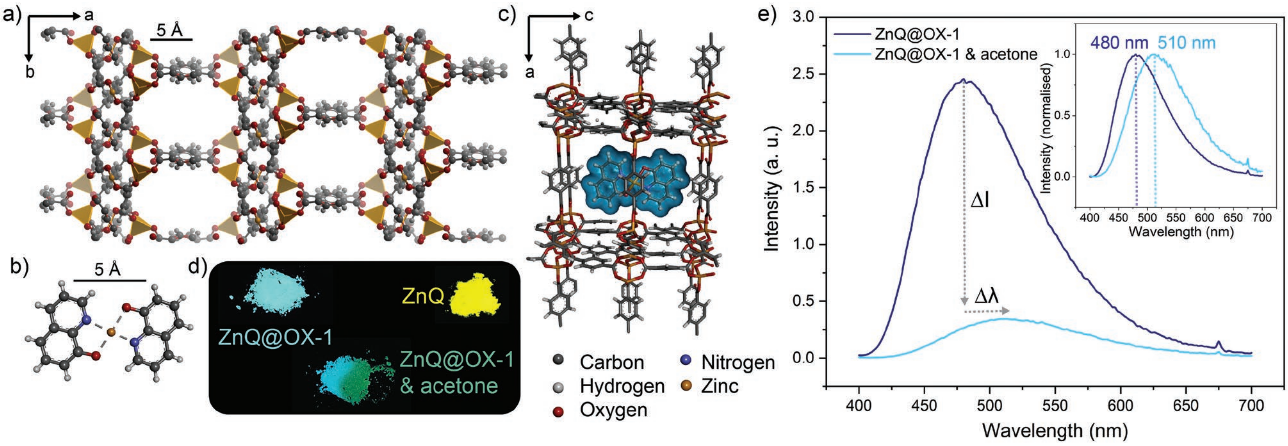

Figure 1. The ZnQ@OX-1 system. a) Structure of OX-1. b) Structure of ZnQ. c) Schematic of ZnQ encapsulated in the pores of OX-1. d) Photos of the samples under UV light (365 nm). e) Emission spectrum of ZnQ@OX-1 when exposed to acetone.

Instead, leveraging the luminescent properties is a promising strategy to design MOF-based sensor devices for the detection of gases: for instance, fluorescent quenching can be observed in the presence of acetone due to the overlap of its absorption band with the characteristic emission of the MOF.[16,17] However, because a decrease in emission intensity (or turn-off behavior) could also stem from photodegradation, or other phenomena, a shift in emission is a simpler way of detection. Such vapochromic behavior, which describes a visible color change when exposed to a gaseous analyte, is a promising way for signal transduction in optical sensors, and yet, this phenomenon is unattainable in most MOF materials. Few exemptions do however exist: the luminescent octahedron@ZIF-8 composite material exhibits a visible color change under UV irradiation when exposed to acetone for more than 15 min.[18] An even faster response (within seconds) is achieved by the "OX-1" framework, a zinc-based MOF with 1,4-benzenedicarboxylic acid (BDC) as the organic linker.[19] Only the confinement of the luminescent guest zinc(II) bis(8-hydroxyquinoline) (ZnQ) inside the pore channels of the host framework leads to the opto-chemically responsive ZnQ@OX-1 complex (**Figure 1**a–c). When subjected to UV radiation, the pristine ZnQ complex, where two 8-hydroxyquinoline (8HQ) aromatic molecules are coordinated to a single Zn center, emits an intense yellow light, or if the molecules are isolated in solution, a green light.[20,21] The ZnQ@OX-1 complex, however, exhibits an emission of blue light (480 nm), which, upon exposure to acetone, changes to a green emission (510 nm), as shown in Figure 1d. This shift in maximum emission wavelength is accompanied by quenching of emission intensity in the macroscopic scale, as the signal is decreased by one order of magnitude (Figure 1e). Hence, it is the unique photochromism, or in other words, its ability to change luminescent color in the presence of volatile acetone, that renders ZnQ@OX-1 such a promising candidate for bespoke application. Of course, solvatochromism, which describes a change in emission (or color) when subjected to different solvents, is a well-known phenomenon in MOFs, however, the fast (approximately seconds), visible response of the ZnQ@OX-1 complex to gaseous acetone is hitherto unique.[18,22,23] And yet, even if the ability of the material to sense volatile acetone has been demonstrated with a proof-of-concept device,[19] little is known about the underlying sensing mechanism. To address this challenge, we use a multimodal approach to unravel the physical and chemical interactions that are responsible for the unique gas sensing behavior. Herein, we employ spectroscopy techniques ranging from near-field and conventional Fourier transform infrared spectroscopy (FTIR) to large-scale facilities such as synchrotron-radiation based FTIR and inelastic neutron scattering (INS); all these empirical observations are further corroborated by density functional theory calculations. As a result, we acquire a thorough understanding of the sensing mechanism itself, which holds the key to tune the material further for enhanced sensing performance towards application.

2. Results and Discussions

2.1. Inelastic Neutron Scattering

Employing the TOSCA spectrometer[24] at ISIS Neutron and Muon Spallation Source, we performed inelastic neutron scattering (INS) measurements to unravel the conformational changes in the framework upon guest encapsulation and subsequent exposure to acetone. Herein, each sample was probed at 10 K for several hours. As a reference, we measured the pristine OX-1 material which does not possess any sensing abilities. When exposed to acetone, all additional peaks emerging in the INS spectrum can directly be assigned to acetone peaks and thus, the resulting spectrum is simply a superposition of the two spectra associated with pristine OX-1 and acetone, respectively, instead of indicating chemical changes (**Figure 2**a). Only in the low-energy region, the sharp peaks of pristine acetone are broadened, since, instead of crystallizing at low temperatures, the acetone molecules are isolated in the pores of the framework resulting in the loss of long-range order. In general, the modes are unaffected, and it is the lack of interactions between OX-1 and the analyte that explains why the material does not respond to the presence of acetone. However, if ZnQ is encapsulated in the framework material, we observe salient changes in the INS spectrum compared to pristine OX-1 (Figure 2b). While the presence of most peaks can be linked with peaks of either ZnQ or OX-1, such as the additional peaks at 190 or 590 cm^{-1},

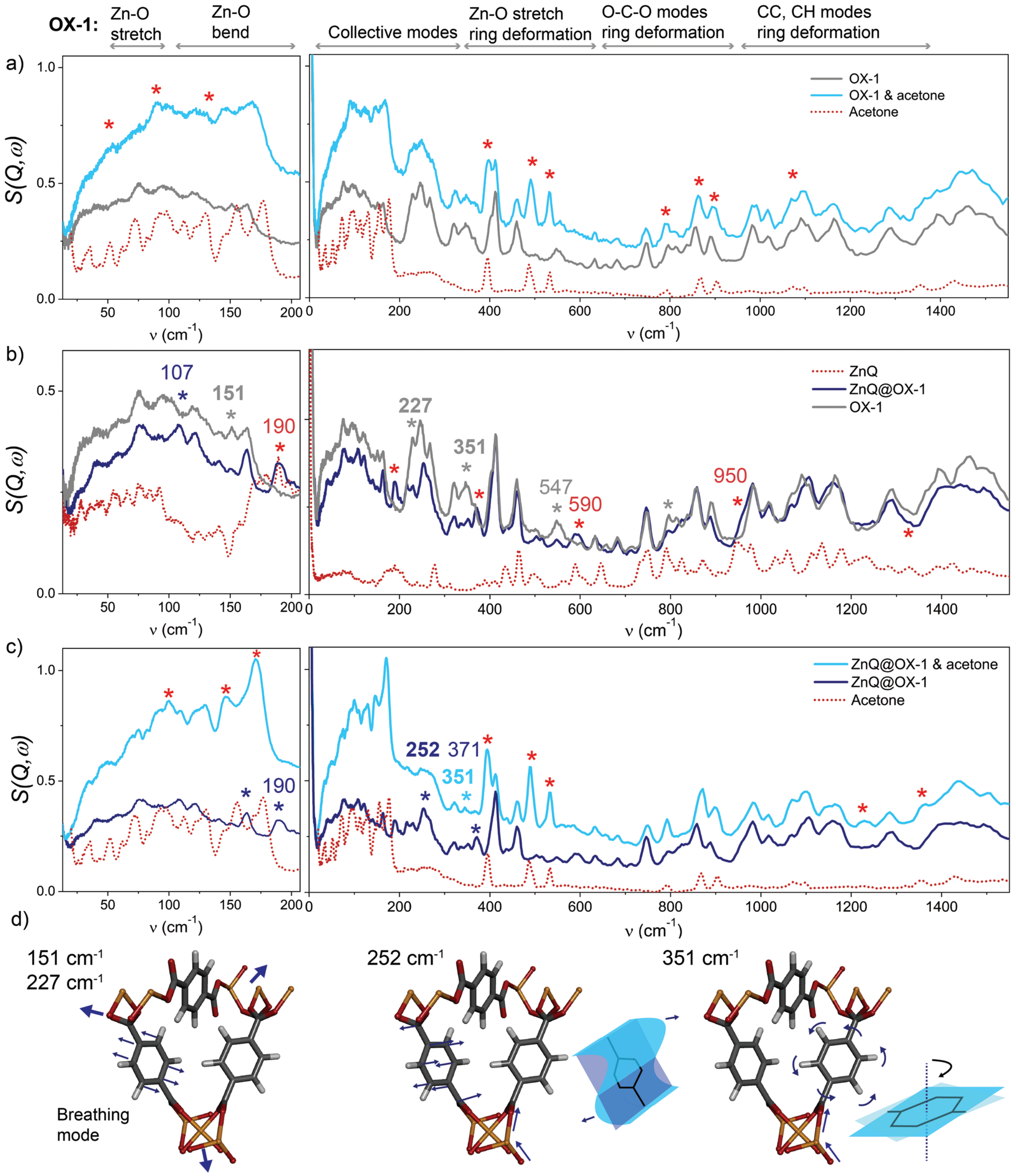

Figure 2. Inelastic neutron scattering (INS) spectra of ZnQ@OX-1 systems (scaled by mass). a) INS spectra of OX-1 before and during exposure to acetone compared with pristine acetone, reproduced from S.F. Parker, ISIS Facility, Chilton, UK. b) INS spectra of ZnQ@OX-1 and pristine host and guest materials. The broadband spectrum of ZnQ was scaled down for better comparison. c) ZnQ@OX-1 before and during exposure to acetone. d) Illustration of key vibrational modes of OX-1 affected by guest encapsulation.

or the shoulder at ≈950 cm^{-1} (all assigned to the ZnQ guest), a few changes which differ from simple superposition can be discovered. For instance, an additional peak at 107 cm^{-1} appears in a region where we observe deformation of the O—Zn—O groups (Figure 2b), as derived from density functional theory calculations (see Table S3 in Supporting Information). This indicates structural changes and stronger O—Zn—O coordination, perhaps due to the interactions with the ZnQ complex. Meanwhile, the intensities of the peaks at 151, 227, 351 and 547 cm^{-1}, associated with pristine OX-1, are reduced, especially in relation to nearby peaks (Figure 2b). The modes at 151 and 227 cm^{-1} are ascribed to symmetric and asymmetric stretches of the Zn—O bonds resulting in out-of-plane deformations of the ring, which, consequently, trigger breathing-like modes of the pore. The two vibrations at 351 and 547 cm^{-1} that are associated with an asymmetric stretch of the Zn—O bond cause in-plane deformations of the ring, such as rotations. Significantly, the reduced intensity of these four "bulky" modes indicates their hindrance due to guest encapsulation.

These observed changes cannot simply be explained by superposition of the INS spectra of the pristine materials and are therefore a strong indicator for interactions between the luminescent guest and host framework in the ZnQ@OX-1 system. Interestingly, when the resulting ZnQ@OX-1 complex is then exposed to acetone, precisely these vibrational bands are among the ones that exhibit noticeable change, even if, at first glance, the spectrum seems to be the sum of the peaks of ZnQ@OX-1 and acetone. A close look reveals that the vibrational band at 190 cm^{-1}, associated with the ZnQ guest molecule, has reduced intensity in the presence of acetone. Similarly, the intensities of the peak at 351 cm^{-1}, which is characteristic for OX-1 but is reduced in the host–guest system, and the one at 371 cm^{-1} change in relation to each other upon exposure to acetone. In addition, the shape of the vibrational band at 252 cm^{-1} (Zn–O asymmetric stretch and tilting of the ring) is broadened, perhaps due to masking by the acetone peak (Figure 2c,d). Given that most spectral variations differ from superposition of the INS spectra of ZnQ@OX-1 and acetone, actual chemical and structural changes that are responsible for the unique sensing behavior, occur in the framework.

2.2. Synchrotron-Based FTIR Spectroscopy

To address these changes that are so crucial to understanding the mechanism itself, we performed density functional theory (DFT) calculations and (synchrotron-radiation) SR-FTIR at the MIRIAM beamline B22 at the Diamond Light Source (Oxfordshire, UK). The main advantage of the latter is that we can measure the full broadband spectrum (far-IR from 40–600 cm^{-1}, and mid-IR from 400 to 2000 cm^{-1}). Herein, we employed the Bruker Vertex FTIR spectrometer under vacuum with two different beam splitters (Mylar and KBr), as well as a bolometer and a built-in detector to measure the far-IR and mid-IR regions, respectively. Only the combination with DFT simulation however can attribute the physical vibrations with the observed peaks, therefore, we performed frequency calculations of OX-1 with the CRYSTAL17 DFT code.[25,26] Because the PBEsol0-3c composite method has recently emerged as a cost-effective way to simulate MOF materials, it was used in this work to provide functionals with basis sets for each of the 202 atoms per unit cell.[27–31] The continuous IR spectrum was obtained by fitting the calculated frequencies with Lorentzian peak shapes with a FWHM of 10 cm^{-1}. As shown in **Figure 3**a, a good match between theory and empirically measured IR spectrum is achieved. Crucially, in the far-IR region, we can observe lattice vibrations, or so-called collective Terahertz modes, which are inherently linked with structural vibrations of the entire framework, while vibrations of specific functional groups are registered in the mid-IR region.

Considering the full broadband spectrum thus reveals both structural and chemical information. For instance, the low-energy or Terahertz region encompasses lattice dynamics where key vibrational modes trigger channel-opening or shearing modes that can underpin physical phenomena ranging from enhanced gas uptake to structural instabilities.[32–34] Below 270 cm^{-1}, vibrational modes of the Zn—O with a change of angle between the bonds introduce structural deformations of the pore and channels, for instance by causing a rotation of the entire linker units. Stretching vibrations of the metal clusters, on the other hand, are prevalent in the region between 270 and 470 cm^{-1}. Even if the Zn atoms are involved in the asymmetric stretching modes observed above 470 cm^{-1} and below 700 cm^{-1}, they remain fixed and instead, in-phase ring deformations are triggered. Accordingly, in-phase and out-of-phase ring deformations are observed in the region of 700–1000 cm^{-1}, more specifically caused by stretching modes of the O—C—O groups below 850 cm^{-1}. Vibrational modes associated with the stretching of C—C bonds and scissoring (or rocking) of the C—H groups appear below 2000 cm^{-1}, while peaks above can be attributed to stretching modes of the C—H bonds. It is worth mentioning that a complete assignment of the vibrational modes of OX-1 can be found in the Supporting Information (see Table S3).

Upon exposure to acetone, OX-1 does not reveal any significant spectral changes (Figure 3a). One might argue that the general intensity is increased in the far-IR region and decreased in the mid-IR region; however, this feature is a bulk shift in intensity rather than spectral changes of individual peaks. It is the encapsulation of ZnQ in OX-1 that leads to spectral changes which cannot simply be explained by the coexistence of guest and host material, as already indicated in the INS spectra. Instead, the host–guest interactions might in fact alter the chemical environment, or even the structural lattice as a whole. This hypothesis can be confirmed by SR-FTIR measurements when comparing two different synthetic routes. First, we encapsulated commercially available ZnQ in the OX-1 framework (termed "ZnQ@OX-1 commercial"). Interestingly, albeit unveiling the same spectral features as OX-1 (Figure 3b), this synthetic route leads to a material without any sensing abilities, already emitting green light (Figure S14, Supporting Information). The second approach involves a one-pot synthesis, where ZnQ and OX-1 form simultaneously from the reactants zinc nitrate hexahydrate, 1,4-benzenedicarboxylate (BDC) linker, and 8-hydroxyquinoline (8HQ). However, the resulting ZnQ@OX-1 system exhibits significant spectral deviations from the pristine OX-1 framework material, in particularly in the far-IR region (Figure 3b). This is precisely where collective modes are prevalent, and the strong changes indicate that indeed, structural changes, remaining *N*,*N*-dimethylformamide (DMF) molecules from the synthesis, or even defects occur in the OX-1 framework when ZnQ is synthesized and confined in the same reaction. In fact, these findings can explain previously reported variations in the PXRD patterns of OX-1 and ZnQ@OX-1.[19] Similarly, actual chemical interactions emerge between the framework, ZnQ

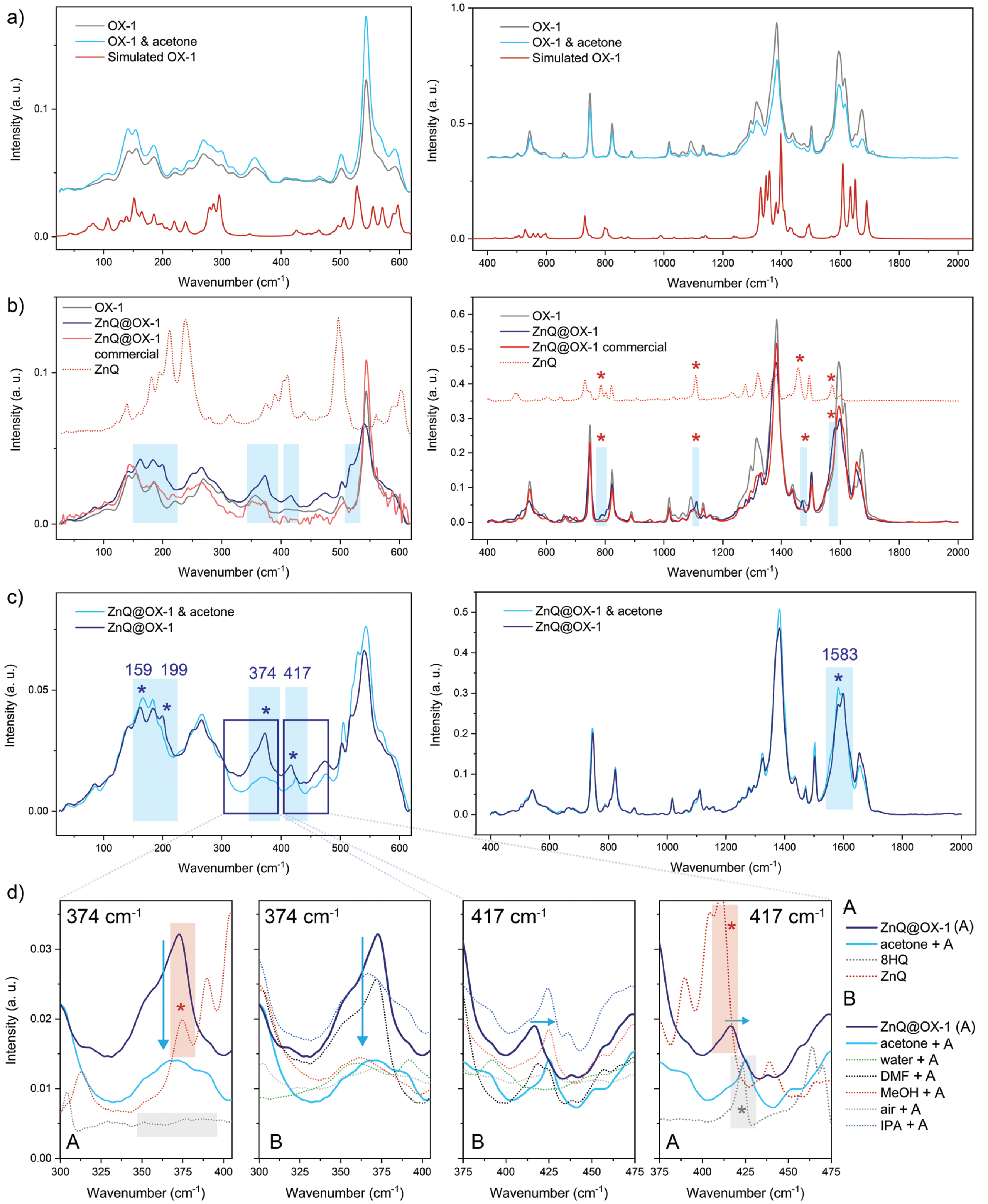

Figure 3. SR-FTIR spectra. a) OX-1 and acetone reveal no spectral changes. b) Simultaneous formation and encapsulation of ZnQ in the OX-1 framework lead to structural and chemical changes that are not observed when commercial ZnQ is added during the synthesis of OX-1 (ZnQ@OX-1 commercial). These chemical interactions are key to the sensing performance. c) Upon exposure to acetone, chemical changes are observed. d) Insets show comparison with pristine guest material and evolution of specific modes upon exposure to various solvents.

complex, and solvents, that are key to the sensing performance, while the functional groups of both materials are still intact, as shown in the mid-IR region, where all additional peaks can be explained by the presence of ZnQ (Figure 3b).

Since the simultaneous formation of ZnQ and OX-1 lattice induce a competition for Zn atoms, some 8HQ molecules might be bound to Zn clusters of the framework, or even interacting with the BDC linker and remaining DMF molecules in the axial position. As a result, the confined ZnQ complex is in fact a derivative, where the altered atomic environment leads to different electronic states, and thus distinctive luminescent behavior. This phenomenon can ultimately explain why we observe the blue emission instead of the green emission, which would be characteristic for ZnQ if isolated in the pores of the framework. As soon as the ZnQ@OX-1 complex is exposed to solvents such as acetone, water, or methanol—all of these relatively "small" solvents that can infiltrate the framework through channels and pores—spectral changes are induced, while "larger" solvents (e.g., DMF) do not disrupt the framework (Figure 3c,d, Figures S10 and S11, Supporting Information), as they do not enter in the pores.

We also probed derivatives of the ZnQ@OX-1 system (8HQ@OX-1, commercial ZnQ@OX-1), exposed to acetone and other solvents, and yet, only the ZnQ@OX-1 complex, as synthesized in a one-pot reaction, exhibited a visible response. Even though small spectral changes can be observed if 8HQ@OX-1 is exposed to acetone, an observation which we attribute to the coordination of some 8HQ molecules to the Zn clusters of OX-1 (and de facto forming ZnQ complexes), their concentration is still too small to produce an emissive material. Therefore, neither a visible change in color nor any optochemical response can be observed for 8HQ@OX-1 as opposed to the ZnQ@OX-1 system. The sensing mechanism of the latter is better understood through a closer look at the spectral changes happening in the presence of acetone. For instance, upon exposure, the peak at 169 cm^{-1} shifts back to a lower energy at 158 cm^{-1}, a peak that is linked with O—Zn—O wagging and ring torsion in pristine OX-1. Similarly, the intensity of the additional peak at 199 cm^{-1}, only observed after guest confinement and attributed to the CH_3 rocking and C–O–Zn rocking in ZnQ, is reduced (Figure 3c). This almost indicates that the framework "recovers" when small solvents enter the framework and disrupt the host–guest interactions between ZnQ and OX-1. The intensity of the peak at 374 cm^{-1}, which is only observed in ZnQ@OX-1 and can be attributed to the vibrations of the Zn—O bonds in ZnQ, decreases when the material is exposed to acetone, or other small solvents, whereas less pronounced changes to this vibrational band are exhibited in the presence of the larger 2-propanol (IPA) molecules, as, due to their size, they will infiltrate the framework at a slower rate (Figure 3d). No changes are observed when the material is exposed to DMF, as remaining solvent molecules are likely to be present in the framework after synthesis. It is worth noting that this peak is absent in the 8HQ molecule without coordination to Zn clusters.

The above finding leads to the conclusion that, upon exposure to small solvents (e.g., water, MeOH, and acetone), the host–guest interactions are disrupted as the solvent molecules enter the framework, and as a result, the guest interacts with the solvent rather than the framework. Now, the Zn—O and Zn—N interactions of the guest that is partially bound to the framework, with the zinc atom initially connected to one quinoline molecule and the framework on the other coordination site, are disturbed, and the guest is not fully coordinated to the framework anymore. The same is true for the peak at 417 cm^{-1}, which, too, is attributed to Zn—O modes in ZnQ. When exposed to acetone or methanol, this peak is shifted to 425 cm^{-1}, a mode associated with 8HQ (Figure 3d). Akin to the previous explanation, the solvent molecules interrupt the interactions between ZnQ and OX-1, and the confined ZnQ complex is not coordinated with the framework anymore. Instead, the spectral fingerprint of the framework is more similar to pristine OX-1, and a mix of conventional ZnQ and 8HQ molecules is prevalent. If the ZnQ@OX-1 system is exposed to acetone or methanol, this phenomenon, coupled with the possibility of guest aggregation, can also explain the observed decrease and shift in emission intensity to the one expected for undistorted ZnQ.

2.3. In Situ Gas Dosing Experiments with Synchrotron-Based FTIR Spectroscopy

While these findings explain the sensing mechanisms, we now turn to the open questions on the level of detection and reversibility of the sensing itself. Again, we employed SR-FTIR, albeit operated with a Harrick flow cell, where small amounts of acetone were injected into dry nitrogen carrier gas. One useful assumption to make is that all the liquid acetone injected into the system vaporizes and passes through the sample cell, although some trace amounts are likely to remain on the metal surfaces of the pipes leading up to the sample cell. For a first approximation, this assumption allows for a calculation of acetone concentration: if the total volume under the surface of the time-resolved acetone vapor spectra corresponds to the amount of acetone injected, then the volume element at any point in time under these spectra corresponds to a proportional fraction of the total volume of acetone injected. Integration over the entire spectrum at a specific time then provides the acetone concentration in the sample cell at that time step (**Figure 4**a–c). The injected volume was altered between 1 and 50 µL, and yet, the maximum concentration of acetone in the cell remained under 8 g L^{-1} or 0.8% of cell volume (Figure 4c). There is no doubt that additional peaks at 392, 492, 529, 1220, 1358, and 1710 cm^{-1} can be observed when acetone reaches the pristine OX-1 sample (Figure 4d). But while this is true, all these peaks can directly be assigned to the peaks of acetone, indicating the lack of chemical interactions between the sample and volatile gas. As expected, the injection of higher amounts of acetone (10, 20, and 30 µL) leads to stronger occurrence of the corresponding peaks, while the recurrent injection of 30 µL demonstrates reversibility of the measurement, although some acetone is deemed to remain on the surface of the cell (Figure 4d).

The optochemically responsive ZnQ@OX-1 complex, in turn, exhibits strong spectral changes upon gas dosing with acetone. As little as 5 µL (or 1.5 g L^{-1} in the sample cell) is enough for the material's response to be detected in the FTIR spectrum (**Figure 5**b). To some extent, the responsiveness scales with the

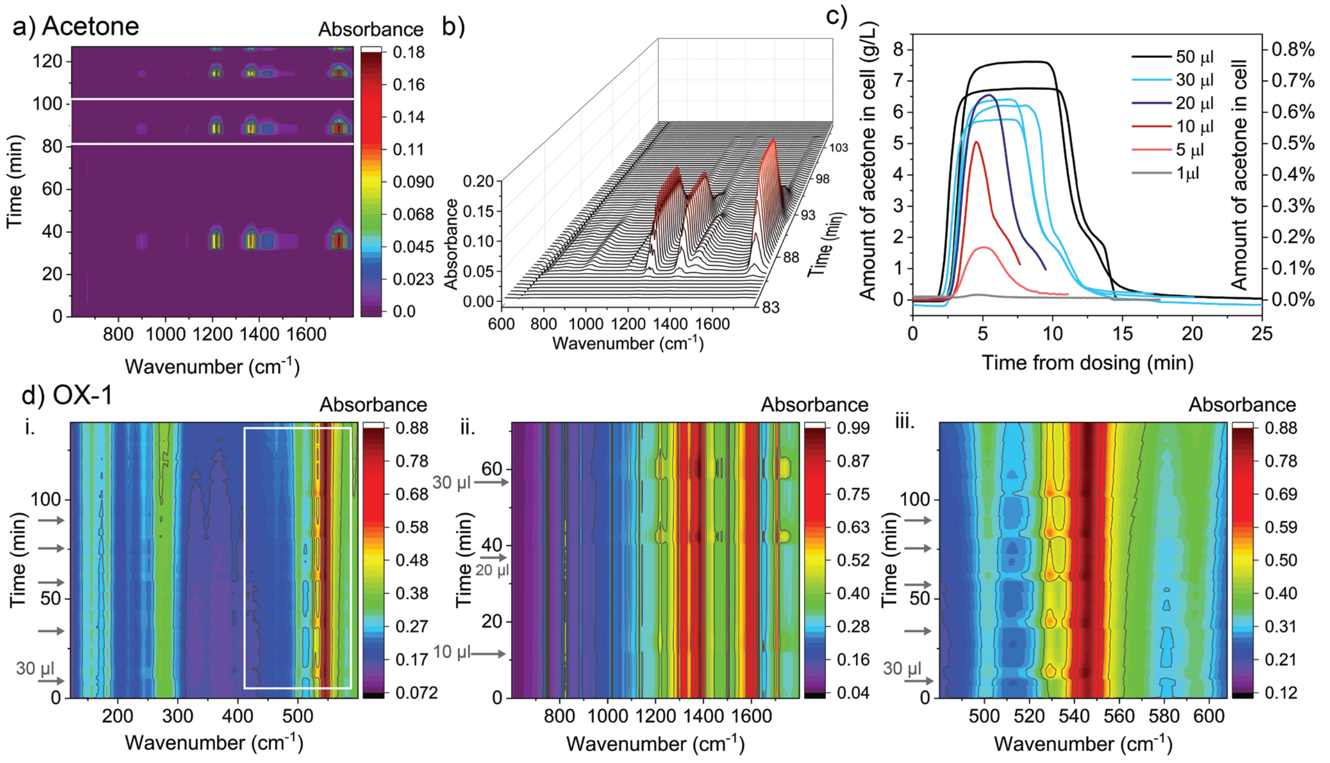

Figure 4. Reference measurements for gas dosing experiments with SR-FTIR. a) Time-resolved spectra of flow cell exposed to N_2 carrier gas with acetone injections. b) 3D plot of transient spectra corresponding to the second injection. At $t = 100$ min, the flow rate was increased to flush the remaining acetone. c) Calculated acetone concentration in cell after injections. d) OX-1 exposed to acetone injections: i) far-IR spectrum, 5 times injected with 30 µL, ii) mid-IR spectrum, injected with 10, 20, and 30 µL, iii) Mid-IR spectrum injected with 5 × 30 µL.

amount of acetone injected, although the system seems to be saturated after high injections and irreversible changes in the spectrum appear. On the question of reversibility, we repeatedly injected 30 µL into the system, and the response is clearly reversible, however, the same trend that large amounts of acetone induce permanent changes in the framework eventually reduce the sensing ability of the material (Figure 5c). As discussed before, the key vibrational band at 169 cm^{-1}, associated with Zn—O wagging and ring torsion in OX-1, is shifted, and the peak at 199 cm^{-1} that has emerged after guest encapsulation is strongly reduced when exposed to acetone (Figure 5d-i). Similarly, the peak at 374 cm^{-1} (Zn—O) decreases, even permanently, and does not recover. An additional peak emerges at 439 cm^{-1}, and the peak at 417 cm^{-1} is shifted to higher energies, indicating that Zn—O bonds are replaced with O—H bonds, as the interactions between the solvent and ZnQ substitute the host–guest interactions (Figure 5d-ii). Turning to the mid-IR region, we observe an increase of the vibrations around 1710 cm^{-1} that are related to the presence of acetone. Interestingly, the linker vibrations at 1582 and 1654 cm^{-1}, both initially decreased and shifted to lower wavenumber when ZnQ is encapsulated, are now subject to changes in intensity and shifted in wavelengths, respectively, while ring modes (such as 1494 cm^{-1}) neither change upon guest encapsulation nor in the presence of acetone (Figure 5d-iii). The main difference lies in the functional groups that are involved: it is mainly the modes associated with the C and O atoms of the linker that are affected by host–guest and solvent interactions rather than the aromatic rings. More specifically, the intensity of the peak at 1654 cm^{-1} (or 1737 cm^{-1} in the unscaled DFT simulation) that is associated with the twisting mode of the O—C—O groups is strongly decreased in the presence of acetone or methanol. The peak at 1494 cm^{-1} (≈1567 cm^{-1} in DFT simulated spectrum), in contrast, is attributed to CH rocking and in-phase ring mode, and thus hardly affected. This is an indicator that ZnQ interacts with both the O atoms in the linker and the Zn clusters, but not with the aromatic ring itself. Similarly, the ring of the ZnQ molecule is unaffected by host–guest interactions, as confirmed by DFT calculations, where two different models were simulated (Figure S18, Supporting Information). Hence, the strong interactions between the Zn and O atoms of the linker, Zn clusters, ZnQ, and DMF that result in a distorted framework and an altered ZnQ complex, hold the key to the extremely sensitive behavior, and the ability to sense volatile acetone, which further relies on the ability of small solvent molecules to enter the framework and disrupt bespoke interactions.

2.4. Fluorescence Spectroscopy and In Situ Gas Dosing with Near-Field Infrared Spectroscopy

The foregoing findings, which in fact suggest that even low amounts of volatile acetone can lead to an optochemical response of the ZnQ@OX-1 complex, motivated us to perform gas dosing experiments with fluorescence spectroscopy, since changes in emission can be detected more easily than

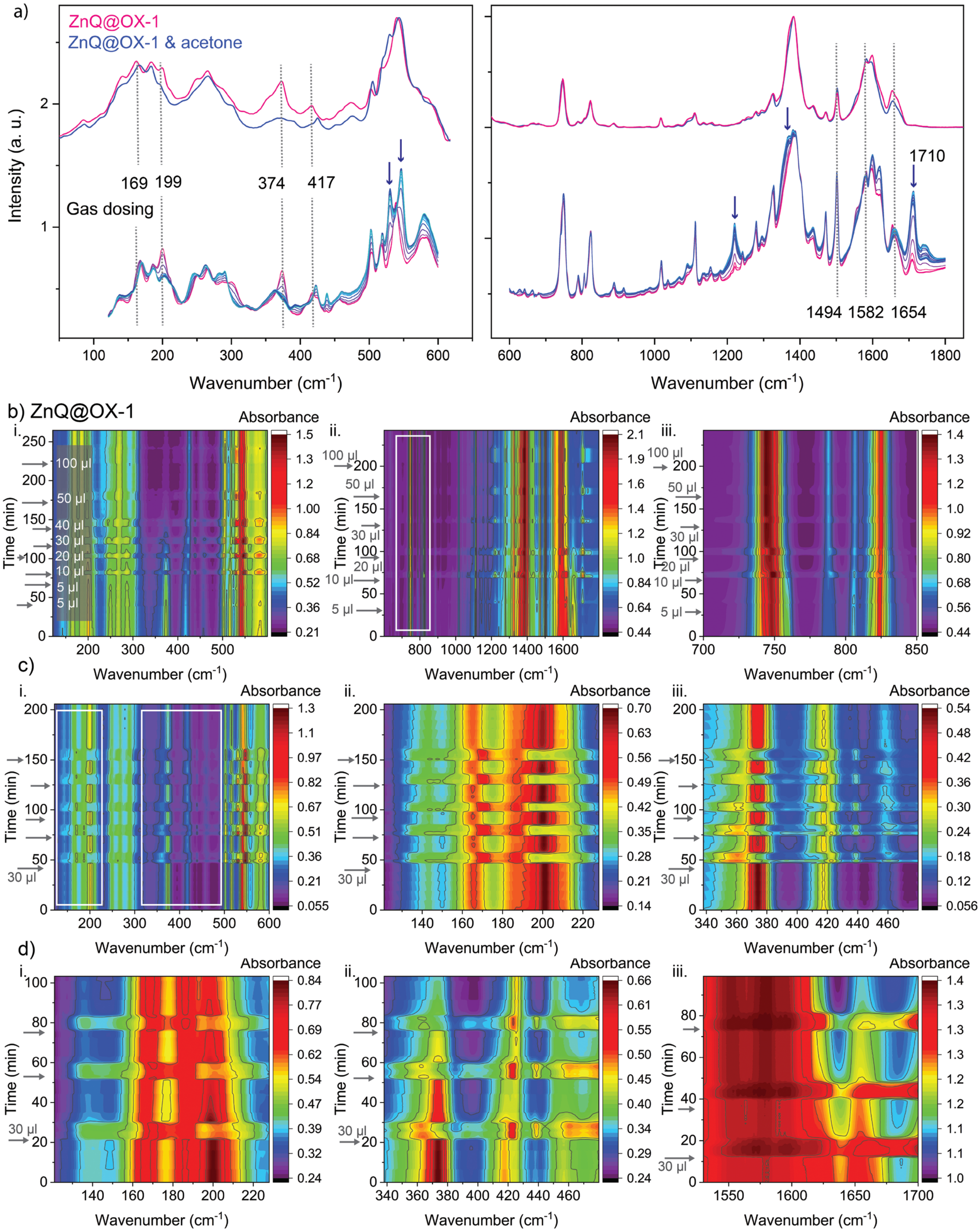

Figure 5. Gas dosing experiments of ZnQ@OX-1 with SR-FTIR. a) SR-FTIR absorption spectra of ZnQ@OX-1 before and after exposure to acetone compared with in situ gas dosing measurements using transmission SR-FTIR. b) Contour plots showing time-dependent spectral data of ZnQ@OX-1 exposed to increasing amounts of acetone (i. far-IR, ii. mid-IR, iii. Zoomed into region 700–850 cm^{-1}). c) ZnQ@OX-1 exposed to 5 injections of 30 µL (i. far-IR, ii. 120–230 cm^{-1}, iii. 340–500 cm^{-1}). d) ZnQ@OX-1 exposed to 3 × 30 µL.

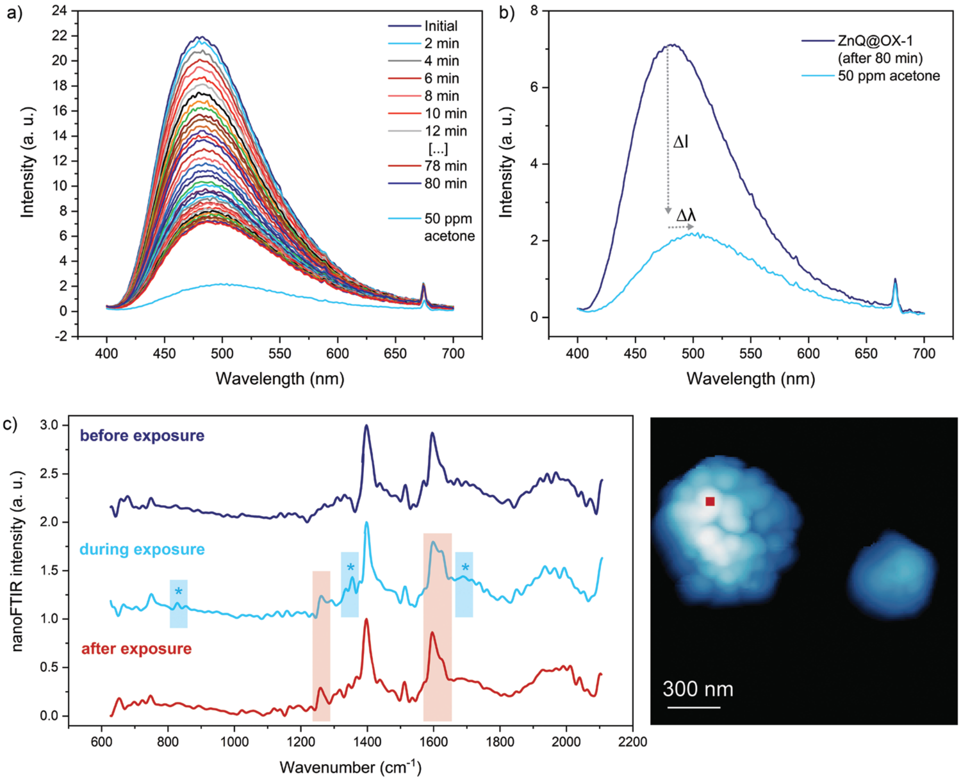

Figure 6. Response of ZnQ@OX-1 to low concentrations of acetone. a) Emission spectra of ZnQ@OX-1 after exposure to air. b) Emission spectra of ZnQ@OX-1 after 80 min (stable emission) and exposed to 50 ppm volatile acetone. c) Near-field infrared spectroscopy on a 20 nm spot on individual crystals of ZnQ@OX-1 before, during and after exposure to acetone (position indicated in AFM image).

chemical transformations in FTIR spectroscopy. In the light of this, we employed a fluorescence spectrometer with a customized gas flow cell to dose the sample with acetone concentrations as low as 5 ppm (see Figure S3, Supporting Information). Prior to dosing, a strong decrease in emission intensity is observed; a trend that we attribute to the initial "activation" of the pristine material (Figure 5a). Either it is the photo-instability induced by the strong emission of the Xenon lamp, or the sensitivity to the humidity of ZnQ@OX-1 in the presence of ambient air. The latter seems to be more likely, especially, since we performed the same experiment without intermediate steps to avoid illumination of the sample, and the same decrease in intensity with time was observed. Nevertheless, after 60 min, the change in emission intensity has stagnated. With this stability being attained, a low concentration of acetone (e.g., 50 ppm) was then injected into the closed system, and vaporized in a round-bottom flask heated at 50 °C before reaching the sample cell through pipes. Interestingly, even such low concentrations of acetone vapor, lead to the shift in emission from 480 to 510 nm, coupled with a strong quenching of emission (**Figure 6**a,b). An irreversible response is however observed if larger amounts of acetone are adsorbed by the sample.

To push the limit of detection even further, we used nanoscale analytical techniques to show in situ gas adsorption from a new perspective: at the single-crystal level. Herein, scattering-type scanning near-field optical microscopy (s-SNOM) in combination with nano-FTIR allowed us to measure the IR spectrum of a 20 nm spot on the ZnQ@OX-1 crystal.[35–37] We then exposed the crystal to acetone vapor by placing an open vial with liquid acetone in proximity to the measurement stage. During the measurement, the acetone evaporates and reaches the ZnQ@OX-1 sample. Interestingly, as shown in Figure 6c, we observe the same spectral changes from a single crystal when compared with "bulk" measurements performed on polycrystalline samples in the order of milligrams (conventional FTIR techniques, fluorescence spectroscopy) to grams (INS). More specifically, only during exposure, the acetone peaks at 1358 and 1710 cm^{-1} emerge in the nano-FTIR spectrum and disappear again, while the acetone-induced chemical changes in the framework, such as the substitution of Zn—O bonds (indicated by the peak at 1654 cm^{-1}) and DMF molecules, are even detectable after exposure. This first exemplar of in situ gas adsorption on single crystal not only demonstrates a new nanoscopic route to study sensing phenomena on much smaller scales, but also unveils the strong response of ZnQ@OX-1 to acetone vapor.

3. Conclusion

In summary, we performed an in depth and multimodal study on the unique sensing behavior of ZnQ@OX-1, which exhibits a visible luminescent color change when exposed to small amounts of volatile acetone. Using high-resolution spectroscopy techniques based on INS and SR-FTIR revealed that the OX-1 framework changes when ZnQ is encapsulated in a one-pot synthetic route. Corresponding DFT simulations explained the empirically shown vibrational changes and provided further insights into the sensing mechanism: during the synthesis, the interaction with DMF solvent molecules and the competition for Zn clusters between the formation of OX-1 and ZnQ led to a distorted framework and a derivative ZnQ complex exhibiting different luminescent behavior when compared to ZnQ either in solution or aggregates (see Figure S15 in the Supporting Information). Upon exposure to acetone, or other small molecule solvents, the host–guest interactions are disrupted and ZnQ returns to its normal state, as revealed by the green emission that is expected when ZnQ is isolated in the pores of OX-1. Using in situ gas dosing experiments with synchrotron radiation, we observed a reversible response, although large amounts of acetone led to irreversible changes. To push the limit of detection, we further employed fluorescence spectroscopy, where amounts as low as 50 ppm of acetone resulted in the quenching and shift in emission. In addition, we achieved the first in situ gas adsorption on single-crystals using near-field infrared nanospectroscopy, which reveal the same spectral changes as observed with conventional FTIR techniques. We found that ZnQ@OX-1 is unstable in water vapor and therefore, the design of a sensing device focusing on human breath needs further development to shield the active material from water-induced degradation (e.g., encapsulation in a hydrophobic polyvinyl difluoride (PVDF) matrix). Our findings explain the underlying mechanism of the exceptional sensing behavior of ZnQ@OX-1 that was previously unknown. Ultimately, this understanding can be leveraged to tune the system further and achieve better stability while maintaining the high-sensitivity sensing performance.

Supporting Information

Supporting Information is available from the Wiley Online Library or from the author.

Acknowledgements

A.F.M. thanks the Oxford Ashton Memorial Scholarship for a D.Phil. studentship award. J.-C.T. and A.F.M. are grateful for funding through the ERC Consolidator Grant (771575 (PROMOFS)) and the EPSRC Impact Acceleration Account Award (EP/R511742/1). The authors are grateful for large facilities access through the ISIS Beamtime at TOSCA (RB2010346) and the Diamond Beamtime at B22 MIRIAM (SM14902-3 and SM25407-2). The authors acknowledge the use of the University of Oxford Advanced Research Computing (ARC) facility in carrying out this work (https://doi.org/10.5281/zenodo.22558). Via the membership of the U.K.'s HEC Materials Chemistry Consortium (MCC), which is funded by EPSRC (EP/R029431), this work used the ARCHER2 UK National Supercomputing Service (http://www.archer2.ac.uk).

Conflict of Interest

The authors declare no conflict of interest.

Data Availability Statement

The data that support the findings of this study are available from the corresponding author upon reasonable request.

Keywords

gas dosing, inelastic neutron scattering, infrared spectroscopy, metal-organic frameworks, sensing mechanism

Received: June 23, 2022
Revised: September 13, 2022

---

[1] L. E. Kreno, K. Leong, O. K. Farha, M. Allendorf, R. P. Van Duyne, J. T. Hupp, *Chem. Rev.* **2012**, *112*, 1105.
[2] G. Matzeu, L. Florea, D. Diamond, *Sens. Actuators, B* **2015**, *211*, 403.
[3] M. Phillips, J. Herrera, S. Krishnan, M. Zain, J. Greenberg, R. N. Cataneo, *J.Chromatogr. B: Biomed. Sci. Appl.* **1999**, *729*, 75.
[4] J. D. Fenske, S. E. Paulson, *J. Air Waste Manage. Assoc.* **1999**, *49*, 594.
[5] S. Das, M. Pal, *J. Electrochem. Soc.* **2020**, *167*, 037562.
[6] I. Stassen, N. Burtch, A. Talin, P. Falcaro, M. Allendorf, R. Ameloot, *Chem. Soc. Rev.* **2017**, *46*, 3185.
[7] H. Furukawa, K. E. Cordova, M. O'Keeffe, O. M. Yaghi, *Science* **2013**, *341*, 1230444.
[8] Z. Hu, B. J. Deibert, J. Li, *Chem. Soc. Rev.* **2014**, *43*, 5815.
[9] W. Li, X. Wu, N. Han, J. Chen, X. Qian, Y. Deng, W. Tang, Y. Chen, *Sens. Actuators, B* **2016**, *225*, 158.
[10] W. Li, X. Wu, N. Han, J. Chen, W. Tang, Y. Chen, *Powder Technol.* **2016**, *304*, 241.
[11] E. Cao, Z. Guo, G. Song, Y. Zhang, W. Hao, L. Sun, Z. Nie, *Sens. Actuators, B* **2020**, *325*, 128783.
[12] J. Xia, K. Diao, Z. Zheng, X. Cui, *RSC Adv.* **2017**, *7*, 38444.
[13] F. Gu, H. Chen, D. Han, Z. Wang, *RSC Adv.* **2016**, *6*, 29727.
[14] I. Ellern, A. Venkatasubramanian, J. H. Lee, P. J. Hesketh, V. Stavila, M. D. Allendorf, A. L Robinson, *ECS Trans.* **2013**, *50*, 469.
[15] S. Homayoonnia, S. Zeinali, *Sens. Actuators, B* **2016**, *237*, 776.
[16] P. Ju, H. Yang, L. Jiang, M. Li, Y. Yu, E. Zhang, *Spectrochim. Acta, Part A* **2021**, *246*, 118962.
[17] F. Klongdee, S. Youngme, J. A. L. Boonmak, *Polyhedron* **2020**, *180*, 114437.
[18] L. Bai, A. Jana, H. P. Tham, K. T. Nguyen, P. Borah, Y. Zhao, *Small* **2016**, *12*, 3302.
[19] A. K. Chaudhari, H. J. Kim, I. Han, J. C. Tan, *Adv. Mater.* **2017**, *29*, 1701463.
[20] T. Tsuboi, Y. Nakai, Y. Torii, *Open Phys.* **2012**, *10*, 524.
[21] H. Jianbo, Z. Tingting, C. Yongjing, Z. Yuanyuan, Y. Weiqing, M. Menglin, *J. Fluoresc.* **2018**, *28*, 1121.
[22] G. Mehlana, S. A. Bourne, *CrystEngComm* **2017**, *19*, 4238.
[23] Y. Li, A.-S. Xiao, B. Zou, H.-X. Zhang, K.-L. Yan, Y. Lin, *Polyhedron* **2018**, *154*, 83.
[24] D. Colognesi, M. Celli, F. Cilloco, R. J. Newport, S. F. Parker, V. Rossi-Albertini, F. Sacchetti, J. Tomkinson, M. Zoppi, *Appl. Phys. A* **2002**, *74*, s64 .
[25] R. Dovesi, V. R. Saunders, C. Roetti, R. Orlando, C. M. Zicovich-Wilson, F. Pascale, B. Civalleri, K. Doll, N. M. Harrison, I. J. Bush, P. D'Arco, M. Llunell, M. Causà, Y. Noël, L. Maschio, A. Erba, M. Rerat, S. Casassa, *CRYSTAL17 User's Manual.*, University of Torino, Torino **2017**.
[26] R. Dovesi, R. Orlando, A. Erba, C. M. Zicovich-Wilson, B. Civalleri, S. Casassa, L. Maschio, M. Ferrabone, M. De La Pierre, P. D' Arco, Y. Noël, M. Causà, M. Rérat, B. Kirtman, *Int. J. Quantum Chem.* **2014**, *114*, 1287.
[27] L. Dona, J. G. Brandenburg, I. J. Bush, B. Civalleri, *Faraday Discuss.* **2020**, *224*, 292.
[28] L. Dona, J. G. Brandenburg, B. Civalleri, *J. Chem. Phys.* **2022**, *156*, 094706.

[29] A. F. Möslein, L. Donà, B. Civalleri, J.-C. Tan, *ACS Appl. Nano Mater.* **2022**, *5*, 6398.

[30] B. E. Souza, L. Dona, K. Titov, P. Bruzzese, A. S. Babal, A. F. Möslein, M. D. Frogley, G. Wolna, G. Cinque, B. Civalleri, J. C. Tan, *ACS Appl. Mater. Interfaces* **2020**, *12*, 5147.

[31] T. Xiong, Y. Zhang, L. Donà, M. Gutiérrez, A. F. Möslein, A. S. Babal, N. Amin, B. Civalleri, J.-C. Tan, *ACS Appl. Nano Mater.* **2021**, *4*, 10321.

[32] M. R. Ryder, B. Civalleri, G. Cinque, J.-C. Tan, *CrystEngComm* **2016**, *18*, 4303.

[33] M. R. Ryder, B. Civalleri, T. D. Bennett, S. Henke, S. Rudic, G. Cinque, F. Fernandez-Alonso, J. C. Tan, *Phys. Rev. Lett.* **2014**, *113*, 215502.

[34] J. Maul, M. R. Ryder, M. T. Ruggiero, A. Erba, *Phys. Rev. B* **2019**, *99*, 014102.

[35] F. Huth, A. Govyadinov, S. Amarie, W. Nuansing, F. Keilmann, R. Hillenbrand, *Nano Lett.* **2012**, *12*, 3973.

[36] B. Knoll, F. Keilmann, *Nature* **1999**, *399*, 134.

[37] A. F. Möslein, M. Gutierrez, B. Cohen, J. C. Tan, *Nano Lett.* **2020**, *20*, 7446.

Statement of Authorship for joint/multi-authored papers for PGR thesis

To appear at the end of each thesis chapter submitted as an article/paper

The statement shall describe the candidate's and co-authors' independent research contributions in the thesis publications. For each publication there should exist a complete statement that is to be filled out and signed by the candidate and supervisor **(only required where there isn't already a statement of contribution within the paper itself).**

Title of Paper	Unravelling the sensing mechanism of a luminescent guest interacting with a metal-organic framework for the detection of volatile acetone
Publication Status	☒Published ☐ Accepted for Publication ☐Submitted for Publication ☐Unpublished and unsubmitted work written in a manuscript style
Publication Details	A.F. Möslein, M. Gutiérrez, K. Titov, L. Donà, B. Civalleri, M.D. Frogley, C. Cinque, S. Rudić, and J.C. Tan, "A multimodal study on the unique sensing behaviour of a guest@metal-organic framework material for the detection of volatile acetone", Advanced Materials Interfaces, 2201401, 2022

Student Confirmation

Student Name:	Annika F. Möslein		
Contribution to the Paper	Synthesis: M.G., A.F.M, K.T. INS measurements: S.R., A.F.M., M.G. SR-FTIR measurements: A.F.M., K.T., M.D.F., C.G. Fluorescence spectroscopy: A.F.M, M.G. Numerical simulations: L.D.. A.F.M. Data analysis: A.F.M, K.T. (preliminary analysis of in situ SR-FTIR measurements) Writing of the original draft: A.F.M. Writing, editing, and reviewing: all authors. Supervision: J.-C.T., B.C.		
Signature		Date	27/07/2022

Supervisor Confirmation

By signing the Statement of Authorship, you are certifying that the candidate made a substantial contribution to the publication, and that the description described above is accurate.

Supervisor name and title:	Prof. Jin-Chong Tan		
Supervisor comments	I support this application and confirm the information entered is correct.		
Signature		Date	29 July 2022

This completed form should be included in the thesis, at the end of the relevant chapter.

Every day is a new day. It is better to be lucky.
But I would rather be exact.
Then when luck comes you are ready.

— Ernest Hemingway, *The Old Man and the Sea*

6

ZIF-71 as a MOF system for improved sensing

Contents

6.1 Structure, synthesis and characterisation of ZIF-71

Because sensitivity to humidity may seriously hinder the application of MOF-based sensors, a material with intrinsic hydrophobicity is truly beneficial for enhanced sensing performance. Therefore, a bottom-up approach, where a hydrophobic

MOF system is selected and thoroughly characterised prior to tuning its properties for targeted sensing application, is suggested here. Although a range of suitable MOF materials exists, we have identified the zeolitic imidazolate framework ZIF-71 for further investigation not only due to its hydrophobicity, chemical and thermal stability, but also because it is easy to synthesise in a time-saving and low-cost one-pot synthesis route; all these features warrant central feasibility for industrial application.[40, 205] More specifically, ZIF-71 is attained by combining 4,5-dichloroimidazolate (dcIm) and zinc acetate, both dissolved in methanol, to form a 3-D coordination network of zinc cations bridged by the dcIm linkers.[206, 207] Crystallising in a RHO-type topology with cubic symmetry (see Figure 6.1), the framework possesses large α-cages with a diameter of 16.5 - 16.8 Å, that even exceed the porosity of other well-studied and promising MOF-materials such as ZIF-8.[124]

Particularly beneficial for gas sensing are, indeed, large pores, as they allow for capture and concentration of the gas species; however, it is also the pore aperture that can enhance sensitivity and selectivity. In the case of ZIF-71, the largest cage window, with aperture dimensions of 4.2 - 4.8 Å, is still significantly smaller than the diameter of the cavity, thus facilitating the trapping of molecules inside the pore. Whilst small pore apertures further lead to size exclusion of larger molecules, another way to achieve selectivity is by leveraging functional adsorption sites: when compared to the mIm linker in ZIF-8, with only hydrogen atoms surrounding the ring, the additional chlorine atoms as part of the linker group in ZIF-71 offer reaction sites for adsorption and tailored host-guest interactions. Yet, the major merit of ZIF-71, which is especially highlighted in comparison to OX-1 (Chapter 5), lies not only in its porosity and structure, but also in its inherent hydrophobicity.[148] Similar to ZIF-8, however, the outermost surface of ZIF-71 could be hydrophilic due to the presence of defects during crystallisation, as exposed in Chapter 4. Because the dcIm in solution may attack the partially positive zinc ions, defect-terminating groups involving -N-H can emerge at the crystal surface, thereby creating possible adsorption sites for hydrogen bonding with water.[206] Unless such functional sites are sought after for specific adsorption application, it

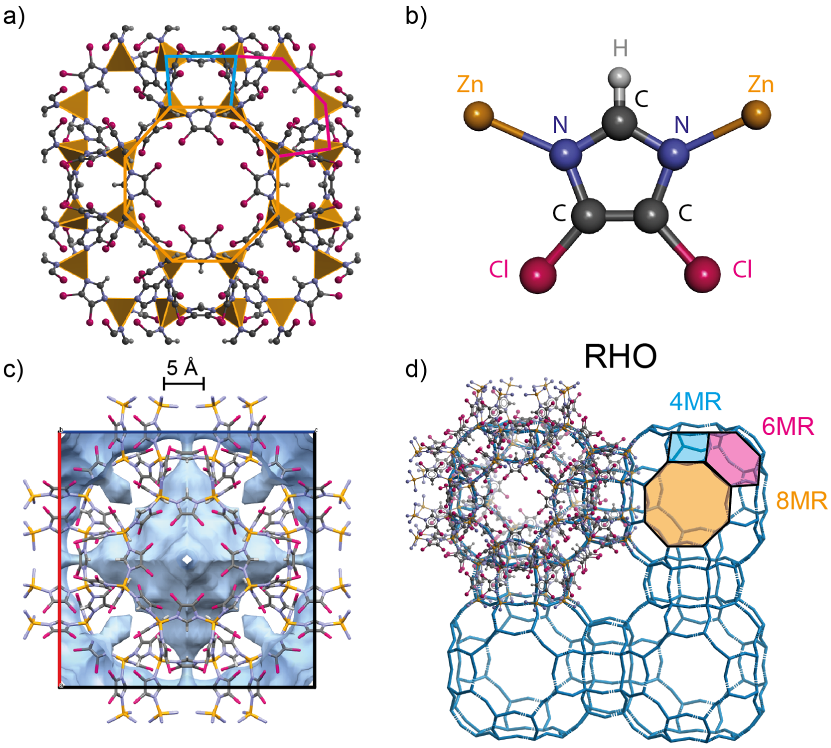

Figure 6.1: Framework structure of ZIF-71: a) ZIF-71 unit cell where the inorganic building blocks are illustrated by the ZnN_4 tetrahedra. b) Building unit showing the Zn–dcIM–Zn linkages. c) Blue surfaces denoting the nanopore, corresponding to the solvent accessible volume (SAV probe radius = 2Å) within the open framework structure. d) Illustration of the RHO topology, highlighting the apertures of the 4-, 6-, and 8-membered rings (MR). Reprinted with permission from [36]. Copyright 2022 American Chemical Society.

is therefore necessary to meticulously control the growth process and crystal size to achieve the desired properties for application.

6.1.1 Crystal size and growth process

How different variables during synthesis, specifically growth time, temperature, use of solvents, molar ratio of reactants, and the addition of modulators, may influence the crystal size has been investigated in several studies (see Table 6.1). In general, it is possible to control the size of ZIF-71 crystals ranging from 50 nm to 1-2 μm while avoiding aggregation. In fact, the growth process itself constitutes of the individual growth of nanoparticles at the beginning, and the subsequent agglomeration of these individual crystals.[208, 209] While the individual growth of nanoparticles is dominated by Ostwald ripening, a spontaneous process by which nanoparticles grow at the expense of other adjacent, smaller nanoparticles to reach a thermodynamically favoured state, the agglomeration is driven by aggregation.[210, 211] The latter refers to the oriented attachment of dispersed nuclei to grow larger crystals, and it is thus the driving force for size enlargement, especially during fast crystal growth.[212]

Because the formation of ZIF-71 crystals depends on the nucleation and growth, and both may occur simultaneously at the beginning of crystallisation, a short reaction time ($<$ 1 hour) leads to a broad range of particle sizes.[213] After a relatively longer reaction time ($>$ 1 hour), nucleation is ceased as the solute is depleted during self-assembly, while the crystals are still growing, and thus, monodispersed particles are attained. This mechanism can be accelerated by increasing the temperature, since this will favour the agglomeration of individual nanoparticles, thereby yielding larger crystals.[213] Turning to the effect of different solvents on the crystal size, it was found that, generally, the use of methanol would provide larger crystals (1-2 μm), while their size is reduced if DMF is used.[214–216] The crystal size does not relate linearly with the amount of DMF present during synthesis, yet, a small amount of DMF increases the deprotonation rate, and thus the nucleation rate, yielding smaller crystals (140 – 300 nm), whereas a reaction environment of pure DMF produces medium-sized crystals ($\sim$500 nm) due to a decreased deprotonation rate.[217] Because DMF molecules are larger than the pore aperture window, it is however challenging to remove the solvent from the ZIF-71 even after extensive washing steps.

Another way to reduce the size of the crystals is by decelerating the growth rate, for example, through the addition of formic acid (HCOOH). In the presence of an acid, the dcIm on the surface of the ZIF-71 nanocrystals are less likely to be deprotonated, yielding smaller crystals ($\sim$400 nm).[218] Or, again focussing on increasing the nucleation rate, the addition of triethylamine in a HCR method may also increase the deprotonation rate to produce small nanocrystals in the range of 50 - 150 nm.[115, 219] In general, the ability to control the crystal size is vital for tailoring the morphology of the material, ranging from single crystals to polycrystalline membranes and composite materials to ensure functionality of targeted application.

Factor	Small crystals	Large crystals	Source
Nucleation	**High nucleation rate**	**Low nucleation rate**	
Solvents	Small amounts of DMF,	Methanol	[214, 216]
	excess dcIm		[192, 217]
Modulators	Triethylamine	-	[220]
Crystal growth	**Low rate**	**High rate**	
Temperature	Decrease temperature	Increase temperature	[213]
Modulators	HCOOH	-	[218]

Table 6.1: Parameters for controlling the size of ZIF-71 crystals during synthesis.

6.2 Potential applications of ZIF-71

6.2.1 Adsorption / separation / pervaporation

Because of its unparalleled structural features, encompassing exceptional porosity with large cages and relatively smaller pore apertures coupled with its hydrophobic and organophilic behaviour, ZIF-71 has naturally emerged as an ideal candidate material for enhanced adsorption and separation, especially for alcohol-water separation.[206, 207, 213, 221, 222] Herein, ZIF-71 membranes have been proven beneficial, as, for example, methanol permeates through it in lieu of water due the water repelling nature of the membrane. In addition, the small aperture windows can be harnessed for the separation of methanol and ethanol, as the transport of the latter is hindered due to its larger molecular size.[207, 222] One way to produce ZIF-71 membranes is by growing crystals onto a support substrate (e.g. ZnO) using DMF in the synthesis: if, alternatively, methanol was used, the reaction would be too fast and the crystals would form in the solvents instead of being attached to the substrate.[213, 214] Another approach involves ZIF-71 as a filler for polymeric mixed-matrix membranes, which, due to ZIF-71 and its interactions with the polymer, simultaneously allow for permeability and selectivity that is uncommon for zeolites or other filler materials.[207, 213] Again, the crystal size plays a key role for the separation performance of the composite materials, however, current research has not yet settled on a reliable rule: on one hand, smaller crystals offer larger surface areas (per unit volume) for better interactions with the polymer, but on the other hand, they may result in agglomerations due to their outer hydrophilic surface.[213, 223] In addition, larger crystals may reduce the transport resistance due to fewer grain boundaries. Regardless of crystal size, well-dispersed crystals without agglomerations are crucial for better performance in separation processes.[222, 224] These not only include alcohol-water, but also organic-organic systems, where the small window size of the ZIF-71 pores acts as an obstacle for larger molecule solvents.[225] However, even if the size of dimethyl carbonate (DMC) exceeds the diameter of the pore aperture, it may still permeate through ZIF-71 membranes – a phenomenon that is assigned to its weak-polar organic character, and a possible 'gate-opening' effect of ZIF-71.[222, 226]

6.2.2 Mechanical energy absorption by liquid intrusion

The same characteristics that are so crucial for separation, more specifically, large pore size, small cage window, and hydrophobicity, are the reasons why ZIF-71 also outperforms other framework materials such as ZIF-8 in applications targeting the storage or dissipation of mechanical energy.[227] Upon intrusion of concentrated electrolytes in liquid phase, ZIF-71 could store almost twice the energy when compared to ZIF-8, which has previously been considered a promising shock absorber.[228] Other energy absorption experiments involving pressurised intrusion of liquid water revealed the same phenomenon: due to the larger pore size and hydrophobicity of ZIF-71, the water network inside the cage is more stabilised than in ZIF-8, and it is energetically less favourable for a water molecule to hop to an adjacent, empty pore.[229] Therefore, the intrusion is hindered, and accordingly, the absorption of mechanical energy is improved compared to other MOF materials if water is used for high-impact energy absorption.

6.2.3 Sensing applications

Naturally, the exceptional performance of ZIF-71 in typical applications of nanoporous materials has further sparked research in its potential use in sensing technologies. Indeed, a few exemplars exist, where ZIF-71 has shown promising potential as a host matrix for sensing applications.[115, 219, 230, 231] For instance, a prototype sensor for the detection of iodine gas was developed with high selectivity, parts per billion (ppb)-level sensitivity, good reversibility and fast response time based on electric sensing. While hydrophilic MOFs usually exhibit a higher iodine adsorption capacity, their sensitivity to moisture decreases their overall reusability and thus performance as a gas phase sensor. Remarkably, ZIF-71, with its interaction sites and hydrophobic nature, matches the iodine adsorption capacity (mass change of 27 %) and the enhancement in electrical response (by 662-fold) of its hydrophilic counterparts, while providing stability in humid air.[232]

Other prototypical sensors based on ZIF-71 leverage the concept of encapsulating luminescent guests to realise sensitivity to mechanical stress, temperature, or volatile organic compounds (VOCs).[219] The nanoconfinement of the fluorescent dye rhodamine B (RhB) in ZIF-71, for instance, led to the RhB@ZIF-71 composite system, whose luminescence was significantly quenched when exposed to certain VOCs, especially DMF. Such turn-off type response is observed, since the encapsulated RhB guest molecules are converted to non-fluorescent lactone in the presence of a polar aprotic solvent. However, because a decrease in emission intensity could also originate from photodegradation, or exposure to other gases, further material tuning is critical to achieve a sensor with higher selectivity.

More promisingly, the same system has demonstrated a turn-off sensing behaviour that is coupled with a red-shift in its emission spectrum in response to temperature variations, whereas all other RhB-based temperature sensors only rely on the decrease in emission intensity.[219] This phenomenon is explained by a caging effect imposed by the framework when the RhB monomers or aggregates are confined in the pores. Because the dimensions of aggregates are relatively larger than RhB monomers, they are strongly affected by nanoconfinement, and due to lower mobility, their luminescent intensity decreases more slowly, resulting in a red-shift in emission of the composite system. Similarly, the caging effect further enables mechanical sensing in the RhB@ZIF-71 material: upon increasing pressure, a tighter formation of J-aggregates with an accompanying red-shift in emission is observed. [219]

Yet, for sensing applications, it is the turn-on type response that is even more favourable, as it may only be triggered by specific stimuli, thereby enhancing selectivity and sensitivity. This has been achieved by encapsulating tetraphenylethylene (TPE) in ZIF-71.[84] Importantly, TPE exhibits aggregation-induced emission, which describes the enhancement of emission intensity when the molecular vibrations are restricted in aggregation. Nanoconfinement within the pores of ZIF-71 produces the same effect of preventing intramolecular rotation, especially under increasing pressure, and an enhanced fluorescence is observed. This turn-on response to mechanical impact (mechanochromic behaviour) is unattainable by the pristine luminescent molecules alone without being confined in the MOF framework.

In addition, sensitivity to acetone vapour was successfully attained with a ZIF-71 layer coated onto ZnO nanorods, where an auxiliary PDMS layer serves as a molecular sieve to improve its selectivity.[233] If ZIF-71 is doped with cobalt, a higher sensitivity to trace amount of acetone (50 ppb) is achieved, as it enhanced the catalytic effect that can also be harnessed for improved sensing.[234] It is, however, the adsorption on the metal-oxide nanorods that is ultimately responsible for the gas-sensing mechanism, whereas ZIF-71 improves the overall resistance to moisture due to its hydrophobicity, and captures and concentrates the gas for higher sensitivity. Despite the operating temperature is lowered (150 °C) by the presence of ZIF-71, these temperatures are still too high for feasible portable gas sensors.

6.3 Physical and chemical properties characterisation

Nonetheless, these first sensor prototypes based on ZIF-71, coupled with its recognised ability to outperform other carefully contrived MOFs, indicate its usability for chemical, mechanical, and pressure sensing. While the intrinsic properties that are vital for gas capture, separation and adsorption may also be harnessed for targeted sensing, they can be tuned even further by leveraging the previously introduced concepts of guest encapsulation, defect engineering and host-guest interactions. Rational design of the tailored sensing mechanism requires a thorough

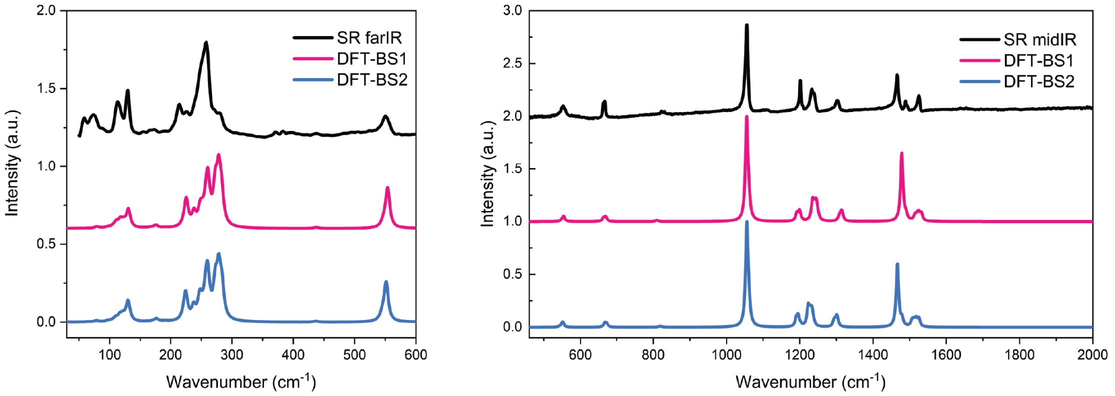

Figure 6.2: Comparison between infrared spectra of ZIF-71 obtained from synchrotron-radiation (SR) experiments and DFT simulations employing two different basis sets (BS1 and BS2).

understanding of the structural dynamics and fundamental physical properties. Indeed, the structure of ZIF-71 has been fully resolved, different synthesis routes to yield various morphologies have been explored, and its physical and chemical properties have been characterised with an emphasis on its hydrophobicity and porosity. However, perhaps owing to the complex chemical structure of ZIF-71, a detailed description of its vibrational dynamics is lacking thus far, even if it would create the link between the chemical structure and physical properties. Knowledge of the vibrational dynamics not only provides evidence for any spectroscopic study on ZIF-71, but the low-energy lattice conformations, in particular, can elucidate many significant physical and mechanical phenomena observed in ZIF-71.

Herein, we report the complete assignment of vibrational frequencies using the complementarity of inelastic neutron scattering (INS) measurements and synchrotron-radiation infrared spectroscopy, jointly with *ab initio* density functional theory (DFT) calculations.

6.3.1 Computational details

All-electron basis sets were used for Zn, C, N, Cl, and H atoms, containing 12,480 (BS1) and 16,032 (BS2) local functions for the 816 atoms per unit cell.

Firstly, the geometry optimisation was carried out using a quasi-Newtonian algorithm, and was considered complete when the calculation converged to the thresholds for both the RMS and maximum value for the force and atomic displacement, simultaneously. The corresponding thresholds were 3 x 10^{-5} (RMS on gradient), 1.2 x 10^{-4} (RMS on displacement), 4.5 x 10^{-5} (largest component of gradient), and 1.8 x 10^{-4}(absolute value of largest displacement). Subsequently, the IR frequencies were calculated at the special point $\Gamma = (0, 0, 0)$. Here, the dynamical matrix ("mass-weighted Hessian matrix") was obtained through numerically evaluating the first derivatives of the atomic gradients. The IR intensities were then calculated with the Berry Phase approach; for a detailed description of the performed calculation, we refer to the work of Pascale *et al.*[202] The continuous spectrum was obtained by fitting the calculated IR intensities with Lorentzian peak shapes with a FWHM of 10 cm^{-1} (see Figure 6.2). To improve the match with experimental data, the calculated IR spectra were scaled by using a scaling factor of 0.98 for wavenumbers (Figure 6.3).[235] The INS spectrum was calculated from the output of the DFT frequency calculation using the AbINS v1 execution in the Mantid software.[196] The excellent match between theory and the experimental broadband spectra is a striking result (see Figures 6.2 and 6.5), since ZIF-71, with its 816 atoms in the unit cell, is among the largest systems yet for which theoretical frequency calculations have been achieved; further benchmarking the massively-parallel performance of the CRYSTAL17 DFT code.

6.3.2 Terahertz phenomena

Through a detailed analysis of each vibrational frequency (see Appendix B), we discover low-energy conformational dynamics and terahertz (THz) modes that can unravel many important physical phenomena recently observed in ZIF-71. For instance, we show that the onset of structural amorphisation detected in ZIF-71 during high-pressure intrusion experiments could be associated with a 'soft mode' observed below ∼0.3 THz.[236] Indeed, mechanical stress can induce anti-parallel shearing forces, which trigger deformations of the 8-member rings (8MR), ultimately

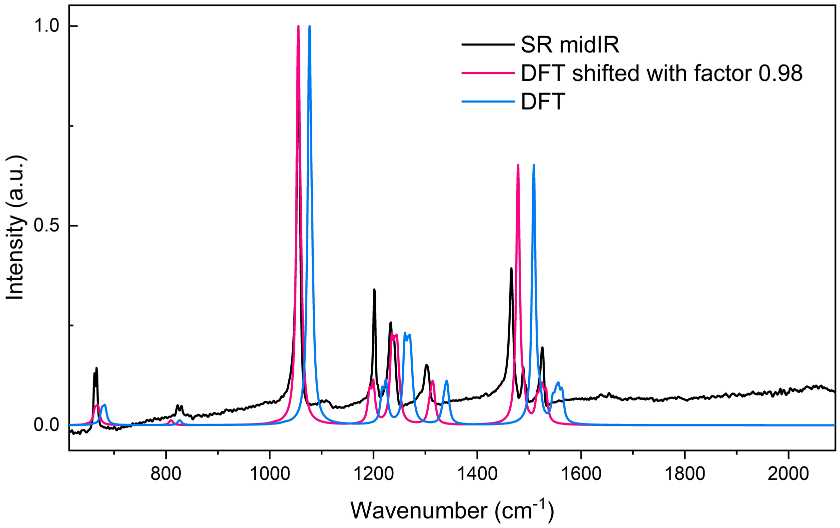

Figure 6.3: Bulk shift of DFT simulated spectrum versus the experimental mid-IR spectrum of ZIF-71.

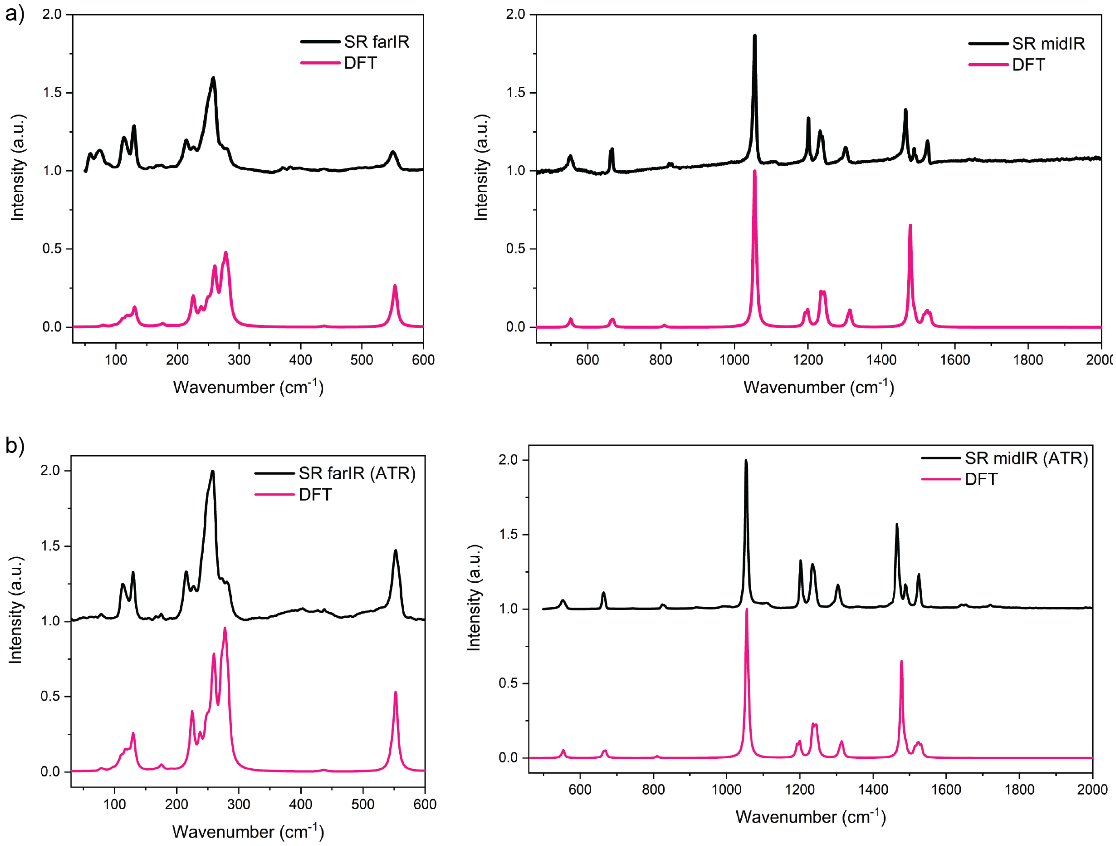

Figure 6.4: Comparison of synchrotron-radiation SR-IR spectroscopy: a) Imaginary part of the complex refractive index, $\kappa(\omega)$, determined from the specular reflectance spectrum *via* Kramer-Kronig Transform, b) ATR-FTIR absorbance spectrum.

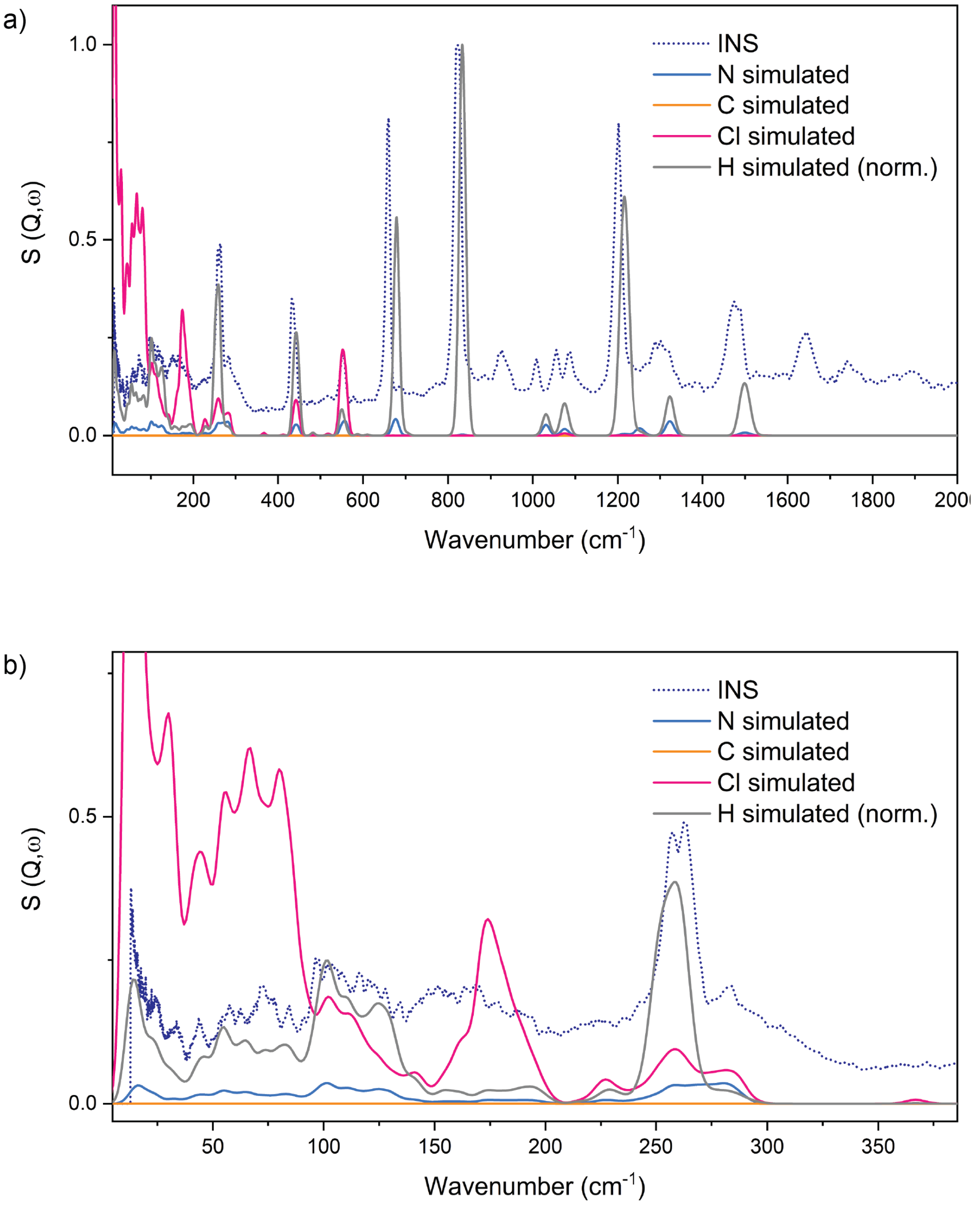

Figure 6.5: INS spectra derived from the phonon calculation compared with experimental measurement for ZIF-71. No shift was applied, but the simulated spectrum for hydrogen (H) has been scaled down (normalization between 0 and 1) for better visualisation.

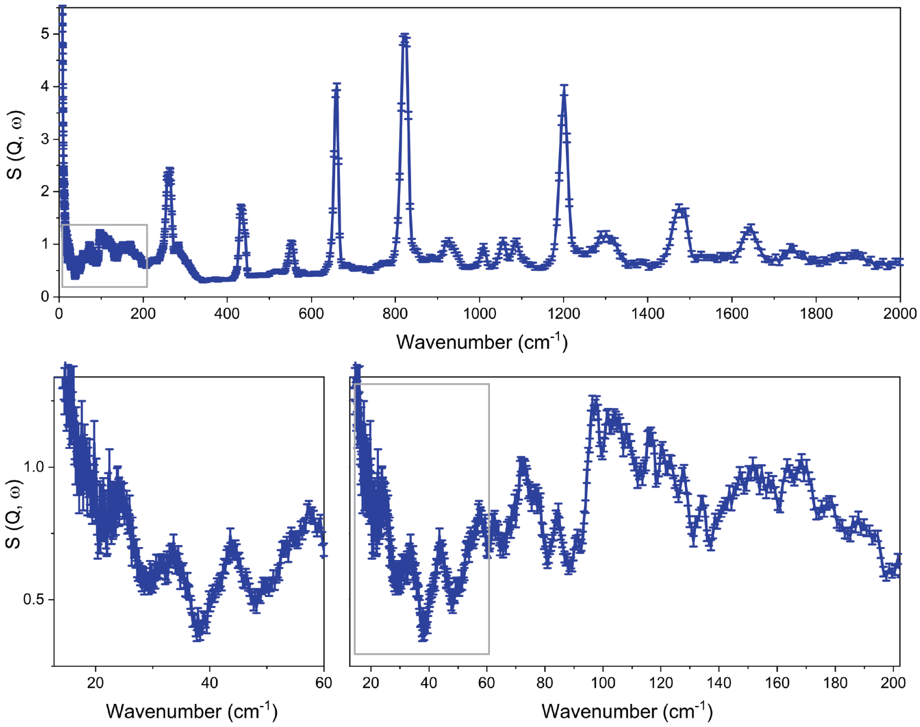

Figure 6.6: Inelastic neutron scattering (INS) data with error bars for a powder sample of ZIF-71.

causing a collapse of the framework. Even if small-pore zeolites, too, possess 8MR, it is the structural flexibility of ZIF materials that instigates their intrinsic tendency to collapse due to amorphisation, e.g. under ball-milling.[237] Considering ZIF-71, mechanical forces can trigger the shearing mode of the 8MR, thereby leading to conformations of the pore, which, in the extreme case, could even lead to phase transitions. The complete collapse of the pore can transform ZIF-71 to a dense, non-porous form: ZIF-72.[40, 238] In fact, this phase transition was observed in high-impact intrusion experiments and can finally be explained by the shearing mode discovered in the complex vibrational dynamics.[236]

Second, we identify characteristic vibrational modes that lead to an increase in pore aperture; this 'gate-opening' behaviour, coupled with the large pore size, is key to the extremely high gas uptake capacity witnessed in ZIF-71. Although the phenomenon of gate-opening has been postulated for ZIF-71 to find an explanation why molecules that are larger than the pore window can infiltrate the framework, unambiguous experimental and theoretical evidence has been lacking thus far. [214, 222, 226] Especially at higher intrusion pressure, even relatively larger molecules can trigger the twisting of the dcIm linkers, and *de facto* increase the accessible pore volume to permeate the framework.[222] This enhanced adsorption capacity is unique for MOFs with gate-opening behaviour, since such structural flexibility is unattainable in rigid frameworks.

6.3.3 Mechanical and single-crystal properties

The possibility of pressure-driven anomalies, including increased adsorption, amorphisation and phase transitions, is ultimately guided by the underpinning vibrational dynamics of a material.[41, 101] Similarly, because these phenomena lead to destabilisation and mechanical anisotropy, they further affect the mechanical properties of the framework.[239] Only little is however known about the mechanical properties of ZIF-71, which, at first glance, is surprising given its significant performance in separation and gas capture. This lack of knowledge is mainly due to the difficulty to grow individual crystals with sufficient size for instrumented nanoindentation: while the largest ZIF-71 crystals are in the range of 1-2 μm, crystals with dimensions of at least hundreds of nanometres would be required for reliable measurements. One way to circumvent this challenge is given by measuring the elastic stiffness and hardness of polycrystalline monoliths.[86] However, avoiding agglomeration has emerged as a favourable criterion for most applications of ZIF-71, and thus, an understanding of the single-crystal properties is paramount for tuning the material towards engineering devices. Because simulation of the mechanical properties was conceived unfeasible based on current resources, we employed nanoscale analytical tools to experimentally investigate the single-crystal behaviour. These include nanoindentation based on AFM, and near-field infrared nanospectroscopy.

AFM nanoindentation was performed with the Veeco Dimension 3100 instrument operating in indentation mode. A Bruker PDNISP probe with a cube-corner diamond indenter tip (cantilever spring constant 152 N/m, and contact sensitivity

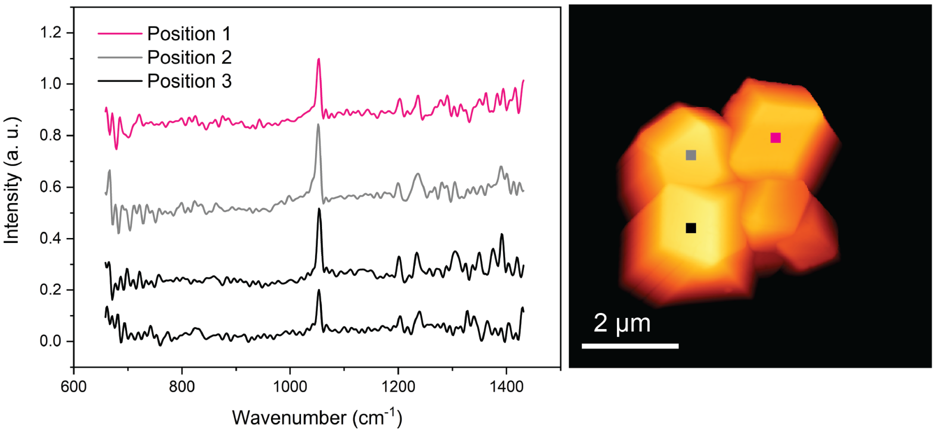

Figure 6.7: Local nanoFTIR spectra measured on individual ZIF-71 crystals reveal chemical homogeneity.

of 156.6 nm/V) was used. The nominal contact area was determined based on the indenter tip geometry established by Zeng and Tan.[240] The mechanical properties – Young's modulus (E) and hardness (H) – were derived from the set of indenter load-vs-displacement curves employing the Oliver and Pharr method, which is applicable to the cube-corner geometry.[241] For a detailed description of the AFM nanoindentation methodology for MOF crystals, we refer to the work of Zeng and Tan.[240] We determined that the Young's modulus and hardness measured on individual single crystals of ZIF-71 are relatively lower than in ZIF-8, which we attributed to the larger pore size of ZIF-71.[159] Further discussion of the AFM nanoindentation results can be found around Figure 4 of the manuscript in Section 6.4.

NanoFTIR spectra were collected from an average of 10 Fourier-processed interferograms with 9 cm^{-1} spectral resolution, 1024 points per interferogram, and 10-ms integration time per pixel. All measurements were carried out under ambient conditions. Although the local nanoFTIR spectra, shown in Figure 6.7, match the ones measured on the polycrystalline, bulk material, thereby evidencing chemical homogeneity of the nanocrystals, they hint the presence of surface-related defects. Specifically, defect-terminating, undercoordinated linker groups may offer adsorption sites for water molecules, which is linked with the hydrophilic behaviour at the outermost surface. These nanoscale measurements therefore invite further studies based on the strategies presented in Chapter 5.

In summary, our approach that comprises experimental and theoretical evidence of the vibrational dynamics and single-crystal behaviour of ZIF-71, offers a detailed description of the fundamental physical properties controlled by its unique chemical structure and topology. This knowledge could further pave the way to downstream applications targeting the design of ZIF-71 systems for sensing technologies, since their physicochemical properties not only outperform hydrophilic frameworks, but also stable ZIF counterparts.

6.4 Vibrational modes and terahertz phenomena of the large-cage zeolitic imidazolate framework-71

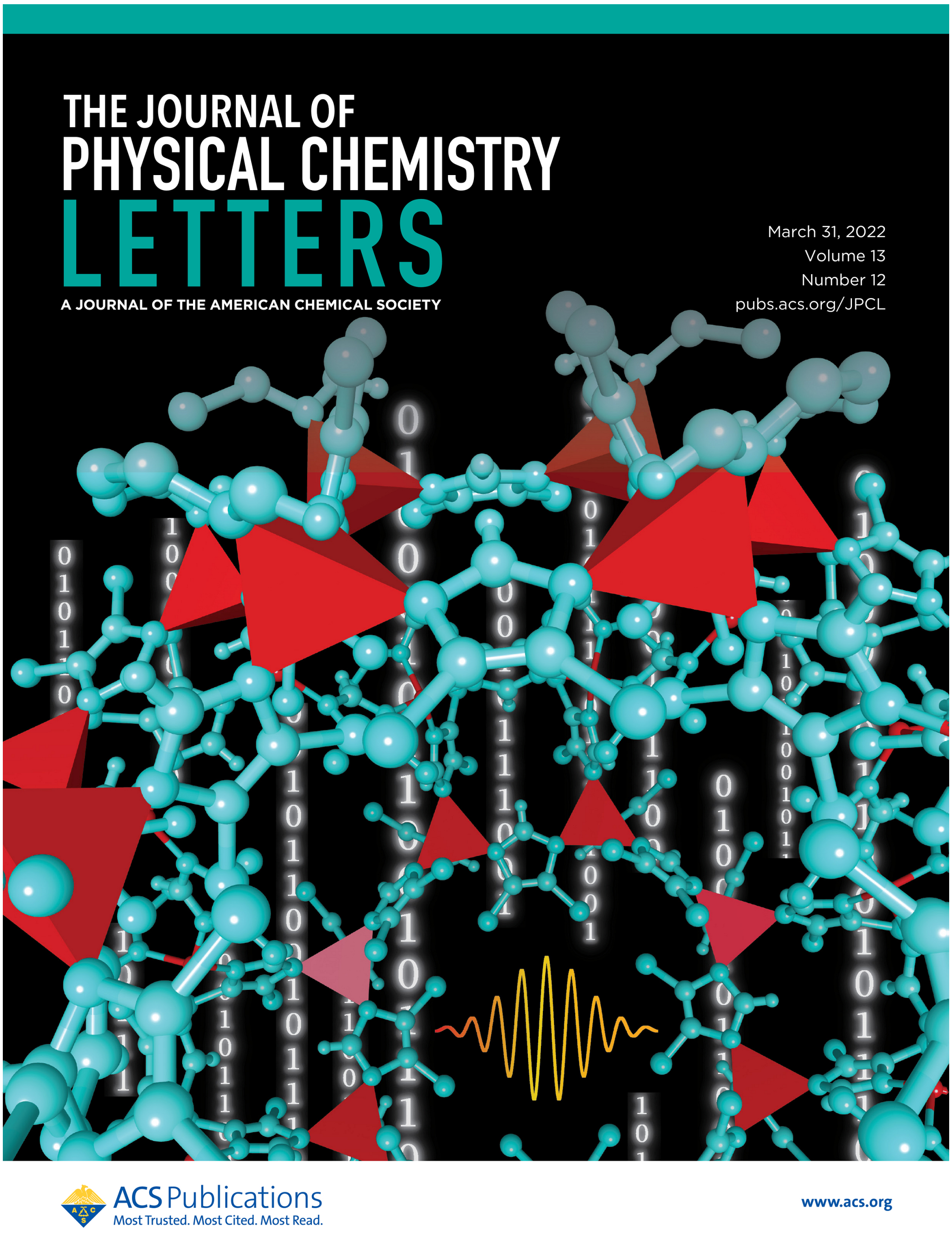

The supporting information for this manuscript can be found here: https://pubs.acs.org/doi/suppl/10.1021/acs.jpclett.2c00081/suppl_file/jz2c00081_si_001.pdf.

THE JOURNAL OF PHYSICAL CHEMISTRY LETTERS
A JOURNAL OF THE AMERICAN CHEMICAL SOCIETY

pubs.acs.org/JPCL Letter

Vibrational Modes and Terahertz Phenomena of the Large-Cage Zeolitic Imidazolate Framework-71

Annika F. Möslein and Jin-Chong Tan*

Cite This: J. Phys. Chem. Lett. 2022, 13, 2838−2844 Read Online

ACCESS | Metrics & More | Article Recommendations | Supporting Information

ABSTRACT: The zeolitic imidazole framework ZIF-71 has the potential to outperform other well-studied metal−organic frameworks due to its intrinsic hydrophobicity and relatively large pore size. However, a detailed description of its complex physical phenomena and structural dynamics has been lacking thus far. Herein, we report the complete assignment of the vibrational modes of ZIF-71 using high-resolution inelastic neutron scattering measurements and synchrotron radiation infrared spectroscopy, corroborated by density functional theory (DFT) calculations. With its 816 atoms per unit cell, ZIF-71 is the largest system yet for which frequency calculations have been accomplished employing the CRYSTAL17 DFT code. We discover low-energy terahertz dynamics such as gate-opening and shearing modes that are central to the functions and stability of the ZIF-71 framework structure. Nanoscale analytical methods based on atomic force microscopy (near-field infrared spectroscopy and AFM nanoindentation) further unravel the local chemical and mechanical properties of ZIF-71 single crystals.

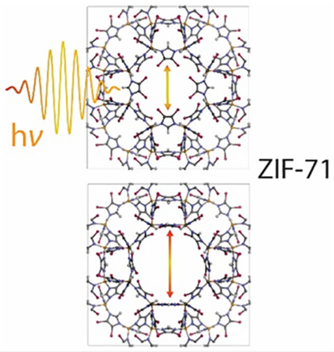

Among the vast field of nanomaterials, metal−organic frameworks (MOFs) have gained considerable interest owing to their unique physical and chemical properties, which are unattainable in other conventional materials. For instance, their open framework structure assembled from metal clusters bridged by organic linkers leads to large surface areas even exceeding those of zeolites, while their organic−inorganic character offers novel, tailorable functional properties.[1] Originating from the traditional use of porous nanomaterials, where MOFs have been proven beneficial for gas capture and storage, the multifunctional nature of MOFs has paved the way for an array of innovative applications, including but not limited to catalysis, drug delivery, microelectronics, and chemical sensors.[2−7]

One of the most promising candidates for the application of MOFs is the zeolitic imidazole framework ZIF-8 [$Zn(mIM)_2$; mIM = 2-methylimidazolate] due to its stability and ease of synthesis.[8] ZIF-8 crystallizes in a sodalite (SOD) topology with an internal pore size of ∼10 Å, and it has become a prototypical and well-studied material among the large family of MOFs.[9] ZIF-8, or materials in the subclass of ZIFs, in general, are constructed from metal cations tetrahedrally coordinated to imidazole-type organic linkers, yielding a chemically stable framework structure with cage-like subunits.[8] While ZIF-8 has indeed sparked considerable scientific and technological interests, other ZIF materials, in fact, might even outperform ZIF-8 in various applications.[10,11] For instance, the far less studied material ZIF-71, built from Zn cations bridged by 4,5-dichloroimidazolate (dcIM) linkers, possesses a RHO-type structure with pore sizes exceeding those of the SOD-type ZIF-8, thus rendering ZIF-71 a promising candidate for enhanced gas capture or mechanical shock absorbance.[12] It crystallizes in a cubic symmetry, and it is constructed from large α-cages (16.5−16.8 Å of diameter) connected by eight-membered ring (8MR) units with cage windows of 4.2−4.8 Å, in addition to four- and six-membered ring (4MR, 6MR) pore apertures (see Figure 1). Besides, the coexistence of hydrogen and chlorine atoms in the dcIM linker offers more versatile interactions with guest molecules than expected for only hydrogen bonds in ZIF-8, advancing reactivity in catalysis or selectivity for sensing applications. Yet, perhaps owning to its complex structure, this material has not been widely explored, which is surprising given that ZIF-71, due to its intrinsic hydrophobicity, provides excellent chemical stability akin to ZIF-8. While a thorough understanding of the physical properties of ZIF-8 and its underpinning lattice dynamics has been developed,[13,14] little is known about the fundamental vibrational characteristics of ZIF-71, which is so central to understanding the physical behavior of the material, and thus there is a gap in knowledge prior to targeting specific applications.

In this work, we provide the first complete assignment of the vibrational modes of ZIF-71 using high-resolution neutron and synchrotron vibrational spectroscopy, in conjunction with *ab*

Received: January 11, 2022
Accepted: February 28, 2022
Published: March 24, 2022

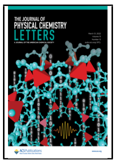

ACS Publications

https://doi.org/10.1021/acs.jpclett.2c00081
J. Phys. Chem. Lett. 2022, 13, 2838−2844

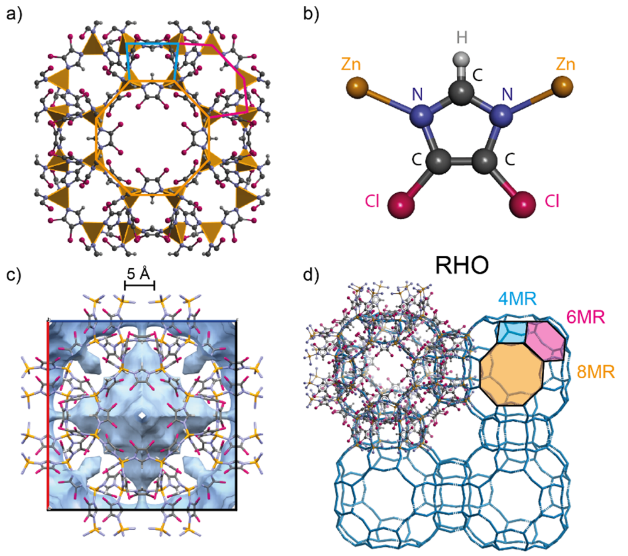

Figure 1. Framework structure of ZIF-71: (a) ZIF-71 unit cell where the inorganic building blocks are illustrated by the ZnN_4 tetrahedra. (b) Building unit showing the Zn−dcIM−Zn linkages. (c) Blue surfaces denoting the nanopore, corresponding to the solvent accessible volume (SAV probe radius = 2 Å) within the open framework structure. (d) Illustration of the RHO topology, highlighting the apertures of the 4-, 6-, and 8-membered rings (MR).

initio quantum mechanical simulations. This multimodal approach allows us to establish the low-frequency terahertz (THz) lattice modes and unravel basic mechanistic dynamics, and further identifies the characteristic vibrational modes in the mid-infrared region. The results are important because not only they provide the missing reference for spectroscopic studies of ZIF-71, but also they hold the key to unlocking complex host−guest interactions underpinning the functions of ZIF-71.

To analyze the physical molecular vibrations corresponding to each mode of ZIF-71, we computed the theoretical spectra and vibrational frequencies using density functional theory (DFT), as implemented in a development version of the CRYSTAL17 code (running in massively parallel processing (MPP) mode on high-performance clusters).[15,16] ZIF-71, with its 816 atoms per unit cell, is hitherto the largest MOF system for which theoretical frequency calculations with DFT have been accomplished, thereby benchmarking the CRYSTAL17 code. We have tested two all-electron basis sets of increasing size, designated as BS1 and BS2, containing 12 480 and 16 032 local functions, respectively. The calculations were performed at the B3LYP-D3 level of theory, including two- and three-body corrections (ABC) to account for dispersion interactions.[17−19] The Fourier transform infrared spectroscopy (FTIR) data were obtained with synchrotron radiation (SR) at the MIRIAM beamline at the Diamond Light Source (Oxfordshire, U.K.). Using two different detectors (bolometer and built-in detector) and beam splitters (Mylar and KBr, respectively), the full broadband IR spectrum from 50−2000 cm^{-1} could be measured. For IR spectroscopy, the interaction between electromagnetic waves and molecular vibrations is based on dipole changes, which are only induced by asymmetric vibrations or rotations leading to the so-called selection rule. To further elucidate the symmetric modes without dipole change, or the IR inactive modes, these data sets were complemented with inelastic neutron scattering (INS) measurements, performed on the TOSCA spectrometer at ISIS Neutron & Muon Spallation Source (Oxfordshire, U.K.).[20] Unlike optical spectroscopy techniques, all molecular motions are observed in INS without the symmetry-based selection rule; however, in practice, this technique shows dominant sensitivity to vibrations encompassing hydrogen due to the exceptionally large scattering cross-section of the hydrogen nuclei.[21] Additionally, the vibrational dynamics in the low-energy THz region, which are so central to the structural mechanics of MOF materials, are revealed with INS, as frequencies as low as 20 cm^{-1} are measured. We further employed nanoscale analytics, such as infrared nanospectroscopy and nanoindentation, to attain the local chemical and physical information on the individual ZIF-71 crystals. Both techniques are based on atomic force microscopy (AFM), albeit operated in different modes: nanoindentation monitors the strain rates of the AFM indenter tip during the indentation process to probe the local mechanical properties, specifically the Young's modulus (E) and hardness (H) of single crystals.[22] Nanospectroscopy is based on a tapping-mode AFM combined with a scattering-type scanning near-field optical microscope, where the illuminated tip serves as a source for an evanescent near-field, to obtain a nanoFTIR spectrum of individual nanocrystals.[23−25] Together, these multimodal techniques gave us a detailed "picture" of ZIF-71, comprising its intrinsic vibrational dynamics, its fundamental physicochemical behavior, and the resulting single-crystal characteristics.

As shown in Figure 2, the calculated IR spectrum yields excellent agreement with the one measured with SR-FTIR. A bulk shift of the simulated peaks to lower frequencies was applied (factor 0.98), which is a common approach considering the "nanocrystal effect", as the strengths of real bonds, even if only slightly, are decreased from the ones of idealized crystal.[26] For reference, the measured INS spectrum for ZIF-71 is also shown in Figure 2d. It can be seen that the shape of the predicted spectrum in the low-energy region matches remarkably well with the INS data (Figure 2c); this is a significant result given that establishing a good agreement between DFT and INS data at low wavenumbers is usually considered as a challenge even for a less complex framework.[13,27,28] Only the combination with DFT can assign the physical motions to each observed peak, and a detailed analysis of all vibrational modes identified different characteristic spectral regions ranging from high to low energies. Above 2000 cm^{-1}, a region typically associated with the stretching vibration of functional groups, C−H stretching modes are observed for ZIF-71. In the transition between functional group and the fingerprint region between 1200 and 2000 cm^{-1}, the high-intensity peaks are assigned to C−N stretching modes of the aromatic ring in combination with C−H bending. Below that, the characteristic modes of the aromatic ring of dcIM are prevalent in the mid-IR fingerprint region: 900−1200 cm^{-1} for vibrations describing the in-plane ring modes and 600−900 cm^{-1} for the out-of-plane ring modes, respectively. It is further evident that the modes involving the ZnN_4 metal clusters appear below 500 cm^{-1}, where stretching and bending between Zn and N are excited at specific frequencies; here, however, the Zn atoms remain fixed, and the main resulting motions are associated with the linker units, thus slightly deforming the pores and channels of ZIF-71. Stronger structural distortions of the pores, and the framework itself, are expected in the low-energy, or THz region (<300 cm^{-1}), involving the low-energy collective modes. This is precisely where relations between the

https://doi.org/10.1021/acs.jpclett.2c00081
J. Phys. Chem. Lett. 2022, 13, 2838−2844

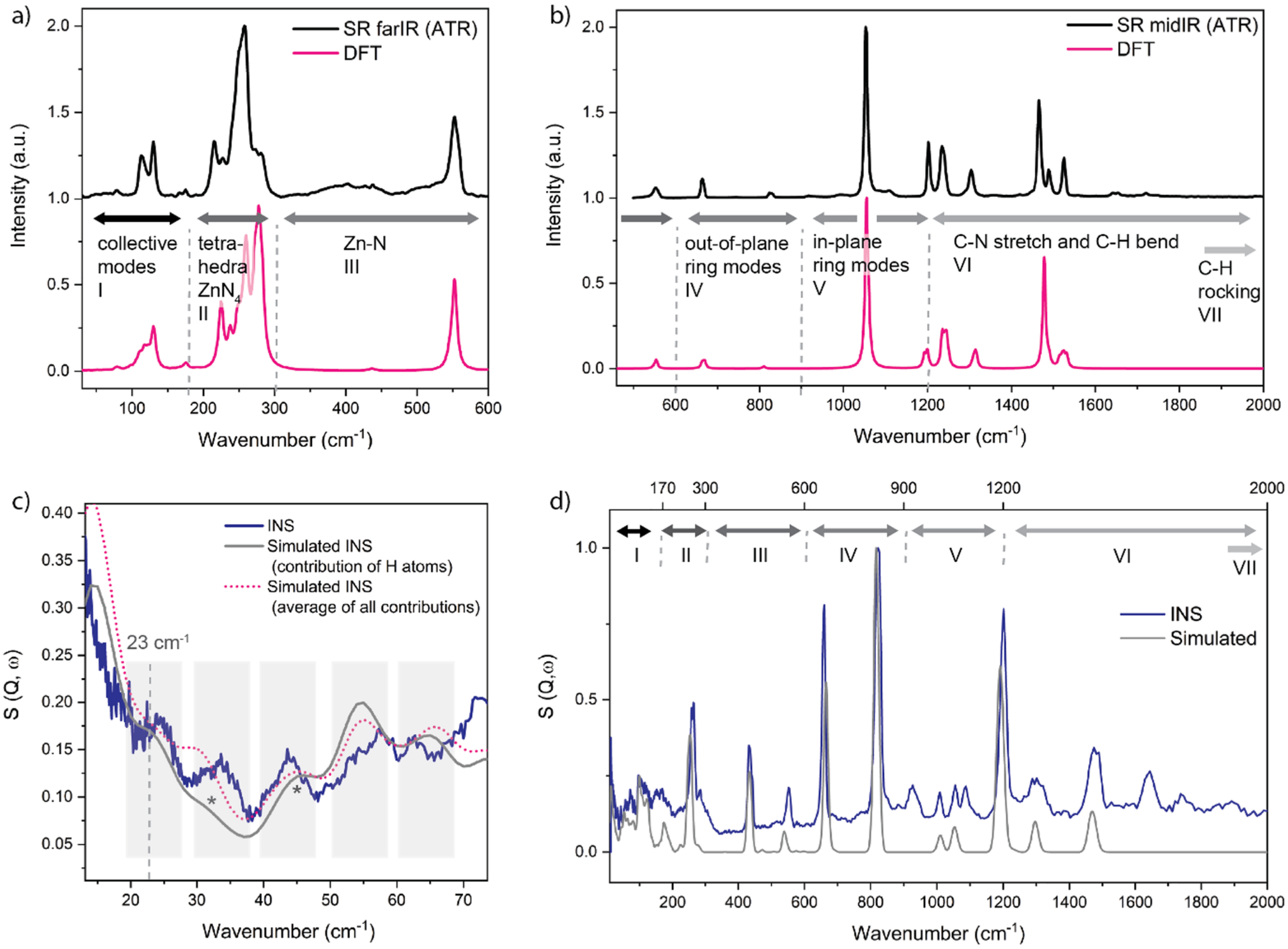

Figure 2. Comparison of experimental and theoretical DFT spectra for ZIF-71. (a) Far-infrared (farIR) spectrum measured with synchrotron radiation (SR) compared with DFT simulated spectrum. (b) Midinfrared (mid-IR) spectrum measured with synchrotron radiation (SR) compared with DFT simulated spectrum (shifted with a factor of 0.98). (c) Low-energy region of the spectrum obtained with inelastic neutron scattering (INS), compared with calculated INS spectra derived from the DFT phonon calculation). (d) Simulated and experimental INS spectra of ZIF-71.

physical properties and the lattice dynamics can be instigated, since soft modes (e.g., breathing modes of the framework), gate-opening, and shearing are linked with adsorption, elasticity, structural transitions, and instability.[13,28−30] Between 170 and 280 cm^{-1}, the N−Zn−N bending and stretching modes are observed introducing tetrahedral deformations, which, in turn, cause distortion of the linker unit, and some—albeit small—structural deformations of the pores will occur. Here, vibrations associated with the Cl atoms are also detected; they can play a key role for they offer additional interaction sites for guest adsorption. Stronger deformations of the 4-, 6-, and 8-membered rings (MR) are revealed in the spectral region below 150 cm^{-1} ($\lesssim$ 4.5 THz): this is where intriguing physical phenomena like gate-opening, shearing, pore breathing, and other structural mechanisms underpinning the fundamental properties of the framework are prevalent.

Herein, we explore the low-energy collective modes of ZIF-71, which encompass contributions from the entire crystalline lattice and thus, are so intrinsically linked with the core physical phenomena observed in ZIF materials. While a full description of the vibrational modes is provided in the Supporting Information, we illustrate in Figure 3 a few crucial lattice modes that strike us as exceptional for understanding the physical phenomena of ZIF-71. Perhaps one of the most significant lattice dynamics among them is the soft mode at 10.46 cm^{-1} (~0.3 THz), which is assigned to a strong shear deformation of the 6- and 8-membered rings (Figure 3a). Such a shearing deformation suggests a propensity to undergo a phase transformation, potentially to ZIF-72 or COK-17, which contain, in essence, the same building blocks as ZIF-71, yet their structures are entirely different: the latter manifests in a SOD topology akin to ZIF-8 but with a distorted configuration, whereas ZIF-72 is a nonporous *lcs*-type framework lacking the exceptional porosity of ZIF-71.[31,32] Transitioning—or even structural amorphization as observed in other ZIF materials[13,33]—seems likely, especially since the shearing mode of the 8MR, which are inherently mechanically unstable subject to antiparallel shear forces given the large pore size of ZIF-71, leads to a decrease of the pore that is even more susceptible to collapse.[34,35] As opposed to small-pore zeolites, which are characterized by eight-member ring (8MR) pores and can exhibit high thermal and mechanical stability, ZIFs are more likely to collapse to amorphization under ball-milling; a tendency that has been demonstrated for five different ZIFs.[36,37] Our findings suggest that, in ZIF-71, too, mechanical stress can trigger shearing deformations of the 8MR leading to subsequent amorphization. This soft mode could further explain the previously observed phase transition reported

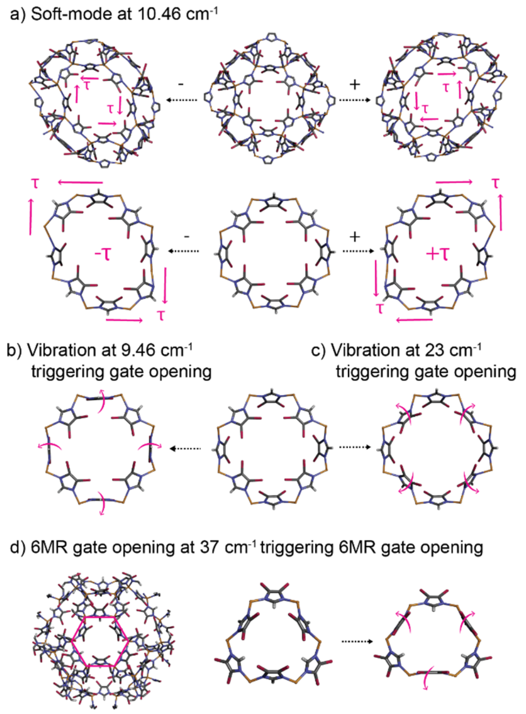

Figure 3. Low-energy lattice modes of ZIF-71. (a) Soft mode associated with a shear deformation of the 8MR. (b, c) Gate-opening mechanisms of the 8-membered ring (MR) via synchronous rocking of opposite organic linkers. Pink arrows designate the collective dynamics affecting the geometry of pore cavity. (d) Vibration triggering gate-opening of the 6MR through synchronous flapping of the bridging linkers.

during intrusion-extrusion experiments, where, despite a major collapse of the ZIF-71 framework, traces of both ZIF-71 and ZIF-72 were found by X-ray diffraction.[38] Consistently, soft modes have been linked with structural flexibility in switchable MOFs such as DUT-8, where lattice vibrations revealed by Raman spectroscopy and computational modeling indicated differences between rigid and flexible, or porous and nonporous forms.[30]

In addition, we discovered three collective modes triggering gate-opening, a mechanism which could facilitate adsorption and significantly raise the gas uptake capacity. This is due to the synchronous flapping (or scissoring mode) of opposite ligands that results in a greater accessible pore volume via an opening of the pore aperture. For the 8MR, we detect two gate opening modes at 9.45 and 23 cm^{-1}, respectively, induced due to the conformational changes of different linker units as they pivot around the metal centers (Figure 3b,c). Directly related to the increase in aperture of the 8MR, a similar, albeit less pronounced, pore breathing mechanism is propagated in the adjacent 6MR, whereas the 4MR exhibits shearing deformation. An actual gate-opening in the 6MR is however identifiable at 37 cm^{-1} (~1 THz), where the coherent scissoring dynamics of the linker units located opposite to each other cause an increase of the pore aperture (Figure 3d). Though much less explicit, the lattice vibrations involving stretching and twisting of the Zn−N bonds and ligands also trigger pore deformations of the 4, 6 or 8MR—be it asymmetric gate-opening, pore breathing, expansion, contraction, or shearing—and while all of these mechanisms indeed distort the cage structure, they are thus far not assigned to the core physical phenomena observed in ZIF-71.

To obtain a better understanding of the physical properties of the individual ZIF-71 crystals, we performed nanoscale analytical measurements comprising near-field infrared spectroscopy and AFM nanoindentation. First, we measure, with a resolution of 20 nm, the local IR vibrational spectra: they not only reveal the homogeneity of the chemical composition of a single crystal (see the Supporting Information, Figure S7), but their average also offers comparison with conventional (far-field) ATR-FTIR techniques and the simulated spectrum, as shown in Figure 4b. For instance, the most pronounced peak at 1054 cm^{-1}, assigned to in-plane ring deformation of the linker with rocking of the C−H groups, is characteristic for ZIF-71, while the smaller peaks associated with C−N stretching modes at 1201 cm^{-1} (with C−H bend), 1234 cm^{-1} (ring breathing), and 1301 cm^{-1} (stretching) are also in agreement with conventional measurements. The small discrepancies between

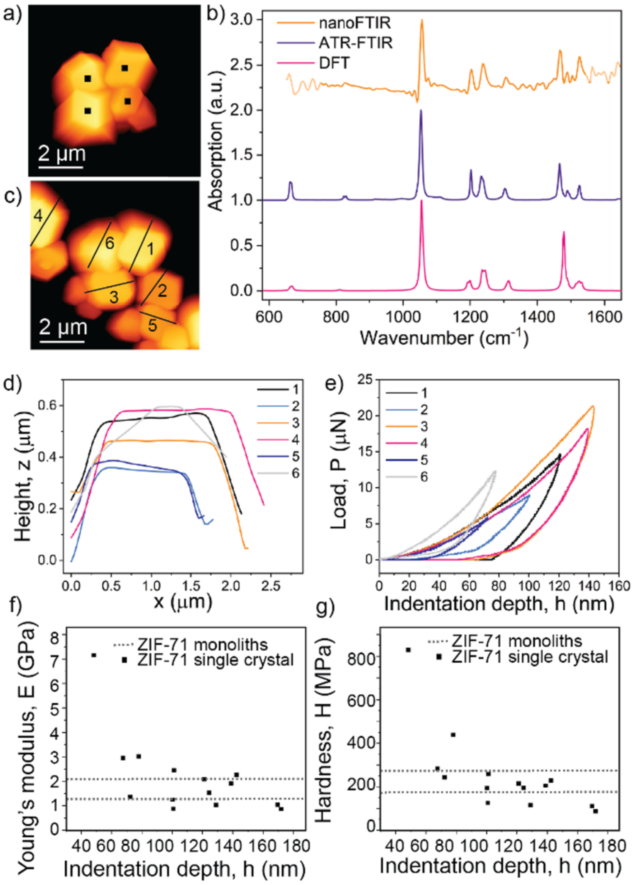

Figure 4. Nanoscale analytics of ZIF-71 single crystals. (a) AFM image of ZIF-71 crystals with indicated positions for nanoFTIR measurements. (b) Corresponding nanoFTIR spectra compared with ATR-FTIR measurements and DFT simulations (shifted with a factor of 0.98). (c) Individual crystals are selected for AFM nanoindentation measurements. (d) AFM height profile of the individual crystals corresponding to the lines designated in part c. (e) AFM nanoindentation load−displacement (*P*−*h*) curves of individual nanocrystals of ZIF-71. (f) Derived Young's modulus and (g) hardness, plotted as a function of the maximum indentation depth. Dashed lines represent values measured on two different samples of ZIF-71 monoliths with instrumented nanoindentation by Tricarico et al.[39]

the theoretical and experimental spectra around 1500 cm^{-1} stem from the fact that, here, symmetric stretches of the undercoordinated N−C−Cl groups at the edge of the unit cell are triggered which are not expected in the ideal, periodic crystal. Thus, the peak splitting observed in the experimental data indicates that these modes are in fact present at the crystal surface. Otherwise, the local single-crystal spectrum matches the ones measured on bulk, polycrystalline material and calculated from a periodic lattice; hence, this technique can be used for direct recognition of the vibrational modes, or the fingerprint, of ZIF-71, thereby facilitating prospective studies on the behavior of ZIF-71 with nanoscale resolution.

In addition, we measured the local mechanical properties of single ZIF-71 crystals by employing AFM nanoindentation. This technique allows us, with a resolution akin to AFM, to accurately characterize the elastic stiffness and hardness of individual ZIF-71 crystals, which is unachievable using standard techniques, since the growth of large single crystals of ZIF-71 crystals (approximately hundreds of micrometers) suitable for instrumented nanoindentation has been proven challenging up to this point. Herein, we obtain a set of load-vs-displacement (P−h) curves of several isolated ZIF-71 crystals with submicrometer size. From these shallow indentations with a surface penetration depth ranging from 60 to 170 nm, the Young's modulus (E) lying in the range of of 1−3 GPa and hardness (H) between 100 and 300 MPa are determined using the Oliver and Pharr method, taking into account the cube-corner geometry of the diamond indenter tip.[40] It is worth mentioning that the outlier (E = 8 GPa, H = 800 MPa) was measured on the inclined crystal (label 6 in Figure 4c−e), and introduces artifacts, as the lack of smooth and flat sample surface led to an unreliable contact area determination. Since it is unfeasible to align the small micrometer-sized crystals (through dropcasting) for orientation-specific measurement, only the exposed top surface of each crystal was probed. Owing to the difficulty to grow significantly (at least 100 times) larger ZIF-71 crystals, the mechanical properties of ZIF-71 from instrumented nanoindentation or Brillouin spectroscopy have not been reported yet, and thus, it is challenging to verify these experimental values from AFM nanoindentation. However, while this is true, it is a method that has been shown to achieve quantitative measurement on the prototypical ZIF-8, where comparison with conventional techniques and DFT calculation were feasible. With the efficacy of this method being proven, we herein report the mechanical properties of ZIF-71 with nanoscale techniques, which further substantiate these findings. Additionally, the values of Young's modulus and hardness are in reasonable agreement with the ones measured on two different ZIF-71 monoliths (Figure 4f,g, dotted lines).[39] While the two differing values for different samples are explained by the random orientation of nanocrystals in the monoliths and intergranular porosity, the discrepancies between monoliths and single crystals can be linked to various factors including use of different tips (Berkovich versus cube-corner geometry), nanostructure packing, anisotropic behavior of single crystals, or compliance of the AFM cantilever probe. In general, Young's modulus of ZIF-71 ($E \sim 2$ GPa) is notably lower than the one previously shown for ZIF-8 (3.15 GPa), an observation which we attribute to the larger pore size of ZIF-71.[14]

Knowledge of the mechanical properties paves the way for further studies targeting pressure-driven mechanical anisotropy, phase transitions, and amorphization. All of these are closely linked with THz phenomena including—but not limited to—gate-opening and shearing modes, as previously shown for ZIF-8.[35] Additionally, the discovered gate-opening modes can finally explain the measured and computed adsorption isotherms for C_2 (ethane, ethene) and C_3 (propane, propene) gases in ZIF-71.[41,42] While, at a first glance, the deviations between experiments and Monte Carlo simulations were assigned to either host−guest interactions or the complex structure of ZIF-71, there might be more to that; for C_2 molecules, as expected, simulations predicted higher loadings, for they assume a perfect crystal structure unattainable in experiment. On the other hand, the experimental gas uptake for C_3 molecules is higher than computationally predicted, especially if the pressure exceeds 0.3 bar. This is a strong indicator that larger molecules at higher pressure trigger bespoke gate-opening and thus, pore expansion, which ultimately leads to increased gas adsorption when compared to the simulations that assume a rigid framework. The same trend of structural flexibility can explain the simulated anomaly of adsorption of water and alcohols at varying pressure in ZIF-71.[43] At low pressure, the affinity for water adsorption is relatively weak due to the hydrophobic, nonionic, and microporous nature of ZIF-71, where only the organic linker rather than the metal sites offer preferential adsorption sites. However, with increasing pressure, when entropy effects determine adsorption, water adsorption increases rapidly owing to its small molecular size and capillary condensation. The confinement of adsorbed molecules in a porous framework material—or, in other words, the hindrance of motion—leads to a loss of entropy;[44] if, however, the framework is flexible upon increased pressure or temperature, entropy rises and adsorption capacity is enhanced compared to a rigid framework.

Yet, we observe less structural flexibility for ZIF-71 in comparison with the SOD-type ZIF-8, where the mIM linkers offer a higher capability to twist than the dcIM moieties. For instance, the swing angle associated with the 8MR aperture seems to be smaller when compared with the one of the 6MR of ZIF-8. In the case of ZIF-71, this could in fact facilitate the trapping of guest molecules, as a higher internal loading would not immediately lead to deformation of the pore aperture. One example is the storage or dissipation of mechanical energy, using the liquid-phase intrusion of concentrated electrolytes in a hydrophobic nanoporous framework, where the stored energy in ZIF-71 is almost doubled compared to that measured for ZIF-8.[12] Similarly, ZIF-71 performed better than ZIF-8 in more recent impact absorbance experiments based on water intrusion: the larger water network in a ZIF-71 cage is more stabilized than in the smaller ZIF-8 cage, and accordingly, it is less favorable for a water molecule to hop to an empty neighboring ZIF-71 cage.[11] This phenomenon increases the intrusion barrier in ZIF-71 compared to ZIF-8. Albeit less significantly, the lower flexibility in ZIF-71 could also hinder water hopping, thereby decelerating the intrusion and thus enhancing the mechanical energy absorption capacity of ZIF-71.

The above exemplar, however, is only one of many possible applications where ZIF-71 can outperform other, well-studied MOF materials and ZIF counterparts.[45] For instance, functionalizing ZIF-8 with halogenated imidazolate linkers could increase the CO_2 uptake, with Cl being the most stable; accordingly, in ZIF-71, the electron-withdrawing Cl groups offer adsorption sites for enhanced gas loading capacity.[46,47] Similarly, ZIF-71 thin films, as a halogenated material, have been shown to be promising for nanofabrication of MOF devices targeting low-*k* dielectrics and photonic sensors.[48] Our work presents the fundamental insights required prior to developing such applications and technologies by contributing a full description of the vibrational dynamics of ZIF-71. Combining DFT calculations with high-resolution synchrotron FTIR spectroscopy and inelastic neutron scattering not only completely characterizes each vibrational mode but also further unravels the key collective modes that are inherently linked with the material's properties and functions. For instance, we discovered shearing modes with potential phase transitioning and gate-opening modes of the different cages, which could increase gas uptake. In addition, we explore the single-crystal properties of ZIF-71 using nanoscale analytical tools. This allows us, while simultaneously imaging the crystals with AFM, to locally probe the chemical composition by measuring a nanoFTIR spectrum from a 20 nm spot, and we further measured the local mechanical properties to complete the detailed picture of ZIF-71. We hope to offer the basis for—and inspire—further studies on the physical behavior of ZIF-71, as a versatile platform for basic research and application stemming from its unique topology, hydrophobicity, large pore size, and nanoscale mechanics.

■ ASSOCIATED CONTENT

Supporting Information

The Supporting Information is available free of charge at https://pubs.acs.org/doi/10.1021/acs.jpclett.2c00081.

Details about theoretical calculations and experimental methods (synthesis, PXRD, synchrotron-radiation FTIR, inelastic neutron scattering, nanoFTIR, AFM), as well as the complete assignment of vibrational modes of ZIF-71 (PDF)

Video clips of representative vibrational modes at 9.46, 10.45, 23.68, 37.42, 1076.38, and 1508.78 cm^{-1} (ZIP)

Transparent Peer Review report available (PDF)

■ AUTHOR INFORMATION

Corresponding Author

Jin-Chong Tan − *Multifunctional Materials and Composites (MMC) Laboratory, Department of Engineering Science, University of Oxford, Oxford OX1 3PJ, U.K.;* orcid.org/0000-0002-5770-408X; Email: jin-chong.tan@eng.ox.ac.uk

Author

Annika F. Möslein − *Multifunctional Materials and Composites (MMC) Laboratory, Department of Engineering Science, University of Oxford, Oxford OX1 3PJ, U.K.;* orcid.org/0000-0002-2056-6437

Complete contact information is available at: https://pubs.acs.org/10.1021/acs.jpclett.2c00081

Notes

The authors declare no competing financial interest.

■ ACKNOWLEDGMENTS

A.F.M. thanks the Oxford Ashton Memorial Scholarship for a D.Phil. studentship award. J.-C.T. and A.F.M. are grateful for funding through the ERC Consolidator Grant (771575 (PROMOFS)) and the EPSRC Impact Acceleration Account Award (EP/R511742/1). We are grateful for large facilities access through the ISIS Beamtime at TOSCA (RB1910059) and the Diamond Beamtime at B22 MIRIAM (SM21472). We acknowledge the use of the University of Oxford Advanced Research Computing (ARC) facility in carrying out this work (DOI: 10.5281/zenodo.22558). Via our membership of the U.K.'s HEC Materials Chemistry Consortium (MCC), which is funded by EPSRC (EP/R029431), this work used the ARCHER2 UK National Supercomputing Service (http://www.archer2.ac.uk). We thank Lorenzo Donà for compiling the development version of CRYSTAL17 on ARCHER2, and Prof. Bartolomeo Civalleri for the provision of DFT basis sets. We are very grateful to Dr. Svemir Rudić (ISIS), Drs. Mark Frogley and Gianfelice Cinque (Diamond) for scientific discussions.

■ REFERENCES

(1) Furukawa, H.; Cordova, K. E.; O'Keeffe, M.; Yaghi, O. M. The Chemistry and Applications of Metal-Organic Frameworks. *Science* **2013**, *341*, 1230444.

(2) Zhu, L.; Liu, X. Q.; Jiang, H. L.; Sun, L. B. Metal-Organic Frameworks for Heterogeneous Basic Catalysis. *Chem. Rev.* **2017**, *117*, 8129−8176.

(3) Horcajada, P.; Gref, R.; Baati, T.; Allan, P. K.; Maurin, G.; Couvreur, P.; Ferey, G.; Morris, R. E.; Serre, C. Metal-Organic Frameworks in Biomedicine. *Chem. Rev.* **2012**, *112*, 1232−1268.

(4) Li, B.; Wen, H. M.; Zhou, W.; Chen, B. Porous Metal-Organic Frameworks for Gas Storage and Separation: What, How, and Why? *J. Phys. Chem. Lett.* **2014**, *5*, 3468−3479.

(5) Lustig, W. P.; Mukherjee, S.; Rudd, N. D.; Desai, A. V.; Li, J.; Ghosh, S. K. Metal-Organic Frameworks: Functional Luminescent and Photonic Materials for Sensing Applications. *Chem. Soc. Rev.* **2017**, *46*, 3242−3285.

(6) Stassen, I.; Burtch, N.; Talin, A.; Falcaro, P.; Allendorf, M.; Ameloot, R. An Updated Roadmap for the Integration of Metal-Organic Frameworks with Electronic Devices and Chemical Sensors. *Chem. Soc. Rev.* **2017**, *46*, 3185−3241.

(7) Stavila, V.; Talin, A. A.; Allendorf, M. D. MOF-Based Electronic and Opto-Electronic Devices. *Chem. Soc. Rev.* **2014**, *43*, 5994−6010.

(8) Park, K. S.; Ni, Z.; Cote, A. P.; Choi, J. Y.; Huang, R.; Uribe-Romo, F. J.; Chae, H. K.; O'Keeffe, M.; Yaghi, O. M. Exceptional Chemical and Thermal Stability of Zeolitic Imidazolate Frameworks. *Proc. Natl. Acad. Sci. U.S.A.* **2006**, *103*, 10186−10191.

(9) Zou, D.; Liu, D.; Zhang, J. From Zeolitic Imidazolate Framework-8 to Metal-Organic Frameworks (MOFs): Representative Substance for the General Study of Pioneering MOF Applications. *Energy Environ. Mater.* **2018**, *1*, 209−220.

(10) Lo, Y.; Kang, D.-Y. Pseudopolymorphic Seeding for the Rational Synthesis of Hybrid Membranes with a Zeolitic Imidazolate Framework for Enhanced Molecular Separation Performance. *J. Mater. Chem. A* **2016**, *4*, 4172−4179.

(11) Sun, Y.; Rogge, S. M. J.; Lamaire, A.; Vandenbrande, S.; Wieme, J.; Siviour, C. R.; Van Speybroeck, V.; Tan, J. C. High-Rate Nanofluidic Energy Absorption in Porous Zeolitic Frameworks. *Nat. Mater.* **2021**, *20*, 1015−1023.

(12) Ortiz, G.; Nouali, H.; Marichal, C.; Chaplais, G.; Patarin, J. Energetic Performances of "ZIF-71−Aqueous Solution" Systems: A Perfect Shock-Absorber with Water. *J. Phys. Chem. C* **2014**, *118*, 21316−21322.

(13) Ryder, M. R.; Civalleri, B.; Bennett, T. D.; Henke, S.; Rudic, S.; Cinque, G.; Fernandez-Alonso, F.; Tan, J. C. Identifying the Role of Terahertz Vibrations in Metal-Organic Frameworks: From Gate-Opening Phenomenon to Shear-Driven Structural Destabilization. *Phys. Rev. Lett.* **2014**, *113*, 215502.

(14) Tan, J.-C.; Civalleri, B.; Lin, C.-C.; Valenzano, L.; Galvelis, R.; Chen, P.-F.; Bennett, T. D.; Mellot-Draznieks, C.; Zicovich-Wilson, C. M.; Cheetham, A. K. Exceptionally Low Shear Modulus in a

Prototypical Imidazole-Based Metal-Organic Framework. *Phys. Rev. Lett.* **2012**, *108*, 095502.

(15) Dovesi, R.; Saunders, V. R.; Roetti, C.; Orlando, R.; Zicovich-Wilson, C. M.; Pascale, F.; Civalleri, B.; Doll, K.; Harrison, N. M.; Bush, I. J.; D'Arco, P.; Llunell, M.; Causà, M.; Noël, Y.; Maschio, L.; Erba, A.; Rerat, M.; Casassa, S. *CRYSTAL17 User's Manual*; University of Torino: Torino, Italy, 2017.

(16) Dovesi, R.; Orlando, R.; Erba, A.; Zicovich-Wilson, C. M.; Civalleri, B.; Casassa, S.; Maschio, L.; Ferrabone, M.; De La Pierre, M.; D' Arco, P.; Noël, Y.; Causà, M.; Rérat, M.; Kirtman, B. CRYSTAL14: A Program for the Ab Initio Investigation of Crystalline Solids. *Int. J. Quantum Chem.* **2014**, *114*, 1287−1317.

(17) Grimme, S.; Antony, J.; Ehrlich, S.; Krieg, H. A Consistent and Accurate Ab Initio Parametrization of Density Functional Dispersion Correction (DFT-D) for the 94 Elements H-Pu. *J. Chem. Phys.* **2010**, *132*, 154104.

(18) Grimme, S.; Ehrlich, S.; Goerigk, L. Effect of the Damping Function in Dispersion Corrected Density Functional Theory. *J. Comput. Chem.* **2011**, *32*, 1456−65.

(19) Grimme, S.; Hansen, A.; Brandenburg, J. G.; Bannwarth, C. Dispersion-Corrected Mean-Field Electronic Structure Methods. *Chem. Rev.* **2016**, *116*, 5105−54.

(20) Colognesi, D.; Celli, M.; Cilloco, F.; Newport, R. J.; Parker, S. F.; Rossi-Albertini, V.; Sacchetti, F.; Tomkinson, J.; Zoppi, M. TOSCA Neutron Spectrometer: The Final Configuration. *Appl. Phys. A-Mater.* **2002**, *74*, s64−s66.

(21) *Neutron Scattering Fundamentals - Experimental Methods in the Physical Sciences*; Fernandez-Alonso, F., Price, D. L., Eds.; Academic Press: New York, 2013.

(22) Zeng, Z.; Tan, J.-C. AFM Nanoindentation to Quantify Mechanical Properties of Nano- and Micron-Sized Crystals of a Metal−Organic Framework Material. *ACS Appl. Mater. Interfaces* **2017**, *9*, 39839−39854.

(23) Möslein, A. F.; Gutierrez, M.; Cohen, B.; Tan, J. C. Near-Field Infrared Nanospectroscopy Reveals Guest Confinement in Metal-Organic Framework Single Crystals. *Nano Lett.* **2020**, *20*, 7446−7454.

(24) Keilmann, F.; Hillenbrand, R. Near-Field Microscopy by Elastic Light Scattering from a Tip. *Philos. Trans. R. Soc. A* **2004**, *362*, 787−805.

(25) Knoll, B.; Keilmann, F. Near-Field Probing of Vibrational Absorption for Chemical Microscopy. *Nature* **1999**, *399*, 134−137.

(26) Rauhut, G.; Pulay, P. Transferable Scaling Factors for Density Functional Derived Vibrational Force Fields. *J. Phys. Chem.* **1995**, *99*, 3093−3100.

(27) Peterson, V. K.; Kearley, G. J.; Wu, Y.; Ramirez-Cuesta, A. J.; Kemner, E.; Kepert, C. J. Local Vibrational Mechanism for Negative Thermal Expansion: A Combined Neutron Scattering and First-Principles Study. *Angew. Chem., Int. Ed.* **2010**, *49*, 585−8.

(28) Ryder, M. R.; Van de Voorde, B.; Civalleri, B.; Bennett, T. D.; Mukhopadhyay, S.; Cinque, G.; Fernandez-Alonso, F.; De Vos, D.; Rudic, S.; Tan, J. C. Detecting Molecular Rotational Dynamics Complementing the Low-Frequency Terahertz Vibrations in a Zirconium-Based Metal-Organic Framework. *Phys. Rev. Lett.* **2017**, *118*, 255502.

(29) Ryder, M. R.; Civalleri, B.; Cinque, G.; Tan, J.-C. Discovering Connections between Terahertz Vibrations and Elasticity Underpinning the Collective Dynamics of the HKUST-1 Metal−Organic Framework. *CrystEngComm* **2016**, *18*, 4303−4312.

(30) Krylov, A.; Vtyurin, A.; Petkov, P.; Senkovska, I.; Maliuta, M.; Bon, V.; Heine, T.; Kaskel, S.; Slyusareva, E. Raman Spectroscopy Studies of the Terahertz Vibrational Modes of a DUT-8 (Ni) Metal-Organic Framework. *Phys. Chem. Chem. Phys.* **2017**, *19*, 32099−32104.

(31) Banerjee, R.; Phan, A.; Wang, B.; Knobler, C.; Furukawa, H.; O'Keeffe, K.; Yaghi, O. M. High-Throughput Synthesis of Zeolitic Imidazolate Frameworks and Application to CO_2 Capture. *Science* **2008**, *319*, 939−943.

(32) Wee, L. H.; Vandenbrande, S.; Rogge, S. M. J.; Wieme, J.; Asselman, K.; Jardim, E. O.; Silvestre-Albero, J.; Navarro, J. A. R.; Van Speybroeck, V.; Martens, J. A.; Kirschhock, C. E. A. Chlorination of a Zeolitic-Imidazolate Framework Tunes Packing and Van Der Waals Interaction of Carbon Dioxide for Optimized Adsorptive Separation. *J. Am. Chem. Soc.* **2021**, *143*, 4962−4968.

(33) Bennett, T. D.; Cheetham, A. K. Amorphous Metal-Organic Frameworks. *Acc. Chem. Res.* **2014**, *47*, 1555−62.

(34) Springer, S.; Heidenreich, N.; Stock, N.; van Wüllen, L.; Huber, K.; Leoni, S.; Wiebcke, M. The ZIF System Zinc(II) 4,5-Dichoroimidazolate: Theoretical and Experimental Investigations of the Polymorphism and Crystallization Mechanisms. *Z. Kristallogr.* **2017**, *232*, 77−90.

(35) Maul, J.; Ryder, M. R.; Ruggiero, M. T.; Erba, A. Pressure-Driven Mechanical Anisotropy and Destabilization in Zeolitic Imidazolate Frameworks. *Phys. Rev. B* **2019**, *99*, 014102.

(36) Dusselier, M.; Davis, M. E. Small-Pore Zeolites: Synthesis and Catalysis. *Chem. Rev.* **2018**, *118*, 5265−5329.

(37) Baxter, E. F.; Bennett, T. D.; Cairns, A. B.; Brownbill, N. J.; Goodwin, A. L.; Keen, D. A.; Chater, P. A.; Blanc, F.; Cheetham, A. K. A Comparison of the Amorphization of Zeolitic Imidazolate Frameworks (ZIFs) and Aluminosilicate Zeolites by Ball-Milling. *Dalton Trans.* **2016**, *45*, 4258−68.

(38) Mortada, B.; Chaplais, G.; Nouali, H.; Marichal, C.; Patarin, J. Phase Transformations of Metal−Organic Frameworks MAF-6 and ZIF-71 During Intrusion−Extrusion Experiments. *J. Phys. Chem. C* **2019**, *123*, 4319−4328.

(39) Tricarico, M.; Tan, J.-C. Mechanical Properties and Nanostructure of Monolithic Zeolitic Imidazolate Frameworks: A Nanoindentation, Nanospectroscopy, and Finite Element Study. *Mater. Today Nano* **2022**, *17*, 100166.

(40) Oliver, W. C.; Pharr, G. M. Measurement of Hardness and Elastic Modulus by Instrumented Indentation: Advances in Understanding and Refinements to Methodology. *J. Mater. Res. Technol.* **2004**, *19*, 3−20.

(41) Bendt, S.; Hovestadt, M.; Böhme, U.; Paula, C.; Döpken, M.; Hartmann, M.; Keil, F. J. Olefin/Paraffin Separation Potential of ZIF-9 and ZIF-71: A Combined Experimental and Theoretical Study. *Eur. J. Inorg. Chem.* **2016**, *2016*, 4440−4449.

(42) Japip, S.; Wang, H.; Xiao, Y.; Shung Chung, T. Highly Permeable Zeolitic Imidazolate Framework (ZIF)-71 Nano-Particles Enhanced Polyimide Membranes for Gas Separation. *J. Membr. Sci.* **2014**, *467*, 162−174.

(43) Nalaparaju, A.; Zhao, X. S.; Jiang, J. W. Molecular Understanding for the Adsorption of Water and Alcohols in Hydrophilic and Hydrophobic Zeolitic Metal-Organic Frameworks. *J. Phys. Chem. C* **2010**, *114*, 11542−11550.

(44) Dauenhauer, P. J.; Abdelrahman, O. A. A Universal Descriptor for the Entropy of Adsorbed Molecules in Confined Spaces. *ACS Cent. Sci.* **2018**, *4*, 1235−1243.

(45) Zhang, Y.; Gutierrez, M.; Chaudhari, A. K.; Tan, J. C. Dye-Encapsulated Zeolitic Imidazolate Framework (ZIF-71) for Fluorochromic Sensing of Pressure, Temperature, and Volatile Solvents. *ACS Appl. Mater. Interfaces* **2020**, *12*, 37477−37488.

(46) Abraha, Y. W.; Tsai, C. W.; Niemantsverdriet, J. W. H.; Langner, E. H. G. Optimized CO_2 Capture of the Zeolitic Imidazolate Framework ZIF-8 Modified by Solvent-Assisted Ligand Exchange. *ACS Omega* **2021**, *6*, 21850−21860.

(47) Tsai, C.-W.; Langner, E. H. G.; Harris, R. A. Computational Study of ZIF-8 Analogues with Electron Donating and Withdrawing Groups for CO_2 Adsorption. *Microporous Mesoporous Mater.* **2019**, *288*, 109613.

(48) Tu, M.; Xia, B.; Kravchenko, D. E.; Tietze, M. L.; Cruz, A. J.; Stassen, I.; Hauffman, T.; Teyssandier, J.; De Feyter, S.; Wang, Z.; Fischer, R. A.; Marmiroli, B.; Amenitsch, H.; Torvisco, A.; Velasquez-Hernandez, M. J.; Falcaro, P.; Ameloot, R. Direct X-Ray and Electron-Beam Lithography of Halogenated Zeolitic Imidazolate Frameworks. *Nat. Mater.* **2021**, *20*, 93−99.

Statement of Authorship for joint/multi-authored papers for PGR thesis

To appear at the end of each thesis chapter submitted as an article/paper

The statement shall describe the candidate's and co-authors' independent research contributions in the thesis publications. For each publication there should exist a complete statement that is to be filled out and signed by the candidate and supervisor **(only required where there isn't already a statement of contribution within the paper itself).**

Title of Paper	Vibrational Modes and Terahertz Phenomena of the Large-Cage Zeolitic Imidazolate Framework-71
Publication Status	☒Published ☐ Accepted for Publication ☐Submitted for Publication ☐Unpublished and unsubmitted work written in a manuscript style
Publication Details	A.F. Möslein and J.C. Tan, "Vibrational Modes and Terahertz Phenomena of the Large-Cage Zeolitic Imidazolate Framework-71", The Journal of Physical Chemistry Letters, 13, 2838−2844 (2022).

Student Confirmation

Student Name:	Annika F. Möslein		
Contribution to the Paper	Experimental design, experimental execution, and data analysis: A.F.M. Numerical simulations: A.F.M. Writing of the original draft: A.F.M. Writing, editing, and reviewing: both co-authors. Supervision: J.-C.T.		
Signature		Date	27/07/2022

Supervisor Confirmation

By signing the Statement of Authorship, you are certifying that the candidate made a substantial contribution to the publication, and that the description described above is accurate.

Supervisor name and title:	Prof. Jin-Chong Tan		
Supervisor comments	I support this application and confirm the information entered is correct.		
Signature		Date	29 July 2022

This completed form should be included in the thesis, at the end of the relevant chapter.

Time to leave now, get out of this room, go somewhere, anywhere; sharpen this feeling of happiness and freedom, stretch your limbs, fill your eyes, be awake, wider awake, vividly awake in every sense and every pore.

— Stefan Zweig, *The Post-Office Girl*

7

Conclusions and further studies

Contents

7.1 Discussions

Targeting sensing applications, the main aim of this thesis was to investigate the interplay of physical, chemical, and structural characteristics of metal-organic framework (MOF) materials. These include host-guest interactions (Chapter 3), defect engineering (Chapter 4), sensing mechanism (Chapter 5), and structure-function relations (Chapter 6) to tune their response to external stimuli. Employing various spectroscopic techniques, ranging from nanoscale analytics to accelerator-based facilities, in combination with quantum mechanical calculations, I have explored these underpinning principles of MOFs for sensing from a new perspective: the single crystal level. In these concluding remarks, I will start by summarising the main findings of each Chapter, while also discussing their strengths and limitations, as well as their contributions to the field of research. Building upon these key findings, I will then expand toward a more general discussion and outlook, demonstrating how this fundamental knowledge will help the design of tailored properties for optoelectronics and sensing devices.

7.1.1 Chapter 3 summary

Chapter 3 described the concept of guest encapsulation in the pores of a MOF host, and summarised the characterisation techniques used to study such guest@MOF systems. Because it remains challenging to reveal the location of the guest, a new strategy is proposed to confirm whether the guest species are in fact encapsulated, or solely attached to the surface of the MOF-type crystals. This chapter comprises the following main contributions:

- The manuscript (*Nano Lett.*, 2020, **20**, 7446-7454.) presents the first systematic use of near-field nanospectroscopy in the field of MOFs. I demonstrate methodologies for sample preparation, data acquisition and analysis; and a detailed comparison with conventional spectroscopy techniques as well as DFT simulated spectra proved the feasibility to unveil the local single-crystal characteristics.

- This is also the first example of these techniques applied for investigating MOFs with loaded guests. Previously, clearly distinguishing between the guests being attached on the surface or encapsulated inside the pores of a MOF has been a controversial matter in the field, especially for applications. In this chapter, I present a strategy that successfully illustrates the location of emissive guests in representative MOFs composed of Zn^{2+} or Zr^{4+}.

- This chapter highlighted the importance of thorough washing for guest@MOF systems, which is necessary to remove any excess guest material adhered to the crystal surface.

Despite yielding nanoscale-resolved structural and vibrational information of guest@MOF systems, the presented methodologies have some important limitations. As it stands, the outlined approach is the best way to prove guest encapsulation on local scales, since the resolution is beyond the limitation of other techniques; and yet, we cannot rule out that tiny amounts of guest material may remain on the surface beyond the sensitivity of detection. However, the strong signal obtained with FLIM indicates the presence of larger amounts of guest material, which, if solely attached to the surface, would be detectable with s-SNOM. Especially together with the observed monoexponential decay of the luminescent monomers, this multimodal approach supports the notion that the guest species are distributed and successfully incorporated in the host framework. On the question of distribution, it still remains challenging to answer how homogeneous the guest molecules are dispersed inside the framework. Even if the FLIM images suggest a homogenous distribution, they only represent a 2-D projection, and it is likely that guest molecules were removed from the unit cells close to the crystal surface during extensive washing. Additionally, because s-SNOM imaging, nanoFTIR and FLIM only provide qualitative data, it is impossible to quantify the precise amount of guest loading. It is further worth noting that only the combination of all presented techniques can probe the confinement of guest molecules, and that this multimodal approach is solely applicable for emissive guest species.

Bearing in mind these limitations, the developed methodologies open the door for verifying the confinement of guests not only in MOF materials, but also in other porous materials, such as zeolites and hybrid frameworks. Nano-and micro-sized crystals are however only one example within the vast array of possible applications, ranging from 2-D nanosheets and mixed-matrix membranes to polycrystalline films for devices.

7.1.2 Chapter 4 summary

Building on the established feasibility to study the local characteristic of MOF-type single crystals, Chapter 4 delves into the presence of defects. Firstly, defect engineering is introduced as another core principle of tuning MOFs for applications. Secondly, a literature review summarised the conventional characterisation techniques to study defects in MOFs, further highlighting that point defects, albeit postulated, have not yet been probed in ZIF materials. Thirdly, this chapter contributes the following key findings reported in the published work *ACS Appl. Nano Mater.*, 2022, **5**, 6398-6409:

- A new set of techniques, comprising nanoFTIR, tip-force microscopy (TFM), and DFT calculations, was proposed to expose and characterise structural defects in crystalline materials.
- For the first time, point defects in ZIF materials were directly probed.
- By tracking the chemical changes during crystallisation, we discovered the co-existence of different structural defects at early stages of crystallisation. While zinc vacancies gradually disappear with prolonged growth time, missing linker defects prevail. These create open metal sites, which decrease hydrophobicity, but could also be leveraged for advanced reactivity in applications such as catalysis, gas adsorption, or chemical sensing.
- The impact of structural defects on the mechanical properties of the framework were revealed by TFM experiments and DFT calculations. In fact, the observed higher anisotropy and reduced Young's modulus can be linked with orientation of defects.

Even if this study focusses on the chemical and structural changes of ZIF-8 during crystallisation, the materials is sampled only at representative steps during the growth process, which depicts a major limitation. Ideally, *in situ* measurements will become feasible as soon as near-field techniques have fully advanced to liquid environments.[242] Another challenge is imposed by tip-force microscopy being strongly affected by local anomalies such as crystalline edges. To overcome this challenge, edges were identified by AFM imaging, and their contributions were filtered out in the measurement of mechanical properties. Yet, because standardised calibration of TFM is difficult, the comparison of Young's moduli, which seem to have similar values for crystals grown for 3 minutes (1.7 ± 0.7 GPa) versus 60 minutes (2.1 ± 0.5 GPa), is still a concern. We therefore consider not only the mean value itself, but also the variance of the individual point measurements as an additional indicator; in particular, a bimodal distribution could be observed for the more defective sample signifying higher anisotropy. To this end, there are no other experimental techniques available to study mechanical properties of individual crystals. This is precisely why we additionally performed computational modelling to simulate the mechanical properties of the ideal and defective ZIF-8 crystals. Here, a point defect was introduced in the unit cell; however, since they are periodic calculation, the DFT simulations assumed a regular repetition of the defect, whereas, in practice, the occurrence of point defects is most likely random. Although extended structural defects may also emerge in ZIF materials, they have not yet been discovered in the sodalite (SOD)-type structures such as ZIF-8. Therefore, in this work, we only consider point defects. We mention that point defects such as open metal sites can potentially be beneficial for applications such as catalysis or gas adsorption, but do not evaluate these crystals for these uses. Instead, we focus on the fundamental characterisation of defects in ZIF-8 rather than defect tuning for applications, for which we referred to reported experimental findings. Indeed, we provide the so far missing link between experiments and simulation revealing defects in ZIF-8 to explain the previous empirical findings, and invite further studies on defects in crystalline materials.

7.1.3 Chapter 5 summary

Turning from promising ways to tune MOFs for sensing applications to the sensing itself, Chapter 5 discusses how MOF materials detect specific gases. More specifically, the interactions of a guest@MOF composite material upon exposure to acetone are scrutinised, not only by near-field analytics and DFT calculations, but also by embracing other spectroscopy techniques. The findings have been published in *Adv. Mater. Interfaces*, 2023, **10**, 202201401.

- Rather than simply observing the response of a MOF to vapour, the underlying response mechanism is studied to answer open questions governing the host-guest interactions, limit of detection, and repeatability.

- Using spectroscopy techniques in the far- and mid-infrared regions, i.e. inelastic neutron scattering and synchrotron-based Fourier transform infrared spectroscopy; we found that conformational changes occur both in the framework and in the luminescent guest molecule upon encapsulation. These findings explain the green emission of the host-guest composite material, whereas ZnQ alone would usually exhibit a yellow (in aggregation) or blue emission (in solution).

- Guided by density functional theory calculations and spectroscopy techniques, we further investigated the chemical changes of the ZnQ@OX-1 system when exposed to acetone by unveiling the vibrational dynamics. Upon exposure to small solvents, the host-guest interactions are disrupted.

- *In situ* gas dosing experiments performed with synchrotron-based FTIR spectroscopy revealed that as little as 5 μL of volatile acetone (or 0.2 % in the cell) led to changes in specific vibrations, and can thus be detected by the material. This is an exciting finding given that materials which solvatochromic behavior alone might not even show any response in their IR spectrum.

- To push the limit of detection even further, we used fluorescence spectroscopy to discover that the shift in emission can be caused by only 50 ppm of volatile acetone.

- The first *in situ* gas dosing experiment on the single crystal level is presented based on near-field infrared nanospectroscopy.

In summary, the multimodal approach we presented here, encompassing spectroscopy at large-scale facilities, novel nano-scale analytics and DFT calculations, offers an in-depth study of the sensing mechanism at the interface of physical properties, chemical structure and optoelectronic response. In the course of this study, we noted that the material is strongly affected by humidity; it is therefore unfeasible to engineer a sensor device solely based on OX-1. Instead, an additional polymeric layer may offer protection, or the material has to be tuned further to achieve better performance under ambient conditions.

Despite our attempts to explain the sensing mechanism of ZnQ@OX-1, some questions remain unanswered. For instance, we postulate a derivative of ZnQ that emerges upon interaction with the framework, but could not yet solve its distinct structure. Similarly, the presence of defects in the OX-1 system is likely, given the conformational changes observed when ZnQ is confined inside the pores, but again, a detailed description remains as future work. Nonetheless, a fundamental understanding of the underpinning mechanism is demonstrated – and in fact crucial to further tune the sensing performance (that is limit of detection, selectivity, response time, reproducibility, and stability). Therefore, our work could pave the way to downstream application targeting the design of novel sensing technologies for the detection of volatile organic compounds in air or human breath to afford environmental monitoring or non-invasive diagnostics and screening.

7.1.4 Chapter 6 summary

To circumvent the main challenge that impedes the application of ZnQ@OX-1 as a sensor material, an alternative, hydrophobic MOF material is investigated in Chapter 6. The framework materials ZIF-71 has the ability to outperform other MOF systems, and even if its structure and synthesis route are well studied, as outlined in the literature review, there is a compelling need to understand its complex structure-function relations. This work has been published in *J. Phys. Chem. Lett.*, 2022, **13**, 2838-2844. To summarise, Chapter 6 provides:

- The complete assignment of all vibrational modes of ZIF-71.
- A link between observed physical and mechanical properties and the underpinning lattice dynamics, including gate-opening, shearing modes, and phase transitions.

- A description of its single-crystal behaviour: the Young's modulus was determined as $E = 1 - 3$ GPa, and the hardness as $H = 100 - 300$ MPa.

- The combined results illustrate a method that could be applied for many other hybrid materials to understand their fundamental properties.

Even if a good match between theoretical simulation and experimental measurement was obtained for the vibrational spectra, there are still a few additional modes that cannot be explained by the theoretical calculations. Ideally, the sample preparation is reproducible, but whether these vibrations observed in experiments are linked to adsorbed contaminants (impurities), or other defects related to the specific synthesis route, cannot be distinguished. Due to time restrictions at large-scale facilities, there are challenges regarding the availability of repeated measurements on different batches of synthesised sample material. Similarly, only a few crystals were probed with AFM nanoindentation, whereas the availability of large datasets would be preferred. This is however unachievable with such local techniques. One way to avoid this incurred challenge is given by performing simulations of the elastic constants; however, they have been proven unfeasible with the available resources. Finally, regarding the relation of vibrational modes triggering phenomena like gate-opening or shearing, it is important to distinguish between elastic and inelastic transformations. While molecular vibrations are elastic motions around their equilibrium position, the actual physical-structural conformations that are responsible for phase transition, amorphisation, or enhanced gas absorption are inelastic transformations. The existence of the specific lattice dynamics only indicate the possibility that inelastic transformation can be triggered. Despite these limitations, I believe that the findings of this chapter will provide the basis and spectroscopic evidence for prospective studies on ZIF-71 targeting its application in optoelectronics and sensing devices.

7.2 Concluding remarks

This thesis provided novel insights into the fundamental concepts of MOF materials for sensing applications. Presented here are strategies to reveal guest encapsulation and probe structural defects, as well as their implications, on the single crystal level. In addition, the importance of host-guest interactions for sensing was highlighted, and fundamental properties were resolved for a promising candidate material with enhanced sensing abilities. Overall, this thesis represents methodologies and insights to unravel the fascinating nanoscopic features of MOF materials, paving the way to downstream applications; in addition, the developed array of approaches is also applicable to other emerging 2-D and 3-D crystalline materials. The ability to confirm guest confinement or probe defects, for instance, is of preeminent importance to assess the performance of any porous host matrix or crystalline material, especially if doped. Perhaps most significant for the design of novel sensing devices are the findings on the sensing mechanism itself: indeed, they have sparked further tuning of the material, leading to the discovery of a similar system with enhanced sensitivity to acetone, and most importantly, resistance to moisture. Similarly, the fundamental description of the physical and structural phenomena in ZIF-71 has shaped the basis for a vibrational study on a photoswitchable guest@ZIF-71 system emerging as a stimuli-responsive, optoelectronic switching device.

In a nutshell, the synergistic use of nanoscale analytics, DFT simulations, and far-IR techniques has clearly proven to yield mechanistic insights into the multi-faceted and rich characteristics of MOFs, aiming to inspire new research in the quest for establishing how nanoscale mechanisms underpin the structure-function relationships. More importantly, and as derived from these first exemplars, unravelling their exceptional features will invite the advancement of MOFs as innovative sensing technologies to solve real-world problems in environmental monitoring, civil security, manufacturing safety, and medical diagnostics.

Appendices

A

Assignment of the vibrational modes of OX-1

The following tables provide a complete assignment of the vibrational modes of OX-1. Abbreviations are as follows:

- **asym**: asymmetric
- **sym**: symmetric
- **ip**: in-phase
- **op**: out-of-phase

Frequency cm^{-1}	**Intensity** a.u.	**Description**
29.81	1	scissoring of entire ring (rotation), rocking of O around Zn, stretching of CH3-Ch2 group
30.24	1	synchronous flapping (scissoring) of entire ring, rocking of O around Zn, stretching of Ch3-CH2 group
34.67	1	Zn-O symm stretch, synchronous flapping of entinre ring, streching of CH3-CH2 group, but all reduced
39.43	1	Zn-O asym stretch, wagging of H-C-C-H
40.45	1	Zn-O sym stretch, asym stretch of the whole CH3-CH2-NH2 group
45.55	22	Zn-O asym stretch, wagging of H-C-C-H
49.31	6	Zn-O rocking, rocking of C-C-N
51.68	3	ZN-O asym stretch, wagging of H-C-C-H, C-C stretch, wagging of whole CH groups
61.51	5	Zn-O rocking, C-C asym stretch, out-of-phase linker rotations (scissoring)
62.53	4	Zn-O-C asym stretch, Zn-O rocking
68.64	20	Zn-O asym stretch, rocking of whole C-C-NH group
75.01	16	Zn-O asym stretch, CH stretch,
77.29	11	Zn-O asym stretch, CH stretch, C-C-C asym stretch
78.26	12	Zn-O asym stretch, CH stretch, C-C-C asym stretch
79.2	29	Zn-O asym stretch, wagging of whole ring
82.57	11	Zn-O twisting, twisting of ring
84.92	32	Zn-O twisting, twisitng of ring
86.77	26	Zn-O sym stretch C-C stretch,
87.07	24	Zn-O sym stretch, C-C stretch, twisting of ring
88.58	7	Zn-O sym stretch, C-C stretch, twisting of ring
91.9	36	ZN-O sym stretch C-C rocking
96.66	9	Zn-O sym stetch, C-C stretch, twisting of ring
98.39	10	Zn-O rocking, rocking of ring
98.89	6	Zn-O rocking, rocking of ring
101.24	8	Zn-O rocking, rocking of ring
110.04	25	Zn-O twisting, C-C asym stretch
111.49	2	Zn-O twisting, C-C asym stretch
113.04	122	Zn-O twisting, C-C asym stretch

Table A.1: Vibrational modes of OX-1 from 0 to 113 cm^{-1}.

Frequency cm^{-1}	**Intensity** a.u.	**Description**
113.22	22	Zn-O twisting, rotation of ring
119.79	2	Zn-O twisting C-C twisting
127.21	9	H rocking, Zn-O twisting
127.81	6	Zn-O wagging
134	75	Zn-O wagging
134.51	2	Zn-O wagging
137.48	43	Zn-O wagging
137.85	16	Zn-O wagging
145.5	16	Zn-O wagging
145.62	123	Zn-O bend (wagging)
152.44	9	Zn-O wagging
157.32	4	Zn-O wagging
158.98	295	Zn-O wagging
161.53	38	Zn-O wagging
166.16	59	Zn-O scissoring
166.85	8	Zn-O scissoring
173.26	163	torsion of ring, Zn-O wagging
173.93	1	Zn-O wagging
177.24	13	Zn-O twisting
179.05	50	Zn-O wagging
186.43	50	Zn-O twisting
194.79	177	ZN-O wagging
203.54	26	Zn-O twisting
204.39	22	Zn-O twisting
208.78	10	Zn-O twisting (but small, mostly CH3)
209.4	67	Zn-O twisting (but small, mostly CH3)
218.37	42	Zn-O twisting
231.18	130	Zn-O twisting
251.06	133	Zn-O twisting
258.23	4	Zn-O wagging
275.77	1	Zn-O twisting
277.3	14	Zn-O twisting (but small, mostly CH3)
281.14	3	only CH3
287.86	8	Zn-O asym stretch, tilting of ring
291.31	89	Zn-O asym stretch
294.02	149	Zn-O asym stretch
301.15	217	Zn-O asym stretch, tilting of ring
303.91	7	only CH3
304.32	2	only CH3
311.2	31	Zn-O asym stretch
311.46	336	Zn-O asym stretch
338.73	1	only CH3
362.85	5	Zn-O asym stretch, in-plane rotation of ring
365.98	16	Zn-O asym stretch, in-plane rotation of ring

Table A.2: Vibrational modes of OX-1 from 113 to 400 cm^{-1}.

Frequency cm^{-1}	**Intensity** a.u.	**Description**
425.77	2	twisting of ring
433.81	2	C-C twisting
447.96	51	only CH3
448.07	3	only CH3
456.1	10	Zn-O sym stretch
469.5	11	mainly HCCH
469.65	9	mainly HCCH
479.63	12	ring wagging (out-of-plane bending), small Zn-O asym stretch
481.2	7	ring wagging (out-of-plane bending), small Zn-O asym stretch
488.13	48	mainly CH3
488.53	3	ring wagging, mainly CH3
512.9	12	mainly CH3
512.96	7	mainly CH3
521.61	2	tiny Zn-O asym stretch, otherwise HCCH
521.78	74	tiny Zn-O asym stretch, otherwise HCCH
532.65	150	mainly CH3
532.89	9	mainly CH3
555.58	420	Zn-O asym stretch, C-C asym stretch, ip ring deformation
561.32	185	Zn-O asym stretch, C-C asym stretch, ip ring deformation
584.49	197	Zn-O asym stretch, C-C asym stretch
584.75	69	Zn-O asym stretch, C-C asym stretch
599.82	36	Zn-O asym stretch, ip ring deformation
601.43	221	Zn-O asym stretch, ip ring deformation
619.46	118	Zn-O asym stretch, ip ring deformation
622.31	58	Zn-O asym stretch, ip ring deformation
628.64	18	Zn-O asym stretch, ip ring deformation
628.89	246	Zn-O asym stretch, ip ring deformation (asym)
648.15	15	Zn-O asym stretch, ip ring deformation (sym, breathing)
711.61	1	op ring deformation, OCO wagging
712.63	1	op ring deformation, OCO wagging
730.66	2	OCO scissoring, ip ring deformation
768.49	445	op ring deformation, HCCH wagging, OCO wagging
768.83	257	op ring deformation, HCCH wagging, OCO wagging
769.92	317	op ring deformation, HCCH wagging, OCO wagging
770.2	235	op ring deformation, HCCH wagging, OCO wagging
777.23	221	mostly CH3
778.48	2	HCCH wagging (in ring)
788.31	102	mostly CH3
801.17	19	mainly CH3
801.37	4	mainly CH3

Table A.3: Vibrational modes of OX-1 from 400 to 800 cm^{-1}.

Frequency cm^{-1}	**Intensity** a.u.	**Description**
839.41	67	ip ring deformation, OCO asym stretch
839.71	382	ip ring deformation, OCO asym stretch
844.2	175	ip ring deformation, OCO sym stretch
845.7	37	ip ring deformation, OCO sym stretch
847.11	12	Op ring deformation, OCO sym stretch
847.42	19	Op ring deformation, OCO sym stretch
849.07	258	ip ring deformation, OCO sym stretch
850.69	67	ip ring deformation, OCO sym stretch
860.83	58	CH3
861.37	1	CH3
887.78	9	op ring deformation, CH wagging
889.15	8	op ring deformation, CH wagging
894.31	19	ip ring breathing
899.97	67	CH3
900.97	8	CH3
921.97	37	CH3
922.32	4	op ring deformation (wagging)
922.7	30	op ring deformation (wagging)
924.83	4	op ring deformation (wagging)
927.84	23	op ring deformation (wagging)
1017.06	1	CH twisting, ip ring deformation
1017.94	1	CH twisting, ip ring deformation
1020.19	4	CH twisting, ip ring deformation
1036.1	47	CH3
1040.11	62	CH rocking, ip ring deformation
1040.14	21	CH rocking, ip ring deformation
1042.72	19	CH rocking, ip ring deformation
1042.76	20	CH rocking, ip ring deformation
1043.34	50	CH rocking, ip ring deformation
1044.41	5	CH rocking, ip ring deformation
1088.61	47	CH3
1127.89	32	CH3
1149.02	32	ip ring deformation, CH scissoring
1154.92	15	CH scissoring
1155.14	20	CH scissoring
1187.07	22	CH scissoring
1187.07	34	CH scissoring
1187.26	1	CH scissoring
1187.62	24	CH scissoring
1192.7	2	ring breathing, CH scissoring
1199.04	49	ip ring deformation, CH rocking
1199.12	16	ip ring deformation, CH rocking

Table A.4: Vibrational modes of OX-1 from 800 to 1200 cm^{-1}.

Frequency cm^{-1}	**Intensity** a.u.	**Description**
1200.69	2	ip ring deformation, CH rocking
1200.88	4	ip ring deformation, CH rocking
1202.46	110	ip ring deformation, CH rocking
1202	121	CH3
1329.57	3	ip ring deformation, CH rocking
1329.86	3	ip ring deformation, CH rocking
1395.97	1225	CH3
1399.41	1264	CH3
1401.51	493	CH3
1412.9	87	ip ring deformation, OCC sym stretch
1412.92	88	ip ring deformation, OCC sym stretch
1417.38	1465	C-C asym stretch
1417.62	1375	C-C asym stretch
1428.44	1544	C-C-O asym stretch
1431.42	2068	C-C-O asym stretch
1434.6	186	C-C-O asym stretch
1450.86	298	C-C sym stretch, CH scissoring
1451.72	27	C-C sym stretch, CH scissoring
1453.33	312	ip ring deformation, CH scissoring
1453.94	323	ip ring deformation, CH scissoring
1454.62	127	ip ring deformation, CH scissoring
1454.76	158	ip ring deformation, CH scissoring
1455.93	67	ip ring deformation, CH scissoring
1456.32	451	ip ring deformation, CH scissoring
1464.41	114	HCC asym stretch
1465.17	70	HCC asym stretch
1471.77	5483	OCO sym stretch, ip ring deformation, CH rocking
1484.19	901	OCO sym stretch, ip ring deformation, CH rocking
1501.69	8	OCO sym stretch
1502.29	207	OCO sym stretch
1504.86	84	OCO sym stretch
1506.09	124	OCO sym stretch
1511.27	8	mainly CH3, CH bend
1511.32	319	mainly CH3, CH bend
1518.36	14	OCO asym stretch, ring breathing
1519.46	6	OCO asym stretch, ring breathing
1520.74	20	OCO asym stretch, ring breathing
1522.98	76	OCO asym stretch, ring breathing
1565.36	179	ip ring deformation, CH rocking
1565.44	6	ip ring deformation, CH rocking
1566.65	246	ip ring deformation, CH rocking
1572.95	545	CH rocking, ip ring deformation
1574.68	132	CH rocking, ip ring deformation

Table A.5: Vibrational modes of OX-1 from 1200 to 1600 cm^{-1}.

Frequency cm^{-1}	**Intensity** a.u.	**Description**
1652.15	52	OCO wagging, ip ring deformation
1652.84	33	OCO wagging, ip ring deformation
1693.05	3975	NH scissoring, small CH scissoring
1705.65	55	C-C rocking
1715.48	143	C-C scissoring
1719.37	307	C-C scissoring
1719.68	1096	C-C scissoring (NH2 scissoring)
1721.27	1240	C-C scissoring
1737.34	3017	OCO twisting
1778.56	1971	CO twisting
1784.97	256	CO twisting
3202.45	1	CH asym stretch
3203.46	3	CH asym stretch
3215.96	8	CH sym stretch and asym stretch
3217.51	5	CH sym stretch
3217.56	2	CH sym stretch
3259.89	34	CH stretch

Table A.6: Vibrational modes of OX-1 from 1600 to 4000 cm^{-1}.

B

Assignment of the vibrational modes of ZIF-71

The following tables provide a complete assignment of the vibrational modes of ZIF-71. Abbreviations are as follows:

- Vibrations with change of bond length:
  - ν Stretching
  - ν_a Asymmetric stretching
  - ν_s Symmetric stretching
- Vibrations with change of an angle between bonds:
  - δ Bending
  - δ_s Scissoring (in-plane)
  - ρ Rocking (in-plane)
  - ω Wagging (out-of-plane)
  - τ Twisting (out-of-plane)

Collective modes 0 - 170 cm^{-1}

	Frequency (cm^{-1})		**Intensity** (a.u.)		**Assignment**
FTIR	BS1	BS2	BS1	BS2	
	9.46	11.61	1	1	8MR gate-opening
	10.45	6.63	1	1	Soft mode with shear deformation of 8MR and 6MR
	10.52	12.7	8	6	ρ opposite linkers in 4MR, asym gate-opening
	17.25		1		ρ opposite linkers in 6MR, asym gate-opening
24	**23.68**	21.9	5	6	8MR gate-opening
	24.21	23.94	2	1	8MR, 4MR shearing, ρ Cl
	25.43	25.35	2	3	8MR breathing
33	33.06	31.95	3	5	ν_a Zn-N, N-C, ω Cl
	37.42	40.18	2	1	6MR gate-opening
43	40.81		3		ν_s Cl-C-N, small 6MR breathing
	46.11	47.47	2	1	ν_s Zn-N, N-C, ω Cl, small 4MR and 8MR breathing
53	51.21	53.74	5	4	flapping of neighbouring linkers, asym gate-opening, ν_a Zn-N
	54.01	55.05	1	1	ν_a Zn-N-C, 4MR breathing
	55.68	58.95	3	1	ν_a Zn-N, 4MR and 8MR shearing, ring breathing
	61.39	62.87	2	2	ω Cl, ring breathing, 4MR and 6MR shearing
62	64.63	65.17	3	6	ring breathing, ω Cl, defomration of 8MR and 4MR
	66.35	68.83	1	3	ν_a Zn-N, ring deformation, small pore deformation
	77.37	75.83	1	5	τ Cl-C-N, ring breathing, very small pore deformation
	79.29	79.59	12	21	τ Cl, 8MR aperture increase, ν_s Zn-N: 4MR pore stretching
74	80.85	80.18	39	16	ν_a Zn-N: 4MR pore deformation
	86.14	83.13	5	3	τ Cl, ν C-H, 8MR and 4MR pore deformation, 6MR breathing
	91.56	85.82	2	1	ν_a Cl-C-N, 6MR pore deformation, 8MR and 4MR deformation
	93.31	90.73	1	1	4MR breathing, 6MR and 8MR small deformation
	99.21	98.65	34	30	ν ring, ω Cl, 4MR and 6MR aperture expansion
	103.96	102.09	4	2	6MR breathing (small)
	107.82	106.79	42	34	8MR breathing (small)
	111.95	110.15	4	7	4MR shearing, 6MR deformation
112	113.09	112.11	168	99	4MR and 6MR deformation, 8MR expansion
112	119.66	118.4	218	162	4MR and 8MR deformation, 6MR expansion
	121.91	121.28	19	19	8MR shearing, 6MR contraction
	125.35	123.79	163	171	8MR breathing, 4MR and 6MR deformation
	130.67	130.17	5	62	δ_s Cl, ν C-N, 4MR and 8MR pore stretching
129	133.15	132.41	600	651	ν Zn-N, ν N-C-H, 4MR breathing
	156.81	158.22	1	1	δ Cl, τ Zn-N, 6MR pore deformation
	161.39	163.13	10	10	ν_a Zn-N, δ_s Cl, 6MR pore deformation
	170.61	171.61	21	9	ν_a Cl, ν_a ring
	173.72	174.13	1	2	ν_a ring, δ_s Cl
	177.17	177.78	15	29	ν Zn-N δ_s Cl, 4MR and 6MR pore deformation

Table B.1: Vibrational modes of ZIF-71 from 0 to 170 cm^{-1}.

Vibrational modes 171 - 600 cm^{-1}

	Frequency (cm^{-1})		**Intensity** (a.u.)		**Assignment**
FTIR	BS1	BS2	BS1	BS2	
	179.63	180.06	28	10	δ Zn-N (tetrahedral deformation), ring deformation
173	179.89	180.54	55	68.75	δ Zn-N bending (tetrahedral deformation), ω Cl
	182.72	183.88	2	1	ν Zn-N, ring deformation
	189.79	190.2	1	7	δ Zn-N, ring stretching
190	195.41	194.86	15	17	δ Zn-N (tetrahedral deformation)
	223.49	223.06	25	20	ν Zn-N, 4MR breathing
	229.01	227.38	169	272	δ Zn-N, 8MR and 6MR deformation
215	230.26	230.87	780	730	δ Zn-N, pore deformation
	236.01	234.78	2	2	δ Zn-N, δ_s Cl
225	242.95	241.98	422	402	ν Zn-N
247	253.13	251.87	434	597	δ Zn-N, 4MR and 8MR expansion
	254.65	253.26	77	71	δ Zn-N, ω N-C-H
	256.51	253.87	45	9	δ Zn-N, ω C-H
	256.79	254.08	5	5	δ Zn-N, ω C-H
	257.44	255.53	185	156	δ Zn-N
	262.35	260.99	138	188	ω ring, 4MR asym gate-opening
	263.05	261.87	296	155	ν_a Zn-N, ω ring
	263.63	261.87	8	140	δ_s Zn-N
258	265.61	264.08	719	431	ρ linker
258	266.4	265.23	686	1082	ω linker
	269.2	268.46	87	90	ν Zn-N, ring deformation
	275.26	274.57	4	2	ν_a Zn-N, ring stretch
271	278.41	278.02	1165	1103	ν_a Zn-N, ring and pore deformation
281	284.04	283.7	1586	1504	ρ Zn-N, ρ C-N-C, small 8MR breathing
	288.77	288.94	969	1020	τ N-C, small 6MR breathing
	439.85	438.99	3	4	ρ linker
	444.45	443.66	7	6	ρ linker
	446.1	444.83	16	17	ν_a N-C-Cl, only incomplete linkers
	449.12	447.88	14	7	δ_s linker
	551.7	548.38	1	1	δ_s N-C, 4MR deformation
	552.08	548.59	2	10	τ N-Zn-N, 4MR expansion
	552.64	548.77	6	1	τ N-Zn-N,
	553.65	550.39	4	8	ω N-Zn-N
	554.53		1		ω N-Zn-N, ring stretching
	558.19	554.87	153	167	ω C-N, τ C-N-Zn
	560.49	557.14	14	15	ν_s Zn-N (Zn fixed)
	563	559.47	120	80	ν_s Zn-N (Zn fixed)
	563.53	559.85	41	95	ν_s Zn-N (Zn fixed), ring shearing
	564.74	560.98	173	216	ν_s Zn-N (Zn fixed), ring deformation
552	565.57	561.99	1044	1000	ν_s Zn-N (Zn fixed), in-plane ring deformation

Table B.2: Vibrational modes of ZIF-71 from 171 to 600 cm^{-1}.

Vibrational modes 601- 1200 cm^{-1} (Ring deformations)

	Frequency (cm^{-1})		**Intensity** (a.u.)		**Assignment**
FTIR	BS1	BS2	BS1	BS2	
	660.64	669.95	6	5	out-of-plane ring deformation
	661.19	670.36	19	1	out-of-plane ring deformation
	662	671.17	3	10	out-of-plane ring deformation
	663.36	672.4	5	10	out-of-plane ring deformation
	674.43	575.91	1	1	out-of-plane ring deformation
	675.12	677.05	99	8	out-of-plane ring deformation
	676.38	678.17	250	375	out-of-plane ring deformation
662	677.3	678.69	346	236	out-of-plane ring deformation
	677.77	678.96	157	354	out-of-plane ring deformation
	679.84	681.17	21	27	out-of-plane ring deformation
	680.36	681.96	65	56	out-of-plane ring deformation
666	682.82	684.58	972	761	out-of-plane ring deformation
	823.1	830.44	3	14	out-of-plane ring deformation
	824.39	831.07	58	1	out-of-plane ring deformation
821	825.09	832.29	70	116	out-of-plane ring deformation
	825.85	832.55	4	14	out-of-plane ring deformation
830	826.46	833.13	99	62	out-of-plane ring deformation
	827.29	835.16	29	81	out-of-plane ring deformation
	827.9	841.68	87	52	out-of-plane ring deformation
	1024.56	1027.14	12	8	in-plane ring deformation
	1028.59	1030.85	6	7	in-plane ring deformation
	1029.4	1031.71	4	2	in-plane ring deformation
	1029.54	1032.1	8	10	in-plane ring deformation
	1029.98	1032.58	4	5	in-plane ring deformation
	1033.14	1035.74	15	18	in-plane ring deformation
	1033.49	1063.7	3	8	in-plane ring deformation
1056	**1076.38**	1074.7	24028	24045	in-plane ring deformation, ρ H-C-N
	1080.26	1078.22	2317	2381	in-plane ring deformation, ρ H-C-N
	1081.76	1079.72	2493	2912	in-plane ring deformation, ρ H-C-N
	1084.43	1082.53	596	513	in-plane ring deformation, ρ H-C-N

Table B.3: Vibrational modes of ZIF-71 from 600 to 1200 cm^{-1}.

Vibrational modes 1201 - 4000 cm^{-1}

	Frequency (cm^{-1})		**Intensity** (a.u.)		**Assignment**
FTIR	BS1	BS2	BS1	BS2	
1201	**1216.57**	1212.3	1839	1699	δ CH, ν_a Cl-C-N, edges of unit cell
	1220.54	1216.47	1	1008	δ CH, ν C-N
1201	1224.07	1218.27	2414	1666	δ CH, ν C-N
	1229.18	1225.51	63	340	δ CH, ν C-N
1233	**1260.24**	1245.5	3319	3431	ν C-N, ring breathing
	1260.38	1245.82	1235	1174	ν C-N, ring breathing
	1264.22	1249.53	46	184	ν C-N
	1266.22	1251.13	2490	2191	ν_a C-N
1238	1270.56	1255.91	3175	4286	ν_a C-N
	1272.64	1237.63	548	411	ν_a C-N
	1273.35	1257.97	368	13	ν C-N
	1276.42	1260..96	486	537	ν C-N
	1332.01	1317.33	190	1367	ν C-N
	1333.06	1320.68	11	275	ν_s C-N
	1334.13	1322.32	238	19	ν C-N
	1334.48	1323.73	5	164	ν_s C-N
1302	1335.65	1324.99	440	1741	ν C-N
	1336.15	1325.64	2	500	ν_s C-N
	1337.46	1325.64	78	5	ν C-N
	1337.97	1326.37	300	83	ν_s C-N
	1339.14	1326.95	532	371	ν_s C-N
	1341.35	1328.42	1053	18	ν_s C-N
	1341.77	1328.6	346	17	ν C-N
1465	**1508.78**	1493.54	16845	15950	δ_s N-CH
	1519.82	1505.77	22	193	δ_s N-CH
1488	1520.47	1506.45	1248	1509	ν C-N, δ CH
	1543.99	1532.58	74	60	ν_a C-C-N
1518	1545.61	1534.23	1168	1307	ν_a C-C-N, ν C-C,
	1551.32	1539.22	503	468	ν_s N-C-N
	1552	1539.91	630	844	ν_s N-C-N
	155.49	1545.15	302	316	ν C-C, ν C-N,
1525	1556.6	1546.23	1331	1399	ν C-C, ν C-N, δ N-C-N
	1562.84	1552379	488	519	ν_s N-C-Cl (edge of unit cell)
	1563.73	1553.68	1273	1423	ν_s N-C-Cl (edge of unit cell)
	3277	3251.24	158	134	ρ CH
	3277.05	3251.28	15	10	ν CH
	3283.44	3260.16	31	38	ν CH
	3283.78	3260.53	12	14	ν CH
	3296.46	3270.69	19	31	ν CH
	3296.78	3270.95	2	3	ν CH
	3305.46	3281.78	74	86	ν CH
	3305.78	3281.96	4	3	ν CH

Table B.4: Vibrational modes of ZIF-71 from 1200 to 4000 cm^{-1}.

References

[1] S. H. Gellman, "Introduction: molecular recognition," *Chemical Reviews*, vol. 97, no. 5, 1231–1232, 1997.

[2] Z. Meng, R. M. Stolz, L. Mendecki, and K. A. Mirica, "Electrically-transduced chemical sensors based on two-dimensional nanomaterials," *Chemical Reviews*, vol. 119, no. 1, 478–598, 2019.

[3] R. Paolesse, S. Nardis, D. Monti, M. Stefanelli, and C. Di Natale, "Porphyrinoids for chemical sensor applications," *Chemical Reviews*, vol. 117, no. 4, 2517–2583, 2017.

[4] U. E. Spichiger-Keller, *Chemical Sensors and Biosensors for Medical and Biological Applications*. Weinheim, Germany: Wiley-VCH, 1998.

[5] P. Kim, J. Albarella, J. Carey, M. Placek, A. Sen, A. Wittrig, and W. McNamara III, "Towards the development of a portable device for the monitoring of gaseous toxic industrial chemicals based on a chemical sensor array," *Sensors and Actuators B: Chemical*, vol. 134, no. 1, 307–312, 2008.

[6] F. Wang, H. Gu, and T. M. Swager, "Carbon nanotube/polythiophene chemiresistive sensors for chemical warfare agents," *Journal of the American Chemical Society*, vol. 130, no. 16, 5392–5393, 2008.

[7] F. Mustafa and S. Andreescu, "Chemical and biological sensors for food-quality monitoring and smart packaging," *Foods*, vol. 7, no. 10, 168, 2018.

[8] B. Pejcic, P. Eadington, and A. Ross, "Environmental monitoring of hydrocarbons: a chemical sensor perspective," *Environmental Science & Technology*, vol. 41, no. 18, 6333–6342, 2007.

[9] P. K. Sekhar, E. L. Brosha, R. Mukundan, and F. Garzon, "Chemical sensors for environmental monitoring and homeland security," *The Electrochemical Society Interface*, vol. 19, 35, 2010.

[10] M. C. Frost and M. E. Meyerhoff, "Implantable chemical sensors for real-time clinical monitoring: Progress and challenges," *Current Opinion in Chemical Biology*, vol. 6, no. 5, 633–641, 2002.

[11] G. Matzeu, L. Florea, and D. Diamond, "Advances in wearable chemical sensor design for monitoring biological fluids," *Sensors and Actuators B: Chemical*, vol. 211, 403–418, 2015.

[12] Y.-H. Shin, M. Teresa Gutierrez-Wing, and J.-W. Choi, "Review—recent progress in portable fluorescence sensors," *Journal of The Electrochemical Society*, vol. 168, no. 1, 017502, 2021.

[13] L. Gatzoulis and I. Iakovidis, “Wearable and portable ehealth systems. technological issues and opportunities for personalized care,” *IEEE Engineering in Medicine and Biology Magazine*, vol. 26, no. 5, 51–56, 2007.

[14] M. Phillips, J. Herrera, S. Krishnan, M. Zain, J. Greenberg, and R. N.Cataneo, “Variation in volatile organic compounds in the breath of normal humans,” *Journal of Chromatography B: Biomedical Sciences and Applications*, vol. 729, no. 1-2, 75–88, 1999.

[15] J. D. Fenske and S. E. Paulson, “Human breath emissions of vocs,” *Journal of the Air & Waste Management Association*, vol. 49, no. 5, 594–8, 1999.

[16] S. Das and M. Pal, “Review—non-invasive monitoring of human health by exhaled breath analysis: A comprehensive review,” *Journal of The Electrochemical Society*, vol. 167, no. 3, 037562, 2020.

[17] “Air quality guidelines for europe,” World Health Organization. Regional Office for Europe, Report, 2000.

[18] V. Soni, P. Singh, and V. Shree V. Goel, “Effects of VOCs on human health,” in *Air Pollution and Control. Energy, Environment, and Sustainability*, N. Sharma, A. Agarwal, P. Eastwood, T. Gupta, and A. Singh, Eds. Singapore: Springer, 2018.

[19] K. Duarte, C. I. L. Justino, A. C. Freitas, A. C. Duarte, and T. A. P. Rocha-Santos, “Direct-reading methods for analysis of volatile organic compounds and nanoparticles in workplace air,” *TrAC Trends in Analytical Chemistry*, vol. 53, 21–32, 2014.

[20] L. Spinelle, M. Gerboles, G. Kok, S. Persijn, and T. Sauerwald, “Review of portable and low-cost sensors for the ambient air monitoring of benzene and other volatile organic compounds,” *Sensors*, vol. 17, no. 7, 1520, 2017.

[21] W. Muangrat, V. Yordsri, R. Maolanon, S. Pratontep, S. Porntheeraphat, and W. Wongwiriyapan, “Hybrid gas sensor based on platinum nanoparticles/poly(methyl methacrylate)-coated single-walled carbon nanotubes for dichloromethane detection with a high response magnitude,” *Diamond and Related Materials*, vol. 65, 183–190, 2016.

[22] R. S. Andre, R. C. Sanfelice, A. Pavinatto, L. H. C. Mattoso, and D. S. Correa, “Hybrid nanomaterials designed for volatile organic compounds sensors: A review,” *Materials & Design*, vol. 156, 154–166, 2018.

[23] J. M. Chalmers and P. R. Griffiths, *Handbook of Vibrational Spectroscopy.* John Wiley & Sons, Ltd, 2006, vol. 1.

[24] G. Gardner, D Venkataraman, J. Moore, and S Lee, “Spontaneous assembly of a hinged coordination network,” *Nature*, vol. 374, no. 6525, 792–795, 1995.

[25] O. M. Yaghi, G. Li, and H. Li, “Selective binding and removal of guests in a microporous metal-organic framework,” *Nature*, vol. 378, 703–706, 1995.

[26] H. Furukawa, K. E. Cordova, M. O’Keeffe, and O. M. Yaghi, “The chemistry and applications of metal-organic frameworks,” *Science*, vol. 341, no. 6149, 1230444, 2013.

[27] B. Li, H. M. Wen, W. Zhou, and B. Chen, “Porous metal-organic frameworks for gas storage and separation: What, how, and why?” *Journal of Physical Chemistry Letters*, vol. 5, no. 20, 3468–3479, 2014.

[28] L. Zhu, X. Q. Liu, H. L. Jiang, and L. B. Sun, "Metal-organic frameworks for heterogeneous basic catalysis," *Chemical Reviews*, vol. 117, no. 12, 8129–8176, 2017.

[29] P. Horcajada, R. Gref, T. Baati, P. K. Allan, G. Maurin, P. Couvreur, G. Ferey, R. E. Morris, and C. Serre, "Metal-organic frameworks in biomedicine," *Chemical Reviews*, vol. 112, no. 2, 1232–1268, 2012.

[30] V. Stavila, A. A. Talin, and M. D. Allendorf, "MOF-based electronic and opto-electronic devices," *Chemical Society Reviews*, vol. 43, no. 16, 5994–6010, 2014.

[31] M. Dincă and F. Léonard, "Metal–organic frameworks for electronics and photonics," *MRS Bulletin*, vol. 41, no. 11, 854–857, 2016.

[32] W. P. Lustig, S. Mukherjee, N. D. Rudd, A. V. Desai, J. Li, and S. K. Ghosh, "Metal-organic frameworks: Functional luminescent and photonic materials for sensing applications," *Chemical Society Reviews*, vol. 46, no. 11, 3242–3285, 2017.

[33] L. E. Kreno, K. Leong, O. K. Farha, M. Allendorf, R. P. Van Duyne, and J. T. Hupp, "Metal-organic framework materials as chemical sensors," *Chemical Reviews*, vol. 112, no. 2, 1105–25, 2012.

[34] Z. Hu, B. J. Deibert, and J. Li, "Luminescent metal-organic frameworks for chemical sensing and explosive detection," *Chemical Society Reviews*, vol. 43, no. 16, 5815–40, 2014.

[35] I. Stassen, N. Burtch, A. Talin, P. Falcaro, M. Allendorf, and R. Ameloot, "An updated roadmap for the integration of metal-organic frameworks with electronic devices and chemical sensors," *Chemical Society Reviews*, vol. 46, no. 11, 3185–3241, 2017.

[36] A. F. Möslein and J. C. Tan, "Vibrational modes and terahertz phenomena of the large-cage zeolitic imidazolate framework-71," *Journal of Physical Chemistry Letters*, vol. 13, no. 12, 2838–2844, 2022.

[37] A. F. Möslein, M. Gutierrez, B. Cohen, and J. C. Tan, "Near-field infrared nanospectroscopy reveals guest confinement in metal-organic framework single crystals," *Nano Letters*, vol. 20, no. 10, 7446–7454, 2020.

[38] A. F. Möslein, L. Donà, B. Civalleri, and J.-C. Tan, "Defect engineering in metal–organic framework nanocrystals: Implications for mechanical properties and performance," *ACS Applied Nano Materials*, vol. 5, no. 5, 6398–6409, 2022.

[39] M. D. Allendorf, M. E. Foster, F. Leonard, V. Stavila, P. L. Feng, F. P. Doty, K. Leong, E. Y. Ma, S. R. Johnston, and A. A. Talin, "Guest-induced emergent properties in metal-organic frameworks," *Journal of Physical Chemistry Letters*, vol. 6, no. 7, 1182–1195, 2015.

[40] R. Banerjee, A. Phan, B. Wang, C. Knobler, H. Furukawa, K. O'Keeffe, and O. M. Yaghi, "High-throughput synthesis of zeolitic imidazolate frameworks and application to CO_2 capture," *Science*, vol. 319, no. 5865, 939–943, 2008.

[41] M. R. Ryder, B. Civalleri, T. D. Bennett, S. Henke, S. Rudic, G. Cinque, F. Fernandez-Alonso, and J. C. Tan, "Identifying the role of terahertz vibrations in metal-organic frameworks: From gate-opening phenomenon to shear-driven structural destabilization," *Physical Review Letters*, vol. 113, no. 21, 215502, 2014.

[42] A. J. Howarth, A. W. Peters, N. A. Vermeulen, T. C. Wang, J. T. Hupp, and O. K. Farha, "Best practices for the synthesis, activation, and characterization of metal–organic frameworks," *Chemistry of Materials*, vol. 29, no. 1, 26–39, 2016.

[43] W. Herschel, "Experiments on the refrangibility of the invisible rays of the sun," *Philosophical Transactions of the Royal Society of London*, vol. 90, 284–292, 1800.

[44] P. R. Griffiths, "Introduction to vibrational spectroscopy," in *Handbook of Vibrational Spectroscopy*, J. M. Chalmers and P. R. Griffith, Eds. John Wiley & Sons, Ltd, 2006, vol. 1.

[45] D. Steele, "Infrared spectroscopy: Theory," in *Handbook of Vibrational Spectroscopy*, J. M. Chalmers and P. R. Griffiths, Eds. John Wiley & Sons, Ltd, 2006, vol. 1.

[46] J. M. Chalmers, "Mid-infrared spectroscopy of the condensed phase," in *Handbook of Vibrational Spectroscopy*, J. M. Chalmers and P. R. Griffiths, Eds. John Wiley & Sons, Ltd, 2006, vol. 1.

[47] P. R. Griffiths, "Far-infrared spectroscopy," in *Handbook of Vibrational Spectroscopy*, J. M. Chalmers and P. R. Griffith, Eds. John Wiley & Sons, Ltd, 2006, vol. 1.

[48] R. Dovesi, V. R. Saunders, C. Roetti, R. Orlando, C. M. Zicovich-Wilson, F. Pascale, B. Civalleri, K. Doll, N. M. Harrison, I. J. Bush, P. D'Arco, M. Llunell, M. Causà, Y. Noël, L. Maschio, A. Erba, M. Rerat, and S. Casassa, *CRYSTAL17 User's Manual.* University of Torino, Torino, 2017.

[49] A. D. Becke, "Density-functional exchange-energy approximation with correct asymptotic behavior," *Physical Review A: General Physics*, vol. 38, no. 6, 3098–3100, 1988.

[50] C. Lee, W. Yang, and R. G. Parr, "Development of the colle-salvetti correlation-energy formula into a functional of the electron density," *Physical Review B*, vol. 37, no. 2, 785–789, 1988.

[51] S. Grimme, J. Antony, S. Ehrlich, and H. Krieg, "A consistent and accurate ab initio parametrization of density functional dispersion correction (dft-d) for the 94 elements h-pu," *Journal of Chemical Physics*, vol. 132, no. 15, 154104, 2010.

[52] H. Matsuura and H. Yoshida, "Calculation of vibrational frequencies by hartree–fock-based and density functional theory," in *Handbook of Vibrational Spectroscopy*, J. M. Chalmers and P. R. Griffith, Eds. John Wiley & Sons, Ltd, 2006, vol. 1.

[53] A. A. Michelson, "On the application of interference-methods to spectroscopic measurements," *The London, Edinburgh, and Dublin Philosophical Magazine and Journal of Science*, vol. 31, no. 191, 338–346, 1891.

[54] R. S. Jackson, "Continuous scanning interferometers for mid-infrared spectrometry," in *Handbook of Vibrational Spectroscopy*, J. M. Chalmers and P. R. Griffiths, Eds. John Wiley & Sons, Ltd, 2006, vol. 1.

[55] P. R. Griffiths and J. A. Haseth, *Fourier Transform Infrared Spectrometry*, 2nd ed. Hoboken, New Jersey: John Wiley & Sons, Inc, 2007.

[56] P. R. Griffiths, "Resolution and instrument line shape function," in *Handbook of Vibrational Spectroscopy*, J. M. Chalmers and P. R. Griffiths, Eds. John Wiley & Sons, Ltd, 2006, vol. 1.

[57] T. L. Cocker, V. Jelic, R. Hillenbrand, and F. A. Hegmann, "Nanoscale terahertz scanning probe microscopy," *Nature Photonics*, vol. 15, no. 8, 558–569, 2021.

[58] H. A. Bethe, "Theory of diffraction by small holes," *The Physical Review*, vol. 66, no. 7,8, 163, 1944.

[59] F. J. G. d. Abajo, "Light transmission through a singlecylindrical hole in a metallic film," *Optics Express*, vol. 10, no. 25, 1475–1484, 2002.

[60] E. Abbe, "Beiträge zur theorie des mikroskops und der mikroskopischen wahrnehmung," *Archiv für Mikroskopische Anatomie*, vol. 9, 413–468, 1873.

[61] F. Zenhausern, M. P. O'Boyle, and H. K. Wickramasinghe, "Apertureless near-field optical microscope," *Applied Physics Letters*, vol. 65, no. 13, 1623–1625, 1994.

[62] F. Zenhausern, Y. Martin, and H. K. Wickramasinghe, "Scanning interferometric apertureless microscopy: Optical imaging at 10 angstrom resolution," *Science*, vol. 269, no. 5227, 1082–1085, 1995.

[63] Y. Inouye and S. Kawata, "Near-field scanning optical microscope with a metallic probe tip," *Optics Letters*, vol. 19, no. 3, 159, 1994.

[64] F. Keilmann and R. Hillenbrand, "Near-field microscopy by elastic light scattering from a tip," *Philosophical Transactions of The Royal Society A Mathematical Physical and Engineering Sciences*, vol. 362, no. 1817, 787–805, 2004.

[65] T. Taubner, R. Hillenbrand, and F. Keilmann, "Nanoscale polymer recognition by spectral signature in scattering infrared near-field microscopy," *Applied Physics Letters*, vol. 85, no. 21, 5064–5066, 2004.

[66] F. Huth, A. Govyadinov, S. Amarie, W. Nuansing, F. Keilmann, and R. Hillenbrand, "Nano-FTIR absorption spectroscopy of molecular fingerprints at 20 nm spatial resolution," *Nano Letters*, vol. 12, no. 8, 3973–3978, 2012.

[67] A. A. Govyadinov, I. Amenabar, F. Huth, P. S. Carney, and R. Hillenbrand, "Quantitative measurement of local infrared absorption and dielectric function with tip-enhanced near-field microscopy," *Journal of Physical Chemistry Letters*, vol. 4, no. 9, 1526–1531, 2013.

[68] R. Hillenbrand, T. Taubner, and F. Keilmann, "Phonon-enhanced light-matter interaction at the nanometre scale," *Nature*, vol. 418, no. 6894, 159–162, 2002.

[69] B. Knoll and F. Keilmann, "Near-field probing of vibrational absorption for chemical microscopy," *Nature*, vol. 399, 134–137, 1999.

[70] N. Ocelic and R. Hillenbrand, "Optical device for measuring modulated signal light," *Patent US 7738115 B2*, 11/997,386, 2010.

[71] F. Keilmann and R. Hillenbrand, "Near-field nanoscopy by elastic light scattering from a tip," in *Nano-Optics and Near-Field Optical Microscopy*, A. Zayats and D. Richards, Eds. Artech House, 2008.

[72] G. Binnig, C. F. Quate, and C. Gerber, "Atomic force microscope," *Physical Review Letters*, vol. 56, no. 9, 930–933, 1986.

[73] A. Huber, F. Keilmann, J. Wittborn, J. Aizpurua, and R. Hillenbrand, "Terahertz near-field nanoscopy of mobile carriers in single semiconductor nanodevices," *Nano Letters*, vol. 8, no. 11, 3766–3770, 2008.

[74] B. Knoll and F. Keilmann, "Enhanced dielectric contrast in scattering-type scanning near-field optical microscopy," *Optics Communications*, vol. 182, no. 4-6, 321–328, 2000.

[75] N. Ocelic, A. Huber, and R. Hillenbrand, "Pseudoheterodyne detection for background-free near-field spectroscopy," *Applied Physics Letters*, vol. 89, no. 10, 101124, 2006.

[76] F. Keilmann, "Scattering-type near-field optical microscopy," *Journal of Electron Microscopy*, vol. 53, no. 2, 187–192, 2004.

[77] A. Cvitkovic, N. Ocelic, and R. Hillenbrand, "Analytical model for quantitative prediction of material contrasts in scattering-type near-field optical microscopy," *Optics Express*, vol. 15, no. 14, 8550–8565, 2007.

[78] S. Dai, M. Tymchenko, Z.-Q. Xu, T. T. Tran, Y. Yang, Q. Ma, K. Watanabe, T. Taniguchi, P. Jarillo-Herrero, I. Aharonovich, D. N. Basov, T. H. Tao, and A. Alù, "Internal nanostructure diagnosis with hyperbolic phonon polaritons in hexagonal boron nitride," *Nano Letters*, vol. 18, no. 8, 5205–5210, 2018.

[79] I. Amenabar, S. Poly, W. Nuansing, E. H. Hubrich, A. A. Govyadinov, F. Huth, R. Krutokhvostov, L. Zhang, M. Knez, J. Heberle, A. M. Bittner, and R. Hillenbrand, "Structural analysis and mapping of individual protein complexes by infrared nanospectroscopy," *Nature Communications*, vol. 4, 2890, 2013.

[80] I. Amenabar, S. Poly, M. Goikoetxea, W. Nuansing, P. Lasch, and R. Hillenbrand, "Hyperspectral infrared nanoimaging of organic samples based on fourier transform infrared nanospectroscopy," *Nature Communications*, vol. 8, 14402, 2017.

[81] A. M. Gigler, A. J. Huber, M. Bauer, A. Ziegler, R. Hillenbrand, and R. W. Stark, "Nanoscale residual stress-field mapping around nanoindents in SiC by IR s-SNOM and confocal raman microscopy," *Optics Express*, vol. 17, no. 25, 22351–22357, 2009.

[82] M. Etxeberria-Benavides, O. David, T. Johnson, M. M. Łozińska, A. Orsi, P. A. Wright, S. Mastel, R. Hillenbrand, F. Kapteijn, and J. Gascon, "High performance mixed matrix membranes (MMMs) composed of ZIF-94 filler and 6FDA-DAM polymer," *Journal of Membrane Science*, vol. 550, 198–207, 2018.

[83] T. Xiong, Y. Zhang, L. Donà, M. Gutiérrez, A. F. Möslein, A. S. Babal, N. Amin, B. Civalleri, and J.-C. Tan, "Tunable fluorescein-encapsulated zeolitic imidazolate framework-8 nanoparticles for solid-state lighting," *ACS Applied Nano Materials*, vol. 4, no. 10, 10321–10333, 2021.

[84] Y. Zhang, T. Xiong, A. F. Möslein, S. Mollick, V. Kachwal, A. S. Babal, N. Amin, and J.-C. Tan, "Nanoconfinement of tetraphenylethylene in zeolitic metal-organic framework for turn-on mechanofluorochromic stress sensing," *Applied Materials Today*, vol. 27, 101434, 2022.

[85] A. S. Babal, B. E. Souza, A. F. Möslein, M. Gutiérrez, M. D. Frogley, and J.-C. Tan, “Broadband dielectric behavior of an MIL-100 metal–organic framework as a function of structural amorphization,” *ACS Applied Electronic Materials*, vol. 3, no. 3, 1191–1198, 2021.

[86] M. Tricarico and J.-C. Tan, “Mechanical properties and nanostructure of monolithic zeolitic imidazolate frameworks: A nanoindentation, nanospectroscopy, and finite element study,” *Materials Today Nano*, vol. 17, 100166, 2022.

[87] M. Gutierrez, A. F. Möslein, and J. C. Tan, “Facile and fast transformation of nonluminescent to highly luminescent metal-organic frameworks: Acetone sensing for diabetes diagnosis and lead capture from polluted water,” *ACS Applied Material Interfaces*, vol. 13, no. 6, 7801–7811, 2021.

[88] T. Man, C. Xu, X. Y. Liu, D. Li, C. K. Tsung, H. Pei, Y. Wan, and L. Li, “Hierarchically encapsulating enzymes with multi-shelled metal-organic frameworks for tandem biocatalytic reactions,” *Nature Communications*, vol. 13, no. 1, 305, 2022.

[89] J. Chae, S. An, G. Ramer, V. Stavila, G. Holland, Y. Yoon, A. A. Talin, M. Allendorf, V. A. Aksyuk, and A. Centrone, “Nanophotonic atomic force microscope transducers enable chemical composition and thermal conductivity measurements at the nanoscale,” *Nano Letters*, vol. 17, no. 9, 5587–5594, 2017.

[90] J. M. Ortega, F. Glotin, R. Prazeres, X. Li, and R. Gref, “Far infrared micro-spectroscopy: An innovative method to detect individual metal-organic framework particles,” *Applied Optics*, vol. 56, no. 23, 6663–6667, 2017.

[91] D. Nowak, W. Morrison, H. K. Wickramasinghe, J. Jahng, E. Potma, L. Wan, R. Ruiz, T. R. Albrecht, K. Schmidt, J. Frommer, D. P. Sanders, and S. Park, “Nanoscale chemical imaging by photoinduced force microscopy,” *Science Advances*, vol. 2, e1501571, 2016.

[92] J. Li, J. Jahng, J. Pang, W. Morrison, J. Li, E. S. Lee, J. J. Xu, H. Y. Chen, and X. H. Xia, “Tip-enhanced infrared imaging with sub-10 nm resolution and hypersensitivity,” *Journal of Physical Chemistry Letters*, vol. 11, no. 5, 1697–1701, 2020.

[93] G. Delen, Z. Ristanovic, L. D. B. Mandemaker, and B. M. Weckhuysen, “Mechanistic insights into growth of surface-mounted metal-organic framework films resolved by infrared (nano-) spectroscopy,” *Chemistry*, vol. 24, no. 1, 187–195, 2018.

[94] G. Delen, M. Monai, F. Meirer, and B. M. Weckhuysen, “In situ nanoscale infrared spectroscopy of water adsorption on nanoislands of surface-anchored metal-organic frameworks,” *Angewandte Chemie*, vol. 60, no. 3, 1620–1624, 2021.

[95] L. Bai, A. Jana, H. P. Tham, K. T. Nguyen, P. Borah, and Y. Zhao, “Remarkable vapochromic behavior of pure organic octahedron embedded in porous frameworks,” *Small*, vol. 12, no. 24, 3302–8, 2016.

[96] J. Jiang, Y. Zhao, and O. M. Yaghi, “Covalent chemistry beyond molecules,” *Journal of the American Chemical Society*, vol. 138, no. 10, 3255–65, 2016.

[97] S. Yuan, L. Feng, K. Wang, J. Pang, M. Bosch, C. Lollar, Y. Sun, J. Qin, X. Yang, P. Zhang, Q. Wang, L. Zou, Y. Zhang, L. Zhang, Y. Fang, J. Li, and H. C. Zhou, "Stable metal-organic frameworks: Design, synthesis, and applications," *Advanced Materials*, vol. 30, no. 37, e1704303, 2018.

[98] J. Hao, X. Xu, H. Fei, L. Li, and B. Yan, "Functionalization of metal-organic frameworks for photoactive materials," *Advanced Materials*, vol. 30, no. 17, e1705634, 2018.

[99] S. Horike, S. Shimomura, and S. Kitagawa, "Soft porous crystals," *Nature Chemistry*, vol. 1, no. 9, 695–704, 2009.

[100] A. Schneemann, V. Bon, I. Schwedler, I. Senkovska, S. Kaskel, and R. A. Fischer, "Flexible metal-organic frameworks," *Chemical Society Reviews*, vol. 43, no. 16, 6062–96, 2014.

[101] M. R. Ryder, B. Civalleri, G. Cinque, and J.-C. Tan, "Discovering connections between terahertz vibrations and elasticity underpinning the collective dynamics of the HKUST-1 metal–organic framework," *CrystEngComm*, vol. 18, no. 23, 4303–4312, 2016.

[102] R. Aniruddha, I. Sreedhar, and B. M. Reddy, "MOFs in carbon capture-past, present and future," *Journal of CO_2 Utilization*, vol. 42, 101297, 2020.

[103] H. Kaur, S. Sundriyal, V. Pachauri, S. Ingebrandt, K.-H. Kim, A. L. Sharma, and A. Deep, "Luminescent metal-organic frameworks and their composites: Potential future materials for organic light emitting displays," *Coordination Chemistry Reviews*, vol. 401, 213077, 2019.

[104] L. S. Xie, G. Skorupskii, and M. Dinca, "Electrically conductive metal-organic frameworks," *Chemical Reviews*, vol. 120, no. 16, 8536–8580, 2020.

[105] A. A. Talin, A. Centrone, A. C. Ford, M. E. Foster, V. Stavila, P. Haney, R. A. Kinney, V. Szalai, F. E. Gabaly, H. P. Yoon, F. Léonard, and M. D. Allendorf, "Tunable electrical conductivity in metal-organic framework thin-film devices," *Science*, vol. 434, no. 6166, 66–69, 2014.

[106] M. D. Allendorf, C. A. Bauer, R. K. Bhakta, and R. J. Houk, "Luminescent metal-organic frameworks," *Chemical Society Reviews*, vol. 38, no. 5, 1330–52, 2009.

[107] M. Gutierrez, Y. Zhang, and J. C. Tan, "Confinement of luminescent guests in metal-organic frameworks: Understanding pathways from synthesis and multimodal characterization to potential applications of LG@MOF systems," *Chemical Reviews*, vol. 122, no. 11, 10438–10483, 2022.

[108] P. L. Feng, K. Leong, and M. D. Allendorf, "Charge-transfer guest interactions in luminescent MOFs: Implications for solid-state temperature and environmental sensing," *Dalton Transactions*, vol. 41, no. 29, 8869–77, 2012.

[109] D. Yan, Y. Tang, H. Lin, and D. Wang, "Tunable two-color luminescence and host-guest energy transfer of fluorescent chromophores encapsulated in metal-organic frameworks," *Scientific Reports*, vol. 4, 4337, 2014.

[110] M. Muller, A. Devaux, C. H. Yang, L. De Cola, and R. A. Fischer, "Highly emissive metal-organic framework composites by host-guest chemistry," *Photochemical & Photobiological Sciences*, vol. 9, no. 6, 846–53, 2010.

[111] J. Juan-Alcañiz, J. Gascon, and F. Kapteijn, “Metal–organic frameworks as scaffolds for the encapsulation of active species: State of the art and future perspectives,” *Journal of Materials Chemistry*, vol. 22, no. 20, 2012.

[112] P. Hester, S. Xu, W. Liang, N. Al-Janabi, R. Vakili, P. Hill, C. A. Muryn, X. Chen, P. A. Martin, and X. Fan, “On thermal stability and catalytic reactivity of Zr-based metal–organic framework (UiO-67) encapsulated Pt catalysts,” *Journal of Catalysis*, vol. 340, 85–94, 2016.

[113] A. K. Chaudhari, M. R. Ryder, and J. C. Tan, “Photonic hybrid crystals constructed from in situ host-guest nanoconfinement of a light-emitting complex in metal-organic framework pores,” *Nanoscale*, vol. 8, no. 12, 6851–9, 2016.

[114] A. K. Chaudhari, H. J. Kim, I. Han, and J. C. Tan, “Optochemically responsive 2d nanosheets of a 3d metal-organic framework material,” *Advanced Materials*, vol. 29, no. 27, 1701463, 2017.

[115] Y. Zhang and J. C. Tan, “Electrospun rhodamine@MOF/polymer luminescent fibers with a quantum yield of over 90 %,” *iScience*, vol. 24, no. 9, 103035, 2021.

[116] R. Haldar, R. Matsuda, S. Kitagawa, S. J. George, and T. K. Maji, “Amine-responsive adaptable nanospaces: Fluorescent porous coordination polymer for molecular recognition,” *Angewandte Chemie International Edition*, vol. 53, no. 44, 11772–7, 2014.

[117] M. Gutiérrez, C. Martín, M. Van der Auweraer, J. Hofkens, and J. Tan, “Electroluminescent guest@MOF nanoparticles for thin film optoelectronics and solid-state lighting,” *Advanced Optical Materials*, vol. 8, no. 16, 2000670, 2020.

[118] T. Song, G. Zhang, Y. Cui, Y. Yang, and G. Qian, “Encapsulation of coumarin dye within lanthanide MOFs as highly efficient white-light-emitting phosphors for white LEDs,” *CrystEngComm*, vol. 18, no. 43, 8366–8371, 2016.

[119] Y. Wen, T. Sheng, X. Zhu, C. Zhuo, S. Su, H. Li, S. Hu, Q. L. Zhu, and X. Wu, “Introduction of red-green-blue fluorescent dyes into a metal-organic framework for tunable white light emission,” *Advanced Materials*, vol. 29, no. 37, 2017.

[120] C. Wang, L. Tian, W. Zhu, S. Wang, P. Wang, Y. Liang, W. Zhang, H. Zhao, and G. Li, “Dye@bio-MOF-1 composite as a dual-emitting platform for enhanced detection of a wide range of explosive molecules,” *ACS Applied Materials & Interfaces*, vol. 9, no. 23, 20076–20085, 2017.

[121] X. Zhao, Y. Wang, X. Hao, and W. Liu, “Fluorescent molecule incorporated metal-organic framework for fluoride sensing in aqueous solution,” *Applied Surface Science*, vol. 402, 129–135, 2017.

[122] Y. Gao, J. Wu, J. Wang, Y. Fan, S. Zhang, and W. Dai, “A novel multifunctional p-type semiconductor@MOFs nanoporous platform for simultaneous sensing and photodegradation of tetracycline,” *ACS Applied Materials & Interfaces*, vol. 12, no. 9, 11036–11044, 2020.

[123] T. Mondal, D. Haldar, A. Ghosh, U. K. Ghorai, and S. K. Saha, “A MOF functionalized with cdte quantum dots as an efficient white light emitting phosphor material for applications in displays,” *New Journal of Chemistry*, vol. 44, no. 1, 55–63, 2020.

[124] K. S. Park, Z. Ni, A. P. Côté, J. Y. Choi, R. Huang, F. J. Uribe-Romo, H. K. Chae, M. O'Keeffe, and O. M. Yaghi, "Exceptional chemical and thermal stability of zeolitic imidazolate frameworks," *Proceedings of the National Academy of Sciences of the United States of America*, vol. 103, no. 27, 10186–10191, 2006.

[125] D. Zou, D. Liu, and J. Zhang, "From zeolitic imidazolate framework-8 to metal-organic frameworks (MOFs): Representative substance for the general study of pioneering MOF applications," *Energy & Environmental Materials*, vol. 1, no. 4, 209–220, 2018.

[126] R. Dovesi, R. Orlando, A. Erba, C. M. Zicovich-Wilson, B. Civalleri, S. Casassa, L. Maschio, M. Ferrabone, M. De La Pierre, P. D' Arco, Y. Noël, M. Causà, M. Rérat, and B. Kirtman, "Crystal14 : A program for the ab initio investigation of crystalline solids," *International Journal of Quantum Chemistry*, vol. 114, no. 19, 1287–1317, 2014.

[127] J. P. Perdew, K. Burke, and M. Ernzerhof, "Generalized gradient approximation made simple," *Physical Review Letters*, vol. 77, no. 18, 3865–3868, 1996.

[128] S. Grimme, "Semiempirical gga-type density functional constructed with a long-range dispersion correction," *Journal of Computational Chemistry*, vol. 27, no. 15, 1787–1799, 2006.

[129] X. F. Zhang, J. Zhang, and L. Liu, "Fluorescence properties of twenty fluorescein derivatives: Lifetime, quantum yield, absorption and emission spectra," *Journal of Fluorescence*, vol. 24, no. 3, 819–26, 2014.

[130] D. Magde, G. E. Rojas, and P. G. Seybold, "Solvent dependence of the fluorescence lifetimes of xanthene dyes," *Photochemistry and Photobiology*, vol. 70, no. 5, 737–744, 1999.

[131] M. M. Martin and L. Lindqvist, "The ph dependence of fluorescein fluorescence," *Journal of Luminescence*, vol. 10, no. 6, 381–390, 1975.

[132] Z. Fang, B. Bueken, D. E. De Vos, and R. A. Fischer, "Defect-engineered metal-organic frameworks," *Angewandte Chemie-International Edition*, vol. 54, no. 25, 7234–54, 2015.

[133] S. Dissegna, K. Epp, W. R. Heinz, G. Kieslich, and R. A. Fischer, "Defective metal-organic frameworks," *Advanced Materials*, vol. 30, no. 37, e1704501, 2018.

[134] M. J. Cliffe, W. Wan, X. Zou, P. A. Chater, A. K. Kleppe, M. G. Tucker, H. Wilhelm, N. P. Funnell, F. X. Coudert, and A. L. Goodwin, "Correlated defect nanoregions in a metal-organic framework," *Nature Communications*, vol. 5, 4176, 2014.

[135] G. C. Shearer, S. Chavan, S. Bordiga, S. Svelle, U. Olsbye, and K. P. Lillerud, "Defect engineering: Tuning the porosity and composition of the metal–organic framework UiO-66 via modulated synthesis," *Chemistry of Materials*, vol. 28, no. 11, 3749–3761, 2016.

[136] G. C. Shearer, S. Chavan, J. Ethiraj, J. G. Vitillo, S. Svelle, U. Olsbye, C. Lamberti, S. Bordiga, and K. P. Lillerud, "Tuned to perfection: Ironing out the defects in metal–organic framework UiO-66," *Chemistry of Materials*, vol. 26, no. 14, 4068–4071, 2014.

[137] C. Atzori, G. C. Shearer, L. Maschio, B. Civalleri, F. Bonino, C. Lamberti, S. Svelle, K. P. Lillerud, and S. Bordiga, “Effect of benzoic acid as a modulator in the structure of UiO-66: An experimental and computational study,” *The Journal of Physical Chemistry C*, vol. 121, no. 17, 9312–9324, 2017.

[138] S. Øien, D. Wragg, H. Reinsch, S. Svelle, S. Bordiga, C. Lamberti, and K. P. Lillerud, “Detailed structure analysis of atomic positions and defects in zirconium metal–organic frameworks,” *Crystal Growth & Design*, vol. 14, no. 11, 5370–5372, 2014.

[139] L. Valenzano, B. Civalleri, S. Chavan, S. Bordiga, M. H. Nilsen, S. Jakobsen, K. P. Lillerud, and C. Lamberti, “Disclosing the complex structure of UiO-66 metal organic framework: A synergic combination of experiment and theory,” *Chemistry of Materials*, vol. 23, no. 7, 1700–1718, 2011.

[140] Y. Wang, A. Glenz, M. Muhler, and C. Woll, “A new dual-purpose ultrahigh vacuum infrared spectroscopy apparatus optimized for grazing-incidence reflection as well as for transmission geometries,” *Review of Scientific Instruments*, vol. 80, no. 11, 113108, 2009.

[141] L. Alaerts, E. Seguin, H. Poelman, F. Thibault-Starzyk, P. A. Jacobs, and D. E. De Vos, “Probing the lewis acidity and catalytic activity of the metal-organic framework [Cu3(btc)2] (BTC=benzene-1,3,5-tricarboxylate),” *Chemistry*, vol. 12, no. 28, 7353–63, 2006.

[142] Z. Fang, J. P. Durholt, M. Kauer, W. Zhang, C. Lochenie, B. Jee, B. Albada, N. Metzler-Nolte, A. Poppl, B. Weber, M. Muhler, Y. Wang, R. Schmid, and R. A. Fischer, “Structural complexity in metal-organic frameworks: Simultaneous modification of open metal sites and hierarchical porosity by systematic doping with defective linkers,” *Journal of the American Chemical Society*, vol. 136, no. 27, 9627–36, 2014.

[143] J. Park, Z. U. Wang, L. B. Sun, Y. P. Chen, and H. C. Zhou, “Introduction of functionalized mesopores to metal-organic frameworks via metal-ligand-fragment coassembly,” *Journal of the American Chemical Society*, vol. 134, no. 49, 20110–6, 2012.

[144] H. Wu, Y. S. Chua, V. Krungleviciute, M. Tyagi, P. Chen, T. Yildirim, and W. Zhou, “Unusual and highly tunable missing-linker defects in zirconium metal-organic framework UiO-66 and their important effects on gas adsorption,” *Journal of the American Chemical Society*, vol. 135, no. 28, 10525–32, 2013.

[145] M. Shöâeè, J. R. Agger, M. W. Anderson, and M. P. Attfield, “Crystal form, defects and growth of the metal organic framework HKUST-1 revealed by atomic force microscopy,” *CrystEngComm*, vol. 10, no. 6, 646–648, 2008.

[146] L. Liu, Z. Chen, J. Wang, D. Zhang, Y. Zhu, S. Ling, K. W. Huang, Y. Belmabkhout, K. Adil, Y. Zhang, B. Slater, M. Eddaoudi, and Y. Han, “Imaging defects and their evolution in a metal-organic framework at sub-unit-cell resolution,” *Nature Chemistry*, vol. 11, no. 7, 622–628, 2019.

[147] K. S. Park, Z. Ni, A. P. Cote, J. Y. Choi, R. Huang, F. J. Uribe-Romo, H. K. Chae, M. O’Keeffe, and O. M. Yaghi, “Exceptional chemical and thermal stability of zeolitic imidazolate frameworks,” *Proceedings of the National Academy of Sciences of the United States of America*, vol. 103, no. 27, 10186–10191, 2006.

[148] A. U. Ortiz, A. P. Freitas, A. Boutin, A. H. Fuchs, and F. X. Coudert, "What makes zeolitic imidazolate frameworks hydrophobic or hydrophilic? the impact of geometry and functionalization on water adsorption," *Physical Chemistry Chemical Physics*, vol. 16, no. 21, 9940–9, 2014.

[149] K. Zhang, R. P. Lively, C. Zhang, W. J. Koros, and R. R. Chance, "Investigating the intrinsic ethanol/water separation capability of ZIF-8: An adsorption and diffusion study," *The Journal of Physical Chemistry C*, vol. 117, no. 14, 7214–7225, 2013.

[150] C. Zhang, C. Han, D. S. Sholl, and J. R. Schmidt, "Computational characterization of defects in metal-organic frameworks: Spontaneous and water-induced point defects in ZIF-8," *The Journal of Physical Chemistry Letters*, vol. 7, no. 3, 459, 2016.

[151] C. Han, R. J. Verploegh, and D. S. Sholl, "Assessing the impact of point defects on molecular diffusion in ZIF-8 using molecular simulations," *Journal of Physical Chemistry Letters*, vol. 9, no. 14, 4037–4044, 2018.

[152] W. Cai, T. Lee, M. Lee, W. Cho, D. Y. Han, N. Choi, A. C. Yip, and J. Choi, "Thermal structural transitions and carbon dioxide adsorption properties of zeolitic imidazolate framework-7 (ZIF-7)," *Journal of the American Chemical Society*, vol. 136, no. 22, 7961–71, 2014.

[153] F. Tian, A. M. Cerro, A. M. Mosier, H. K. Wayment-Steele, R. S. Shine, A. Park, E. R. Webster, L. E. Johnson, M. S. Johal, and L. Benz, "Surface and stability characterization of a nanoporous ZIF-8 thin film," *The Journal of Physical Chemistry C*, vol. 118, no. 26, 14449–14456, 2014.

[154] M. J. Lee, H. T. Kwon, and H.-K. Jeong, "Defect-dependent stability of highly propylene-selective zeolitic-imidazolate framework ZIF-8 membranes," *Journal of Membrane Science*, vol. 529, 105–113, 2017.

[155] P. Cheng and Y. H. Hu, "H_2O-functionalized zeolitic zn(2-methylimidazole)2 framework (ZIF-8) for H_2 storage," *The Journal of Physical Chemistry C*, vol. 118, no. 38, 21866–21872, 2014.

[156] R. Gaillac, P. Pullumbi, and F. X. Coudert, "Elate: An open-source online application for analysis and visualization of elastic tensors," *Journal of Physics: Condensed Matter*, vol. 28, no. 27, 275201, 2016.

[157] A. Marmier, Z. A. D. Lethbridge, R. I. Walton, C. W. Smith, S. C. Parker, and K. E. Evans, "ELAM: A computer program for the analysis and representation of anisotropic elastic properties," *Computer Physics Communications*, vol. 181, no. 12, 2102–2115, 2010.

[158] Computer Program, 2015.

[159] J.-C. Tan, B. Civalleri, C.-C. Lin, L. Valenzano, R. Galvelis, P.-F. Chen, T. D. Bennett, C. Mellot-Draznieks, C. M. Zicovich-Wilson, and A. K. Cheetham, "Exceptionally low shear modulus in a prototypical imidazole-based metal-organic framework," *Physical Review Letters*, vol. 108, no. 9, 095502, 2012.

[160] V. Galstyan, "Porous tio(2)-based gas sensors for cyber chemical systems to provide security and medical diagnosis," *Sensors*, vol. 17, no. 12, 2947, 2017.

[161] Y. Li, A.-S. Xiao, B. Zou, H.-X. Zhang, K.-L. Yan, and Y. Lin, “Advances of metal–organic frameworks for gas sensing,” *Polyhedron*, vol. 154, 83–97, 2018.

[162] Z. Z. Lu, R. Zhang, Y. Z. Li, Z. J. Guo, and H. G. Zheng, “Solvatochromic behavior of a nanotubular metal-organic framework for sensing small molecules,” *Journal of the American Chemical Society*, vol. 133, no. 12, 4172–4, 2011.

[163] R. B. Lin, S. Y. Liu, J. W. Ye, X. Y. Li, and J. P. Zhang, “Photoluminescent metal-organic frameworks for gas sensing,” *Advanced Science*, vol. 3, no. 7, 1500434, 2016.

[164] M. D. Allendorf, R. Medishetty, and R. A. Fischer, “Guest molecules as a design element for metal–organic frameworks,” *MRS Bulletin*, vol. 41, no. 11, 865–869, 2016.

[165] N. T. Shaked, “Quantitative phase microscopy of biological samples using a portable interferometer,” *Optics Letters*, vol. 37, no. 11, 2016–2018, 2012.

[166] N. Sabri, S. A. Aljunid, M. S. Salim, R. B. Ahmad, and R. Kamaruddin, “Toward optical sensors: Review and applications,” *Journal of Physics: Conference Series*, vol. 423, 012064, 2013.

[167] A. S. Babal, L. Donà, M. R. Ryder, K. Titov, A. K. Chaudhari, Z. Zeng, C. S. Kelley, M. D. Frogley, G. Cinque, B. Civalleri, and J.-C. Tan, “Impact of pressure and temperature on the broadband dielectric response of the HKUST-1 metal–organic framework,” *The Journal of Physical Chemistry C*, vol. 123, no. 48, 29427–29435, 2019.

[168] T. S. Park and J.-Y. Yoon, “Smartphone detection of *Escherichia coli* from field water samples on paper microfluidics,” *IEEE Sensors Journal*, vol. 15, no. 3, 1902–1907, 2015.

[169] I. Moreno, J. A. Davis, I. Ruiz, and D. M. Cottrell, “Decomposition of radially and azimuthally polarized beams using a circular-polarization and vortex-sensing diffraction grating,” *Optics Express*, vol. 18, no. 7, 7173–7183, 2010.

[170] S. Achmann, G. Hagen, J. Kita, I. M. Malkowsky, C. Kiener, and R. Moos, “Metal-organic frameworks for sensing applications in the gas phase,” *Sensors*, vol. 9, no. 3, 1574–89, 2009.

[171] K. M. Goeders, J. S. Colton, and L. A. Bottomley, “Microcantilevers: Sensing chemical interactions via mechanical motion,” *Chemical Reviews*, vol. 108, 522–542, 2008.

[172] J. W. Grate, “Acoustic wave microsensor arrays for vapor sensing,” *Chemical Reviews*, vol. 100, 2627–2648, 200.

[173] G. Lu, O. K. Farha, L. E. Kreno, P. M. Schoenecker, K. S. Walton, R. P. Van Duyne, and J. T. Hupp, “Fabrication of metal-organic framework-containing silica-colloidal crystals for vapor sensing,” *Advanced Materials*, vol. 23, no. 38, 4449–52, 2011.

[174] R. Grunker, V. Bon, A. Heerwig, N. Klein, P. Muller, U. Stoeck, I. A. Baburin, U. Mueller, I. Senkovska, and S. Kaskel, “Dye encapsulation inside a new mesoporous metal-organic framework for multifunctional solvatochromic-response function,” *Chemistry*, vol. 18, no. 42, 13299–303, 2012.

[175] L. Chen, J. W. Ye, H. P. Wang, M. Pan, S. Y. Yin, Z. W. Wei, L. Y. Zhang, K. Wu, Y. N. Fan, and C. Y. Su, "Ultrafast water sensing and thermal imaging by a metal-organic framework with switchable luminescence," *Nature Communications*, vol. 8, 15985, 2017.

[176] F. Drache, V. Bon, I. Senkovska, M. Adam, A. Eychmüller, and S. Kaskel, "Vapochromic luminescence of a zirconium-based metal–organic framework for sensing applications," *European Journal of Inorganic Chemistry*, vol. 2016, no. 27, 4483–4489, 2016.

[177] P. L. Wang, L. H. Xie, E. A. Joseph, J. R. Li, X. O. Su, and H. C. Zhou, "Metal-organic frameworks for food safety," *Chemical Reviews*, vol. 119, no. 18, 10638–10690, 2019.

[178] Z. Xie, L. Ma, K. E. deKrafft, A. Jin, and W. Lin, "Porous phosphorescent coordination polymers for oxygen sensing," *Journal of the American Chemical Society*, vol. 132, no. 3, 922–923, 2009.

[179] J.-W. Ye, H.-L. Zhou, S.-Y. Liu, X.-N. Cheng, R.-B. Lin, X.-L. Qi, J.-P. Zhang, and X.-M. Chen, "Encapsulating pyrene in a metal–organic zeolite for optical sensing of molecular oxygen," *Chemistry of Materials*, vol. 27, no. 24, 8255–8260, 2015.

[180] Z. Dou, J. Yu, Y. Cui, Y. Yang, Z. Wang, D. Yang, and G. Qian, "Luminescent metal-organic framework films as highly sensitive and fast-response oxygen sensors," *Journal of the American Chemical Society*, vol. 136, no. 15, 5527–30, 2014.

[181] L.-H. Xie, X.-M. Liu, T. He, and J.-R. Li, "Metal-organic frameworks for the capture of trace aromatic volatile organic compounds," *Chem*, vol. 4, no. 8, 1911–1927, 2018.

[182] U. Simon, U. Flesch, W. Maunz, R. Mueller, and C. Plog, "The effect of NH_3 on the ionic conductivity of dehydrated zeolites na beta and h beta," *Microporous and Mesoporous Materials*, vol. 21, 111–116, 1998.

[183] R. Kaur, A. K. Paul, and A. Deep, "Highly sensitive chemosensing of trinitrotoluene with europium organic framework/gold nanoparticle composite," *Inorganic Chemistry Communications*, vol. 43, 118–120, 2014.

[184] A. Lan, K. Li, H. Wu, D. H. Olson, T. J. Emge, W. Ki, M. Hong, and J. Li, "A luminescent microporous metal-organic framework for the fast and reversible detection of high explosives," *Angewandte Chemie International Edition*, vol. 48, no. 13, 2334–8, 2009.

[185] C. Montoro, F. Linares, E. Q. Procopio, I. Senkovska, S. Kaskel, S. Galli, N. Masciocchi, E. Barea, and J. A. Navarro, "Capture of nerve agents and mustard gas analogues by hydrophobic robust MOF-5 type metal-organic frameworks," *Journal of the American Chemical Society*, vol. 133, no. 31, 11888–91, 2011.

[186] R. Sesha Vemuri and P. Armatis, "An overview of detection and neutralization of chemical warfare agents using metal organic frameworks," *Journal of Bioterrorism & Biodefense*, vol. 6, no. 3, 1000137, 2015.

[187] X. Huang, Z. Gong, and Y. Lv, “Advances in metal-organic frameworks-based gas sensors for hazardous substances,” *TrAC Trends in Analytical Chemistry*, vol. 153, 116644, 2022.

[188] A. Rydosz, “Sensors for enhanced detection of acetone as a potential tool for noninvasive diabetes monitoring,” *Sensors*, vol. 18, no. 7, 2298, 2018.

[189] W. Li, X. Wu, N. Han, J. Chen, X. Qian, Y. Deng, W. Tang, and Y. Chen, “MOF-derived hierarchical hollow ZnO nanocages with enhanced low-concentration VOCs gas-sensing performance,” *Sensors and Actuators B: Chemical*, vol. 225, 158–166, 2016.

[190] F. Gu, H. Chen, D. Han, and Z. Wang, “Metal–organic framework derived Au@ZnO yolk–shell nanostructures and their highly sensitive detection of acetone,” *RSC Advances*, vol. 6, no. 35, 29727–29733, 2016.

[191] I. Ellerna, A. Venkatasubramaniana, J. H. Leeb, P. J. Hesketha, V. Stavilac, M.D.Allendorfc, and A. Robinsond, “Characterization of piezoresistive microcantilever sensors with metal organic frameworks for the detection of volatile organic compounds,” *ECS Transactions*, vol. 50, 469, 2013.

[192] S. Homayoonnia and S. Zeinali, “Design and fabrication of capacitive nanosensor based on MOF nanoparticles as sensing layer for VOCs detection,” *Sensors and Actuators B: Chemical*, vol. 237, 776–786, 2016.

[193] D. Colognesi, M. Celli, F. Cilloco, R. J. Newport, S. F. Parker, V. Rossi-Albertini, F. Sacchetti, J. Tomkinson, and M. Zoppi, “TOSCA neutron spectrometer: The final configuration,” *Applied Physics A-Materials Science & Processing*, vol. 74, 64–66, 2002.

[194] R. S. Pinna, M. Zanetti, S. Rudić, S. F. Parker, J. Armstrong, S. P. Waller, D. Zacek, C. Smith, S. M. Harrison, G. Gorini, and F. Fernandez-Alonso, “The TOSCA spectrometer at isis: The guide upgrade and beyond,” *Journal of Physics: Conference Series*, vol. 1021, 012029, 2018.

[195] S. F. Parker, F. Fernandez-Alonso, A. J. Ramirez-Cuesta, J. Tomkinson, S. Rudic, R. S. Pinna, G. Gorini, and J. Fernández Castañon, “Recent and future developments on TOSCA at isis,” *Journal of Physics: Conference Series*, vol. 554, 012003, 2014.

[196] O. Arnold, J. C. Bilheux, J. M. Borreguero, A. Buts, S. I. Campbell, L. Chapon, M. Doucet, N. Draper, R. Ferraz Leal, M. A. Gigg, V. E. Lynch, A. Markvardsen, D. J. Mikkelson, R. L. Mikkelson, R. Miller, K. Palmen, P. Parker, G. Passos, T. G. Perring, P. F. Peterson, S. Ren, M. A. Reuter, A. T. Savici, J. W. Taylor, R. J. Taylor, R. Tolchenov, W. Zhou, and J. Zikovsky, “Mantid—data analysis and visualization package for neutron scattering andµsr experiments,” *Nuclear Instruments and Methods in Physics Research Section A: Accelerators, Spectrometers, Detectors and Associated Equipment*, vol. 764, 156–166, 2014.

[197] L. Dona, J. G. Brandenburg, I. J. Bush, and B. Civalleri, “Cost-effective composite methods for large-scale solid-state calculations,” *Faraday Discussions*, vol. 224, 292–308, 2020.

[198] I. J. Bush, S. Tomić, B. G. Searle, G. Mallia, C. L. Bailey, B. Montanari, L. Bernasconi, J. M. Carr, and N. M. Harrison, "Parallel implementation of the ab initio crystal program: Electronic structure calculations for periodic systems," *Proceedings of the Royal Society A: Mathematical, Physical and Engineering Sciences*, vol. 467, no. 2131, 2112–2126, 2011.

[199] L. Dona, J. G. Brandenburg, and B. Civalleri, "Extending and assessing composite electronic structure methods to the solid state," *The Journal of Chemical Physics*, vol. 151, no. 12, 121101, 2019.

[200] B. E. Souza, L. Dona, K. Titov, P. Bruzzese, A. S. Babal, A. F. Möslein, M. D. Frogley, G. Wolna, G. Cinque, B. Civalleri, and J. C. Tan, "Elucidating the drug release from metal-organic framework nanocomposites via in situ synchrotron microspectroscopy and theoretical modelling," *ACS Applied Materials & Interfaces*, vol. 12, 5147–5156, 2020.

[201] L. Dona, J. G. Brandenburg, and B. Civalleri, "Metal-organic frameworks properties from hybrid density functional approximations," *The Journal of Chemical Physics*, vol. 156, no. 9, 094706, 2022.

[202] F. Pascale, C. Zicovich-Wilson, F. Lopez, B. Civalleri, R. Orlando, and R. Dovesi, "The calculation of the vibration frequencies of crystalline compounds and its implementation in the crystal code," *Journal of Computational Chemistry*, vol. 25, 888–897, 2004.

[203] F. Fernandez-Alonso and D. L. Price, *Neutron Scattering Fundamentals, Experimental Methods in the Physical Sciences.* New York: Academic Press, 2013.

[204] K. Titov, "Towards practical metal-organic framework materials: Operando and in situ studies by leveraging synchrotron and neutron sources," DPhil Thesis, 2019.

[205] A. Phan, C. J. Doonan, F. J. Uribe-Romo, C. B. Knobler, M. O'Keeffe, and O. M. Yaghi, "Synthesis, structure, and carbon dioxide capture properties of zeolitic imidazolate frameworks," *Accounts of Chemical Research*, vol. 43, no. 1, 58–67, 2010.

[206] R. P. Lively, M. E. Dose, J. A. Thompson, B. A. McCool, R. R. Chance, and W. J. Koros, "Ethanol and water adsorption in methanol-derived ZIF-71," *Chemical Communications*, vol. 47, no. 30, 8667–9, 2011.

[207] S. Liu, G. Liu, X. Zhao, and W. Jin, "Hydrophobic-ZIF-71 filled PEBA mixed matrix membranes for recovery of biobutanol via pervaporation," *Journal of Membrane Science*, vol. 446, 181–188, 2013.

[208] J. Cravillon, R. Nayuk, S. Springer, A. Feldhoff, K. Huber, and M. Wiebcke, "Controlling zeolitic imidazolate framework nano- and microcrystal formation: Insight into crystal growth by time-resolved in situ static light scattering," *Chemistry of Materials*, vol. 23, no. 8, 2130–2141, 2011.

[209] N. A. Wynblatt P.; Gjostein, "Particle growth in model supported metal catalysts," *Acta Metallurgica*, vol. 24, 1165–1174, 1976.

[210] A. Kolmakov and D. W. Goodman, "In situ scanning tunneling microscopy of oxide-supported metal clusters: Nucleation, growth, and thermal evolution of individual particles," *The Chemical Record*, vol. 2, no. 6, 446–57, 2002.

[211] W. Ostwald, “Studien über die bildung und umwandlung fester körper,” *Zeitschrift für Physikalische Chemie*, vol. 22, 289–330, 1897.

[212] J. F. Penn R. L.; Banfield, “Imperfect oriented attachment: Dislocation generation in defect-free nanocrystals,” *Science*, vol. 281, no. 5379, 969–971, 1998.

[213] H. Yin, A. Khosravi, L. O’Connor, A. Q. Tagaban, L. Wilson, B. Houck, Q. Liu, and M. L. Lind, “Effect of ZIF-71 particle size on free-standing ZIF-71/pdms composite membrane performances for ethanol and 1-butanol removal from water through pervaporation,” *Industrial & Engineering Chemistry Research*, vol. 56, no. 32, 9167–9176, 2017.

[214] S. Japip, H. Wang, Y. Xiao, and T. Shung Chung, “Highly permeable zeolitic imidazolate framework (ZIF)-71 nano-particles enhanced polyimide membranes for gas separation,” *Journal of Membrane Science*, vol. 467, 162–174, 2014.

[215] Y. Li, L. H. Wee, J. A. Martens, and I. F. J. Vankelecom, “ZIF-71 as a potential filler to prepare pervaporation membranes for bio-alcohol recovery,” *Journal of Materials Chemistry A*, vol. 2, no. 26, 10034–10040, 2014.

[216] M. Tu, C. Wiktor, C. Rosler, and R. A. Fischer, “Rapid room temperature syntheses of zeolitic-imidazolate framework (ZIF) nanocrystals,” *Chemical Communications*, vol. 50, no. 87, 13258–60, 2014.

[217] L. H. Wee, Y. Li, K. Zhang, P. Davit, S. Bordiga, J. Jiang, I. F. J. Vankelecom, and J. A. Martens, “Submicrometer-sized ZIF-71 filled organophilic membranes for improved bioethanol recovery: Mechanistic insights by monte carlo simulation and FTIR spectroscopy,” *Advanced Functional Materials*, vol. 25, no. 4, 516–525, 2015.

[218] Y.-H. Wang, Q. Shi, H. Xu, and J.-X. Dong, “The synthesis and tribological properties of small- and large-sized crystals of zeolitic imidazolate framework-71,” *RSC Advances*, vol. 6, no. 22, 18052–18059, 2016.

[219] Y. Zhang, M. Gutierrez, A. K. Chaudhari, and J. C. Tan, “Dye-encapsulated zeolitic imidazolate framework (ZIF-71) for fluorochromic sensing of pressure, temperature, and volatile solvents,” *ACS Applied Materials & Interfaces*, vol. 12, no. 33, 37477–37488, 2020.

[220] P. J. Dauenhauer and O. A. Abdelrahman, “A universal descriptor for the entropy of adsorbed molecules in confined spaces,” *ACS Central Science*, vol. 4, no. 9, 1235–1243, 2018.

[221] A. Nalaparaju, X. S. Zhao, and J. W. Jiang, “Molecular understanding for the adsorption of water and alcohols in hydrophilic and hydrophobic zeolitic metal-organic frameworks,” *Journal of Physical Chemistry C*, vol. 114, 11542–11550, 2010.

[222] X. Dong and Y. S. Lin, “Synthesis of an organophilic ZIF-71 membrane for pervaporation solvent separation,” *Chemical Communications*, vol. 49, no. 12, 1196–8, 2013.

[223] T. Yang, Y. Xiao, and T.-S. Chung, “Poly-/metal-benzimidazole nano-composite membranes for hydrogen purification,” *Energy & Environmental Science*, vol. 4, no. 10, 4171, 2011.

[224] T.-S. Chung, L. Y. Jiang, Y. Li, and S. Kulprathipanja, "Mixed matrix membranes (MMMs) comprising organic polymers with dispersed inorganic fillers for gas separation," *Progress in Polymer Science*, vol. 32, no. 4, 483–507, 2007.

[225] S. Bendt, M. Hovestadt, U. Böhme, C. Paula, M. Döpken, M. Hartmann, and F. J. Keil, "Olefin/paraffin separation potential of ZIF-9 and ZIF-71: A combined experimental and theoretical study," *European Journal of Inorganic Chemistry*, vol. 2016, no. 27, 4440–4449, 2016.

[226] C. Gücüyener, J. v. d. Bergh, J. Gascon, and F. Kapteijn, "Ethane/ethene separation turned on its head: Selective ethane adsorption on the metal-organic framework ZIF-7 through a gate-opening mechanism," *Journal of the American Chemical Society*, vol. 132, no. 50, 17704–17706, 2010.

[227] I. Khay, G. Chaplais, H. Nouali, G. Ortiz, C. Marichal, and J. Patarin, "Assessment of the energetic performances of various ZIFs with sod or rho topology using high pressure water intrusion-extrusion experiments," *Dalton Transactions*, vol. 45, no. 10, 4392–400, 2016.

[228] G. Ortiz, H. Nouali, C. Marichal, G. Chaplais, and J. Patarin, "Energetic performances of "ZIF-71–aqueous solution" systems: A perfect shock-absorber with water," *The Journal of Physical Chemistry C*, vol. 118, no. 37, 21316–21322, 2014.

[229] Y. Sun, S. M. J. Rogge, A. Lamaire, S. Vandenbrande, J. Wieme, C. R. Siviour, V. Van Speybroeck, and J. C. Tan, "High-rate nanofluidic energy absorption in porous zeolitic frameworks," *Nature Materials*, vol. 20, no. 7, 1015–1023, 2021.

[230] M. Tu, B. Xia, D. E. Kravchenko, M. L. Tietze, A. J. Cruz, I. Stassen, T. Hauffman, J. Teyssandier, S. De Feyter, Z. Wang, R. A. Fischer, B. Marmiroli, H. Amenitsch, A. Torvisco, M. J. Velasquez-Hernandez, P. Falcaro, and R. Ameloot, "Direct x-ray and electron-beam lithography of halogenated zeolitic imidazolate frameworks," *Nature Materials*, vol. 20, no. 1, 93–99, 2021.

[231] M. Tu, M. L. Díaz Ramírez, I. A. Ibarra, J. Hofkens, and R. Ameloot, "Fluorescence photoswitching in a series of metal-organic frameworks loaded with different anthracenes," *European Journal of Inorganic Chemistry*, vol. 2021, no. 29, 2986–2992, 2021.

[232] A. S. Babal, S. Mollick, W. Kamal, S. Elston, A. A. Castrejón-Pita, S. M. Morris, and J.-C. Tan, "Parts-per-billion (ppb) selective iodine sensors leveraging metal-organic framework nanoenvironmen," *Materials Today*, vol. 58, 91–99, 2022.

[233] T. Zhou, Y. Sang, Y. Sun, C. Wu, X. Wang, X. Tang, T. Zhang, H. Wang, C. Xie, and D. Zeng, "Gas adsorption at metal sites for enhancing gas sensing performance of ZnO@ZIF-71 nanorod arrays," *Langmuir*, vol. 35, no. 9, 3248–3255, 2019.

[234] T. Zhou, S. Chen, X. Wang, C. Xie, and D. Zeng, "Catalytic activation of cobalt doping sites in ZIF-71-coated ZnO nanorod arrays for enhancing gas-sensing performance to acetone," *ACS Applied Materials & Interfaces*, vol. 12, no. 43, 48948–48956, 2020.

[235] G. Rauhut and P. Pulay, "Transferable scaling factors for density functional derived vibrational force fields," *Journal of Physical Chemistry*, vol. 99, no. 10, 3093–3100, 1995.

[236] B. Mortada, G. Chaplais, H. Nouali, C. Marichal, and J. Patarin, “Phase transformations of metal–organic frameworks MAF-6 and ZIF-71 during intrusion–extrusion experiments,” *The Journal of Physical Chemistry C*, vol. 123, no. 7, 4319–4328, 2019.

[237] E. F. Baxter, T. D. Bennett, A. B. Cairns, N. J. Brownbill, A. L. Goodwin, D. A. Keen, P. A. Chater, F. Blanc, and A. K. Cheetham, “A comparison of the amorphization of zeolitic imidazolate frameworks (ZIFs) and aluminosilicate zeolites by ball-milling,” *Dalton Transactions*, vol. 45, no. 10, 4258–68, 2016.

[238] L. H. Wee, S. Vandenbrande, S. M. J. Rogge, J. Wieme, K. Asselman, E. O. Jardim, J. Silvestre-Albero, J. A. R. Navarro, V. Van Speybroeck, J. A. Martens, and C. E. A. Kirschhock, “Chlorination of a zeolitic-imidazolate framework tunes packing and van der waals interaction of carbon dioxide for optimized adsorptive separation,” *Journal of the American Chemical Society*, vol. 143, no. 13, 4962–4968, 2021.

[239] J. Maul, M. R. Ryder, M. T. Ruggiero, and A. Erba, “Pressure-driven mechanical anisotropy and destabilization in zeolitic imidazolate frameworks,” *Physical Review B*, vol. 99, no. 1, 014102, 2019.

[240] Z. Zeng and J.-C. Tan, “AFM nanoindentation to quantify mechanical properties of nano- and micron-sized crystals of a metal–organic framework material,” *ACS Applied Materials & Interfaces*, vol. 9, no. 45, 39839–39854, 2017.

[241] W. C. Oliver and G. M. Pharr, “Measurement of hardness and elastic modulus by instrumented indentation: Advances in understanding and refinements to methodology,” *Journal of Materials Research and Technology*, vol. 19, 3–20, 2004.

[242] K. J. Kaltenecker, T. Golz, E. Bau, and F. Keilmann, “Infrared-spectroscopic, dynamic near-field microscopy of living cells and nanoparticles in water,” *Scientific Reports*, vol. 11, no. 1, 21860, 2021.